BULLETIN OF THE EARTHQUAKE RESEARCH INSTITUTE,
UNIVERSITY OF TOKYO. Vol. 38, Part 2. June, 1960.

東京大学
地震研究所彙報

第 38 号　第 2 冊

昭和 35 年 6 月

目　次

論文及報告

頁

10. 褶曲境界面における弾性波の反射，屈折
第1報 SH 波入射の場合（英文）……浅野周三 177
11. 地球熱学（第5報）堆積岩における熱伝導度と含水量の関係（英文）……宝来帰一・上田誠也 199
12. 大地震発震スペクトルの方位特性に関する一つの試み（アラスカ地震の場合）（英文）……笠原慶一 207
13. コロンビア型地震計による表面波の観測(第一報) ―海洋底を伝わるレーリー波の分散―（英文）……三東哲夫 219
14. 脈動源について（第三報）―波浪観測点における脈動観測―（英文）……三東哲夫 241
15. 蔵王火山の地質学的研究（第5報）（英文）……市村毅 255
16. 浅間山仏岩火山体岩石の主化学成分組成（英文）……南英一・松井義人 291
17. 妙高火山東麓に分布する火砕堆積物（英文）……村井勇 307
18. プロトン磁力計による地磁気傾度計（英文）……力武常次・棚岡巖 317
19. 木造家屋の耐震性（第3報）（英文）……西村源六郎・鈴木正治 329
20. 地震計用トランジスター増幅器（邦文）……松本英照 345
21. 和歌山―御坊間水準測量結果（邦文）……宮村摂三・岡田惇 355

所　報

(The titles in occidental languages are given on the back cover.)

地震研究所彙報は，年4回定期に（ただし，第1号より第6号までは不定期に，第7号は3冊として刊行された），彙報別冊は不定期に刊行される．

この彙報に載せられた論文及び報告についての責任は，すべてその著者のみにある．

この彙報についての照会通信は，すべて東京大学地震研究所長にあてられたい．

The Bulletin is published quarterly. (Vols. 1–6 were published at irregular intervals and Vol. 7 consisted of three parts.)
Supplementary Volume is published at irregular interval.

The authors of the papers alone are responsible for the statements and opinions contained in their respective papers.

All communications relating to this Bulletin should be addressed to the Director of the Earthquake Research Institute, University of Tokyo, Japan.

Earthquake Research Institute, University of Tokyo
Address:
No. 1, Motofuji-cho, Bunkyo-ku,
Tokyo Metropolis, Japan.
Telephone: 921-3161-Extension 6506
Cable address: ZISINKEN, TOKYO.

東京大学地震研究所
所在地
東京都文京区本富士町一番地
電話 小石川 921—3161 (代) 構内 6506
電略 ブンケウ トウダイ ヂシン

BULLETIN OF THE EARTHQUAKE
RESEARCH INSTITUTE
Vol. 38 (1960), pp. 177-197

10. *Reflection and Refraction of Elastic Waves at a Corrugated Boundary Surface. Part I. The Case of Incidence of SH Wave.*

By Shûzô ASANO,

Earthquake Research Institute.

(Read Oct. 27, 1959; Jan. 26, 1960.—Received Feb. 22, 1960.)

1. Introduction

To say nothing of the small scale geological structures near the earth's surface, we have good reason to believe that the crustal layers in the earth's interior are not restricted to plane surfaces. It seems to the writer that the following facts may be attributed at least in part to the undulations of the boundary surfaces of the earth's crustal layers.

1) Gravity anomalies which are well-explained by the Airy hypothesis of isostasy.

2) Irregular intensity distributions of earthquakes other than those attributable to the surface ground conditions.

3) The obliteration of reflected artificial earthquake waves from the Moho (Mohorovičić discontinuity) as observed by H. E. Tatel, L. H. Adams, and M. A. Tuve in western California[1] where the lower crustal boundary is considered to be roughly disturbed as is easily inferred from the isostatic view point by the topographical irregularity.

4) The larger attenuation of artificial seismic waves across the Andes as compared to the path parallel to the mountain range, as observed by H. E. Tatel, M. A. Tuve and their colleagues.[2]

In view of these facts, we are naturally led to the inference that the roughness or the irregular undulation of a boundary surface of the media, through which the seismic wave is propagated, plays a certain

1) H. E. TATEL, L. H. ADAMS, and M. A. TUVE, *Proc. Amer. Phil. Soc.*, **97** (1953), 658.

2) H. E. TATEL, M. A. TUVE, and COLLEAGUES, "Abstract of paper presented at 39th Annual Meeting of American Geophysical Union held in 1958," *Trans. Amer. Geophys. Un.*, **39** (1958), 533.

role in the energy distribution of reflected and refracted waves according to the relative situations to the boundary surface. It is therefore desirable to study the effect of the undulation of the boundary surface on the reflection and refraction of elastic waves theoretically. In this paper the writer intends to study this problem under a simplified assumption that the undulation of the boundary surface is only in one direction, and the incident wave is a plane wave whose plane of incidence is perpendicular to the boundary surface.

Although there may be various methods to deal with this sort of problem, in this paper, the writer adopted the method which was first used by Lord Rayleigh in his classical theory of gratings,[3] and recently applied by R. Sato in his theoretical study of reflection of elastic waves at an undulatory free surface.[4]

In the present part, discussions are restricted to the case of incident SH waves, and the other cases of P and SV waves will be reported in the near future.

2. Equation of boundary surface

The coordinate axes were taken as shown in Fig. 1. That is, x- and y-axis are on the horizontal surface, and z-axis is taken vertically downwards. The equation of boundary surface is given by $z=\zeta$, where ζ is a periodic function of x and independent of y, the mean value of which being zero. Then ζ can be represented by Fourier's series as follows:

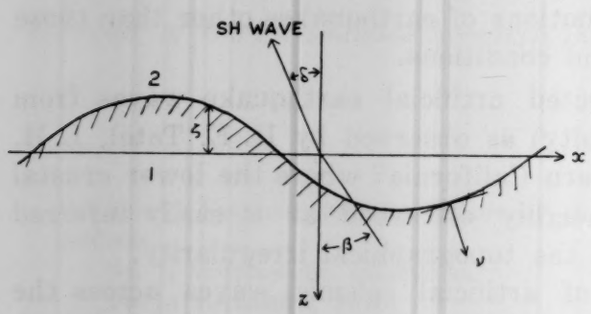

Fig. 1.

$$\zeta=\sum_{n=1}^{\infty}(\zeta_n e^{inpx}+\zeta_{-n}e^{-inpx})$$

$$=c_1\cos px+c_2\cos 2px+s_2\sin 2px+\cdots+c_n\cos npx+s_n\sin npx+\cdots,$$

where

$$\zeta_1=\zeta_{-1}=c_1/2\,,$$

$$\zeta_{\pm n}=(c_n\mp is_n)/2\,.$$

3) LORD RAYLEIGH, *Proc. Roy. Soc. Lond.*, **A**, **79** (1907), 399.

4) R. SATO, *Zisin*, [ii], **8** (1955), 8, (in Japanese).

When the boundary surface is expressible by one cosine term, i.e. $\zeta = c\cos px$, the wave length of the corrugation is $2\pi/p$.

3. Equations of motion, and incident, reflected and refracted wave

Let us consider the case when the plane SH wave with period of $2\pi/\omega$ is incident with an angle of β to z-axis from the lower to the upper medium. The quantities concerning the lower medium will be shown by suffix 1 and those of the upper medium, by suffix 2. If the displacement v of incident SH wave is parallel to the y-axis, the equations of motion are as follows:

$$(\nabla^2+\sigma_i h_i^2)v_i=0\ , \qquad (i=1,\ 2)$$

where ∇^2=Laplacian,

$\sigma_i=(\lambda_i+2\mu_i)/\mu_i$,

$h_i^2=\rho_i\omega^2/(\lambda_i+2\mu_i)$,

λ_i, μ_i=Lamé's constants,

ρ_i=density.

It is sufficient to consider only the following solutions of above equations if the boundary surface is plane.

Incident wave: $v_1=e^{i\sqrt{\sigma_1}h_1(V_{s1}t+z\cos\beta+x\sin\beta)}$,

Regularly reflected wave: $v_1=B_0e^{i\sqrt{\sigma_1}h_1(V_{s1}t-z\cos\beta+x\sin\beta)}$,

Regularly refracted wave: $v_2=D_0e^{i\sqrt{\sigma_2}h_2(V_{s2}t+z\cos\delta+x\sin\delta)}$,

where V_{s1} and V_{s2} are the velocity of S waves in the lower and upper medium respectively and δ is the angle of refraction which is connected with incident angle β by Snell's law

$$\sqrt{\sigma_1}h_1\sin\beta=\sqrt{\sigma_2}h_2\sin\delta\ .$$

In the case of corrugated boundary surface it is necessary to take, in addition to these regular waves, the effect of corrugation on reflections and refractions of elastic waves into consideration and introduce the following irregular waves:

(1) Irregularly reflected waves whose spectrum of the nth order is:

$$v_1=B_n e^{i\sqrt{\sigma_1}h_1(V_{s1}t-z\cos\beta_n+x\sin\beta_n)}+B'_n e^{i\sqrt{\sigma_1}h_1(V_{s1}t-z\cos\beta'_n+x\sin\beta'_n)}$$

(2) Irregularly refracted waves whose spectrum of the nth order is:

$$v_2=D_n e^{i\sqrt{\sigma_2}h_2(V_{s2}t+z\cos\delta_n+x\sin\delta_n)}+D'_n e^{i\sqrt{\sigma_2}h_2(V_{s2}t+z\cos\delta'_n+x\sin\delta'_n)}$$

where β_n, β'_n, δ_n and δ'_n are given by the following spectrum theorem,

$$\sin\beta_n-\sin\beta=np/(\sqrt{\sigma_1}h_1)\ ,\qquad \sin\beta'_n-\sin\beta=-np/(\sqrt{\sigma_1}h_1)\ ,$$
$$\sin\delta_n-\sin\delta=np/(\sqrt{\sigma_2}h_2)\ ,\qquad \sin\delta'_n-\sin\delta=-np/(\sqrt{\sigma_2}h_2)\ .$$

The above relations have physical meanings that only in the directions with difference of path of n wave lengths of SH wave the waves can propagate. The variation of v, for example for irregularly reflected waves, in the direction parallel to x-axis at a certain fixed level z in the case of normal incidence, i.e. $\beta=0$ is given by the sum of factors $e^{i\sqrt{\sigma_1}h_1x\sin\beta_n}=e^{inpx}$ and $e^{i\sqrt{\sigma_1}h_1x\sin\beta'_n}=e^{-inpx}$. That is to say, in the x-direction at a fixed level, the variation of v is a harmonic function of x. This agrees with that of diffraction of light.

The total displacement v_1 in the lower medium is the sum of those of incident, regularly reflected and irregularly reflected waves. That is, by the spectrum theorem and neglecting common time factor $e^{i\omega t}$,

$$v_1=e^{i\sqrt{\sigma_1}h_1x\sin\beta}[e^{i\sqrt{\sigma_1}h_1z\cos\beta}+B_0e^{-i\sqrt{\sigma_1}h_1z\cos\beta}+\sum_n B_n e^{inpx}e^{-i\sqrt{\sigma_1}h_1z\cos\beta_n}$$
$$+\sum_n B'_n e^{-inpx}e^{-i\sqrt{\sigma_1}h_1z\cos\beta'_n}]\ .$$

Similarly,

$$v_2=e^{i\sqrt{\sigma_1}h_1x\sin\beta}[D_0e^{i\sqrt{\sigma_2}h_2z\cos\delta}+\sum_n D_n e^{inpx}e^{i\sqrt{\sigma_2}h_2z\cos\delta_n}$$
$$+\sum_n D'_n e^{-inpx}e^{i\sqrt{\sigma_2}h_2z\cos\delta'_n}]\ .$$

4. Boundary conditions

The boundary conditions are given by the condition that y-component of normal stress of boundary surface and the displacement are continuous at $z=\zeta$.

The y-component of normal stress of boundary surface Y_ν is given as

$$Y_\nu=[Y_z-Y_x\zeta']/\sqrt{1+\zeta'^2}\ .$$

In the case of SH wave, $Y_\nu=\mu(\partial v/\partial z-\partial v/\partial x\cdot\zeta')/\sqrt{1+\zeta'^2}$. Since ζ' is independent of medium, and depends only on the functional form of ζ, it is enough to ensure the continuity of $\sqrt{1+\zeta'^2}\cdot Y_\nu$ at $z=\zeta$ instead of the condition of continuity of Y_ν. From the condition of continuity of v at $z=\zeta$,

$$\begin{aligned}&e^{i\sqrt{\sigma_1}h_1\zeta\cos\beta}+B_0e^{-i\sqrt{\sigma_1}h_1\zeta\cos\beta}+\sum_n B_ne^{inpx}e^{-i\sqrt{\sigma_1}h_1\zeta\cos\beta_n}\\&\quad+\sum_n B'_ne^{-inpx}e^{-i\sqrt{\sigma_1}h_1\zeta\cos\beta'_n}\\&=D_0e^{i\sqrt{\sigma_2}h_2\zeta\cos\delta}+\sum_n D_ne^{inpx}e^{i\sqrt{\sigma_2}h_2\zeta\cos\delta_n}+\sum_n D'_ne^{-inpx}e^{i\sqrt{\sigma_2}h_2\zeta\cos\delta'_n}.\end{aligned}\tag{1}$$

From the condition of continuity of $\sqrt{1+\zeta'^2}\cdot Y_\nu$ at $z=\zeta$,

$$\begin{aligned}&\mu_1[\sqrt{\sigma_1}h_1(\cos\beta-\zeta'\sin\beta)e^{i\sqrt{\sigma_1}h_1\zeta\cos\beta}-\sqrt{\sigma_1}h_1(\cos\beta+\zeta'\sin\beta)B_0e^{-i\sqrt{\sigma_1}h_1\zeta\cos\beta}\\&\quad-\sum_n\{\sqrt{\sigma_1}h_1\cos\beta_n+(\sqrt{\sigma_1}h_1\sin\beta+np)\zeta'\}B_ne^{inpx}e^{-i\sqrt{\sigma_1}h_1\zeta\cos\beta_n}\\&\quad-\sum_n\{\sqrt{\sigma_1}h_1\cos\beta'_n+(\sqrt{\sigma_1}h_1\sin\beta-np)\zeta'\}B'_ne^{-inpx-i\sqrt{\sigma_1}h_1\zeta\cos\beta'_n}]\\&=\mu_2[(\sqrt{\sigma_2}h_2\cos\delta-\sqrt{\sigma_1}h_1\zeta'\sin\beta)D_0e^{i\sqrt{\sigma_2}h_2\zeta\cos\delta}\\&\quad+\sum_n\{\sqrt{\sigma_2}h_2\cos\delta_n-\zeta'(\sqrt{\sigma_1}h_1\sin\beta+np)\}D_ne^{inpx}e^{i\sqrt{\sigma_2}h_2\zeta\cos\delta_n}\\&\quad+\sum_n\{\sqrt{\sigma_2}h_2\cos\delta'_n-\zeta'(\sqrt{\sigma_2}h_2\sin\beta-np)\}D'_ne^{-inpx}e^{i\sqrt{\sigma_2}h_2\zeta\cos\delta'_n}].\end{aligned}\tag{2}$$

5. The solutions of the first approximation

Now the extent of corrugation, ζ, is assumed as very small and by iteration the approximations are advanced. First of all, the solutions of the first approximation for B_0 and D_0 can be obtained by picking up the term independent of x and ζ in (1) and (2).

$$1+B_0=D_0$$

$$\mu_1\sqrt{\sigma_1}h_1(1-B_0)\cos\beta-\mu_2\sqrt{\sigma_2}h_2D_0\cos\delta=0\,.$$

These formulas give the amplitudes of reflected and refracted waves in the case of plane boundary surface. From these two formulas, B_0 and D_0 can be solved as follows:

$$B_0=(\mu_1\sqrt{\sigma_1}\,h_1\cos\beta-\mu_2\sqrt{\sigma_2}\,h_2\cos\delta)/(\mu_1\sqrt{\sigma_1}\,h_1\cos\beta+\mu_2\sqrt{\sigma_2}\,h_2\cos\delta)\ , \tag{3}$$

$$D_0=2\mu_1\sqrt{\sigma_1}\,h_1\cos\beta/(\mu_1\sqrt{\sigma_1}\,h_1\cos\beta+\mu_2\sqrt{\sigma_2}\,h_2\cos\delta)\ . \tag{4}$$

From the coefficients of e^{inpx} in (1) and (2), the solutions of the first approximation for B_n and D_n can be obtained as follows:

$$B_n-D_n=-i\sqrt{\sigma_1}\,h_1\zeta_n(1-B_0)\cos\beta+i\sqrt{\sigma_2}\,h_2\zeta_nD_0\cos\delta\ ,$$

$$\begin{aligned}&\mu_1B_n\sqrt{\sigma_1}\,h_1\cos\beta_n+\mu_2D_n\sqrt{\sigma_2}\,h_2\cos\delta_n\\&\quad=i\mu_1\sqrt{\sigma_1}\,h_1\zeta_n(1+B_0)(\sqrt{\sigma_1}\,h_1\cos^2\beta-np\sin\beta)\\&\qquad-i\mu_2\zeta_nD_0(\sigma_2h_2^2\cos^2\delta-\sqrt{\sigma_1}\,h_1np\sin\beta)\ .\end{aligned}$$

Similarly from the coefficients of e^{-inpx} in (1) and (2), the solutions of the first approximation for B'_n and D'_n can be obtained as follows:

$$B'_n-D'_n=-i(1-B_0)\sqrt{\sigma_1}\,h_1\zeta_{-n}\cos\beta+iD_0\sqrt{\sigma_2}\,h_2\zeta_{-n}\cos\delta\ ,$$

$$\begin{aligned}&\mu_1\sqrt{\sigma_1}\,h_1B'_n\cos\beta'_n+\mu_2\sqrt{\sigma_2}\,h_2D'_n\cos\delta'_n\\&\quad=i\mu_1\sqrt{\sigma_1}\,h_1\zeta_{-n}(1+B_0)(\sqrt{\sigma_1}\,h_1\cos^2\beta+np\sin\beta)\\&\qquad-i\mu_2\zeta_{-n}D_0(\sqrt{\sigma_1}\,h_1np\sin\beta+\sigma_2h_2^2\cos^2\delta)\ .\end{aligned}$$

For B_0 and D_0 involved in the above formulas (3) and (4) are used. From the above formulas we can see that the solutions of the first approximation for B_n, D_n, B'_n, and D'_n are proportional to ζ_n or ζ_{-n} and of order of ζ_n or ζ_{-n} as in the case of reflection of elastic waves at a corrugated free surface.[5]

6. The solutions of the second approximation

Next if the terms of higher order than ζ^2 in the equations (1) and (2) are neglected, the following two equations are obtained.

$$\begin{aligned}&1+i\sqrt{\sigma_1}\,h_1\zeta\cos\beta+B_0(1-i\sqrt{\sigma_1}\,h_1\zeta\cos\beta)\\&\quad+\sum_n B_ne^{inpx}(1-i\sqrt{\sigma_1}\,h_1\zeta\cos\beta_n)+\sum_n B'_ne^{-inpx}(1-i\sqrt{\sigma_1}\,h_1\zeta\cos\beta'_n)\\&=D_0(1+i\sqrt{\sigma_2}\,h_2\zeta\cos\delta)+\sum_n D_ne^{inpx}(1+i\sqrt{\sigma_2}\,h_2\zeta\cos\delta_n)\\&\quad+\sum_n D'_ne^{-inpx}(1+i\sqrt{\sigma_2}\,h_2\zeta\cos\delta'_n)\ ,\end{aligned}$$

$$\begin{aligned}&\mu_1[\sqrt{\sigma_1}\,h_1(1-B_0)\cos\beta+\sqrt{\sigma_1}\,h_1(1+B_0)(i\sqrt{\sigma_1}\,h_1\zeta\cos^2\beta-\zeta'\sin\beta)\\&\quad-\sum_n\{\sqrt{\sigma_1}\,h_1\cos\beta_n+(\sqrt{\sigma_1}\,h_1\sin\beta+np)\zeta'-i\sigma_1h_1^2\zeta\cos^2\beta_n\}B_ne^{inpx}\end{aligned}$$

5) R. SATO, *loc. cit.*, 4).

$$-\sum_n \{\sqrt{\sigma_1}\,h_1\cos\beta'_n+(\sqrt{\sigma_1}\,h_1\sin\beta-np)\zeta'-i\sigma_1h_1^2\zeta\cos^2\beta'_n\}B'_ne^{-inpx}]$$

$$=\mu_2[(\sqrt{\sigma_2}\,h_2\cos\delta+i\sigma_2h_2^2\zeta\cos^2\delta-\sqrt{\sigma_1}\,h_1\zeta'\sin\beta)D_0$$

$$+\sum_n \{\sqrt{\sigma_2}\,h_2\cos\delta_n+i\sigma_2h_2^2\zeta\cos^2\delta_n-\zeta'(\sqrt{\sigma_1}\,h_1\sin\beta+np)\}D_ne^{inpx}$$

$$+\sum_n \{\sqrt{\sigma_2}\,h_2\cos\delta'_n+i\sigma_2h_2^2\zeta\cos^2\delta'_n-\zeta'(\sqrt{\sigma_1}\,h_1\sin\beta-np)\}D'_ne^{-inpx}.$$

From above two equations we can obtain the solutions of the second approximation for B_0 and D_0 by picking up the terms independent of x. They are as follows:

$$(\mu_1\sqrt{\sigma_1}\,h_1\cos\beta+\mu_2\sqrt{\sigma_2}\,h_2\cos\delta)D_0$$

$$=2\mu_1\sqrt{\sigma_1}\,h_1\cos\beta+i\mu_1\sum_n B_n\zeta_{-n}\{np(\sqrt{\sigma_1}\,h_1\sin\beta+np)$$

$$-\sigma_1h_1^2(\cos\beta-\cos\beta_n)\cos\beta_n\}$$

$$-i\mu_1\sum_n B'_n\zeta_n\{np(\sqrt{\sigma_1}\,h_1\sin\beta-np)+\sigma_1h_1^2(\cos\beta-\cos\beta'_n)\cos\beta'_n\}$$

$$-i\sum_n D_n\zeta_{-n}\{\mu_2np(\sqrt{\sigma_1}\,h_1\sin\beta+np)$$

$$+\sqrt{\sigma_2}\,h_2(\mu_1\sqrt{\sigma_1}\,h_1\cos\beta+\mu_2\sqrt{\sigma_2}\,h_2\cos\delta_n)\cos\delta_n\}$$

$$+i\sum_n D'_n\zeta_n\{\mu_2np(\sqrt{\sigma_1}\,h_1\sin\beta-np)$$

$$-\sqrt{\sigma_2}\,h_2(\mu_1\sqrt{\sigma_1}\,h_1\cos\beta+\mu_2\sqrt{\sigma_2}\,h_2\cos\delta'_n)\cos\delta'_n\}\ ,$$

$$B_0-D_0=-1+\sum_n iB_n\zeta_{-n}\sqrt{\sigma_1}\,h_1\cos\beta_n+\sum_n iB'_n\zeta_n\sqrt{\sigma_1}\,h_1\cos\beta'_n$$

$$+\sum_n iD_n\zeta_{-n}\sqrt{\sigma_2}\,h_2\cos\delta_n+\sum_n iD'_n\zeta_n\sqrt{\sigma_2}\,h_2\cos\delta'_n\ ,$$

where for B_n, D_n, etc. those of the first approximation are used.

From the coefficients of e^{inpx} the solutions of the second approximation for B_n and D_n can be obtained as follows:

$$B_n-D_n=-i\sqrt{\sigma_1}\,h_1\zeta_n(1-B_0)\cos\beta+i\sqrt{\sigma_2}\,h_2D_0\zeta_n\cos\delta$$

$$+i\Big(\sum_{j=1}^{n-1}+\sum_{j=n+1}^{\infty}\Big)B_j\zeta_{n-j}\sqrt{\sigma_1}\,h_1\cos\beta_j+i\sum_{j=n+1}^{\infty}B'_{j-n}\zeta_j\sqrt{\sigma_1}\,h_1\cos\beta'_{j-n}$$

$$+i\Big(\sum_{j=1}^{n-1}+\sum_{j=n+1}^{\infty}\Big)D_j\zeta_{n-j}\sqrt{\sigma_2}\,h_2\cos\delta_j+i\sum_{j=n+1}^{\infty}D'_{j-n}\zeta_j\sqrt{\sigma_2}\,h_2\cos\delta'_{j-n}\ ,$$

$$\mu_1B_n\sqrt{\sigma_1}\,h_1\cos\beta_n+\mu_2D_n\sqrt{\sigma_2}\,h_2\cos\delta_n$$

$$=i\mu_1\sqrt{\sigma_1}\,h_1\zeta_n(1+B_0)(\sqrt{\sigma_1}\,h_1\cos^2\beta-np\sin\beta)$$

$$-i\mu_2\zeta_nD_0(\sigma_2h_2^2\cos^2\delta-\sqrt{\sigma_1}\,h_1\,np\sin\beta)$$

$$-i\mu_1\Big(\sum_{j=1}^{n-1}+\sum_{j=n+1}^{\infty}\Big)\{p(n-j)(\sqrt{\sigma_1}h_1\sin\beta+jp)-\sigma_1h_1^2\cos^2\beta_j\}\zeta_{n-j}B_j$$

$$-i\mu_1\sum_{j=n+1}^{\infty}[jp\{\sqrt{\sigma_1}h_1\sin\beta+(n-j)p\}-\sigma_1h_1^2\cos^2\beta'_{j-n}]\zeta_jB'_{j-n}$$

$$-i\mu_2\Big(\sum_{j=1}^{n-1}+\sum_{j=n+1}^{\infty}\Big)\{\sigma_2h_2^2\cos^2\delta_j-p(n-j)(\sqrt{\sigma_1}h_1\sin\beta+jp)\}D_j\zeta_{n-j}$$

$$-i\mu_2\sum_{j=n+1}^{\infty}[\sigma_2h_2^2\cos^2\delta'_{j-n}-jp\{\sqrt{\sigma_1}h_1\sin\beta-(j-n)p\}]\zeta_jD'_{j-n}\ .$$

From the coefficients of e^{-inpx}, the following equations which determine B'_n and D'_n of the second approximation are obtained.

$$B'_n-D'_n=-i\sqrt{\sigma_1}h_1\zeta_{-n}(1-B_0)\cos\beta+i\sqrt{\sigma_2}h_2\zeta_{-n}D_0\cos\delta$$
$$+i\sqrt{\sigma_1}h_1\sum_{j=n+1}^{\infty}\zeta_{-j}B_{j-n}\cos\beta_{j-n}+i\sqrt{\sigma_1}h_1\Big(\sum_{j=1}^{n-1}+\sum_{j=n+1}^{\infty}\Big)B'_j\zeta_{j-n}\cos\beta'_j$$
$$+i\sqrt{\sigma_2}h_2\sum_{j=n+1}^{\infty}D_{j-n}\zeta_{-j}\cos\delta_{j-n}+i\sqrt{\sigma_2}h_2\Big(\sum_{j=1}^{n-1}+\sum_{j=n+1}^{\infty}\Big)D'_j\zeta_{j-n}\cos\delta'_j\ ,$$

$$\mu_1B'_n\sqrt{\sigma_1}h_1\cos\beta'_n+\mu_2D'_n\sqrt{\sigma_2}h_2\cos\delta'_n$$
$$=i\mu_1\sqrt{\sigma_1}h_1\zeta_{-n}(1+B_0)(\sqrt{\sigma_1}h_1\cos^2\beta+np\sin\beta)$$
$$-i\mu_2\zeta_{-n}D_0(\sigma_2h_2^2\cos^2\delta+\sqrt{\sigma_1}h_1\,np\sin\beta)$$
$$+i\mu_1\sum_{j=n+1}^{\infty}[jp\{\sqrt{\sigma_1}h_1\sin\beta+(j-n)p\}+\sigma_1h_1^2\cos^2\beta_{j-n}]\zeta_{-j}B_{j-n}$$
$$+i\mu_1\Big(\sum_{j=1}^{n-1}+\sum_{j=n+1}^{\infty}\Big)\{p(n-j)(\sqrt{\sigma_1}h_1\sin\beta-jp)+\sigma_1h_1^2\cos^2\beta'_j\}\zeta_{j-n}B'_j$$
$$-i\mu_2\sum_{j=n+1}^{\infty}[\sigma_2h_2^2\cos^2\delta_{j-n}+jp\{\sqrt{\sigma_1}h_1\sin\beta+(j-n)p\}]\zeta_{-j}D_{j-n}$$
$$-i\mu_2\Big(\sum_{j=1}^{n-1}+\sum_{j=n+1}^{\infty}\Big)\{\sigma_2h_2^2\cos^2\delta'_j+p(n-j)(\sqrt{\sigma_1}h_1\sin\beta-jp)\}\zeta_{-n}D'_j\ .$$

By iterating this procedure, we can get solutions of sufficient approximation.

7. The case of normal incidence on the boundary surface $\zeta=c\cos px$

For the simplicity's sake, the case of normal incidence on the boundary surface given by the equation $\zeta=c\cos px$ was calculated. In this case, $\zeta_n=\zeta_{-n}=0$ $(n\neq1)$, $\zeta_1=\zeta_{-1}=c/2$, $\beta=\delta=0$, $\cos\beta_1=\cos\beta'_1$, and $\cos\delta_1=\cos\delta'_1$. Then the solutions of the first approximation for B_0, D_0, B_1, and D_1 are given as follows:

$$B_0=(\mu_1\sqrt{\sigma_1}\,h_1-\mu_2\sqrt{\sigma_2}\,h_2)/(\mu_1\sqrt{\sigma_1}\,h_1+\mu_2\sqrt{\sigma_2}\,h_2)\ ,$$

$$D_0=2\mu_1\sqrt{\sigma_1}\,h_1/(\mu_1\sqrt{\sigma_1}\,h_1+\mu_2\sqrt{\sigma_2}\,h_2)\ ,$$

$$B_1-D_1=-i\sqrt{\sigma_1}\,h_1\zeta_1(1-B_0)+i\sqrt{\sigma_2}\,h_2\zeta_1 D_0\ ,$$

$$\mu_1 B_1\sqrt{\sigma_1}\,h_1\cos\beta_1+\mu_2 D_1\sqrt{\sigma_2}\,h_2\cos\delta_1=i\mu_1\zeta_1(1+B_0)\sigma_1 h_1^2-i\mu_2\zeta_1 D_0\sigma_2 h_2^2\ ,$$

$$B_1'=B_1\ ,\qquad D_1'=D_1\ .$$

The solutions of the second approximation for B_0, D_0, B_1, D_1, B_2 and D_2 are given as follows:

$$(\mu_1\sqrt{\sigma_1}\,h_1+\mu_2\sqrt{\sigma_2}\,h_2)D_0=2\mu_1\sqrt{\sigma_1}\,h_1+2i\mu_1 B_1\zeta_{-1}\{p^2-\sigma_1 h_1^2(1-\cos\beta_1)\cos\beta_1\}$$
$$-2iD_1\zeta_{-1}\{\mu_2 p^2+\sqrt{\sigma_2}\,h_2(\mu_1\sqrt{\sigma_1}\,h_1+\mu_2\sqrt{\sigma_2}\,h_2\cos\delta_1)\cos\delta_1\}\ ,$$

$$B_0-D_0=-1+2iB_1\zeta_{-1}\sqrt{\sigma_1}\,h_1\cos\beta_1+2iD_1\zeta_{-1}\sqrt{\sigma_2}\,h_2\cos\delta_1\ ,$$

$$B_1-D_1=-i\sqrt{\sigma_1}\,h_1\zeta_1(1-B_0)+i\sqrt{\sigma_2}\,h_2 D_0\zeta_1\ ,$$

$$\mu_1 B_1\sqrt{\sigma_1}\,h_1\cos\beta_1+\mu_2 D_1\sqrt{\sigma_2}\,h_2\cos\delta_1=i\mu_1\sigma_1 h_1^2\zeta_1(1+B_0)-i\mu_2\sigma_2 h_2^2\zeta_1 D_0\ ,$$

$$B_2-D_2=iB_1\zeta_1\sqrt{\sigma_1}\,h_1\cos\beta_1+iD_1\zeta_1\sqrt{\sigma_2}\,h_2\cos\delta_1\ ,$$

$$\mu_1 B_2\sqrt{\sigma_1}\,h_1\cos\beta_2+\mu_2 D_2\sqrt{\sigma_2}\,h_2\cos\delta_2$$
$$=-i\mu_1\zeta_1 B_1(p^2-\sigma_1 h_1^2\cos^2\beta_1)+i\mu_2\zeta_1 D_1(p^2-\sigma_2 h_2^2\cos^2\delta_1)\ ,$$

$$B_1'=B_1\ ,\qquad D_1'=D_1\ ,\qquad B_2'=B_2\ ,\qquad D_2'=D_2\ .$$

In the above formulas, B_1 and D_1 are the same to those of the first approximation because terms of higher order than ζ are of order of ζ^3.

The constants necessary for the calculations are taken as follows:

$$V_{s1}/V_{s2}=3.5/4.6=V_{p1}/V_{p2}=6.0/8.0\ ,\qquad \mu_2/\mu_1=2.1\ ,$$

where V_{p1} and V_{p2} are the velocity of P waves in the lower and upper medium respectively, and Poisson's relation $\lambda_i=\mu_i$ is assumed. The results are given in Tables 1, 2, and 3, and Figs. 2–9.

From Figs. 2 and 3, we can see following trends as to B_0 and D_0. (1) The variations of B_0 and D_0 with the wave length L of corrugation are very small. (2) The influence of corrugation is larger on reflection than on refraction. As seen from Fig. 2(a) and Fig. 3(a), the difference of $|B_0|$ is larger than that of $|D_0|$ for different c/L_{s1} at the same L/L_{s1} where L_{s1} is the wave length of the incident SH wave. Furthermore, this result is ascertained by Fig. 6, and Fig. 7,

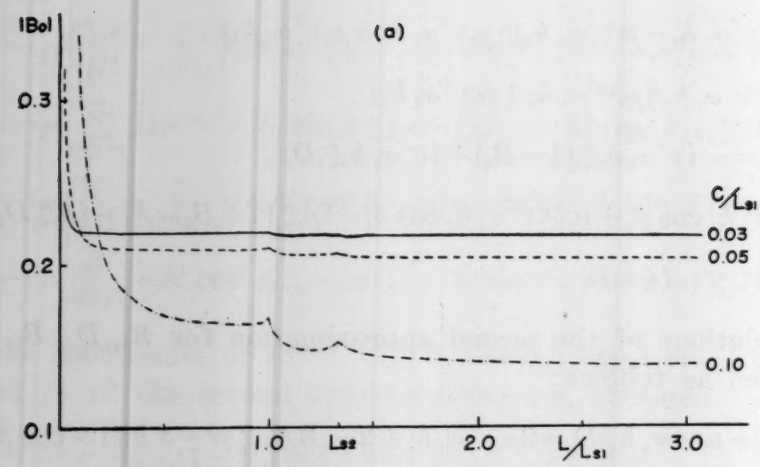

Fig. 2 (a). $|B_0|$.

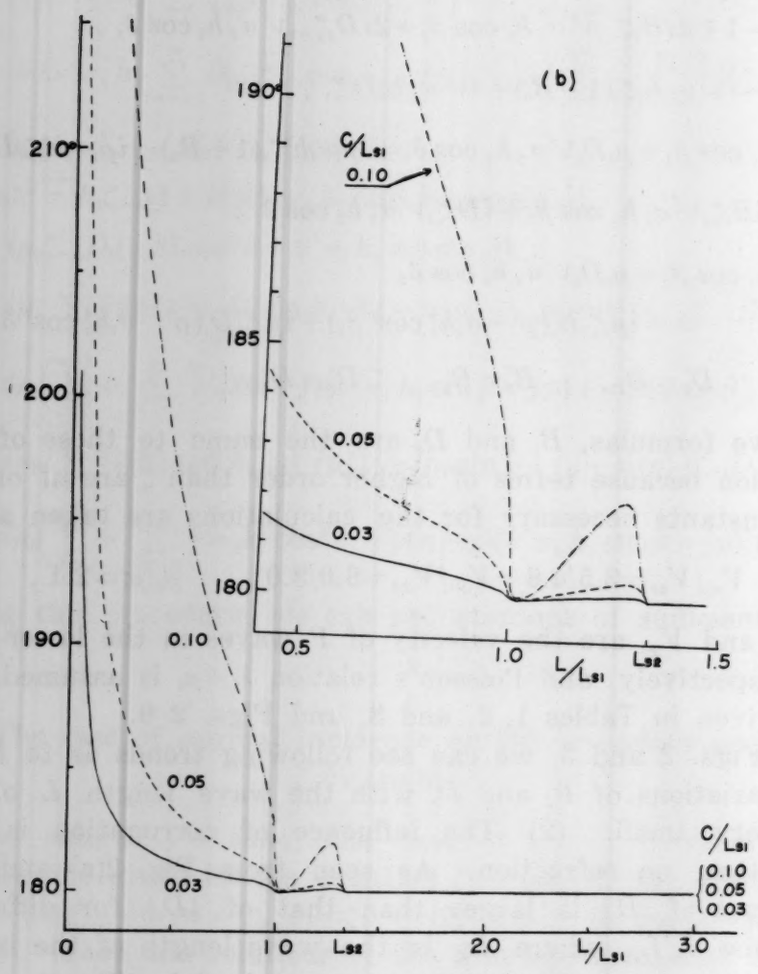

Fig. 2 (b). The variation of phase angle of B_0.

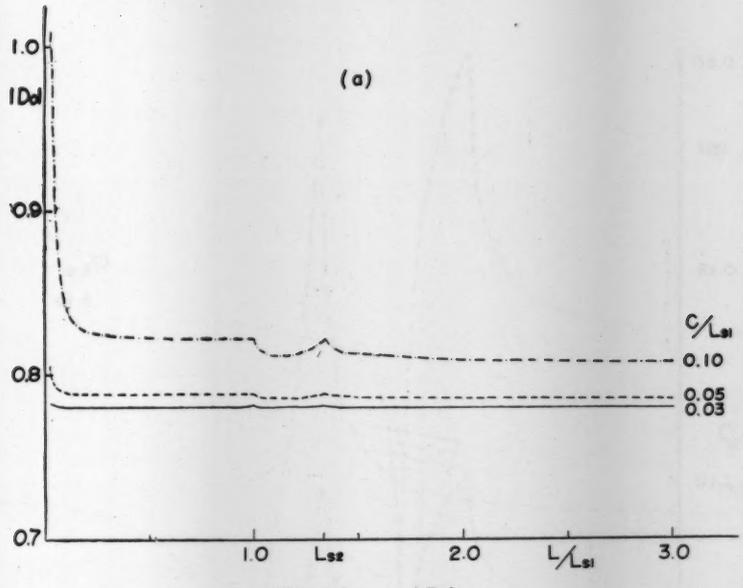

Fig. 3(a). $|D_0|$.

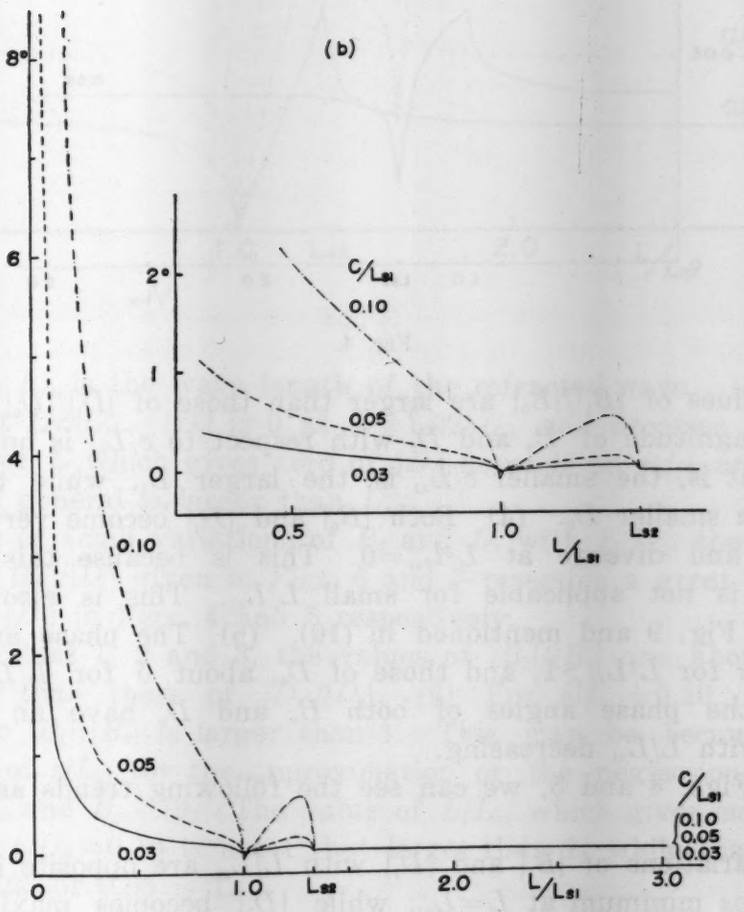

Fig. 3(b). The variation of phase angle of D_0.

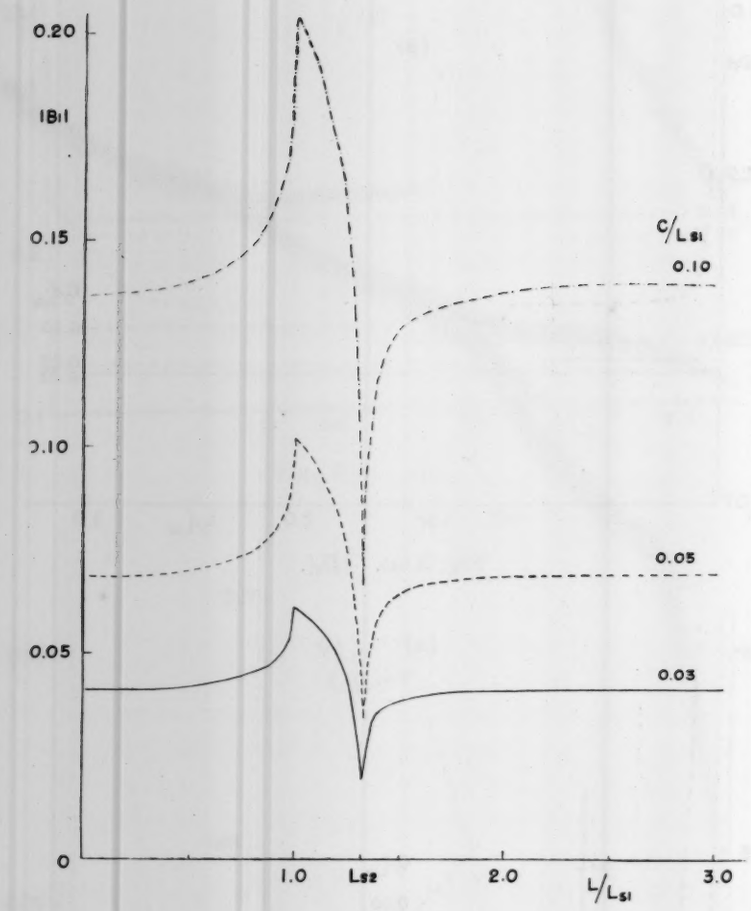

Fig. 4.

for the values of $|B_1|/|B_0|$ are larger than those of $|D_1|/|D_0|$. (3) The order of magnitude of B_0 and D_0 with respect to c/L_{s1} is opposite each other. That is, the smaller c/L_{s1} is, the larger B_0, while the smaller c/L_{s1} is, the smaller D_0. (4) Both $|B_0|$ and $|D_0|$ become very large for $L/L_{s1}<0.3$ and diverge at $L/L_{s1}=0$. This is because this method of calculation is not applicable for small L/L_{s1}. This is also shown in Fig. 8 and Fig. 9 and mentioned in (10). (5) The phase angles of B_0 are about π for $L/L_{s1}>1$, and those of D_0, about 0 for $L/L_{s1}>1$. For $L/L_{s1}<1$, the phase angles of both B_0 and D_0 have an increasing tendency with L/L_{s1} decreasing.

From Figs. 4 and 5, we can see the following trends as to B_1 and D_1.

(6) The variations of $|B_1|$ and $|D_1|$ with L/L_{s1} are opposite in general. $|B_1|$ becomes minimum at $L=L_{s2}$, while $|D_1|$ becomes maximum at L

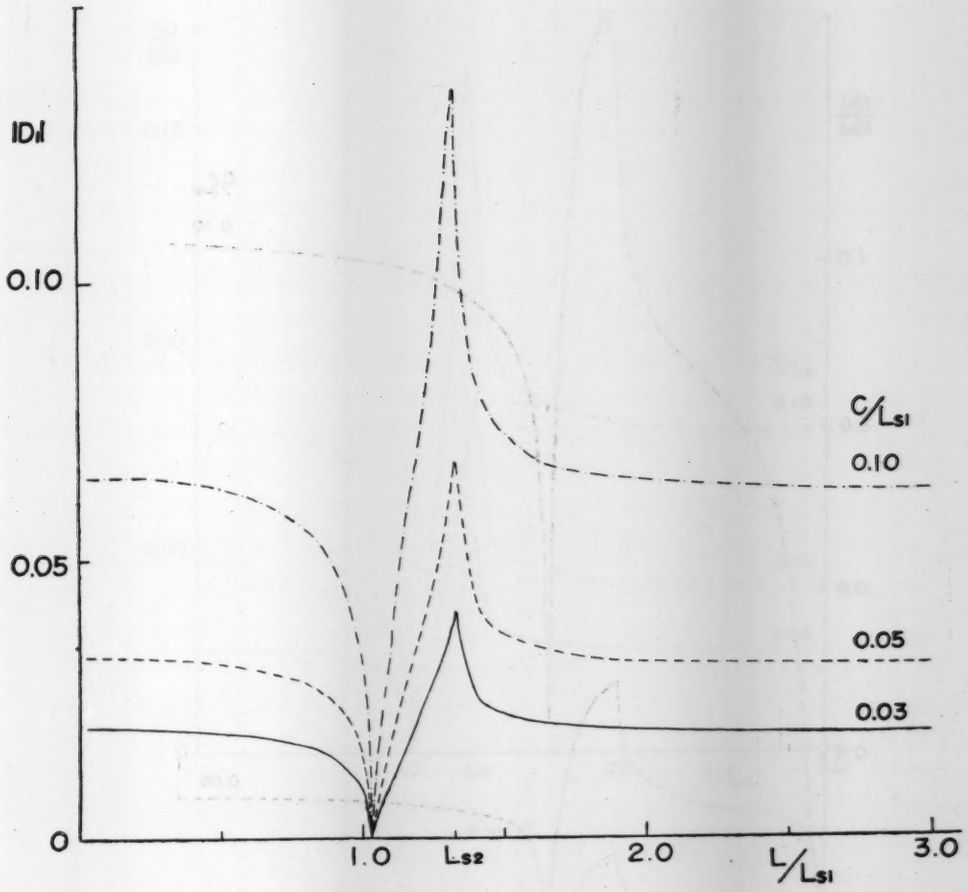

Fig. 5.

$=L_{s2}$ where L_{s2} is the wave length of the refracted wave. $|B_1|$ reaches maximum at $L=L_{s1}$. $|D_1|$ is 0 at $L=1.025L_{s1}$ and becomes minimum. The value of L which gives zero of $|D_1|$ depends on μ_2/μ_1 and velocity ratio and in general is larger than L_{s1}.

Because of small variations of B_0 and D_0 with L/L_{s1}, the curves of $|B_1|/|B_0|$ and $|D_1|/|D_0|$ given in Figs. 6 and 7 resemble a great deal those of $|B_1|$ and $|D_1|$ in Figs. 4 and 5 respectively.

(7) From Tables 1, 2 and 3, the values of $|B_1|/|B_0|$ are about several times larger than those of $|D_1|/|D_0|$. (8) For $c/L_{s1}=0.10$, there is a range where $|B_1|/|B_0|$ is larger than 1. This may be because of too large value of c/L_{s1} for the approximation or the neglection of phase angles of B_0 and B_1. (9) The value of L/L_{s1} which gives maximum of $|B_1|/|B_0|$ for $c/L_{s1}=0.10$ is not 1, but larger than 1, while that of L/L_{s1} for $c/L_{s1}=0.03$ or 0.05 is 1.

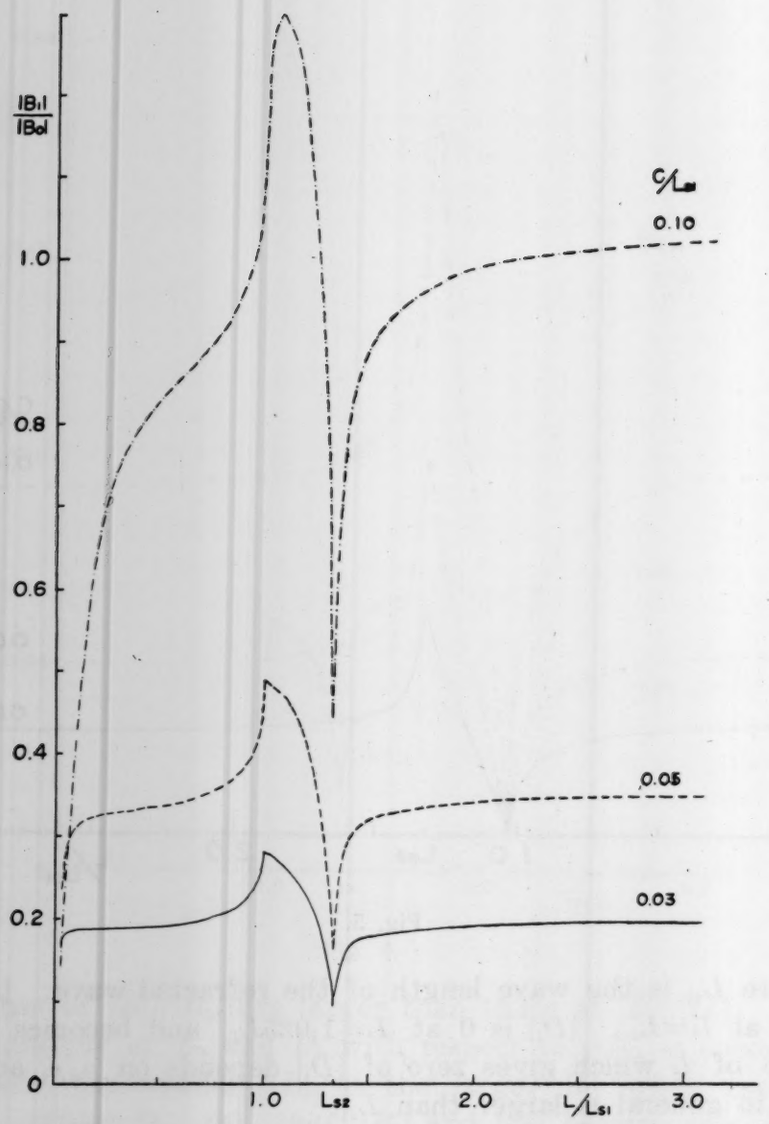

Fig. 6.

From Figs. 8 and 9, the following tendency is seen as to $|B_2|$ and $|D_2|$.

(10) Both $|B_2|$ and $|D_2|$ are very small in comparison with $|B_0|$ and $|D_0|$ except for $L/L_{s1}\approx 0$. In the neighbourhood of $L/L_{s1}=0$, both $|B_2|$ and $|D_2|$ increase very rapidly with L/L_{s1} tending to 0 until they reach infinity at just $L/L_{s1}=0$. This shows that this method of calculation is not fit for $L/L_{s1}<0.5$, since $d\zeta/dx$ is very large. (11) Both $|B_2|$ and $|D_2|$ have two maxima and two minima. (12) There exists a certain

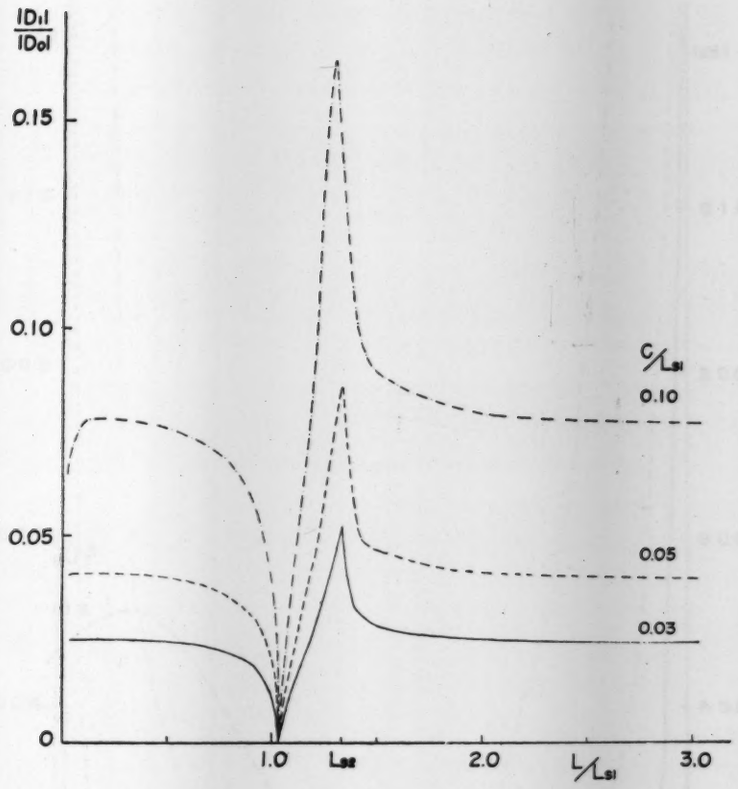

Fig. 7.

kind of boundary waves. That is, in the range of $L/L_{s2}>2$ all waves are bodily waves, while for $2L_{s2}>L$ some of irregular waves seem to be a kind of boundary waves amplitudes of which decrease with $|z|$ increasing. In the range of $2L_{s2}>L>2L_{s1}$, only the irregularly refracted wave with spectrum of the second order which is represented by D_2 is like the boundary wave. In the range of $2L_{s1}>L>L_{s2}$, in addition to the irregularly refracted wave with spectrum of the second order, the irregularly reflected wave with spectrum of the second order represented by B_2 becomes like the boundary wave. Furthermore, in the range of $L_{s2}>L>L_{s1}$, only the irregularly reflected wave with spectrum of the first order represented by B_1 is a bodily wave, and other waves are like boundary waves. For $L_{s1}>L$, all waves are like boundary waves. The amplitude of these waves decreases in such a way that the higher is the order of spectrum of irregular waves, and the smaller, the wave length of the corrugation, and the larger, the wave length of the incident SH wave, the larger, the decrease of the amplitude.

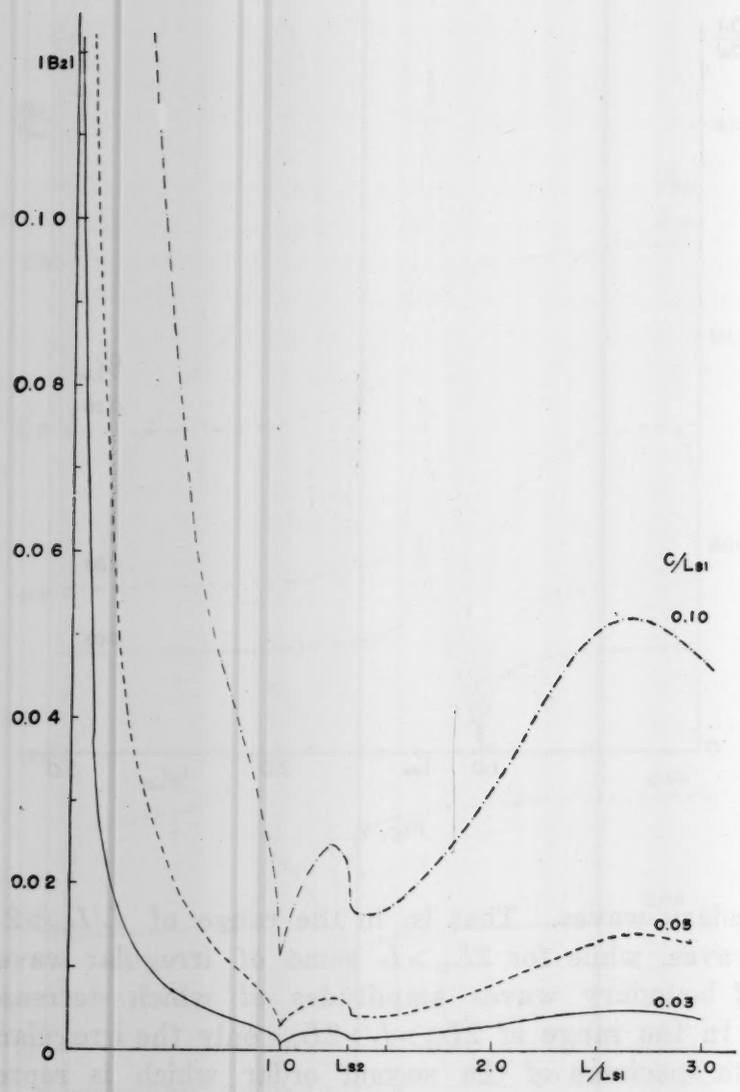

Fig. 8.

8. Conclusion

In order to see the effect of a corrugated boundary surface on reflection and refraction of elastic waves, the case of incidence of SH wave on the corrugated boundary surface which can be represented by Fourier's series is treated in the present paper. For the simplicity's sake, numerical calculation was carried out for the case of normal incidence on the boundary surface given by $\zeta = c \cos px$. The results are given in Tables 1, 2 and 3, and Figs. 2–9. From these figures, it will

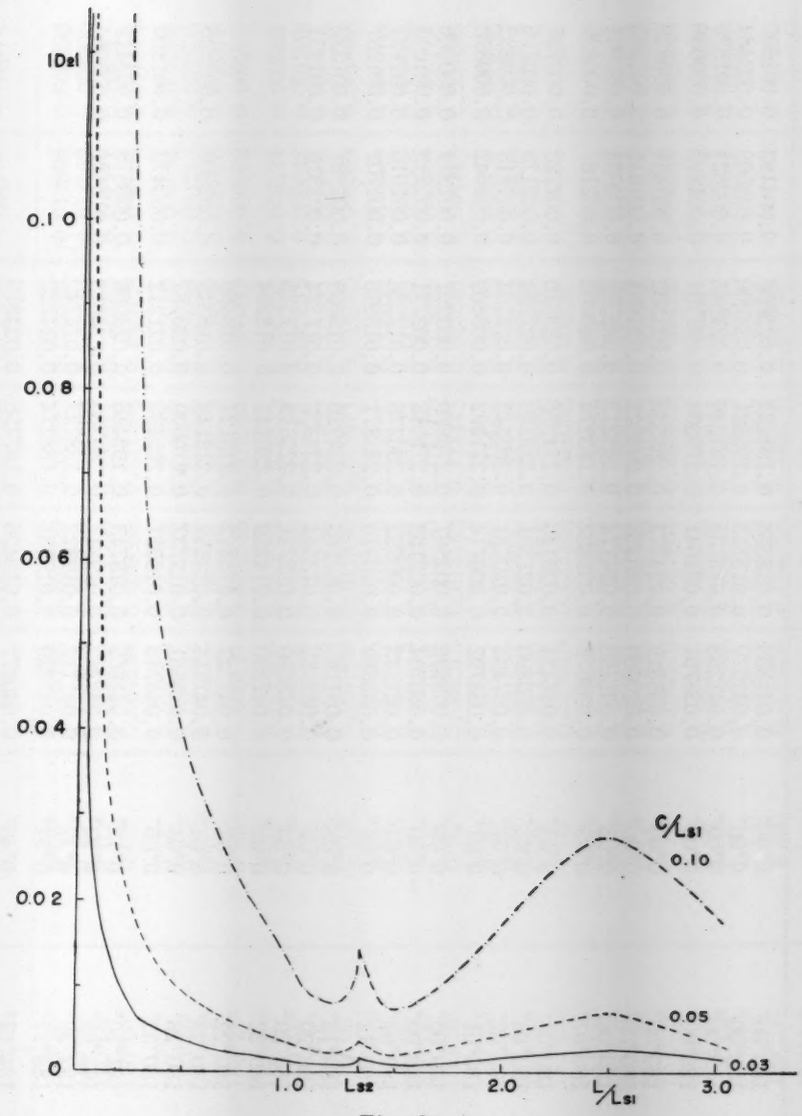

Fig. 9.

be seen that at a certain value of L/L_{s1}, for example, $L=L_{s1}$ or $L=L_{s2}$, irregularly reflected or refracted waves become of comparable order with that of regular waves, or they become very small in comparison with regular waves.

Furthermore, the effect of amplitude of corrugation on the amplitude of a regularly reflected wave is opposite to and larger than its effect on a regularly refracted wave. That is, the larger the amplitude of corrugation is, the smaller, the amplitude of a regularly reflected wave, while the larger the amplitude of corrugation is, the larger, the amplitude of a regularly refracted wave.

Table 1. $|B_0|$, $|D_0|$, etc. in the case of $c/L_{s1}=0.03$.

L/L_{s1}	$\lvert B_0\rvert$	$\lvert D_0\rvert$	Phase angle of B_0	Phase angle of D_0	$\lvert B_1\rvert$	$\lvert D_1\rvert$	$\lvert B_1\rvert/\lvert B_0\rvert$	$\lvert D_1\rvert/\lvert D_0\rvert$	$\lvert B_2\rvert$	$\lvert D_3\rvert$
3.0	0.215522	0.779392	180°00′	0°00′	0.041838	0.018554	0.194124	0.023806	0.004193	0.001650
2.5	0.215595	0.779442	180°00′	0°00′	0.041679	0.018713	0.193321	0.024008	0.004599	0.002484
2.0	0.215739	0.779542	180°00′	0°00′	0.041258	0.019134	0.191240	0.024545	0.002834	0.001570
1.5	0.216119	0.779838	180°00′	0°00′	0.038751	0.021641	0.179304	0.027751	0.001495	0.000638
1.4	0.216382	0.780024	180°00′	0°00′	0.035819	0.024573	0.165536	0.031502	0.001459	0.000828
1.333333	0.216816	0.780683	180°00′	0°00′	0.020060	0.040333	0.092521	0.051664	0.001516	0.001282
1.31	0.216641	0.780411	180°06′	0°03′	0.031459	0.036174	0.145213	0.046352	0.002038	0.000961
1.28	0.216495	0.780156	180°07′	0°03′	0.039678	0.031522	0.183274	0.040405	0.002187	0.000820
1.24	0.216399	0.779935	180°07′	0°03′	0.046434	0.026140	0.214576	0.033516	0.002223	0.000735
1.2	0.216387	0.779809	180°06′	0°03′	0.050890	0.021354	0.235180	0.027384	0.002175	0.000716
1.1	0.216676	0.779801	180°02′	0°01′	0.057494	0.010281	0.265345	0.013184	0.001818	0.000833
1.07	0.216871	0.779885	180°01′	0°01′	0.058792	0.006714	0.271092	0.008609	0.001642	0.000898
1.04	0.217152	0.780034	180°00′	0°00′	0.059899	0.002567	0.275839	0.003291	0.001374	0.000966
1.015	0.217528	0.780255	180°00′	−0°00′	0.060704	0.002162	0.279063	0.002771	0.001213	0.001045
1.0	0.218151	0.780658	180°02′	0°01′	0.061143	0.009552	0.280278	0.012236	0.001016	0.001131
0.98	0.217956	0.780693	180°12′	0°01′	0.053589	0.010910	0.245871	0.013975	0.001702	0.001257
0.96	0.217895	0.780705	180°15′	0°02′	0.051187	0.012185	0.234916	0.015608	0.001987	0.001328
0.93	0.217841	0.780715	180°20′	0°03′	0.048982	0.013564	0.224852	0.017374	0.002316	0.001431
0.92	0.217834	0.780716	180°20′	0°03′	0.048690	0.013721	0.223519	0.017575		
0.91	0.217815	0.780720	180°22′	0°03′	0.047950	0.014259	0.220141	0.018264		
0.905	0.217811	0.780720	180°22′	0°03′	0.047727	0.014412	0.219121	0.018460		
0.9	0.217805	0.780721	180°23′	0°04′	0.047514	0.014559	0.218149	0.018648	0.002600	0.001526
0.85	0.217764	0.780730	180°28′	0°04′	0.045861	0.015737	0.210600	0.020157		
0.8	0.217738	0.780736	180°33′	0°05′	0.044743	0.016561	0.205490	0.021212	0.003472	0.001860
0.5	0.217541	0.780752	181°10′	0°12′	0.041865	0.018743	0.192446	0.024006	0.006975	0.003415
0.3	0.217787	0.780767	182°05′	0°22′	0.041242	0.019217	0.189369	0.024613	0.012427	0.005964
0.25	0.217854	0.780774	182°32′	0°27′	0.041115	0.019323	0.188727	0.024749		
0.20	0.217975	0.780792	183°12′	0°34′	0.041039	0.019381	0.188274	0.024822		
0.15	0.218246	0.780819	184°17′	0°46′	0.040977	0.019426	0.187756	0.024879		
0.1	0.219022	0.780905	186°29′	1°09′	0.040942	0.019478	0.186931	0.024943	0.038418	0.018310
0.05	0.223161	0.781382	192°47′	2°18′	0.040918	0.019475	0.183356	0.024924	0.077045	0.036696
0.03	0.232691	0.782499	200°43′	3°50′	0.040913	0.019478	0.175825	0.024892	0.121708	0.061185

Table 2. $|B_0|$, $|D_0|$, etc. in the case of $c/L_{s1}=0.05$.

L/L_{s1}	$\lvert B_0\rvert$	$\lvert D_0\rvert$	Phase angle of B_0	Phase angle of D_0	$\lvert B_1\rvert$	$\lvert D_1\rvert$	$\lvert B_1\rvert/\lvert B_0\rvert$	$\lvert D_1\rvert/\lvert D_0\rvert$	$\lvert B_2\rvert$	$\lvert D_2\rvert$
3.0	0.201695	0.784178	180°00′	0°00′	0.069730	0.030923	0.345720	0.039434	0.012899	0.003293
2.5	0.201899	0.784316	180°00′	0°00′	0.069464	0.031189	0.344053	0.039766	0.013162	0.006900
2.0	0.202297	0.784595	180°00′	0°00′	0.068763	0.031890	0.339911	0.040646	0.007872	0.004361
1.5	0.203354	0.785416	180°00′	0°00′	0.064584	0.036068	0.317594	0.045922	0.004156	0.001773
1.4	0.203886	0.785931	180°00′	0°00′	0.059699	0.040954	0.292806	0.052109	0.004052	0.002302
1.333333	0.205286	0.787767	180°00′	0°00′	0.033432	0.067222	0.162856	0.085332	0.004210	0.003500
1.31	0.204802	0.787011	180°18′	0°07′	0.052432	0.060291	0.256013	0.076608	0.005670	0.002670
1.28	0.204402	0.786305	180°21′	0°08′	0.066131	0.052535	0.323534	0.066813	0.006072	0.002277
1.24	0.204132	0.785691	180°20′	0°08′	0.077389	0.043566	0.379113	0.055449	0.006174	0.002041
1.2	0.204100	0.785340	180°16′	0°07′	0.084816	0.035588	0.415561	0.045315	0.006043	0.001988
1.1	0.204900	0.785315	180°05′	0°03′	0.095823	0.017136	0.467657	0,021821	0.005053	0.002314
1.07	0.205438	0.785551	180°02′	0°02′	0.097988	0.011190	0.476971	0.014245	0.004560	0.002493
1.04	0.206219	0.785963	180°00′	0°01′	0.099832	0.004279	0.484107	0.005444	0.003942	0.002700
1.015	0.207264	0.786577	180°00′	0°01′	0.101173	0.003603	0.488131	0.004581	0.003352	0.002903
1.0	0.208997	0.787695	180°06′	−0°02′	0.101904	0.015920	0.487586	0.019958	0.002822	0.003143
0.98	0.208463	0.787794	180°35′	0°04′	0.089315	0.018183	0.428445	0.023081	0.004729	0.003493
0.96	0.208297	0.787827	180°45′	0°06′	0.085311	0.020309	0.409564	0.025779	0.005517	0.003698
0.93	0.208153	0.787856	180°57′	0°08′	0.081637	0.022606	0.392197	0.028693	0.006436	0.003974
0.92	0.208135	0.787860	180°59′	0°08′	0.081149	0.022868	0.389886	0.029025		
0.91	0.208086	0.787871	181°04′	0°09′	0.079916	0.023766	0.384053	0.030165		
0.905	0.208073	0.787872	181°05′	0°09′	0.079544	0.024022	0.382289	0.030490		
0.9	0.208060	0.787875	181°07′	0°10′	0.079191	0.024267	0.380616	0.030801	0.007221	0.004241
0.85	0.207962	0.787899	181°22′	0°12′	0.076435	0.026229	0.367543	0.033290		
0.8	0.207906	0.787915	181°35′	0°15′	0.074570	0.027601	0.358672	0.035030	0.009642	0.005166
0.5	0.207988	0.787982	183°22′	0°33′	0.069774	0.031238	0.335471	0.039643	0.019374	0.009487
0.3	0.208751	0.788075	186°04′	1°01′	0.068736	0.032028	0.329273	0.040641	0.034520	0.016565
0.25	0.209292	0.788135	187°21′	1°14′	0.068524	0.032205	0.327409	0.040862		
0.20	0.210295	0.788246	189°14′	1°33′	0.068398	0.032302	0.325248	0.040980		
0.15	0.212458	0.788480	192°19′	2°05′	0.068302	0.032377	0.321485	0.041063		
0.1	0.218527	0.789150	198°14′	3°09′	0.068237	0.032428	0.312259	0.041092	0.106717	0.050862
0.05	0.248761	0.792746	213°27′	6°18′	0.068197	0.032459	0.274147	0.040945	0.214014	0.101935
0.03	0.308828	0.801226	227°46′	10°26′	0.068189	0.032467	0.220799	0.040522	0.356898	0.169962

Table 3. $|B_0|$, $|D_0|$, etc. in the case of $c/L_s=0.10$.

L/L_{s1}	$\lvert B_0\rvert$	$\lvert D_0\rvert$	Phase angle of B_0	Phase angle of D_0	$\lvert B_1\rvert$	$\lvert D_1\rvert$	$\lvert B_1\rvert/\lvert B_0\rvert$	$\lvert D_1\rvert/\lvert D_0\rvert$	$\lvert B_2\rvert$	$\lvert D_2\rvert$
3.0	0.136883	0.806611	180°00′	0°00′	0.139460	0.061846	1.018826	0.076674	0.046592	0.018339
2.5	0.137696	0.807165	180°00′	0°00′	0.138928	0.062377	1.008947	0.077279	0.051101	0.027594
2.0	0.139290	0.808279	180°00′	0°00′	0.137526	0.063780	0.987336	0.078908	0.031490	0.017446
1.5	0.143515	0.811566	180°00′	0°00′	0.129169	0.072137	0.900038	0.088886	0.016625	0.007091
1.4	0.145641	0.813624	180°00′	0°00′	0.119398	0.081908	0.819810	0.100671	0.016256	0.009291
1.333333	0.151239	0.820973	180°00′	0°00′	0.066863	0.134442	0.442102	0.163759	0.016840	0.014240
1.31	0.149312	0.817963	180°38′	0°27′	0.104864	0.120583	0.702315	0.147419	0.022679	0.010676
1.28	0.147770	0.815150	181°58′	0°33′	0.132260	0.105069	0.895040	0.128895	0.023544	0.009109
1.24	0.146693	0.812690	181°51′	0°32′	0.154776	0.087129	1.055101	0.107211	0.024704	0.008163
1.2	0.146537	0.811282	181°31′	0°28′	0.169632	0.071175	1.157605	0.087732	0.024171	0.007956
1.1	0.149700	0.811171	180°29′	0°13′	0.191647	0.034273	1.280207	0.042251	0.020209	0.009257
1.07	0.151847	0.812113	180°13′	0°08′	0.195973	0.022381	1.290595	0.027559	0.018238	0.009973
1.04	0.154977	0.813757	180°02′	0°03′	0.199663	0.008557	1.288340	0.010515	0.001574	0.010585
1.015	0.159157	0.816230	180°02′	0°02′	0.202345	0.007206	1.271027	0.008828	0.001341	0.011613
1.0	0.166093	0.820682	180°29′	−0°06′	0.203808	0.031840	1.227072	0.038797	0.011285	0.012571
0.98	0.164119	0.821086	182°56′	0°14′	0.178631	0.036366	1.088424	0.044290	0.018912	0.013971
0.96	0.163588	0.821221	183°51′	0°22′	0.170621	0.040618	1.042992	0.049460	0.022070	0.014793
0.93	0.163180	0.821350	184°52′	0°30′	0.163273	0.045212	1.000570	0.055046	0.025725	0.015993
0.92	0.163147	0.821368	185°04′	0°32′	0.162298	0.045735	0.994796	0.055681		
0.91	0.163033	0.821415	185°26′	0°35′	0.159832	0.047531	0.980366	0.057865		
0.905	0.163009	0.821427	185°34′	0°36′	0.159088	0.048043	0.975946	0.058487		
0.9	0.162988	0.821440	185°42′	0°37′	0.158382	0.048533	0.971740	0.059083	0.028886	0.016963
0.85	0.162912	0.821556	186°57′	0°47′	0.152869	0.052459	0.938353	0.063853		
0.8	0.163043	0.821647	188°08′	0°57′	0.149141	0.055201	0.914734	0.067183	0.038572	0.020667
0.5	0.167893	0.822247	196°57′	2°08′	0.139548	0.062477	0.831172	0.075983	0.077500	0.037948
0.3	0.183057	0.823593	208°47′	3°52′	0.137472	0.064057	0.750979	0.077777	0.138076	0.066262
0.25	0.192878	0.824400	213°41′	4°49′	0.137048	0.064410	0.710542	0.078130		
0.20	0.209631	0.826160	220°05′	5°56′	0.136796	0.064606	0.652556	0.078200		
0.15	0.242067	0.829729	228°31′	7°58′	0.136606	0.064753	0.564331	0.078041		
0.1	0.316955	0.839837	239°37′	11°55′	0.136474	0.064857	0.430578	0.077226	0.426865	0.203450
0.05	0.571421	0.892456	253°42′	22°58′	0.136394	0.064918	0.238693	0.072741	0.856053	0.407740
0.03	0.928658	1.006230	260°03′	35°15′	0.136378	0.064930	0.146855	0.064528	1.427560	0.679857

The method adopted in this paper is that used by Lord Rayleigh in the theory of gratings and is not appropriate in the neighbourhood of $L/L_{s1}=0$ because of the assumption that ζ and $d\zeta/dx$ are small in comparison with wave length of incident SH wave. Concretely speaking, this method seems to be invalid for $L/L_{s1}<0.3$ or $L/L_{s1}<0.5$ depending on the amplitude of corrugation as seen from Fig. 2(a), Fig. 3(a), Fig. 8 and Fig. 9. In this range of wave length of corrugation, other appropriate methods had better be adopted. The consideration of other methods and the study of the cases of incidence of P and SV waves will be made in the near future.

In addition to these results, it was found that depending on the ratio of the wave length of corrugation to that of the incident SH wave, there exist waves which appear to propagate along the boundary surface because their amplitude decreases exponentially with the distance from the boundary surface increasing. The amplitude of these waves decreases depending on the order of spectrum, the wave length of corrugation, etc.

In concluding, the writer expresses his hearty thanks to Professor Hirosi Kawasumi, Assistant Professor Yasuo Sato and Mr. Ryosuke Sato for their useful advices and discussions. To Mr. Noriaki Matsumoto and Miss Junko Takahashi, he is also indebted for their assistance in calculation and preparation of text figures.

---

10. 褶曲境界面における弾性波の反射，屈折
第 1 報　SH 波入射の場合

地震研究所　浅　野　周　三

地球内部では，層の境界面が平面でない場合がかなりあり，原因の一部は褶曲の影響と考えられる現象もあるので，弾性波の反射屈折におよぼす褶曲の影響を調べてみた．方法はかつて，Lord Rayleigh が格子による音の回折を取り扱つた方法で，最近，佐藤良輔が褶曲した自由表面における弾性波の反射に応用したものを採用した．

本報では，平面 SH 波が，Fourier 級数に展開可能な境界面に入射する場合を計算した．褶曲の程度 ζ が小さいとして，第 2 近似，すなわち，ζ^2 の程度まで求めた．実際の数値計算は，簡単のために，$\zeta=c\cos px$ で与えられる境界面に平面 SH 波が鉛直に入射する場合について行なつた．結果は，Tables1–3, Figs. 2–9 に与えられているが，取り扱つた程度の褶曲では，概して影響は小さいが，褶曲の波長が上下の層の S 波の波長に等しい付近では，必ずしも無視し得ない影響を与えること，褶曲の影響の仕方は，屈折波よりも，反射波の方に大きく，きき方は逆であること，褶曲の波長と入射 SH 波の波長の比によるが，境界面から遠ざかるにしたがつて，振巾が指数関数で減少する波が，境界面に沿つて伝播すること等が判つた．さらに褶曲の波長が入射 SH 波の波長の 3 割あるいは 5 割以下になると，各種反射波，屈折波共，急に大きくなるので本報で用いた近似方法では十分でないことを知り得る．

BULLETIN OF THE EARTHQUAKE
RESEARCH INSTITUTE
Vol. 38 (1960), pp. 199-206

11. *Studies of the Thermal State of the Earth. The Fifth Paper: Relation between Thermal Conductivity of Sedimentary Rocks and Water Content.*

By Ki-iti HÔRAI,
Graduate School, University of Tokyo
and
Seiya UYEDA,
Earthquake Research Institute.

(Read March 22, 1960.—Received March 31, 1960.)

Summary

Relation between thermal conductivity of soft sediments and water content was studied. It was ascertained experimentally that, starting from a dry state, the thermal conductivity increases with water content until its maximum value is attained when water saturates the pore of the sample, and decreases gradually in the oversaturated region. Observed variation of thermal conductivity in the oversaturated region was found to be in agreement with Bullard's model. The model was extended to account for the features in the undersaturated region as well.

1. Introduction

The dependence of thermal conductivity of rocks on water content has been studied by several investigators. Clark's unpublished work, as referred to in "Handbook of Physical Constants"[1], reports that the thermal conductivity of sedimentary rocks increases considerably after soaking in water, while Bullard et al.[2] find that it decreases with water content in a water-rich region. To the authors' knowledge, however, no result covering the whole range of water content has been reported. In the course of determination of the terrestrial heat flow at the Innai Oil Field, Akita Prefecture, Japan[3], the writers happened to estimate the thermal conductivity of some soft porous shale which is

1) *Handbook of Physical Constants* edited by F. Birch, *Special Papers* Number 36, Geological Society of America, (1954).

2) E. C. BULLARD, A. E. MAXWELL and R. REVELLE, *Adv. Geophys., III* (1956), 153.

3) To be published in the next issue of this Bulletin.

considered to be saturated with water *in situ*. The results presented below describe the variation with water content of the thermal conductivity of the shale obtained as a byproduct of the authors' geothermal studies.

2. Experiments

Two samples used in the present study were cores of shale collected by the Teikoku Oil Company in a bore-hole at the Innai Oil Field, Akita Prefecture, Japan. They belong to the lower Sasaoka-bed and the Tentokuzi-bed at depths of 635 m and 827 m below the surface respectively.[3] Quick X-ray examination by a "Norelco" diffractometer showed that their principal constituent minerals are quartz, feldspar and clay minerals, such as kaoline and montmorillonite.

The samples were easily powdered and could be mixed with water in various proportions. The thermal conductivity was measured by the divided-bar device[4),5)]. For water-rich specimens a thin ring of perspex fitted between the bars was used as a container. The thickness of the ring was 1.0 mm and its height, i.e. the thickness of the specimen, was 6.0 mm. In order to prevent evaporation and leakage of water during measurements, ordinary cellophane tape was pasted around the contacts between the ring and the brass bars. Thermal contact between the specimen and the bars was found to be perfect for the water-rich specimen, so that only one specimen was sufficient for one value of water content. For the water-poor specimens, pressure of 150–180 kg/cm^2 was applied to consolidate the specimen in a disc-shape and no perspex ring was used. In this case, measurement on three or four discs with different thickness and with identical water content was necessary for the elimination of the interfacial temperature drop. Specimens were weighed immediately after the conductivity measurement and after completely getting rid of water contained for the determination of water content. Necessary corrections were made when the perspex ring was used.

3. Results and Interpretation

Results obtained are shown in Figs. 1 and 2. The outstanding feature to be observed in these figures is that the thermal conductivity

4) S. UYEDA, T. YUKUTAKE and I. TANAOKA, *Bull. Earthq. Res. Inst.*, **36** (1958) 251.
5) K. HÔRAI, *Bull. Earthq. Res. Inst.*, **37** (1959), 571.

has a maximum value at approximately 16 and 14 percent of water content (weight percentage), realizing the two effects of water on thermal conductivity mentioned in the Introduction. The whole situation may be interpreted as follows: in the water-rich region, the thermal conductivity decreases with the *increase* of water content because the solid particles having a greater thermal conductivity than water are

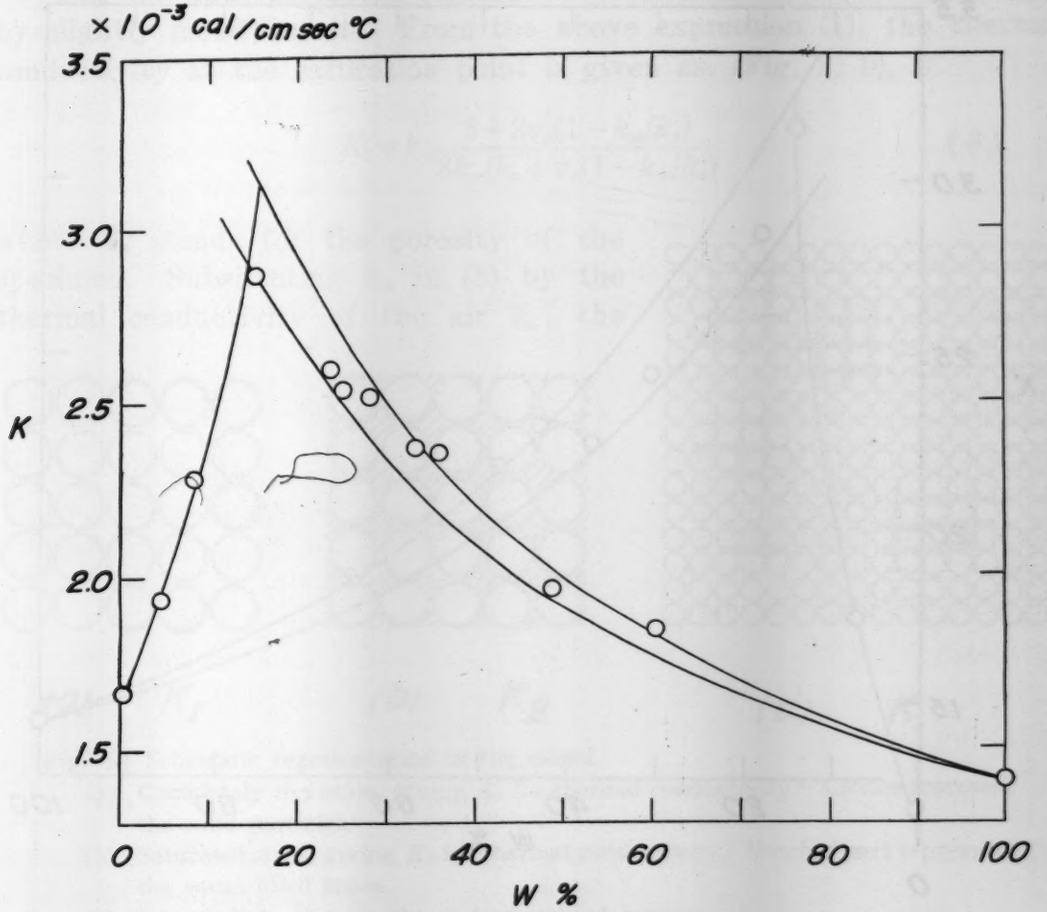

Fig. 1. Relation between thermal conductivity and water content (weight percentage): (Specimen IN VIII, Lower Sasaoka Bed).

more and more replaced by water by increment of water content, while in the water-poor region, the decreases of conductivity with *decrease* of water content is caused by substitution of water by the air, a poorer conductor of heat, because dense packing of solid particles no longer permits subtraction of water without forming air-cavities. These two regions, thus, may properly be called the oversaturated region and the undersaturated region.

The above interpretation may be formulated in the following way. For the oversaturated region, Bullard et al.[6] showed that the following relation based on the model that the solid particles of spherical shape are dispersed in water without mutual interaction[7] :

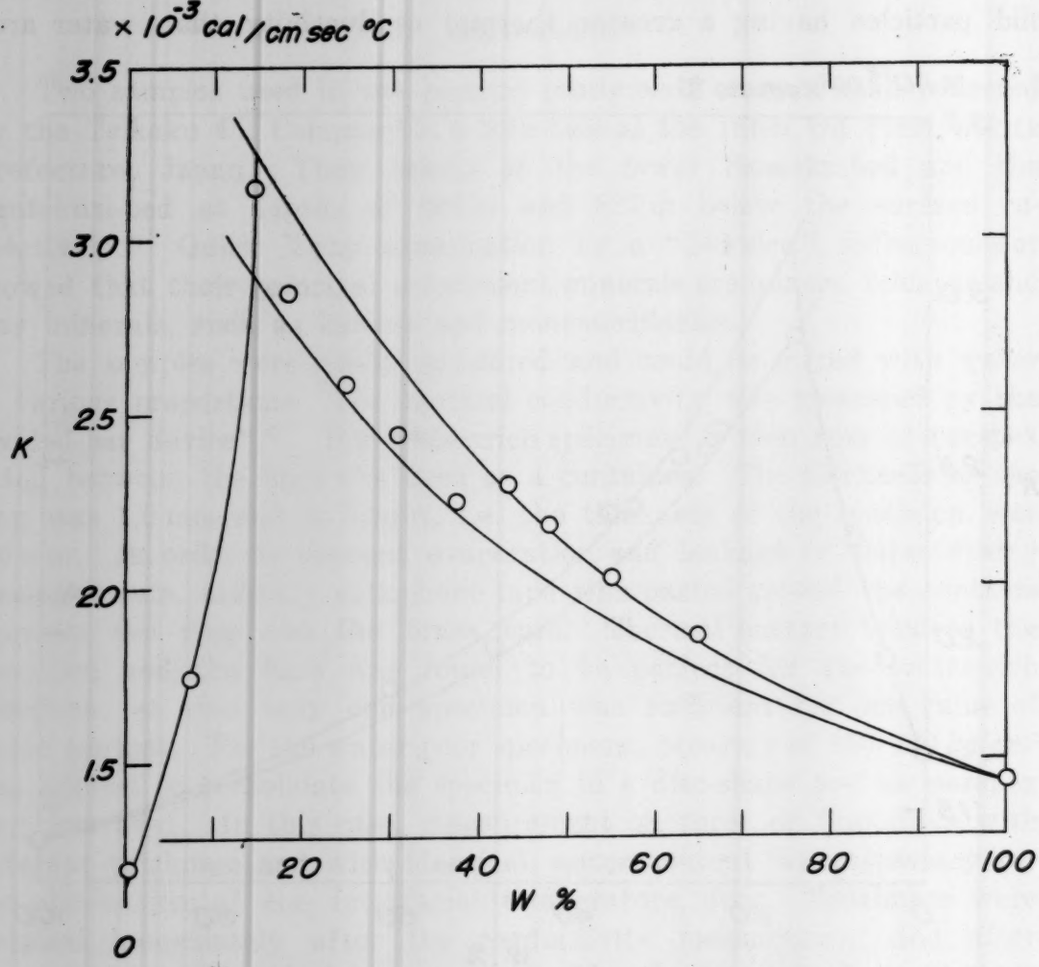

Fig. 2. Relation between thermal conductivity and water content (weight percentage): (Specimen IN X, Tentokuzi Bed).

$$k=k_w\frac{3-2v(1-k_w/k_s)}{3k_w/k_s+v(1-k_w/k_s)} \qquad (1)$$

where the thermal conductivity of the specimen k is expressed as a function of the thermal conductivities of water k_w, and of the solid

6) E. C. BULLARD et al., *loc. cit.* (2).

7) J. C. MAXWELL, "*A Treatise on Electricity and Magnetism*", 3rd ed. [ii], **1** (1904), Dover.

particles k_s and the water content by volume v. v is related to the water content by weight w as,

$$v=w/[w+(1-w)\rho_w/\rho_s] \qquad (2)$$

where ρ_w and ρ_s denote the density of water and the solid particles.

For the undersaturated region, we deduced a similar formula to (1) by slightly modifying it. From the above expression (1), the thermal conductivity at the saturation point is given as, (Fig. 3, b),

$$K_2=k_w\frac{3-2v_p(1-k_w/k_s)}{3k_w/k_s+v_p(1-k_w/k_s)} \qquad (3)$$

where v_p stands for the porosity of the specimen. Substituting k_w in (3) by the thermal conductivity of the air k_a, the

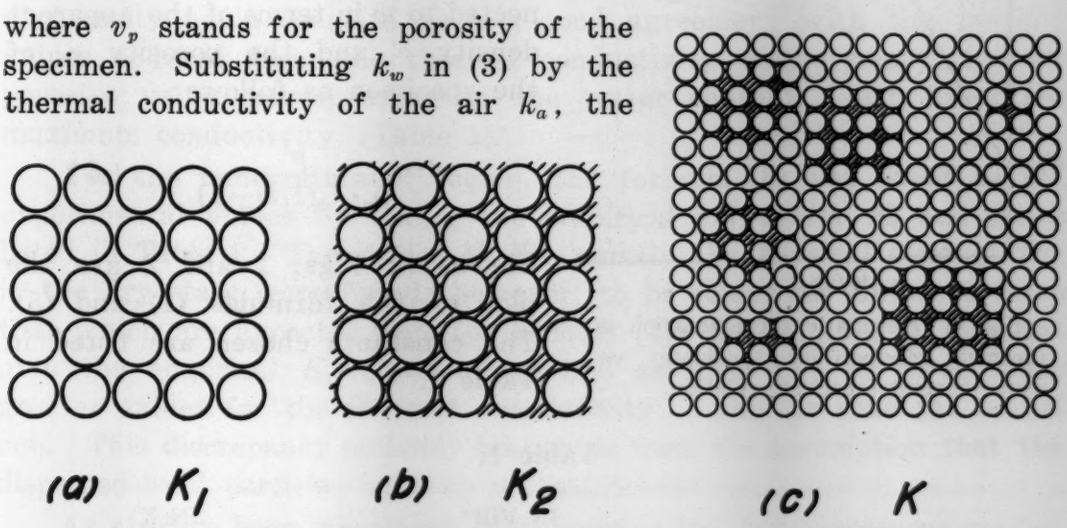

Fig. 3. Schematic representation of the model.
(a) Completely dry state, giving K_1 for thermal conductivity. Circles represent the solid particles.
(b) Saturated state, giving K_2 for thermal conductivity. Hatched part represents the water-filled space.
(c) Intermediate state in the undersaturated region.

conductivity value in the completely dry state may be expressed as, (Fig. 3, a),

$$K_1=k_a\frac{3-2v_p(1-k_a/k_s)}{3k_a/k_s+v_p(1-k_a/k_s)}. \qquad (4)$$

These quantities are illustrated in Fig. 4. In the intermediate states in the undersaturated region, the water contained in the specimen would be in such a state as shown in Fig. 3, c, i.e. as if patches of the ap-

parent thermal conductivity K_2 are dispersed in the medium of apparent thermal conductivity K_1. Application of the same idea as in (1) to such a situation gives the thermal conductivity of the specimen in bulk as,

$$K=K_1\frac{3-2(1-v')(1-K_1/K_2)}{3K_1/K_2+(1-v')(1-K_1/K_2)} \qquad (5)$$

where $1-v'$ is the volume ratio of the air contained to the interstitial space in the specimen. v' is connected to w in terms of the apparent density ρ' and the porosity p_v of the specimen as follows:

$$v'=\frac{\rho'}{p_v\cdot\rho_w(1/w-1)}\,. \qquad (6)$$

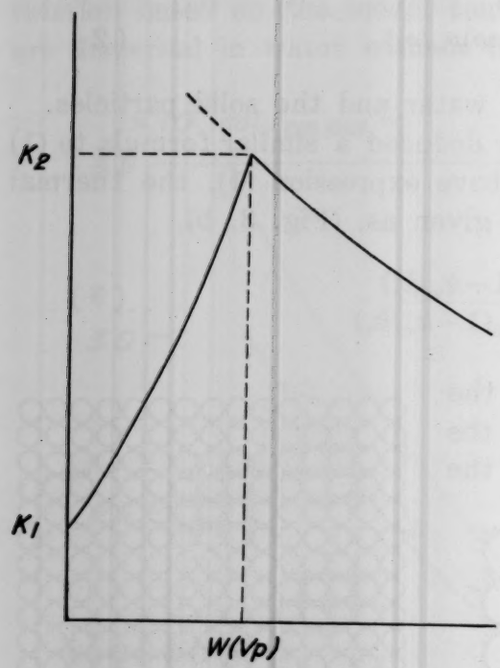

Fig. 4. Schematic representation of thermal conductivity (ordinate) vs. water content (abscissa) relation.

Curves in Figs. 1 and 2 are the plot of the formulas (1) and (5). The constants chosen are listed in Table 1.

Table 1.

Specimen	IN VIII* (Lower Sasaoka Bed)	IN X (Tentokuzi Bed)
k_w (10^{-3} *cal/cm sec deg*)	1.41 (22°C)	1.44 (30°C)
k_s (〃)	upper curve in Fig. 1 3.86	upper curve in Fig. 2 3.76
	lower curve in Fig. 1 4.45	lower curve in Fig. 2 4.69
K_1 (〃)	1.65	1.15
K_2 (〃)	2.95	3.20
ρ' (apparent) (*gr/cc*)	1.67	1.48
$\rho(=\rho_s)$ (true) (*gr/cc*)	2.39	2.19
p_v from conductivity measurement	0.16	0.14
p_v from density measurement	0.15	0.18

* "IN" stands for the Innai oil field.

4. Discussion

The values of k_s in Table 1 were chosen by trial and error in order to fit the formula (1) to the experimental results. In fact, the two curves in Figs. 1 and 2 seem to indicate the limits of the possible k_s values: they are 3.86×10^{-3} *cal/cm sec deg* and 4.45×10^{-3} *cal/cm sec deg* for the lower Sasaoka bed sample (IN VIII) and 3.76×10^{-3} *cal/cm sec deg* and 4.69×10^{-3} *cal/cm sec deg* for the Tentokuzi bed sample (IN X) respectively. These values are quite reasonable for the thermal conductivity of the minerals concerned in order of magnitude.

Porosity of the samples was estimated from the measured values of apparent density and of true density as listed in Table 1. These values of porosity again seem to be in a good agreement with the porosity values deduced from the thermal conductivity measurement, i.e. the porosity value corresponding to the water content which gives the maximum conductivity, (Table 1).

For the undersaturated region, the formula (5) was fitted to the experimental values by taking the empirical values for K_2 and K_1 as listed in Table 1. The values of K_1, namely the thermal conductivity in the dry state were found, however, to be somewhat different from that which are expected from the formula (4): the formula (4) does not give the empirical K_1-values unless one assumes two or three times greater values for the thermal conductivity of the air than the actual one. This discrepancy probably originates from the assumption that the dispersed solid particles have no mutual interaction.

As already been mentioned, a pressure of 150–180 kg/cm^2 was applied for consolidating the specimens. This pressure may correspond to the rock-pressure prevailing at the depth of some 500–600 m in the earth, so that the soft sediments, such as shales studied here, will have the same porosity *in situ* as the compressed samples in our experiments. In the actual state, water fills up the pore to saturation. As the thermal conductivity relevant to the geothermal studies, therefore, one may adopt the values at the saturation condition, i.e. the maximum values in Figs. 1 and 2.

Acknowledgment

The authors thank the staff of the Teikoku Oil Company who provided us with the rock samples and Dr. J. Ossaka, Earthquake Research In-

stitute, and Mr. Y. Ono, Japan Geological Survey for their kind help in the density work. Their sincere thanks are also due to Dr. T. Rikitake and Prof. C. Tsuboi.

---

11. 地球熱学 (第 5 報)
堆積岩における熱伝導度と含水量の関係

東京大学大学院
地球物理学専門課程　宝　来　帰　一
地震研究所　上　田　誠　也

岩石の熱伝導度と含水量の関係については，水のきわめてすくない場合，および水の多い場合について Clark, Bullard 等の研究があるが，今回一つの試料について乾燥状態から含水量 100% (試料全体が水) の場合までを測定することによつて，その最大値が，含水量約 20% 弱のところに存在することが明らかになつた (第一図，第二図)．熱伝導度の最大値をあたえる含水量はわれわれが用いた秋田県院内油田の shale においては，水が丁度試料の空孔を満した場合に相当するが，上記の事情は一般的なものと解される．この最大値を境にして含水量が増減するときは熱伝導度は減少するが，この性質は簡単なモデルによつて定量的に説明し得ることを示した．なお，この研究は，院内油田での地殻内熱流量の推定に用いられる (続報)．

BULLETIN OF THE EARTHQUAKE
RESEARCH INSTITUTE
Vol. 38 (1960), pp. 207-218

12. An Attempt to Detect Azimuth Effect on Spectral Structures of Seismic Waves (The Alaskan Earthquake of April 7, 1958).

By Keichi KASAHARA,

Earthquake Research Institute.

(Read March 22, 1960.—Received March 31, 1960.)

Summary

The author worked out a spectral analysis of the seismic waves radiated by the Alaskan earthquake of April 7, 1958. It purposes to make a kind of tests whether or not the "point" or the "spherical" origin models of earthquakes explain the actual mechanism of wave radiation completely. Because, suppose these models represent the nature of earthquake origins very well, then the waves of the same spectral structure (*P*- and *S*-waves) are to be observed at all the azimuths.

Seismograms recorded with the Press-Ewing type seismographs at Tsukuba and other six stations were used conveniently. These stations except Resolute Bay are located at nearly equal epicentral distances (40–55°), so that the comparison of their data can be made fairly simply.

It was found out that no special azimuth effect was observed in the spectra of *P*-waves. On the other hand, as to *S*-waves, a notable difference in the spectrum type was detected between three groups of stations. This difference is more likely to be attributed to the mechanism of wave radiation, rather than to the distortion of spectra caused by some conditions of wave propagation. Since the available data are very few at present, definite conclusions will be postponed until more examples are obtained.

1. Introduction

The mechanism of earthquake origins has been studied by many seismologists on the basis of simplified models of spherical (or point) origins.[1] In fact, we know numbers of examples reported by them, in which the model provides a reasonable explanation for the observational

1) *f.i.* J. H. HODGSON (Editor), *Publ. Dominion Obs.*, **20** (1958), 251–418.

results, such as azimuthal distribution of push-pull sense and amplitude of the initial disturbances. These models assume suitable types of stress distribution changing in time over an spherical surface which is imagined in the earth. The patterns of wave radiation from them, whether we take the force type I or II, are independent of the frequency of the origin forces. In other words, it is the amplitude (including polarity) of waves that are seriously influenced by the azimuth whereas the same wave-form (or the spectral structures) must be observed at different points around the origin.

The author's previous study has found out a notable characteristics of the fault origin model. The pattern of wave radiation from it is given by $C_0+C_2\cos 2\theta+\cdots$ for S-waves, where θ is the azimuth and $C_0, C_2, \cdots$ are the constants.[2] Since the ratios of C_0 to $C_2, C_4, \cdots$ are the functions of ω (frequency of origin excitation), the radiation pattern will take different types for different values of ω. That is to say, the wave-form changes from azimuth to azimuth. As to P-waves, such an effect is not expected to be remarkable, because its pattern is given by the single term of $B_2\sin 2\theta$ approximately, provided the effect of very high frequencies is negligible. Because of the difficulty in numerical calculation, the author could not show the above-stated effect in detail. In the F. Press's[3] paper reporting a model study, however, we clearly notice the variation of wave-form (S-waves) with azimuth, which might be the proof for the azimuth effect of the fault origin model.

Taking these circumstances into consideration, we may say that it is worth attempting to detect the effect of azimuth on the actual seismograms. Whether we obtain positive results or not, it must give us valuable information about the physical state of earthquake origins.

2. Analysis of seismograms

The present paper deals with a set of seismograms of the Alaskan earthquake of April 7, 1958 recorded with the Press-Ewing seismographs. According to the report from the U.S. Coast and Geodetic Survey, the epicentre was located at 66°½N, 157°W, and the magnitude was estimated at about $7-7\frac{1}{2}$ by several stations.[4] The depth of the origin has not

2) K. KASAHARA, *Bull. Earthq. Res. Inst.*, **36** (1958), 21–53.

3) F. PRESS, *Publ. Dominion Obs.*, **20** (1958), 271–277.

4) *Seismological report from the Central International Bureau of Seismology, I.U.G.G.* (Strasbourg).

been known accurately, but the station at Saint Louis reported h=0.00 R. As to the macroseismic features, this earthquake has not been known very well except the preliminary report written by T. N. Davis, who observed a great volume of mud appearing on the surface at the epicentre[5]. The focal mechanism has not been reported yet by any authority, but according to the author's rough estimation, it is to be sorted into the strike-slip group (see section 4).

The Press-Ewing seismograph is very useful for the present purpose, because it keeps large magnification over a wide range of low frequency. This type of seismograph has been distributed over the world during the IGY. The records at seven stations among them were used for the analysis, they are Tsukuba, Honolulu, Pasadena, Waynesburg, Palisades, Resolute Bay and Uppsala. All of these stations, except Resolute Bay, are located at the distance of about 40–55° from the epicentre. Use of the seismo-

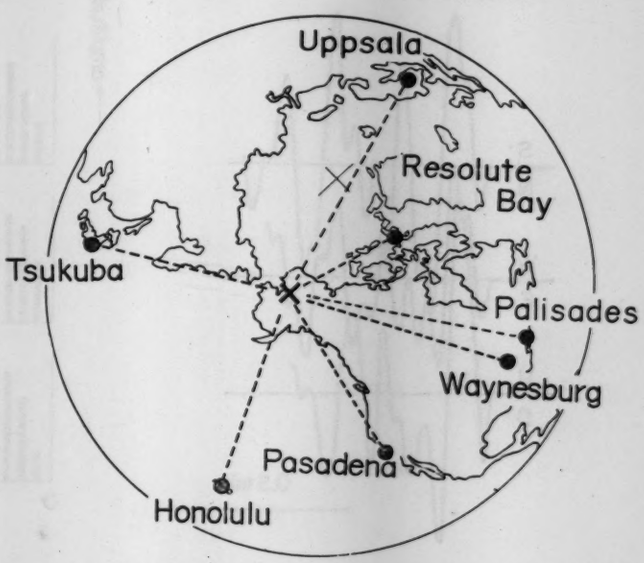

Fig. 1. Epicentre of the earthquake (×) and the seismograph stations (●).

Table 1. Stations and seismographs used for the analysis.

Station	Abbreviation	Distance	Azimuth	Seismograph	Component of Record		Remark
					P	*S*	
Tsukuba	Ts.	46°	N 97°W	"Press-Ewing" 15ˢ– 75ˢ	NS, EW, UD	EW	
Honolulu	Ho.	44	N175°W	15 – 75	—	EW	
Pasadena	Ps.	38	N125°E	30 – 90	UD	UD	
Waynesburg	Wy.	52	N 85°E	15 – 75	UD	UD	
Palisades	Pl.	52	N 80°E	30 –100	UD	UD	
Resolute Bay	Re.	21	N 43°E	15 – 75	NS	—	
Uppsala	Up.	55	N 5°E	15 – 75	UD	NS, EW, UD	

5) T. N. DAVIS, *Trans. Amer. Geophys. Union*, **39** (1958), 941–942.

grams recorded with the instruments of the same type at nearly equal epicentral distance made the following comparison of data fairly simple.

It would be reasonable to investigate the spectrum of *P*-waves

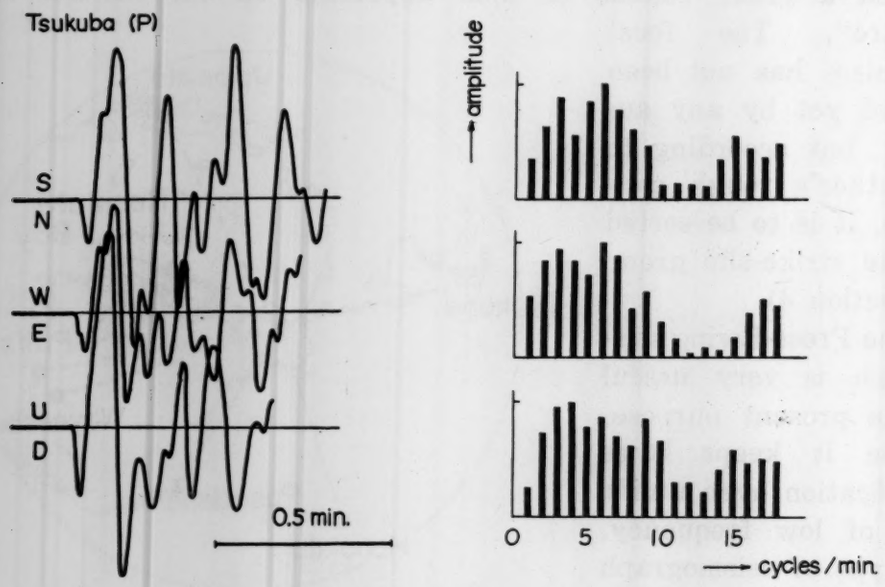

Fig. 2. Spectra of the three-component records at Tsukuba (*P*-phase).

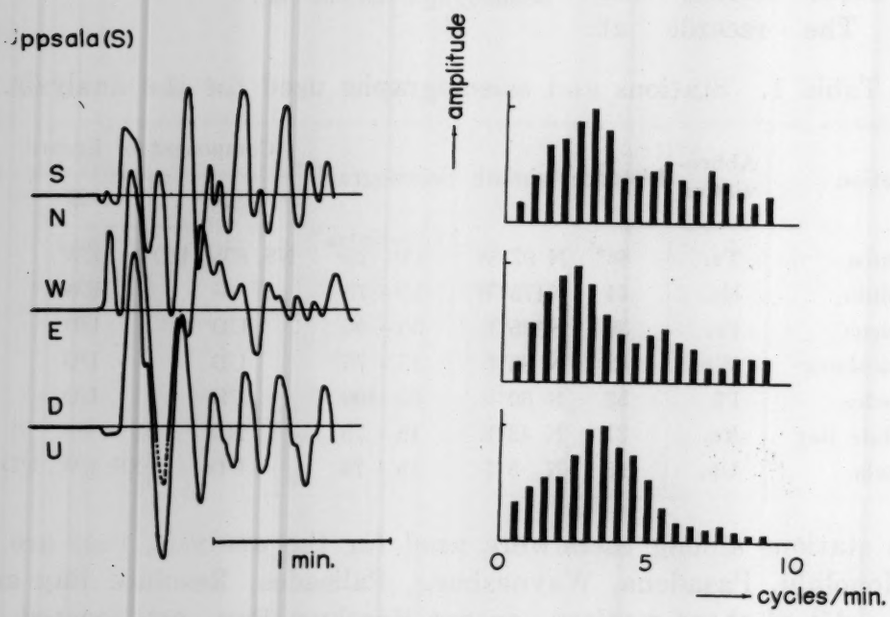

Fig. 3. Spectra of the three-component records at Uppsala (*S*-phase). A part of the EW-component record was off scale, which was assumed as shown with broken line (see also Fig. 5).

putting most stress on the records of vertical component, whereas to study *S*-waves taking one of the two horizontal components which is most responsible to *SH*-waves. However, this standard of selection could not be applied to all the stations, where the other component was used

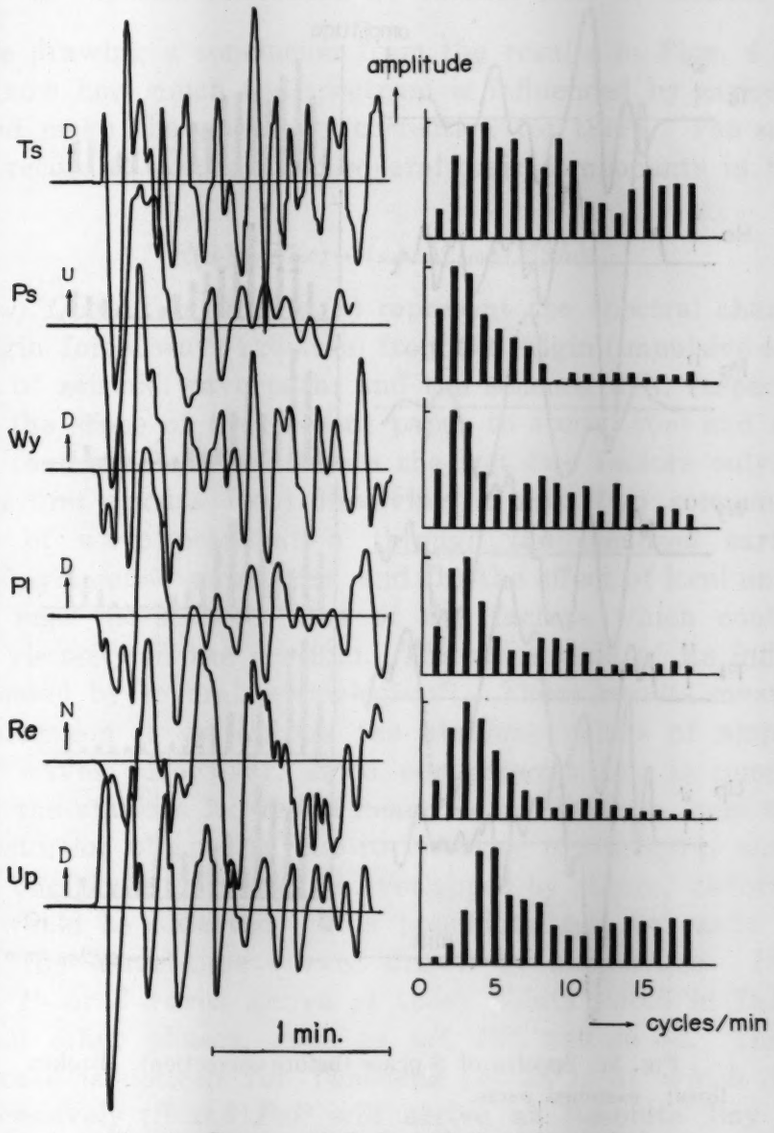

Fig. 4. Spectra of *P*-phase (before correction).

temporarily (see Table 1). This sort of replacing is believed to cause no serious troubles in conclusions as can be seen in the following examples.

Fig. 2 illustrates the spectra of the three-components of *P*-phase recorded at Tsukuba (before the correction for the frequency response of

the instruments), in which we observe no remarkable discrepancy between them. For the same purpose Fig. 3 is drawn taking the three component records of *S*-phase at Uppsala. The two horizontal components have the spectral structures quite similar with one another. The vertical

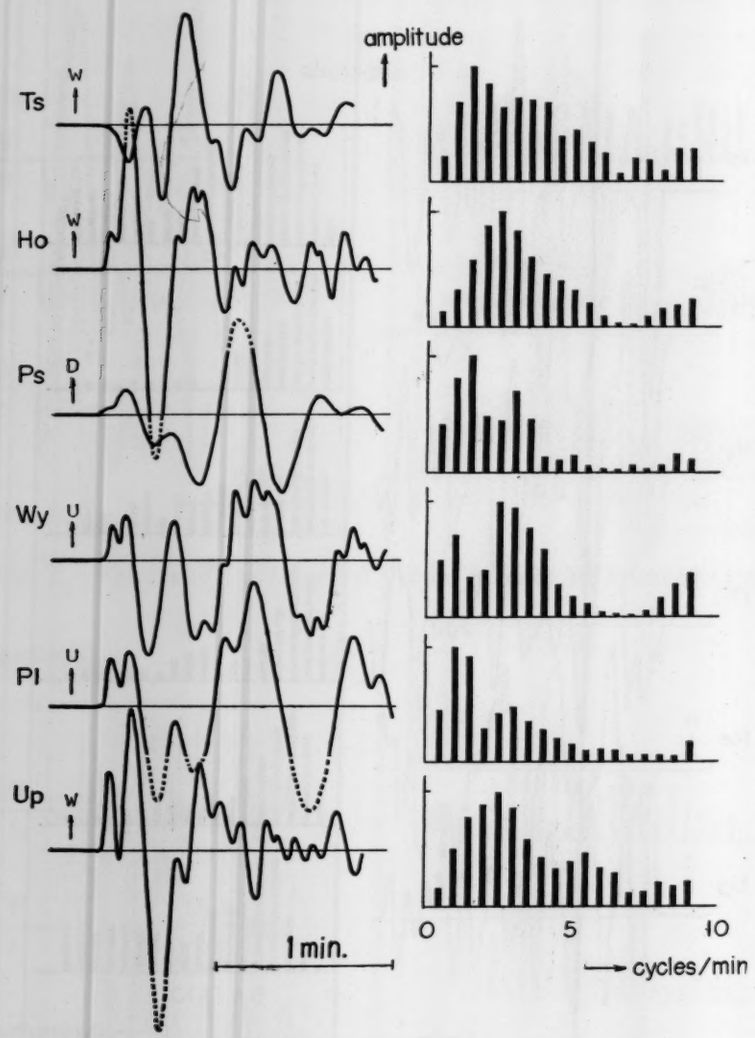

Fig. 5. Spectra of *S*-phase (before correction). Broken lines: assumed parts.

component is likely to show somewhat different feature. But the difference is not so large that replacement of the data of horizontal component with the vertical one might be allowed in such cases when the former is unavailable.

The method of analysis, used here, is quite same with that explained

in the previous paper[6]. The fundamental period is 1 min. for *P*-phase whereas 2 min. for *S*. Figs. 4 and 5 are the spectra drawn in this way, where no correction is made for the frequency response of the instruments.

3. Spectra influenced by various sorts of factors

Before drawing a conclusion from the results in Figs. 4 and 5, we have to know how much the spectrum is influenced by various sorts of factors and make the necessary correction for them. The spectrum of a seismic record $R(\omega)$ consists of several basic components in the following way,

$$R(\omega)=P(\omega)\cdot O(\omega)\cdot Y_1(\omega)\cdot Y_2(\omega)\ , \qquad (1)$$

where, $P(\omega)$, $O(\omega)$, $Y_1(\omega)$ and $Y_2(\omega)$ represent the spectral characteristics of the origin force, wave radiation from the origin (impulsive excitation), conditions of seismic wave path, and the seismograph, respectively. It is beyond the scope of the present paper to study $P(\omega)$ and $O(\omega)$ separately, so that we shall investigate the last two factors only.

Let us first discuss $Y_1(\omega)$ dissolving it into two components: (a) the effect of wave propagation through the idealized earth having spherically symmetric structures, and (b) the effect of local underground structures near the station. One of the factors which contributes to (a) is the viscosity in the medium. The magnitude of its influence has been estimated by several seismologists[7]. These results must be taken into consideration if we discuss the absolute values of amplitudes or spectra of waves. However, since our interest lies in comparing the data from the stations located at nearly equal distance from the origin, relative distortion of spectra due to viscosity is negligibly small.

When one phase of waves is overlapped by others, distortion in the spectrum would be observed. This possibility can be easily tested by examining the travel-time curves drawn by authorities. It is clear, then, that *P*- or *S*-waves arrive at those points listed in Table 1 separately from other phases, such as *pP*, *PP*, and so on. The only exceptional case is noticed for Pasadena ($\Delta=38°$), at which *S* and *PcS* arrive successively (*S* and *PcP* will arrive at Resolute Bay nearly at the same time, but the latter will have no much influence upon the records of horizontal components). However, this effect might be neglected when the energy of *PcS* is not so large as that of *S*.

6) K. KASAHARA, *Bull. Earthq. Res. Inst.*, **35** (1957), 473–532.

7) *f.i.* A. KUBOTERA, *Zisin (Journ. Seis. Soc. Japan)*, [ii], **5** (1952), 77.

Magnitude estimation of the factor (b) is more difficult than that of (a). Incidence of the original waves to the earth's surface of complicated structures will cause multiple reflection and conversion of waves there. If these waves have sufficiently large energy they will cause the distortion of spectrum. After simple consideration[8], we know that this effect can not be disregarded particularly when the waves attack the surface successively with the time delay that falls in the range of period in which the predominant components of spectrum appear. Since our interest lies in the range of period from several seconds up to several tens seconds, the effect due to structures of very small scale, that sometimes plays an important role in the vibration characteristics of the ground, might be neglected. The lack of our knowledge about fairly large scale structures of the crust makes it quite difficult to discuss the present effect quantitatively. The only possible way is to arrange the results of analysis in the order of azimuth of each station and examine whether or not this undesirable effect disturbs the systematic characteristics of the phenomenon. From this point of view, comparison of the data at Honolulu with that at Uppsala gives us an interesting suggestion. As to the crustal structures, Honolulu must show remarkable contrast with other stations lying one the continental structures. Nevertheless, its record has spectral structures quite similar to that of Uppsala, located at the opposite position with respect to the origin (see Fig. 5 or Fig. 7). Similarity of the spectra of Waynesburg's data to those of Palisades is also notable. These two stations are a few hundred kilometres apart from one another, but the records of similar features have been obtained there.

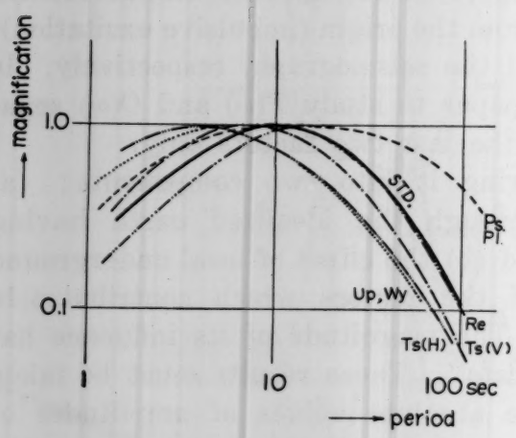

Fig. 6. Frequency response curves of seismographs.

These facts might be the evidence for the influences of the local structures being not remarkable on the spectrum of long period components, though there still remains some uncertainty in this supposition.

The influence of the frequency characteristics of a seismograph is more easily corrected than the above effects. Fig. 6 shows the response

8) K. KASAHARA, *loc cit.* 6).

curves for all the stations in the same coordinates. We shall temporarily take the curve of thick line (STD.) as the standard and reduce the results from all the stations to it. Since our purpose is in the comparison of the data, such temporary way of correction may be permitted. Fig. 7 illustrates the curves of spectra after this correction.

4. Discussion

Taking the above discussion into account, we may regard the curves in Fig. 7 as representing the fundamental characteristics of wave radiation without much distortion. First we compare the curves for *P*-phase with each other. All of them have a quite similar appearance to each other although a slight discrepancy is noticed for the curve of Tsukuba. They have a single peak at the frequency of about 3 cycles/min. and the slope monotonously approaching zero at lower frequency. In the high frequency range no remarkable peaks can be seen. The present result is very interesting and is to be explained reasonably by the ordinary models of spherical origins.

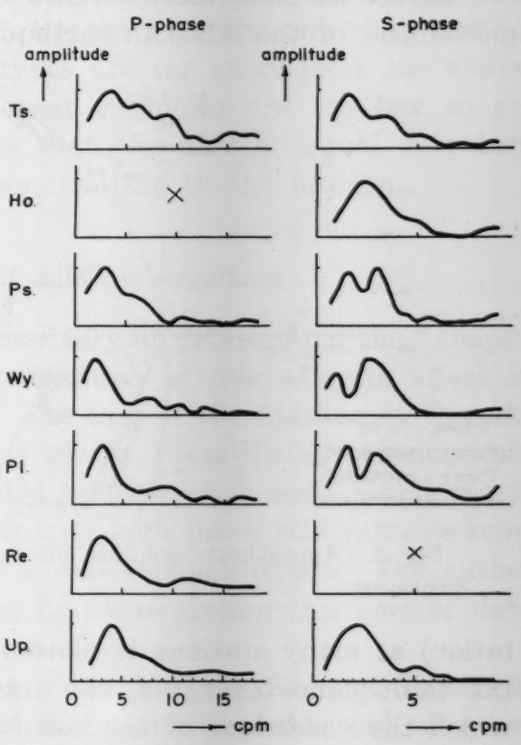

Fig. 7. Spectra of *P*- and *S*-phases (after correction).

The curves for *S*-phase pre sent, on the other hand, another notable tendency. We can see no such similarity there as was noticed for *P*-phase. Roughly speaking, we may say that the curves are classified into two or three groups. The first group, which includes Honolulu and Uppsala, is of a single-peak type having its maximum at the frequency 2 or 3 cycles/min. The data at Pasadena, Waynesburg, and Palisades are likely to present the second type. This type has double peaks, the first peak at about 1.5 cycles/min. and the second one at 3 cycles/min or so. One may say that this difference should be attributed not to the mechanism of wave

radiation but to the application of the vertical component record in place of the horizontal one. Since the horizontal component data were unavailable at these stations, the author can not strongly deny this objection. However, he would dare say that this is not the apparent effect but the real one, because the difference is still remarkable even if we compare these spectra with that for the vertical component record at Uppsala (see Figs. 3 and 5).

The data at Tsukuba is similar neither to the first group nor to the second one. In this sense, it must be classified as a third one, which is likely to be the intermediate type of the first two.

Before we make more definite discussion, we have to know the focal mechanism of the Alaskan earthquake in relation to the distribution of the stations. Unfortunately, this sort of study has not been reported by any seismologists yet. Therefore, let us take here a fault-plane technique in order to obtain a solution for temporary use. The seismological report from Strasbourg is used together with the materials given by some other observatories. Fig. 8 illustrates the result, in which the sense of the first *P*-phase (contraction or dilatation) at many stations is plotted with suitable symbols. By applying the fault-plane technique, the author draw a pair of nodal lines, from which the conditions of the nodal planes are estimated as shown in the same figure. It is interesting to examine whether or not this solution is consistent with the observational data of *S*-phase with respect to its polarity. The arrow marks in the same figure indicates the polarity of *S*-phase determined from the records of the Press-Ewing seismographs. On the other hand, the broken lines are the nodal lines of *S*-phase, which are given uniquely if we assume the mechanism of wave radiation to be the force type II[9]. It is very clear that these lines harmonize well with the observational data. It seems difficult to explain these data by

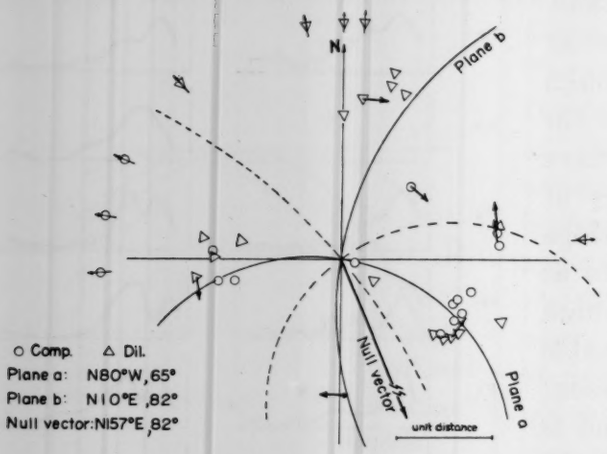

Fig. 8. Approximate solution for the focal mechanism.

9) *loc cit.* 1).

taking the model of the force type I. It is not the author's purpose to insist that the present solution is very decisive ; however, he considers it to represent the mechanism of the earthquake, approximately.

It is an interesting problem to make comparison of Fig. 7 with Fig. 8 for the purpose of finding out some relationship between the focal mechanism and the distribution of spectral types. From this point of view, it might be a notable fact that Honolulu and Uppsala are very close to the line of the plane b. These two stations belong to the first type of spectrum (*S*-phase) having a single peak, and the energy of *S*-waves observed there is likely to be larger than that of the other stations (this point is not very clear since magnification of all the seismographs is not known accurately). On the contrary, the other stations belonging to the second or the third types are far away from the above-stated line. Unfortunately, the present examples are too few to get a definite conclusion from them, so that the author would like here only to point out a bit of information relating to the problem.

5. Conclusions and acknowledgement

The author has pointed out a possibility of determining the "shape" of an earthquake origin by the examination of the azimuth effect on the spectral structures of *S*-waves. The case of the Alaskan earthquake is tested as a trial using the records of the Press-Ewing seismographs distributed over the world. A notable tendency has been found out in relation to the azimuth of the stations, though there still remains some uncertainty in concluding this to be a real azimuth effect. The author wishes to make this point very clear by accumulating this sort of data in future.

The author wishes to express many thanks to the Lamont Geological Observatory, the Seismological Laboratory at Pasadena, and all other stations which kindly gave him facility for using the seismograms recorded by them. He is also thankful to Prof. N. Nasu, Prof. T. Hagiwara and Dr. Y. Satô, who gave him encouragement and valuable advice in the course of this work.

12. 大地震発震スペクトルの方位特性に関する一つの試み (アラスカ地震の場合)

地震研究所 笠 原 慶 一

1958 年 4 月 7 日に起きたアラスカ地震の記録についてスペクトル解析を行なつた．その目的は，震源から伝わる P 波および S 波のそれぞれが，あらゆる方向に同一のスペクトル構造をもつて射出されているか否かを検討しようとするものである．ふつう震源機構を説明するのには“点源”または“球状源”の模型を適用するのが常識になつているが，これらに共通する性質として P 波·S 波のスペクトル構造は各方位に同一の型を示すはずである．一方，断層模型などのようにスペクトル構造が規則的な方位特性を示すものも考えられる．従つて，観測事実が方位特性を肯定するか否定するかを明らかにすることは，震源の形を知る上に重要な手がかりを与えてくれる．

解析にあたつては，筑波をはじめとする計 7 カ所の記録を資料として用いた．これらの観測所はすべて Press-Ewing 型長周期地震計を備えており，しかも Resolute Bay を除いてはほぼ同一の震央距離 (40～55°) にある．このことは解析結果を相互に比較する上に大へん有利である．

P 波のスペクトル構造に関しては格別の方位特性は認められない．これに反し S 波のそれは，いろいろな因子の影響を考慮してもすべての観測点で同一型式とは考え難いように見える．数少ない資料であるから具体的にどういう方位特性であるか断定できないし，まして，どういう震源模型が最適であるか決めることは難しい．しかし，今後この種の資料が集積されるにしたがつて，震源の性状に関する一つの決め手が得られるものと期待される．

BULLETIN OF THE EARTHQUAKE
RESEARCH INSTITUTE
Vol. 38 (1960), pp. 219-240

13. *Observation of Surface Waves by Columbia-type Seismograph Installed at Tsukuba Station, Japan. (Part 1) — Rayleigh Wave Dispersions across the Oceanic Basin. —*

By Tetsuo A. SANTÔ,

Earthquake Research Institute.

(Read Feb. 23, and March 22, 1960.—Received March 25, 1960.)

1. Introduction

As the Long-Period Seismology Program of the International Geophysical Year, Columbia University, U.S.A. installed the long period electromagnetic seismographs (15–80)[1] at many stations in the world. In Japan, this instrument was installed at Tsukuba Station, the Earthquake Research Institute of Tokyo University, and seismic observations have been continued since the beginning of 1958. Constants of this seismograph at Tsukuba Station are as follows:

Component	V_{max}	T_0	T_g	h_1	h_2	σ
EW	585	15.1	77	3.6	2.0	0.16
NS	610	15.1	97	3.6	2.1	0.16
UD	1460	15.0	104	1.5	2.1	0.15

in which, T_0: the natural period of Pendulum
T_g: „ of Galvanometer
h_1: damping constant of pendulum
h_2: „ of galvanometer
σ: coupling factor

This instrument could record many distant earthquakes and most of them showed clear surface waves (Fig. 1). The present work was done in order to see the differences between many dispersion curves of surface waves which travel through various paths around Japan. The epicenters, dates, and other data of shocks are given in Table 1, and their locations are shown in Fig. 2, together with travelling paths to Tsukuba Station.

1) G. SUTTON and J. OLIVER, "Seismographs of High Magnification at Long Periods", *Annales de Géophysique, t. 5, fasc.*, **4** (1959), 1.

As will be seen in the following many figures, we are lacking in the dispersion data for short period range. Therefore, the determinations of crustal structures in various regions must be postponed till the future. However, the abundant dispersion data due to as many as eighty shocks

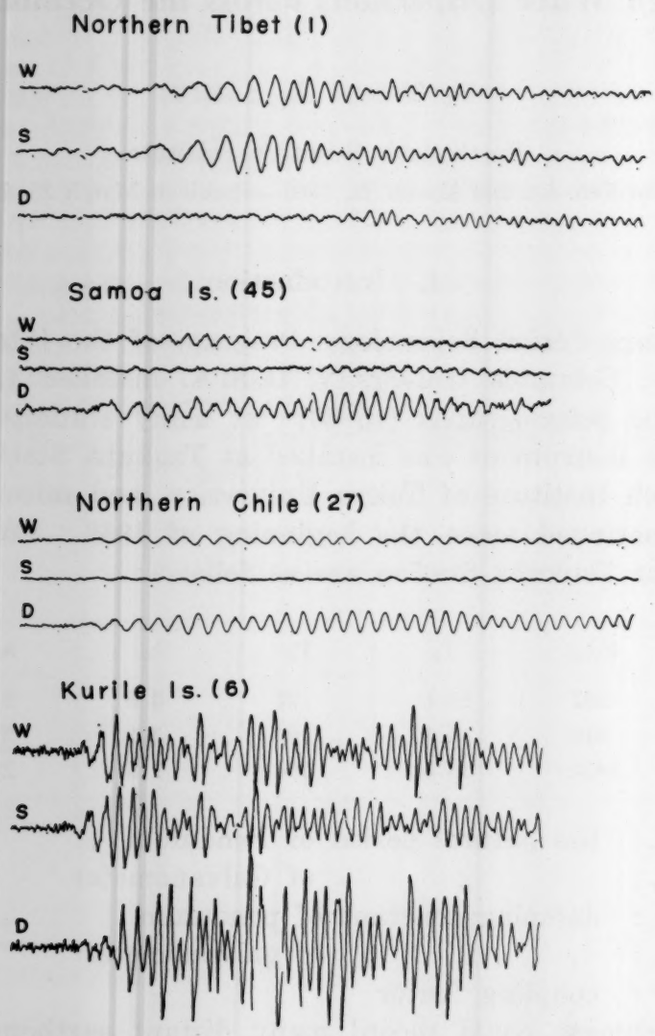

Fig. 1. Some examples of surface wave forms recorded by Columbia type seismograph.

gave us plenty of information about the qualitative features on the crustal structure of various regions around Japan. Besides, they offered us important problems to be studied.

In this first paper, only Rayleigh wave dispersions across the oceanic basin around Japan will be treated. Dispersion data were all taken on *Z*-component seismograms.

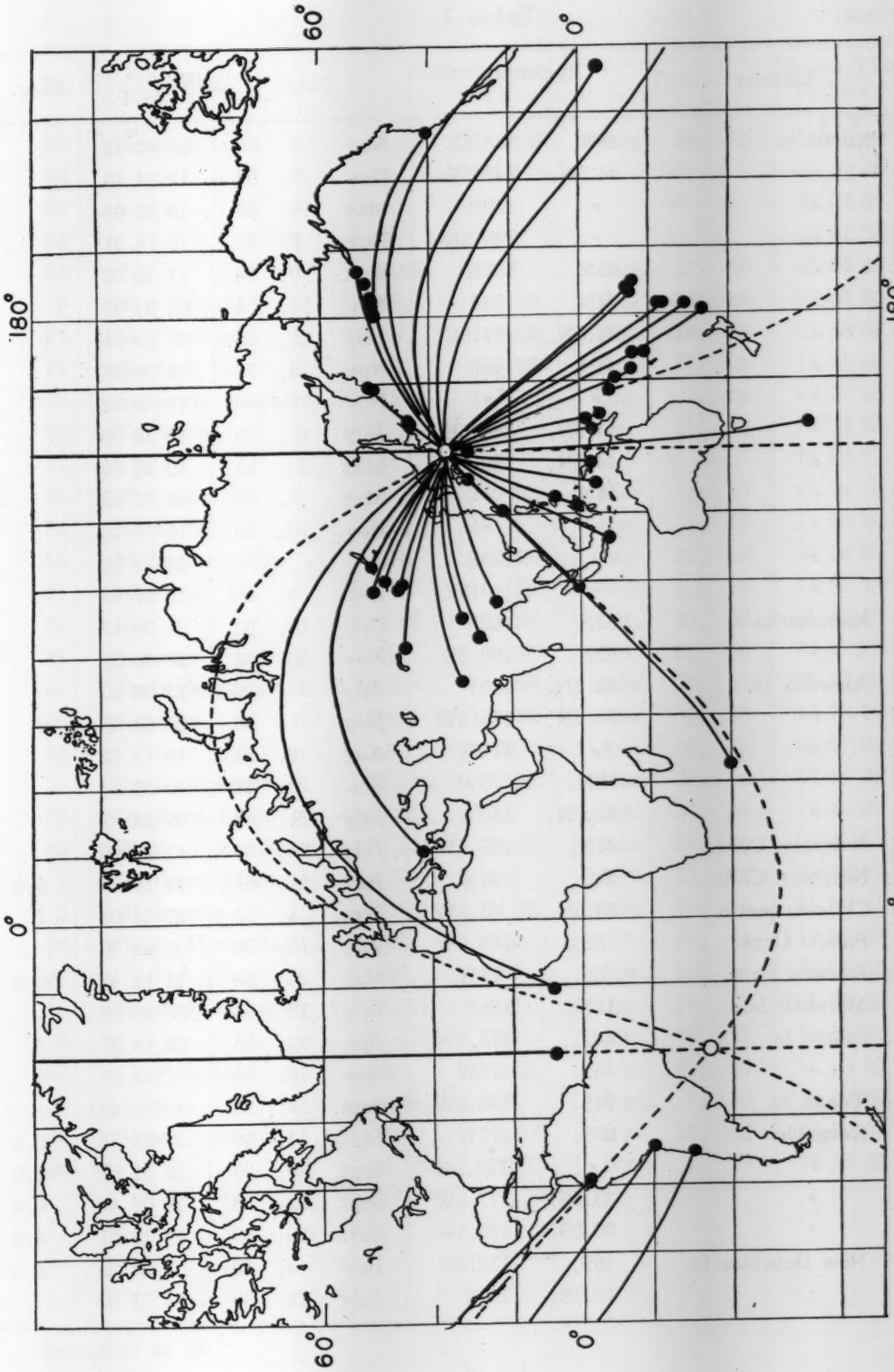

Fig. 2. Epicenters and travelling paths of surface waves. The paths represented by broken curves are those through which W_2 or W_3 were observed.

Table 1.

No.	District	Epicenter λ	Epicenter φ	Date	Origin Time (G.M.T.) h m s	Mag.
5	Kurile Is.	44N,	148.5E	Nov. 7, 58	17 32 42	
6	〃	44.5N,	149.5E	Nov. 7, 58	11 24 19	
7	〃	〃	149E	May 19, 59	19 35 08	
8	〃	〃	149.5E	Nov. 8, 58	19 14 31	
23	〃	46N,	151E	Sept. 9, 58	11 32 05	
24	〃	44N,	149E	Nov. 14, 58	05 34 53	
41	〃	44.5N,	147.5E	July 21, 58	07 24 58	6
35	〃	44N,	148E	Nov. 13, 58	02 56 26	
25	〃	〃	〃	Nov. 19, 58	17 52 52	
63	〃	44.5N,	148.5E	July 11, 59	18 23 00	
64	〃	44.5N,	150E	May 20, 59	19 35 08	
68	〃	44N	〃	May 9, 59	23 57 03	
79	〃	〃	〃	Nov. 19, 58	10 17 30	
80	〃	〃	148E	〃	17 52 52	
81	〃	〃	149.5E	Dec. 8, 58	12 08 23	
75	Kamchatka	53N,	160E	Oct. 10, 58	08 30 17	
78	〃	52N,	159.5E	Nov. 20, 58	05 36 33	
46	Aleutian Is.	52.5N,	170W	July 24, 58	13 08 05	
4	〃	51.5N,	176.5W	July 1, 58	05 53 07	6
42	〃	〃	176W	Aug. 16, 58	13 17 52	
49	〃	52N,	175W	Oct. 20, 58	00 55 34	
52	〃	51.5N,	178W	July 21, 58	05 53 07	
59	Northern Calif.	41N,	125.5W	July 24, 59	01 23 09	
27	Northern Chile	21S,	69W	July 11, 58	19 10 20	6.5
30	Chile-Argentin	33.5S,	65.5W	Sept. 4, 58	21 51 08	7
18	Pacific Ocean	5S,	106.5W	July 12, 58	00 48 30	
20	Ecuador-Peru	3S,	77W	May 25, 58	21 11 45	6.5
19	Marshall Is.	12N,	165E	July 12, 58	03 29 58	
17	Samoa Is.	15S,	174.5W	Apr. 22, 58	20 14 27	7
45	〃	16S,	172W	Nov. 16, 58	17 44 48	6
13	Tonga Is.	24S,	176.5W	Sept. 14, 59	13 15 49	
9	Kermadec Is.	29S,	177W	Sept. 14, 59	22 23 53	6.5
10	〃	〃	176.5W	Sept. 29, 59	15 31 57	6.5
11	〃	33.5S,	177.5W	Sept. 22, 58	19 05 44	6.5
12	〃	29.5S,	176.5W	Oct. 29, 59	14 19 51	6.5
60	New Hebrides Is.	16S,	172.5E	July 3, 59	17 55 29	6.5
61	〃	18.5S,	169E	July 11, 59	04 51 30	

(to be continued)

(continued)

No.	District	Epicenter λ	Epicenter φ	Date	Origin Time (G.M.T.)	Mag.
					h m s	
15	Solomon Is.	10.5S,	161.5E	Aug. 24, 59	15 41 40	6.5
82	〃	〃	161E	〃	21 30 46	
83	〃	〃	〃	〃	23 32 23	
84	〃	〃	〃	〃	23 41 34	
53	〃	7.5S,	156E	Aug. 17, 59	21 04 40	7
3	New Britain	6S,	150.5E	Aug. 15, 58	02 26 51	
74	New Ireland	1S,	149.5E	Aug. 19, 58	21 48 07	
71	Bismark Sea	3S,	145.5E	Aug. 17, 58	18 01 05	
33	Antarctic Ocean	57S,	147E	Oct. 1, 58	09 29 43	6
72	Torishima	30.5N,	140E	Dec. 11, 58	15 33 25	
73	〃	〃	〃	〃	18 38 12	
21	New Guinea	3.5S,	135.5E	May 1, 59	07 19 16	
34	Banda Sea	6S,	131E	Nov. 14, 58	13 48 20	
56	Molluca Passage	2N,	126.5E	July 22, 59	20 15 33	
77	Mindanao I.	7N,	126.5E	Sept. 11, 58	18 01 45	
29	Java I.	9.5S,	112.5E	Oct. 20, 58	01 12 30	
28	Sumatra I.	2N,	98.5E	Oct. 12, 59	03 41 10	6
87	South Indian Oc.	40S,	45.5E	July 26, 58	06 13 50	
58	Formosa	23N,	121.5E	June 2, 58	19 13 30	
54	〃	〃	12E	Aug. 15, 59	08 57 04	7
26	Burma-Pakistan	23.5N,	94.5E	Mar. 22, 58	10 11 27	
32	Southern Tibet	30.5N,	85E	Oct. 28, 58	10 46 27	
39	Western Sinkiang	30.5N,	78.5E	June 24, 58	04 48 15	6.5
1	Northern Tibet	36N,	89E	Nov. 10, 59	20 56 12	
2	Afganistan	33N,	68.5E	May 19, 59	15 17 44	
38	Outer Mongolia	45N,	99E	Feb. 24, 58	12 27 06	
37	〃	46N,	98E	Apr. 13, 58	04 08 56	
70	Western Sinkiang	44.5N,	81E	Dec. 21, 58	05 46 26	
36	〃	51.5N,	99E	Apr. 10, 58	10 55 31	
55	Lake Baikal	52N,	106.5E	Aug. 29, 59	17 03 10	6.5
22	Albania	41.5N,	20E	Sept. 1, 59	12 00 39	6.5
76	Atlantic Ocean	9N,	39.5W	Sept. 25, 58	07 20 02	
66	〃	0.9N,	18W	June 7, 59	13 39 38	

2. Group velocity dispersion curves of Rayleigh waves for the paths in central, southern and south-western Pacific Ocean

There were several cases in which more than two dispersion data were obtained for the same travelling paths. Such examples are shown

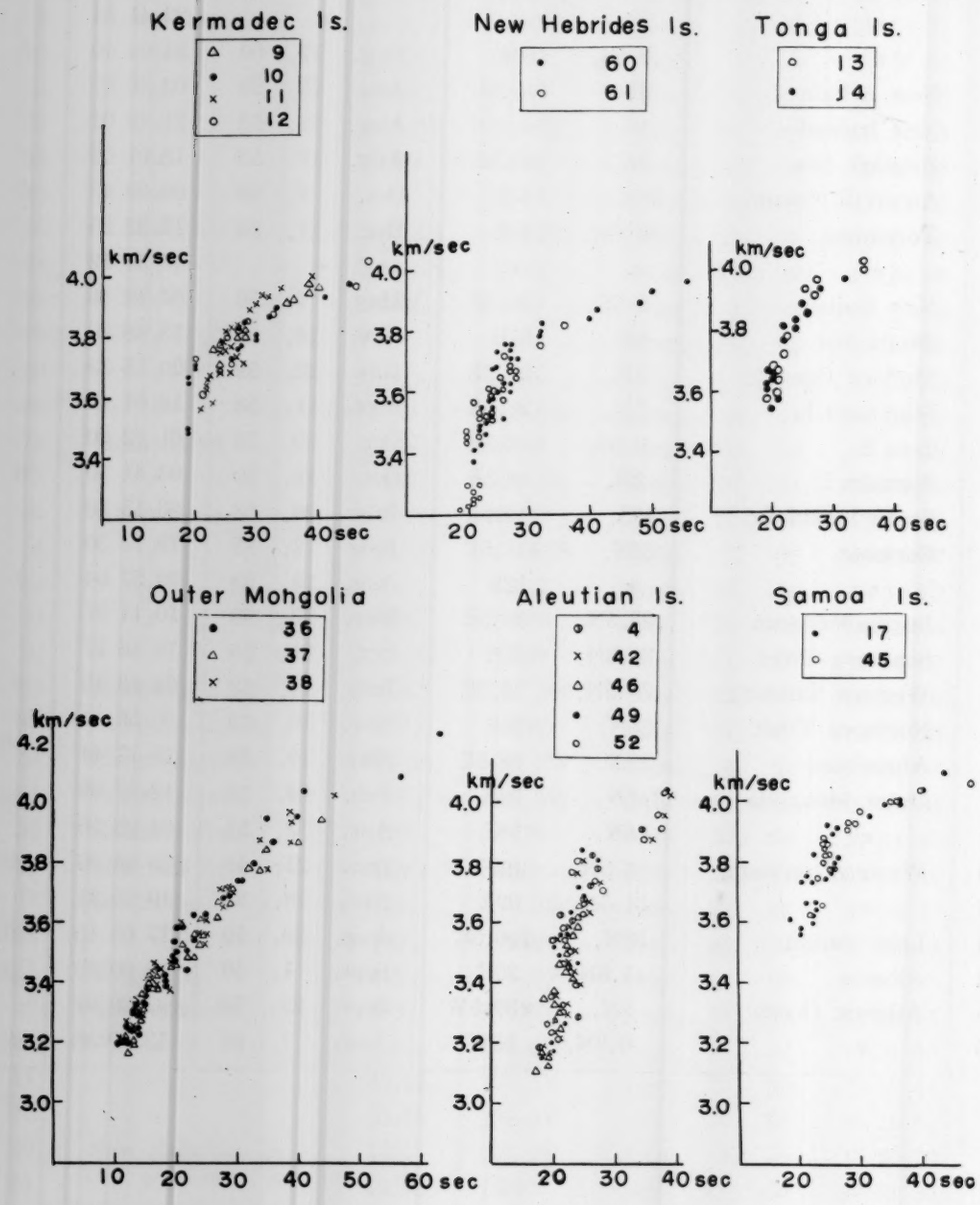

Fig. 3. Dispersions due to more than two shocks which occurred at the same district.

in Fig. 3. Of course, we cannot recognize the differences between the dispersive feature corresponding to each shock.

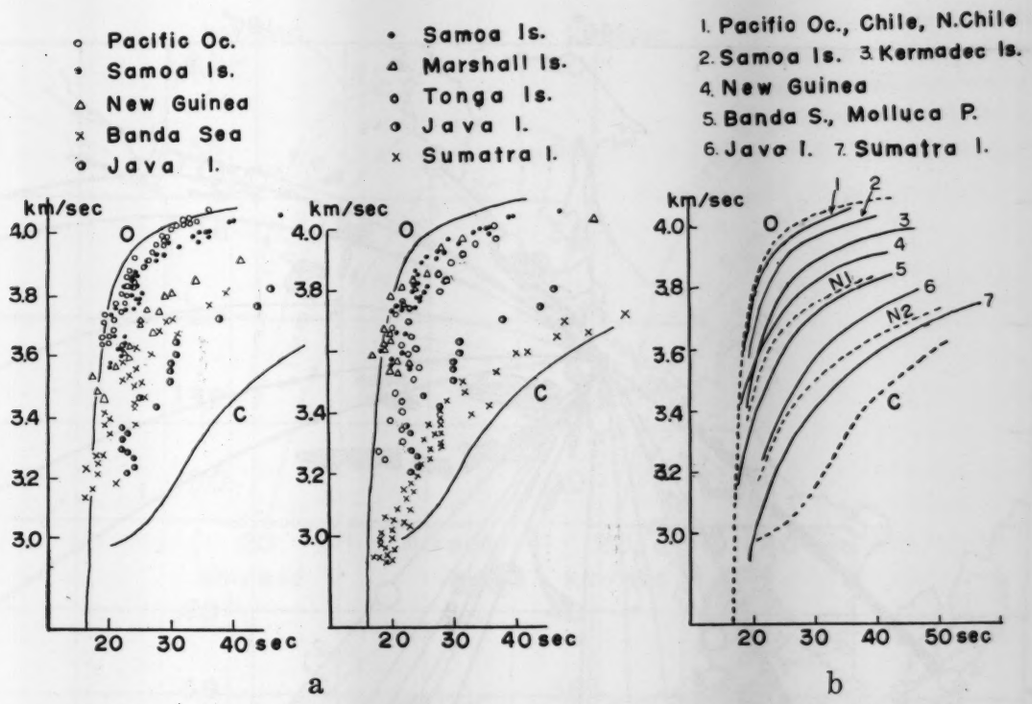

Fig. 4a. Dispersions of various travelling paths through the central, southern and western Pacific Ocean. The typical dispersion curves for oceanic (O) and continental (C) paths are, for comparison, shown by solid curves.

Fig. 4b. Summarized results of smoothed dispersion curves for the central, southern and western Pacific Ocean paths. Beside O and C curves (the same as in Fig. 4a), two curves N_1 and N_2 which were observed by Nagamune for southern and western paths are represented for comparison.

Fig. 4a shows the dispersions obtained by the shocks represented above them. Replacing by continuous curves, they are summarized in Fig. 4b. In this figure, four dispersion curves are also shown for comparison. *O*-curve, the uppermost one, is a theoretical dispersion curve of W.S. Jardetzky and F. Press[2] for oceanic paths with the structure as the right figure,

h	α	ρ
5.3 km	1.52 km/sec	1.0
5.3 〃	6.90 〃	2.67
∞	8.1 〃	3.00

in which, h, α and ρ mean the thickness, the velocity of P-waves, and

2) W. S. JARDETZKY and F. PRESS, "Crustal Structure and Surface Wave Dispersion, Part III; Theoretical Dispersion Curves for Suboceanic Rayleigh Waves," *Bull. Seism. Soc. Amer.*, [ii], **43** (1953), 137.

the density respectively. The lowermost curve C is the observational continental curve which the present writer[3] found for the paths from

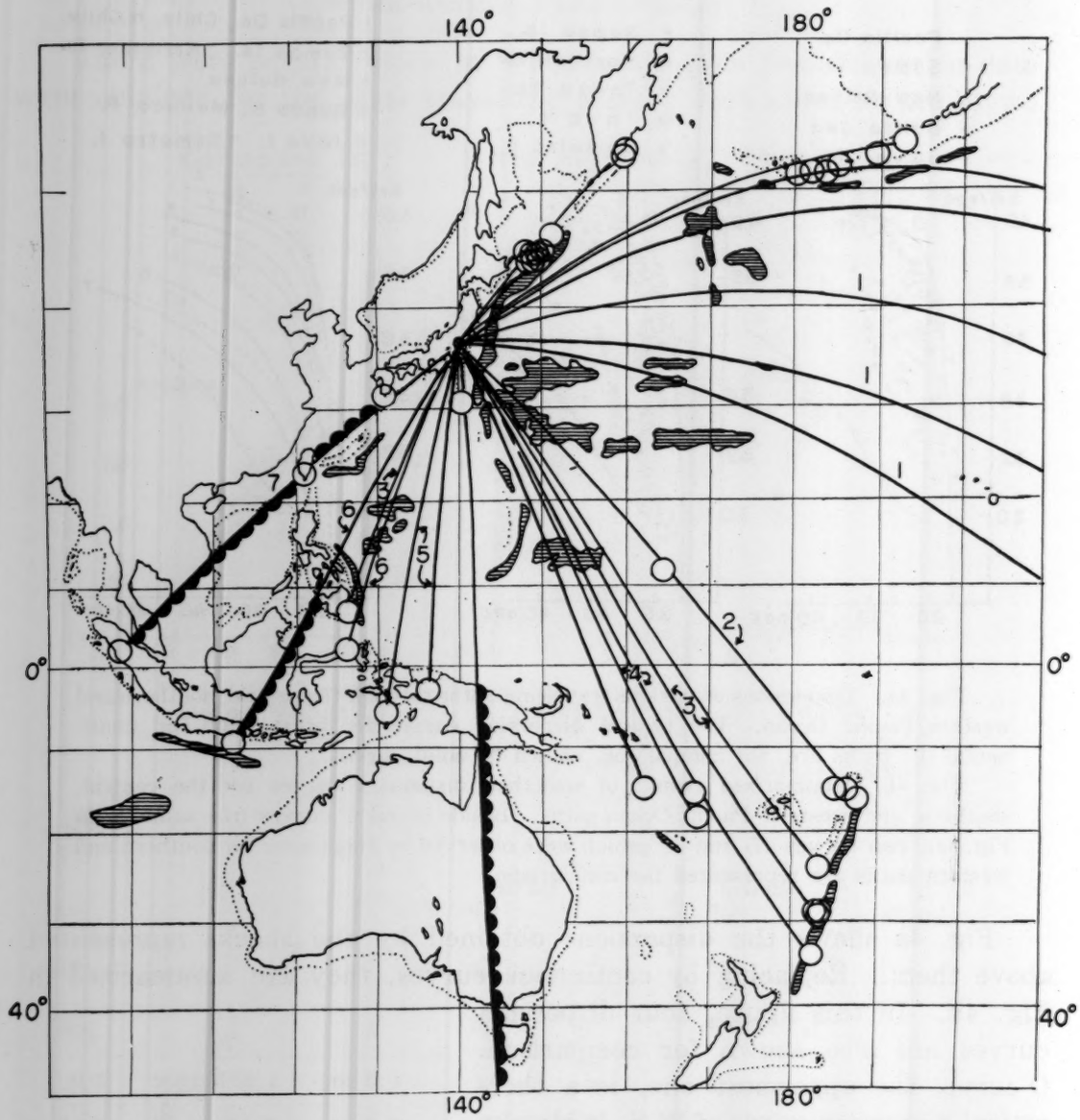

Fig. 5. Detailed map which shows the epicenters and travelling paths of Rayleigh waves for oceanic basin around Japan. Dotted lines are contour lines for the water depth of 1000 m, and the regions with horizontal lines are deep sea regions of more than 6000 m in depth. The paths indicated by the series of semi-circles mean those for which the dispersion curves were computed by subtractions.

3) T. AKIMA, "On Dispersion Curves of Surface Waves from the Great Assam Earthquake of August 15, 1950," *Bull Earthq. Res. Inst.*, **30** (1952), 237.

Assam district to the south-western Japan. Other two curves "N_1" and "N_2" are also the observational ones obtained by T. Nagamune[4] for

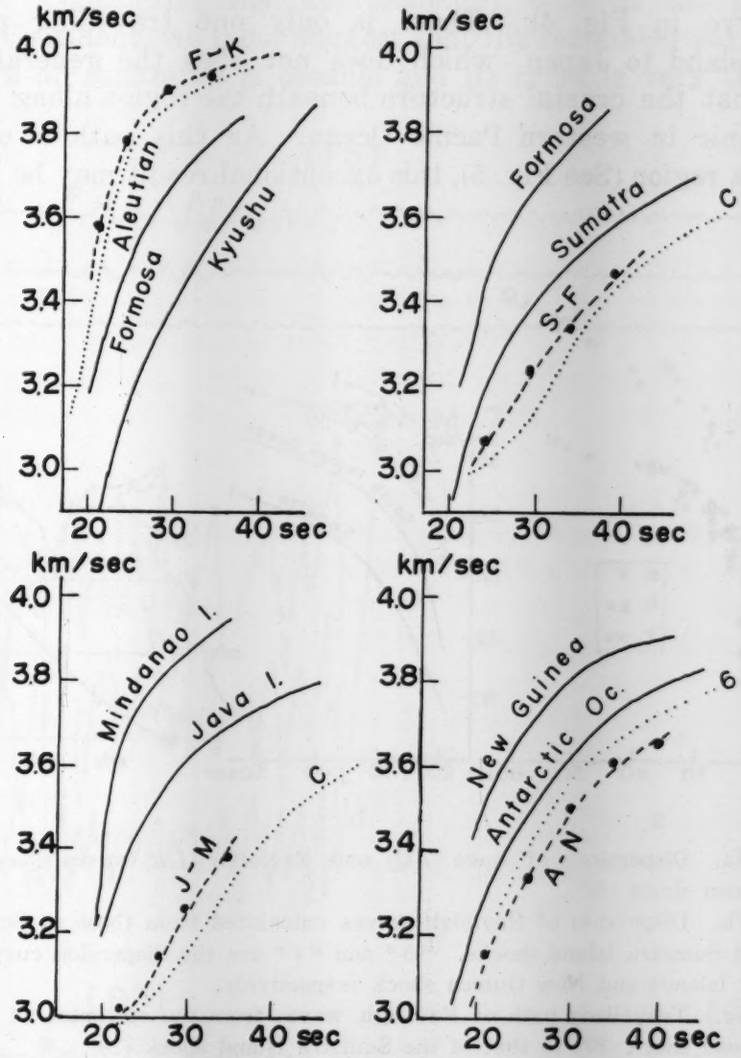

Fig. 6. The dispersion curves (broken lines) derived from the two dispersion curves (solid lines). The dotted dispersion curves of another shocks are represented for comparison with the resultant curves.

the paths from the region of Solomon Islands and from the region of New Guinea or Selebes Islands to central Japan respectively.

Fig. 4b shows us an interesting fact that these dispersion curves,

4) T. NAGAMUNE, "On the Travel Time and the Dispersion of Surface Waves (III), *Geophys. Mag.*, [i], **27** (1956), 93.

approach to the continental one as the corresponding travelling paths shift westward. This tendency is also shown in Fig. 5, in which the numerals beside each travelling path correspond to the respective dispersion curve in Fig. 4b. There is only one travelling path, from Mindanao Island to Japan, which does not obey the general tendency. It means that the crustal structure beneath the region along this path is rather oceanic in western Pacific Ocean. As this path is occupied by the deep sea region (See Fig. 5), this exceptional result may be reasonable.

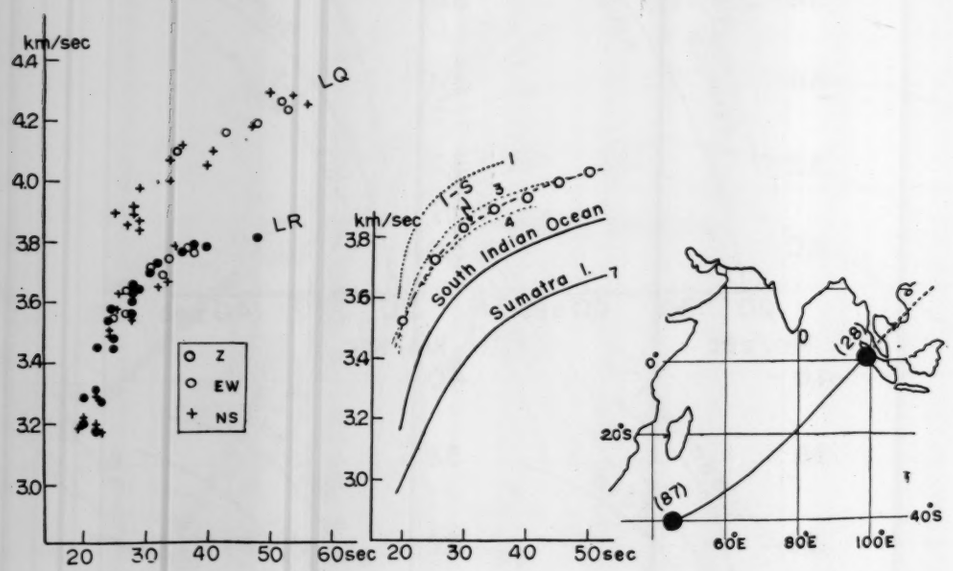

Fig. 7a. Dispersions of Love (*LQ*) and Rayleigh (*LR*) waves due to South Indian Ocean shock (87).

Fig. 7b. Dispersion of Rayleigh waves calculated from those of South Indian Ocean and Sumatra Island shocks. "3" and "4" are the dispersion curves due to Kermadec Islands and New Guinea shock respectively.

Fig. 7c. Travelling path of Rayleigh waves from the epicenter of the South Indian Ocean shock (87) to that of the Sumatra Island shock (28).

There are several favourable cases in which the travelling path of the surface waves occupies a part of the path for another shock. In these cases, we can easily subtract the travel-time of surface waves and obtain a new group velocity dispersion curve for this remaining path. Broken curves in Fig. 6 are all such resultant dispersion curves, and corresponding paths are shown in the previous map (Fig. 5) by the mark like a warm front.

These results tell us that the crustal structures from Sumatra Island

to Formosa and from Java Island to Mindanao Island are both continental, while that from the Antarctic Ocean to New Guinea is not so continental. Considering that approximately 60% of the path is the Australian Continent, we must suggest that the remaining part (Antarctic Ocean south of Australia) is oceanic and its crust is very thin.

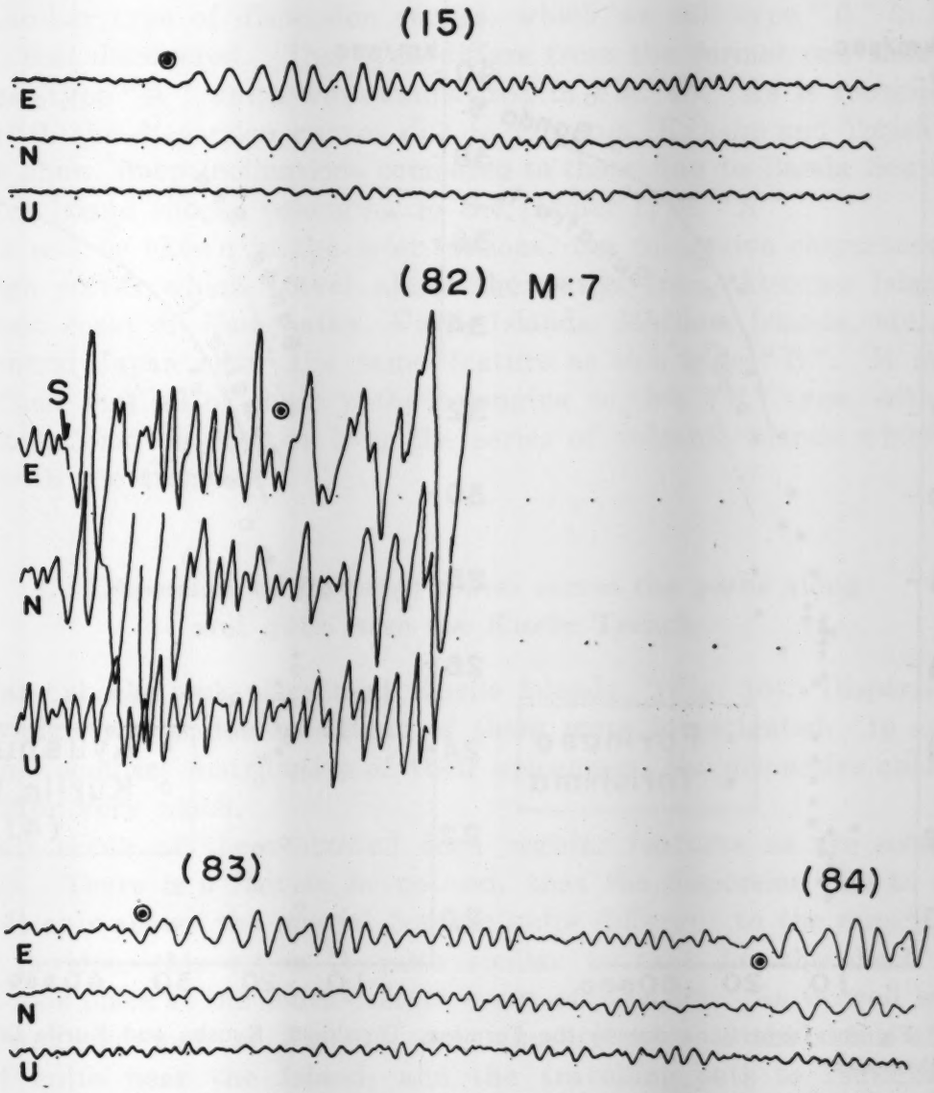

Fig. 8. Seismograms of Solomon Islands shocks which did not sent out Rayleigh waves. Double circles in horizontal records show the beginnings of Love waves.

Further, by subtracting the travel time due to Sumatra Island shock from that due to South Indian Ocean shock, we can obtain an information about the crustal structure beneath the region shown in Fig. 7c. The

resultant dispersion character represented by white circles in Fig. 7b differs from the curve 1 (for the central Pacific Ocean) but is rather similar to the curve 3 (for Kermadec Islands shocks) or 4 (for New Guinea shocks).

There was an interesting phenomenon for the surface waves due to

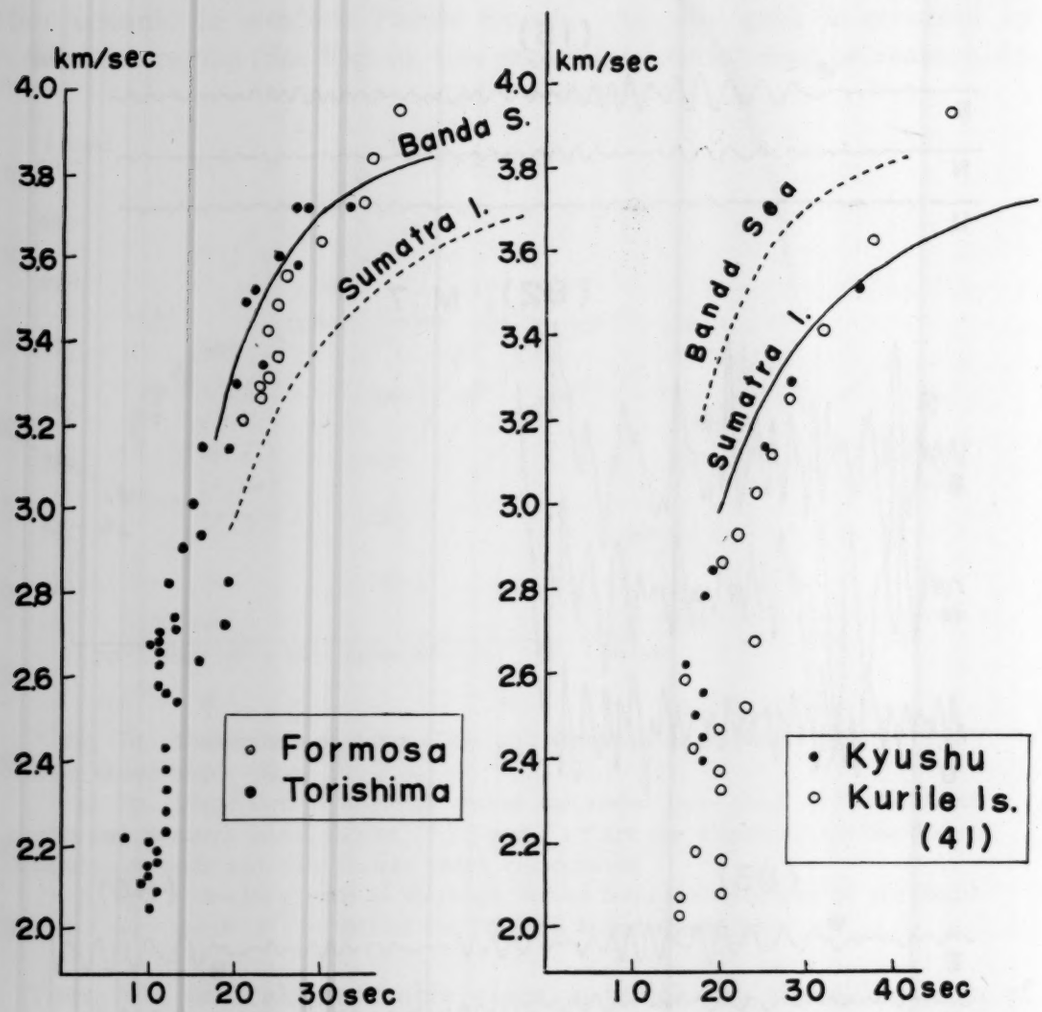

Fig. 9. Dispersions due to the Formosa, Torishima, Kyushu and Kurile Islands (41) shocks.

Solomon Islands shocks. On August 24, 1959, four shocks took place in the Solomon Islands. (See Table 1). The wave forms are partly shown in Fig. 8. The interesting fact is that, as is well seen in this figure, there are no dispersive wave forms in all of the Z component seismograms. (The onsets of P waves were as remarkable as any other

shocks and the travel-time of P_n were also normal.) That is, these four Solomon shocks sent out remarkable Love waves, but not Rayleigh waves.

Is it possible to assume such mechanism of P wave generation at the origin that sent out P_n but not Rayleigh waves to a certain direction ? This must be studied in the future.

Another type of dispersion curves, which we call type " B " in this paper, was discovered. This type differs from the former one that we call here type " A " which was summarized in Fig. 4b. As is recognized in Fig. 9, the dispersion curves due to Formosa, Kyushu and Torishima shocks show steep inclinations compared to those due to Banda Sea and Sumatra Island shocks belonging to the former type " A ".

As will be shown in the later sections, the dispersive characters of Rayleigh waves which travel along the paths from Aleutian Islands, southeast coast of Kamchatka, Kurile Islands, Mariana Islands, etc., to the central Japan show the same feature as this type " B ". It must be noticed that all of these paths belonging to this " B " type, without any exceptions, lie near or over the series of volcanic islands which is lined with the trenches.

3. Dispersion of Rayleigh waves across the paths along and quite near the Kurile Trench

Many shocks took place near Kurile Islands. (Fig. 10). Dispersions of Rayleigh waves due to fifteen of them were investigated. In spite of rather compact distribution of their epicenters, the dispersive characters differ very much.

Only seven of them showed such regular features as are seen in Fig. 10. There is a fact to be noticed, that the dispersion due to the shock 41 only shows the special feature quite different to the remaining ones. Besides, this curve is quite similar to that for the shock 32, which took place at the south-eastern coast of Kyushu. As is well seen in the annexed map of Fig. 10, only the epicenter of the shock 41 is located quite near the Island, and the travelling path to Tsukuba is farthest from Kurile Trench.

As the dispersion curves obtained are limited to those of narrow period range, we cannot determine the crustal structure along this travelling path at present. However, the fact given above must be kept in mind as an interesting fact to be solved.

The middle dispersion curve (Fig. 10) corresponds to the shocks 63, 7 and 64, which are located nearer to the Trench. This curve is similar to that of the shock 72 which took place at Torishima. The last curve,

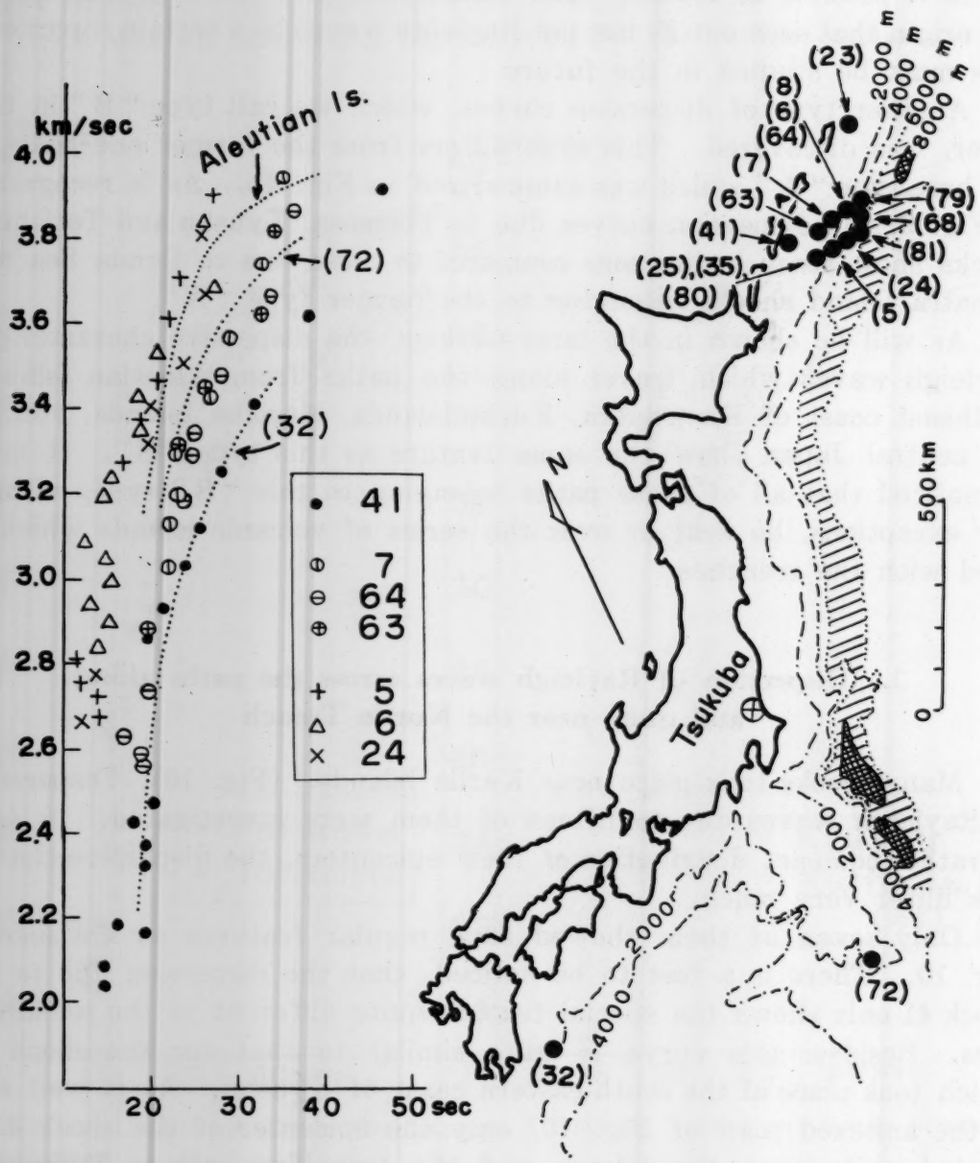

Fig. 10. The epicenters of Kurile Islands shocks and their dispersions. Dispersion curves due to Kyushu (32), Torishima (72) and Aleutian Islands shocks are also represented for comparison.

the leftmost one, corresponds to the shocks 5,6 and 24, and these epicenters are located quite near the Trench. The dispersive characters

for the remaining eight shocks were so diverged that the writer could not draw smoothed curves.

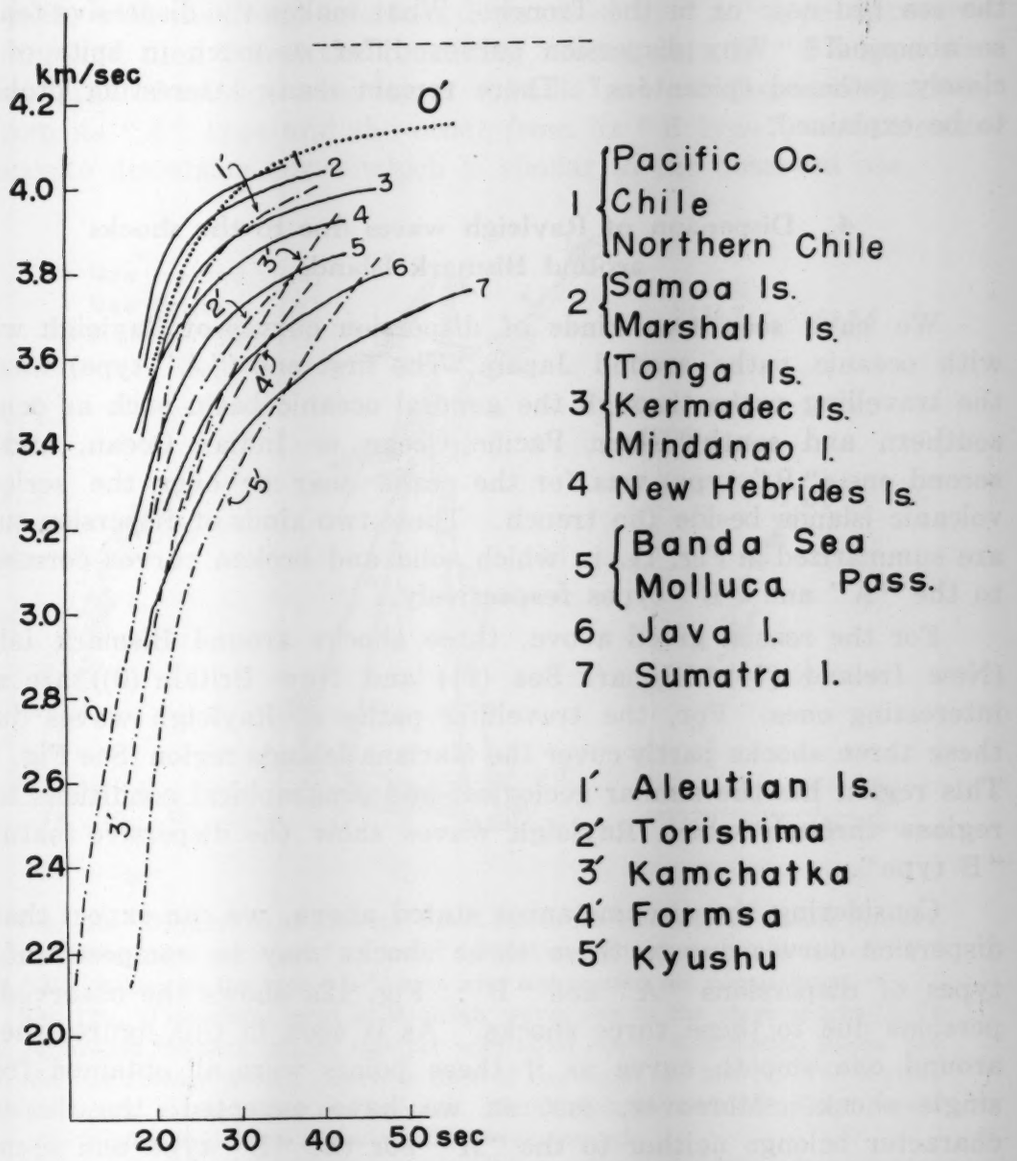

Fig. 11. Summarized dispersion curves of Rayleigh waves for various oceanic paths around Japan. Nagamune's observed curve for northern Pacific Ocean path[5] is given by O' curve. Horizontal broken line means the symptote line of Rayleigh wave velocity for α (the velocity of P-waves under the Mohorovičić discontinuity)=8.1 km/sec.

5) T. NAGAMUNE, "On the Travel Time and the Dispersion of Surface Waves (III): Dispersion of Surface Waves and Structure of North and Central Pacific Basins," *Geophys. Mag.*, [i], **28** (1957), 1.

The above feature of special dispersive character for Kurile Islands shocks is based, undoubtedly, upon the exceptional condition beneath the sea bed near or in the Trench. What makes the dispersive feature so abnormal? Why dispersion curves differ so much in spite of the closely gathered epicenters? There remain many interesting problems to be explained.

4. Dispersion of Rayleigh waves due to the shocks around Bismark Islands

We have seen two kinds of dispersion curves of Rayleigh waves with oceanic paths around Japan. The first one ("A" type) was for the travelling paths through the general oceanic basin such as central, southern and southwestern Pacific Ocean or Indian Ocean, and the second one ("B" type) was for the paths near or over the series of volcanic islands beside the trench. These two kinds of dispersion curves are summarized in Fig. 11, in which solid and broken curves correspond to the "A" and "B" types respectively.

For the reason given above, three shocks around Bismark Islands (New Ireland (74), Bismark Sea (71) and New Britain (3)) are quite interesting ones. For, the travelling paths of Rayleigh waves due to these three shocks partly cover the Mariana Islands region (See Fig. 12b). This region has the similar geological and geographical conditions to the regions through which Rayleigh waves show the dispersive feature of "B type".

Considering the circumstances stated above, we can expect that the dispersion curves due to these three shocks may be composed of two types of dispersions "A" and "B". Fig. 12a shows the observed dispersions due to these three shocks. As is seen in this figure, they lie around one smooth curve as if these points were all obtained from a single shock. Moreover, just as we have expected, the dispersion character belongs neither to the "A" nor the "B" type and seems to be influenced by both of them.

Seeing the travelling paths due to these shocks (See Fig. 12b), they can be divided into two parts. The first is from the epicenters to the southern edge of 2000 m sea depth contour line which envelopes Mariana Islands and the second is the remainder parts which contain the series of volcanic islands such as Mariana, Volcano and Bonin Islands. The dispersion of Rayleigh waves through the first and the second part will

belong to the "A" and "B" type of dispersion respectively. Namely, Rayleigh waves will travel the first part (approximately 36% of the total path) with the group velocities determined by "A" type dispersive character and then travel the remaining second part by "B" type dispersion. Therefore, by selecting a suitable pair of dispersion curves, one from its "A" type and the other from its "B type", we can make a composite dispersion curve which is similar to the observed one.

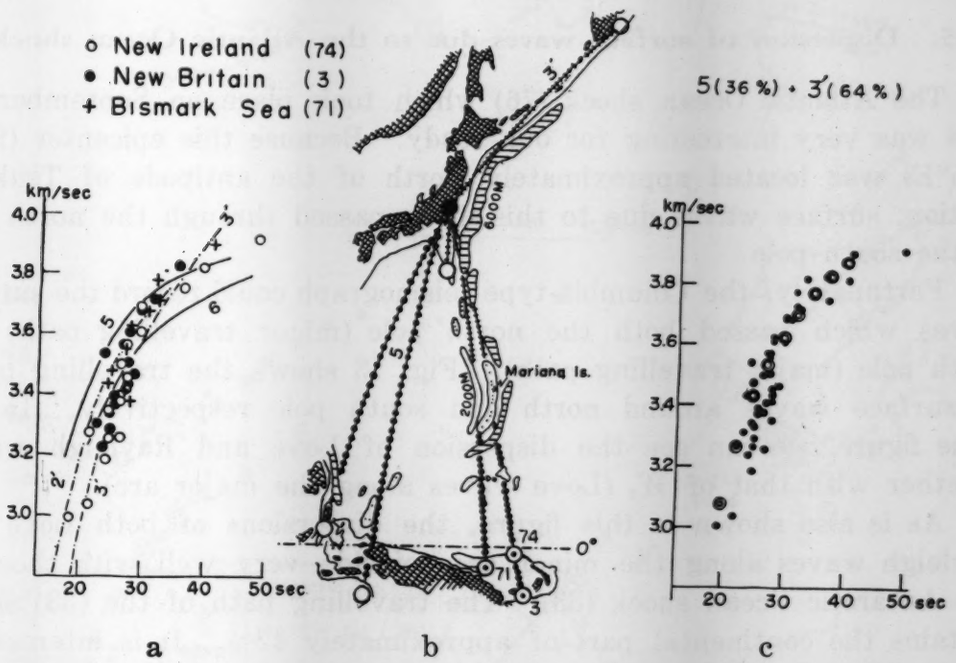

Fig. 12a. Dispersions of Rayleigh waves due to the three shocks around Bismark Islands. Dispersion curves of "5" and "6" (belong to the type "A") and of "2'" and "3'" (belong to the type "B") were also represented for comparisons.

Fig. 12b. Travelling paths of Rayleigh waves due to the three shocks (3, 71 and 74) around Bismark Islands together with those due to Kamchatka, Banda Sea and Molluca Passage shocks. Contour lines of Sea depth are 2000 m. The regions with horizontal hatched lines are trenches. Paths through which Rayleigh waves show the similar dispersion are distinctively represented.

Fig. 12c. The resultant dispersion curves by the composition of two curves "5" and "3'".

The results are shown in Fig. 12c represented by double circles. In this figure, the observed data for the three shocks are all represented by black circles. Though there is a little departure in short period range, this result tells us that the dispersion of Rayleigh waves due to the three shocks around Bismark Islands is well explained by the com-

position of "5" and "3′" which belong to the "A" and "B" type respectively. In other words, the crustal structure from the epicenters to Mariana Islands are, in average, similar to that from Molluca Passage or Banda Sea to central Japan, and the region of Mariana, Volcano and Bonin Islands has the similar crustal structure to the region from southeast coast of Kamchatka (through Kurile Islands and side of Japan Trench) to central Japan.

5. Dispersion of surface waves due to the Atlantic Ocean shock

The Atlantic Ocean shock (76) which took place on September 25, 1958 was very interesting for our study. Because this epicenter (9°N, 39.5°E) was located approximately north of the antipode of Tsukuba Station, surface waves due to this shock passed through the north pole or the south pole.

Fortunately, the Columbia-type seismograph could record the surface waves which passed both the north pole (minor travelling path) and south pole (major travelling path). Fig. 13 shows the travelling paths of surface waves around north and south pole respectively. In the same figure, we can see the dispersion of Love and Rayleigh waves together with that of W_2 (Love waves along the major arc).

As is also shown in this figure, the dispersions of both Love and Rayleigh waves along the minor arc coincide very well with those of the Antarctic Ocean shock (33). The travelling path of the (33) shock contains the continental part of approximately 47%. It is interesting, on the other hand, that if we assume the crustal structure of Greenland and Arctic region to be purely continental and oceanic respectively, the travelling path of Rayleigh waves due to the Atlantic shock (76) contains the continental part of approximately 49%, which is nearly the same as the former. J. Oliver and others[6] investigated the crustal structure of the Arctic region from the *Lg* phase and found that the Greenland and Arctic regions have continental and oceanic crustal structure respectively. From the present results just obtained, we can make the same suggestion.

Fig. 13 also shows the dispersion data of W_2. As the data of these waves are limited to long period range, we cannot compare them well with that of Love waves data for minor travelling paths. However,

6) J. OLIVER, M. EWING and F. PRESS, "Crustal Structure of the Arctic Regions from the Lg Phase." *Bull. Geol. Soc. Amer.* **66** (1955), 1063.

they look like to lie on one dispersion curve. In this case also, the travelling path contains 44% of continental part, if we assume the Antarctic region along the path to have purely continental structure.

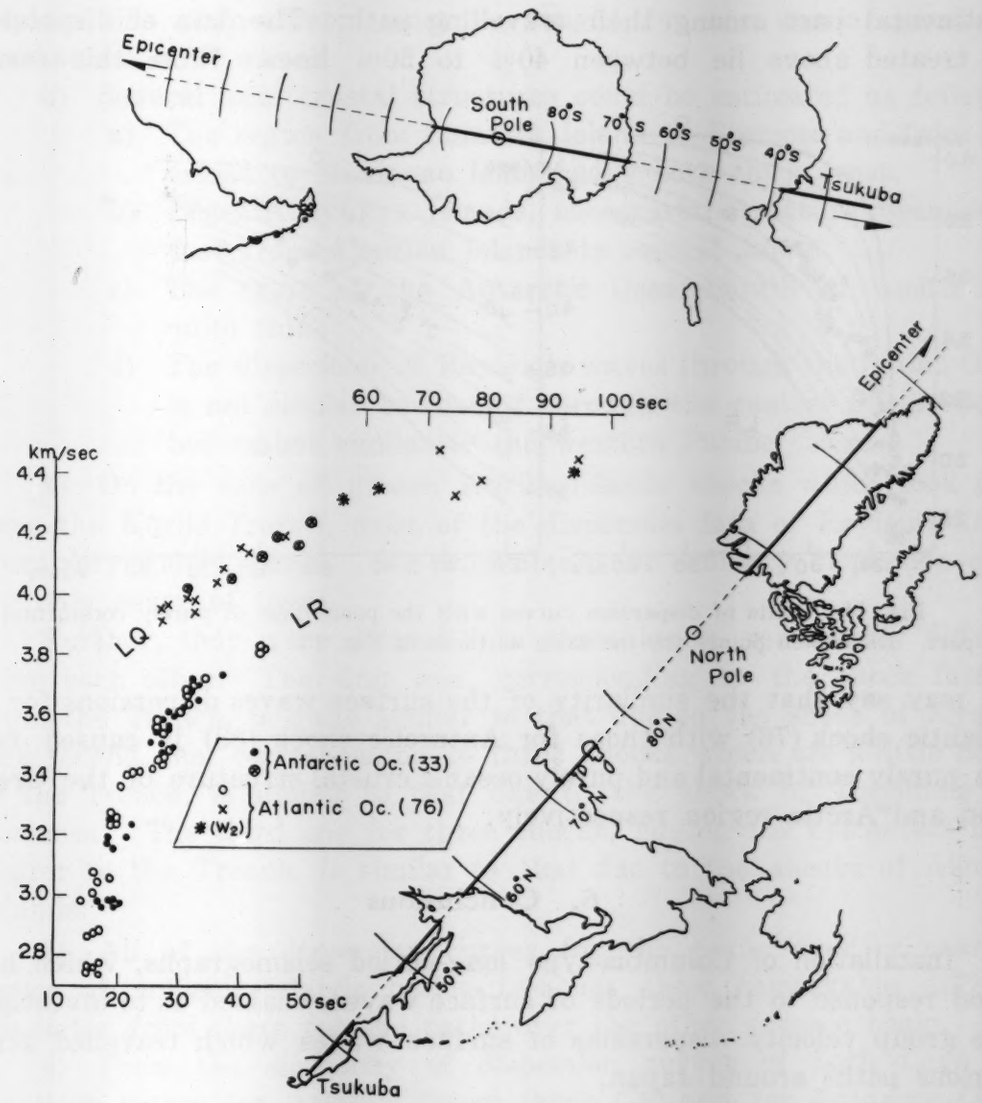

Fig. 13. Dispersions of surface waves due to the shocks (33) and (76). The annexed maps show the travelling paths of LQ, LR and W_2. Solid lines show the continental parts along the paths.

This value is quite similar to the former two. From this result, we may suggest that the Antarctic region has, at least along the present travelling path, a continental crustal structure. This suggestion is

consistent with the results obtained by C. R. Bentley and others[7] by gravity observations.

The writer shows in Fig. 14, for reference, how the dispersion curves of Love and Rayleigh waves change with the percentage of purely continental part among their travelling path. The data of dispersions we treated above lie between 40% to 50% lines. From this result,

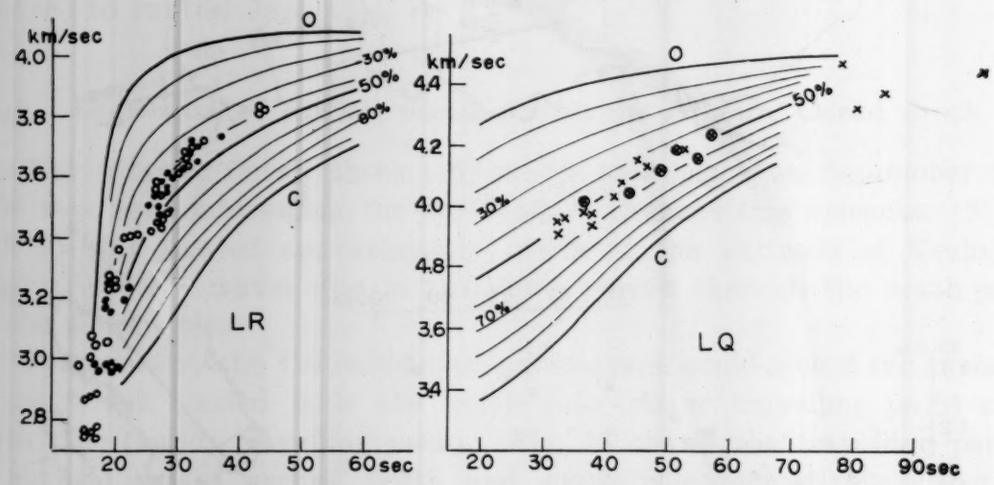

Fig. 14. Shifts of dispersion curves with the percentage of purely continental part. Dispersion points are the same as those of Fig. 13.

we may say that the similarity of the surface waves dispersions for the Atlantic shock (76) with those for Antarctic shock (33) is caused from the purely continental and purely oceanic crustal structure of the Greenland and Arctic region respectively.

6. Conclusions

Installation of Columbia-type long-period seismographs, which have good response to the periods of surface waves, enabled us to investigate the group velocity dispersions of surface waves which travelled across various paths around Japan.

In this first paper, only dispersion data of the Rayleigh waves across oceanic paths were treated, nevertheless, not a few noticeable facts were discovered. That is:

1) In the south-western Pacific Ocean, the Rayleigh wave dispersion curve becomes more continental for the western region. It means that

7) C. R. BENTLEY, A. P. CRARY, N. A. OSTENSO and E. C. THIEL, "Structure of West Antarctica," *Science*, **131** (1960), 131.

the crust of the earth beneath the Ocean becomes, in average, thicker for the western Pacific Ocean.

2) Rayleigh waves could not be observed for several Solomon shocks which took place at the same place on August 24, 1959. One way to explain this phenomenon must be sought for the special generation mechanism of *P* waves.

3) Several local crustal structures could be estimated as follows:

a) The region from Sumatra Island to Formosa and from Java Island to Mindanao Island have both thick crust.

b) Beneath Ryukyu Islands, the crustal structure resembles to that from Aleutian Islands to central Japan.

c) The crust at the Antarctic Ocean south of Australia is quite thin.

d) The dispersion of Rayleigh waves through the Indian Ocean is not similar to that of through the central Pacific Ocean, but rather similar to the western Pacific Ocean.

4) On the case of fifteen Kurile Islands shocks which took place near the Kurile Trench, most of the dispersion data of Rayleigh waves were very widely spread. We could obtain the ordinary dispersion curve for only seven of them.

Further, they were divided into three kinds, remarkably different from each other. The first one, corresponding to the shock farthest from the Trench, is quite similar to that due to the shock of Kyushu. The second one, corresponding to three shocks which are a little nearer to the Trench, is similar to that due to the shock of Torishima and Formosa. The third one for three shocks, having the epicenters much nearer to the Trench, is similar to that due to the shocks of Aleutian Islands.

5) All of the dispersion curves for the paths over or near the series of volcanic islands beside trenches show remarkable different character from those for the paths over the other oceanic basin.

6) From the similarity of dispersion curves of both Love and Rayleigh waves for Atlantic Ocean shock (76) and for Antarctic Ocean shock (33), the crustal structure of the Arctic zone and Greenland are considered to be purely oceanic and continental structure respectively. Antarctic region along the longitude of 40°W to 140°E may have continental structure.

7) The crustal structure of the South Indian Ocean differs from that of the central Pacific Ocean. It is similar to the southern Pacific

Ocean (the region from Kermadec Islands or New Guinea to central Japan).

7. Acknowledgements

In conclusion, the writer wishes to express his hearty thanks to Lamont Geological Observatory for permission to use the seismograms obtained by the Columbia seismographs installed at Tsukuba Station.

---

13. コロンビア型地震計による表面波の観測 (第一報)
——海洋底を伝わるレーリー波の分散——

地震研究所　三　東　哲　夫

I.G.Y. 期間中の遠地地震観測計画の一つとして，アメリカのコロンビア大学では，振子および検流計の固有周期がそれぞれ15秒および90秒前後の長周期電磁式地震計を世界の10数カ所に設置したが，そのうちの一台が地震研究所の筑波支所に置かれて，1958年初頭から常時観測が開始されて今日におよんでいる．この地震計によつて，非常にたくさんの表面波が記録され，現在までに約80ケの地震の表面波の分散を調べることができた．しかも，それらの表面波の伝播径路は，日本を中心としてほとんどあらゆる領域を占めている (第2図)．第1報では，このうち，海洋底を伝わつてきたレーリー波の分散の様子だけについて述べるが，径路が多岐にわたつているだけに，予想以上にいろいろの注目すべき結果が得られ，また今後の研究を必要とする問題点も出て来た．すなわち，

1) 海溝に沿つてならんだ火山性列島付近を通つてくるレーリー波の分散曲線を多数調べたが，何れも普通の海洋底を通つてくるレーリー波の分散曲線とは明瞭に区別できる一群の曲線群を形成する (第11図)．これ等の曲線群を説明するためには，特別な速度分布を地殻に与える必要が起るかも知れない．
2) 南太平洋の部分については，地震波の径路が西に移るにつれて，分散曲線は次第に陸型に近づいてゆく (第4図 b)．
3) エトロフ島沖の地震群に限つて，分散がひどく乱れる．また，明瞭な分散曲線を示した地震についても，震央が僅かに海溝よりから島よりに移つただけで，その分散の様子がひどく変化する．これ等の地震は，その震源もまたそれらによるレーリー波の伝播径路も，海溝から火山列島への狭い漸移地帯中にはさまれている点が注目される (第10図)．
4) P_n 波や S 波やラブ波などは明瞭に記録されたが，レーリー波だけが記録されなかつた地震がソロモン群島で4ケあつた (第8図)．
5) 観測点からほぼ同じ方向にあつて，しかも震央距離がかなりちがつた二つの地震によるレーリー波の分散曲線を使つて，周期毎に走時を差引くことにより，残つた区域に関する分散曲線が作れる．この方法で若干の地域の平均的な地殻の厚さの質的な推定をしてみると，
   a) スマトラ島から台湾，ジャワ島からミンダナオ島に至る範囲の地殻は厚い．
   b) 琉球列島の地殻構造は，アリューシャン列島から中部日本に至る部分のそれと似ている．
   c) オーストラリヤ大陸南部の海洋の地殻はきわめてうすい．
   d) インド洋南部の地殻の厚さは，中部太平洋よりはやや厚く，南部太平洋なみである (第7図 b)．
6) 径路が丁度南北両極を通過する表面波の分散曲線が，南極洋の地震のそれとほとんど一致することを利用して (第13図)，北極が海であること，グリーンランドと南極が陸であることを認めた．

BULLETIN OF THE EARTHQUAKE
RESEARCH INSTITUTE
Vol. 38 (1960), pp. 241-254

14. *The Observation of Microseisms at a Wave Gauge Station.* —*On the Origin of Microseisms (Part III).*—

By Tetsuo A. SANTÔ,

Earthquake Research Institute.

(Read Nov. 24, 1959.—Received March 28, 1960)

1. Introduction

In Part I[1], the writer made an investigation into the features of microseismic occurrence due to the passing of a single cyclone, a typhoon or a strong cold front, using many observational data at many stations in Japan.

The most important feature was that when a cyclone or a typhoon is travelling towards northeast over the ocean, the microseismic storm shifts from one region to another as if running after the cyclonic center, and further, the largest microseismic storm at a given station occurs considerably later than the passing of a cyclonic center. This feature was quite conspicuous for northern stations, when the travelling speed of cyclonic center had become very high.

This phenomenon is quite similar to the arriving of the water wave pattern caused by a single vibrating source which runs over the water with a velocity higher than the group velocity of the water wave.

Not a few authors[2] found the fact that a microseismic storm at a certain station becomes heaviest after the passing of a cyclonic center offshore, but this feature was reported only as an observational fact, and has never been explained. For the present author, however, this fact seems to be very important in order to explain the origin of microseisms. That is the problem of where the energy of the swell turns to microseismic waves.

1) T. A. SANTÔ, "Investigations into Microseisms Using the Observational Data of Many Stations in Japan (Part I).—On the Origin of Microseisms.—", *Bull. Earthq. Res. Inst.*, **37** (1959), 307.

2) For instance, F. I. MONAKHOV, "Development of Microseismic Method of Tracing Storms at Sea," *Abstracts of the Reports at the XI General Assembly of the International Union of Geodesy and Geophysics* (1957), 76.

In paper II[3], this phenomenon was further investigated adding the data of microseismic storms due to the passing of many typhoons. The method was to check the relation between V and L/D measuring the three values V (the travelling speed of a cyclonic center), D (the shortest distance from a coast near a station to the travelling course of a cyclone), and L ($=Vt$, in which t means the "delayed time") on a map. (See Fig. 2a)

This was examined and the approximate linear relation between V and L/D was observed.

2. The "eye of a microseismic storm" around the cyclonic center

The nature of the occurrence of microseismic storms due to the passing of a cyclone or a typhoon can be explained more clearly as follows, if we examine the relation between D and L/V instead of V and L/D.

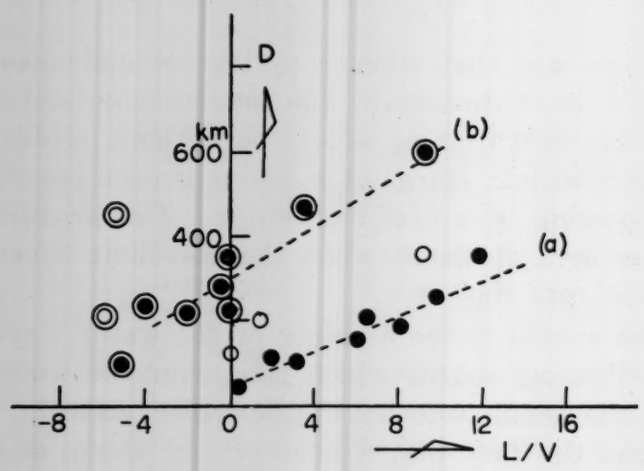

Fig. 1. Observed relation for $D-L/V$. Black and double black circles correspond to the cyclones with $p_0>1000$ mb. and with $p_0<985$ mb. respectively. White and double white circles are for the cases when cyclonic centers ($p_0>1000$ mb. and $p_0<985$ mb. respectively) passed at the left side of the station.

The relation between D and L/V is given in Fig. 1. From this figure we can recognize that the data for the cyclones of $p_0>1000$ mb. (black circles) and for those of $p_0<985$ mb. (double black circles) distribute around the two straight lines, which can be expressed as

$$D=v(p_0)(L/V)+D_0(p_0). \quad (1)$$

In this figure, the white circles (for $p_0>1000$ mb.) and double white circles (for $p_0<985$ mb.) show the data for the cases when cyclonic centers passed on the left side of the station.

3) T. A. SANTÔ, "Investigations into Microseisms by the Observational Data of Many Stations (Part II).—Further Considerations on the Origin of Microseisms.—". *Bull. Earthq. Res. Inst.*, **37** (1959), 483.

The above equation (1) can be explained as follows.

Suppose a region which is enveloped by a curve C around a cyclonic center (Fig. 2b) and the highest swells which arrived at some coast near the station had been sent out from this boundary. Then,

$$D'=D-D_0=vt' \qquad \text{and} \qquad L=Vt' , \qquad (2)$$

in which t' mean the travel time of the swell which cover the distance D'. From these equations,

$$(D-D_0)/v=L/V$$

From this, we can reduce the same equation as (1), namely,

$$D=v(L/V)+D_0$$

Therefore, D_0 on the right hand of the equation (1) means the radius of the assumed region towards the station. Further, our observed results concerning the relation between D and L/V tell that the heaviest microseismic storm occurs at the time when the highest swell which had started from the boundary C reaches some coast near the station. For this reason, this enveloped region around a cyclonic center can be called "the eye of the microseismic storm".

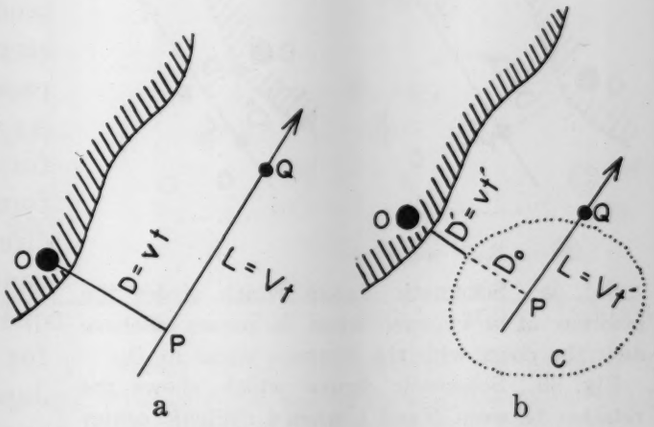

Fig. 2a. Schematic figure which shows the relation between L and D for the case of a single point source travelling over the water with the velocity V which is greater than the group velocity of water waves v.

Fig. 2b. Assumed envelope curve C (dotted line) around a cyclonic center.

The values of v estimated from the inclinations of these lines are approximately 20 km/hr and 30 km/hr respectively, which are reasonable for the velocities of swells belonging to the cyclones with these central pressure ranges. The radius (D_0) of the enveloped region can be read by the intercept points of these straight lines at the D axis. They are read as approximately several tens kilometers from the line (a) (for $p_0>1000$ mb.) and as few hundreds kilometers from the line (b) (for $p_0<985$ mb.) re-

spectively. It must be noticed in the same figure that D_0 was estimated somewhat larger for the data represented by white and double white circles. It means that the envelope curve swells to the right for travelling directions of cyclones as is shown in the schematic figures of 2b. This result is also quite reasonable. For, as is well known, the energy of a cyclone is, in the northern Hemisphere, stronger on the right side of its travelling direction.

In equation (1), when $D=D_0$, L becomes 0, that is, when a cyclone passed offshore so near as to contact the "eye of the microseismic storm" C on the coast (Fig. 3a), the microseismic storm becomes largest at the time when the cyclonic center passes offshore near the coast.

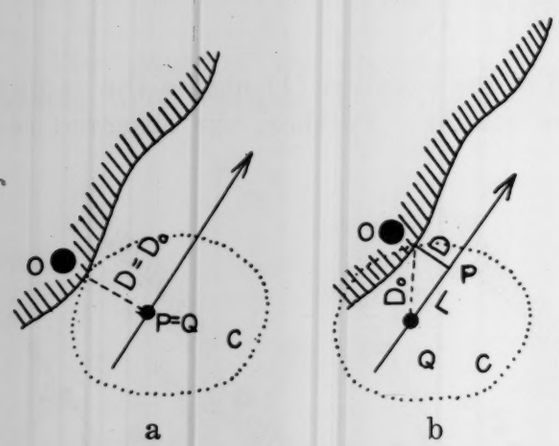

Fig. 3a. Schematic figure which shows the position of a cyclone when it passes offshore near the coast with the distance equal to D_0.

Fig. 3b. Schematic figure which shows the relation between D and L when a cyclonic center passes offshore near the coast so near as $D<D_0$.

Further, when $D<D_0$, L becomes minus (See Fig. 3b). It means that when a cyclone passes much nearer the coast as the "eye" enters into the land, the heaviest microseismic storm occurs earlier than the passing of the cyclone offshore. As was found before, D_0 is larger for smaller values of p_0. Therefore, when p_0 is very small, the circumstances which satisfy the condition $D<D_0$ occur more frequently. They were thecases for the southern stations in Japan, around which typhoons are generally still quite strong. (All of the data of minus side of L/V axis in Fig. 1 correspond to the data obtained at southern stations.)

In this case, as is shown in Fig. 3b,

$$D_0=\sqrt{D^2+L^2}\,. \qquad (3)$$

By this equation (when $L<0$) and by the equation (1) (when $L\geqq 0$), we can again estimate the values of D_0 by using the data of L, V and D of each case. In these estimations, v were calculated by the equation $v=gT/4\pi$, in which g and T mean the acceleration due to gravity and

the period of swells respectively[4]. The results are shown in Fig. 4. In this figure, the marks are all the same with those used in Fig. 1. The expected tendency that D_0 will be a decreasing function of p_0 can be seen in this figure although the points are scattered because of the difference of the meteorological conditions around the cyclonic center. The values of D_0 thus estimated are approximately equal to the previous ones. Moreover, it can also be seen that the values of D_0 determined by the white and double white circles are larger than by the others. It means, as we expected, that the "eye" swells to the right in the course of its travel as is shown in the schematic figure of 3.

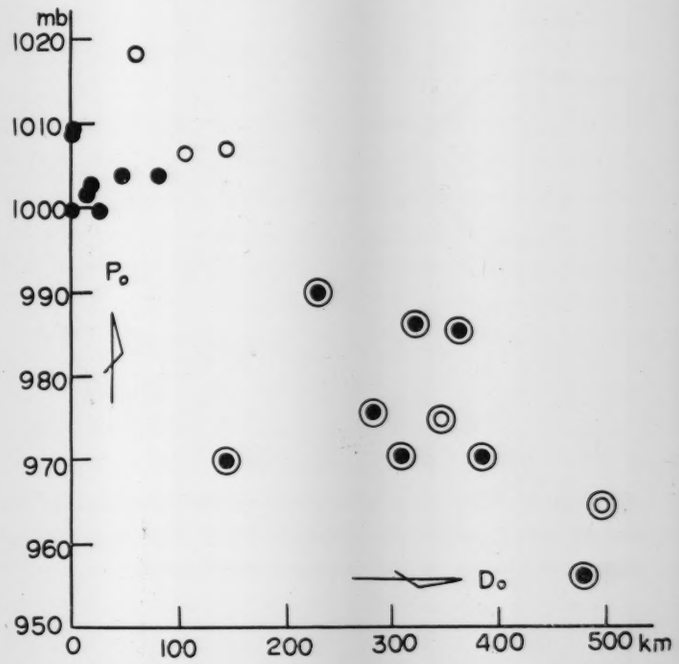

Fig. 4. Values of D_0 estimated by the equation $D_0 = D - v(L/V)$ when $L \geqq 0$, and by the equation $D_0 = \sqrt{D^2 + L^2}$ when $L < 0$ respectively.

In any case, it became clear that the largest microseismic storm due to the passing of cyclones or typhoons occurs at the time when the highest swell reaches some part of the coast near the stations.

In order to make this conclusion clearer, the direct method was taken. Namely, the simultaneity between the occurrence of the largest microseismic storm and the arriving of the highest swells at the same station was examined.

3. The position and the method

Microseismic observation began from September, 1959 at one of the wave gauge stations Naarai, approximately 100 km east of Tokyo and situated nearly at the top of the Inubô Promontory (Fig. 5). In Fig. 5,

4) S. UNOKI, "On the Speed, Travel Time and Direction of Ocean Waves due to Tropical Cyclones," *Journ. Met. Soc. Japan*, **34**, 2, (1956), 354.

the wave gauge and the seismograph station are shown respectively by S and O.

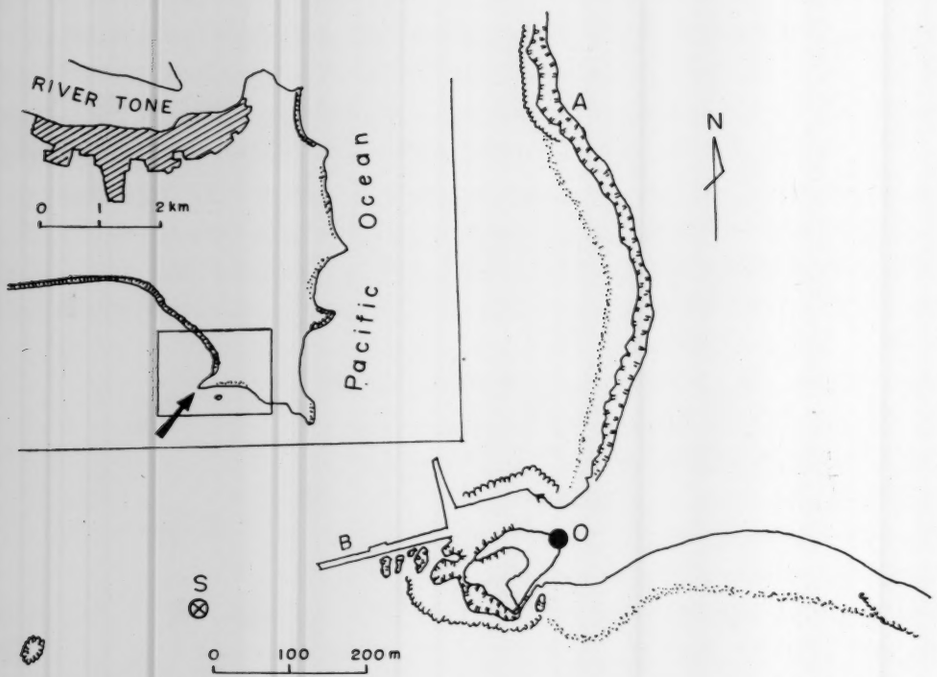

Fig. 5. The map which shows the positions of microseismic observations (O) and of wave gauge (S) respectively. The location of this wave gauge stations Naarai is shown in the annexed small map.

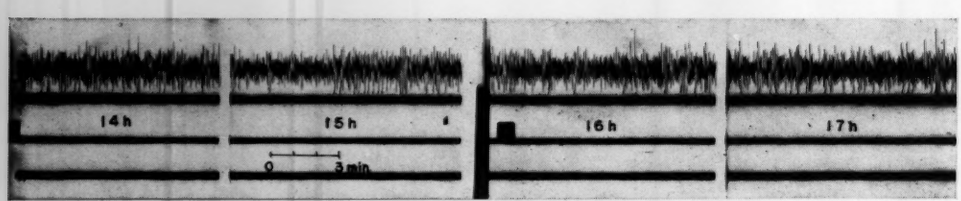

T-5919, OCT. 21^{d} 14^{h}~17^{h}

Fig. 6. An example of microseismic records obtained by slow speed recording camera.

As the purpose of the present work is to find out the times when microseismic amplitudes become largest, and to compare them with those of swells, the running speed of the recording camera of the seismograph was slowed down to as little as 1 cm/min. The recording mechanism was so designed as to start at 00 minutes, continue to work 10 minutes and then stop automatically. A sample of the records thus obtained is shown in Fig. 6.

4. The results

The results of time variations between M (the microseismic amplitudes) and S (swell heights) due to the passing of five typhoons 5914, 5915, 5916, 5918 and 5919 are shown in Fig. 7. In this figure, other data W (the wind velocity measured at the same station Naarai), D (the distance of cyclonic center from Naarai) and p_0 (central pressure) are also shown for reference. The vertical broken lines show the time

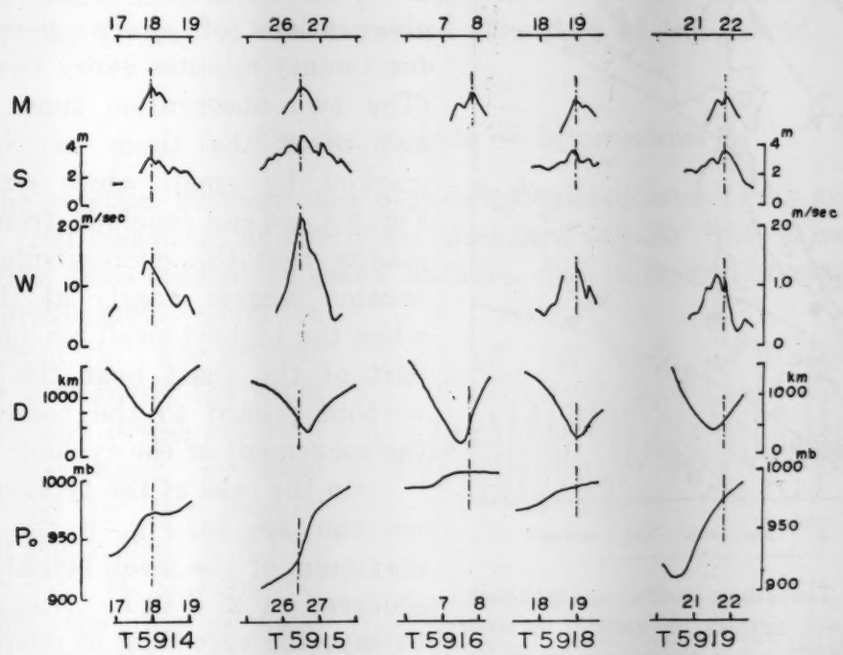

Fig. 7. Variations of microseismic amplitudes (M), swell heights (S), wind velocities (W) at Naarai due to the passing of typhoons. Variations of distances (D) from the cyclonic centers to the station and of central pressure (p_0) are also shown.

when M reached maximum. This figure shows the remarkable correlation between the growth and decay of M and S. However, since the difference between the times of M_{max} and S_{max} is not clear on too narrow a times scale, another representation was taken in Fig. 8, in which the times of M_{max}, S_{max} and W_{max} are shown by three kinds of arrows on every travelling path of typhoon. Seeing this figure, the times of M_{max} and S_{max} seem to be slightly different. But we need not expect them to coincide exactly. For, the standing wave of swells cannot be caused just at the wave gauge station S. From the topographical features

around Naarai (See Fig. 5), the coast along the steep cliff beyond "*A*" may be one of the suitable region where a standing sea wave occurs due to the interference between the incident and reflected waves. If this assumption is the case and microseismic amplitudes were mainly effected by this origin, the times of M_{max} will be measured about forty or fifty minutes later than those of S_{max}. (The swells were always coming from the south).

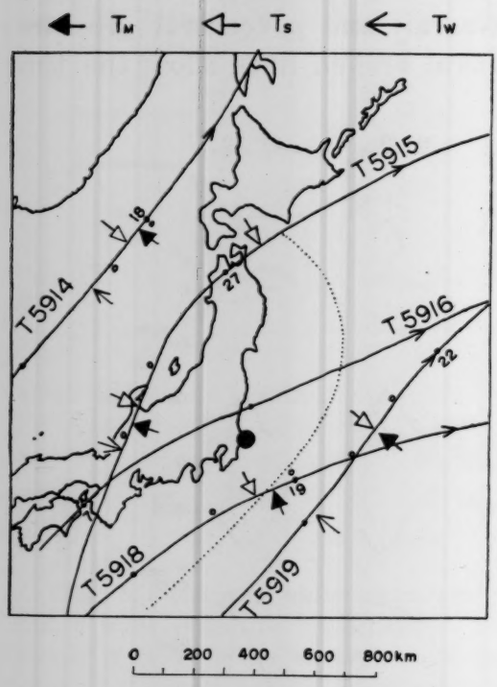

Fig. 8. Travelling paths of typhoons. The different arrows on each path show the times of T_M (when the maximum microseismic amplitudes were recorded), T_S (when the highest swells were recorded), and T_W (when the largest wind velocity were recorded). Small circles mean the recording times of swells before and after the T_S.

Further, considering that the observations of swells were made for twenty minutes every two hours (The two observation times before and after the times of S_{max} are marked by small white circles in Fig. 8.), we can conclude from these results that the microseismic storm became largest nearly at the time when the highest swell reached some part of the coast near the station without regard to the position and the movement of the cyclonic center.

On the case of the typhoon 5915, we can see in Fig. 8 the second maximum of the swell heights which occurred at 27 d 01 h. (Regrettable to say, the recording of microseisms had already been stopped by this time.) Examining the weather map around that time, it was found that this cyclonic center (typhoon 5915 had already weakened and had changed into a cyclone) was followed by a strong cold front (dotted lines in Fig. 8) which was just entering into the Pacific Ocean. Remembering here the feature that microseismic storms in Japan become heaviest due to the same circumstances[5], we can guess from this fact also that the heaviest microseismic storm occurred at the same time.

There is another fact to be noticed. That is, even in such a case as that of typhoon 5914 which travelled through the Japan Sea, the

5) *loc. cit.* (1).

microseisms at Naarai were greatly influenced by the swells on the Pacific Ocean. Since the microseismic storm region due to the passing of a single cyclonic center is not large in Japan (See Fig. 3 or Fig. 5 in Part I), we can conclude that the microseisms at a certain station are mostly influenced by the swells near the station.

It was firstly noticed by B. Gutenberg that microseisms can propagate for a great distance over the continental path with a uniform structure, but they suffer marked attenuation in geologically disturbed areas. In Japan, microseisms show, as is stated above, rather large attenuation, which may be due to the disturbed structure of the Island.

5. On the periods of Microseisms

The relation between the periods of microseisms (*Pm*) and that of swells (*Ps*) measured at the same time and nearly the same position has often been studied by many authors, and it is well known that *Pm* is approximately equal to the half of *Ps*. The present author also found the same relation and it was reported in the first paper. By these facts and by the experimental study done by R.I.B. Cooper and M. S. Longuet-Higgins[6], the standing wave theory theoretically established by Higgins[7] has become the most powerful one to explain the mechanism of the generation of microseisms.

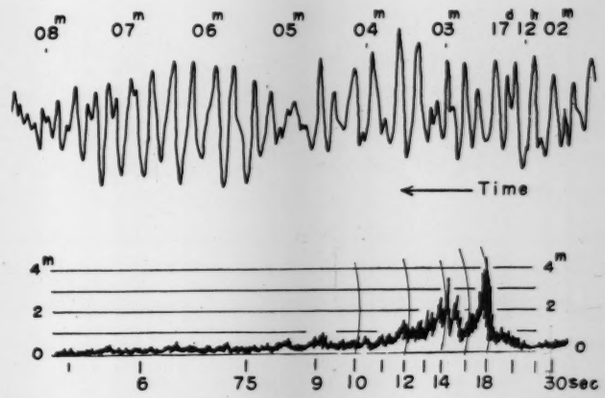

Fig. 9. Wave form of swells recorded at Naarai at the passing of the typhoon 5821 (above), and the corresponding period spectrum (below).

However, before we adopt his theory to explain the period relation above stated, we must clear up the doubt whether the swells contained second harmonic waves and whether the instruments for microseisms having a good respone from four to seven seconds predominantly recorded

6) M. S. LONGUET-HIGGINS and R. I. B. COOPER, "An Experimental Study of the Pressure Variations in Standing Water Waves," *Proc. Roy. Soc. A*, **206** (1951), 424.

7) M. S. LONGUET-HIGGINS, "A Theory of the Origin of Microseisms," *Phil. Trans. Roy. Soc. London, A*, **243** (1950), 1.

such second harmonic waves.

Recently, a spectrum computor "MERIAC-I-F" has been completed at the Oceanographical Laboratory, Meteorological Research Institute, Tokyo[8]. The period spectrum of swell at Naarai were obtained by this computor. An example of the wave form of swells and the corresponding spectrum are given in Fig. 9. As is well recognized in this example, the spectrum of swells does not contain any noticeable second harmonics. Therefore, in order to explain the relation of $Pm=\frac{1}{2}Ps$, we have to adopt the standing wave theory.

6. Some experimental observations

Occasionally, running speed of the recording paper was increased in order to see the fine structure of a wave. Fig. 10 shows some examples thus obtained, in which the upper two records (A) are those by two horizontal seismographs both installed in NS direction in order

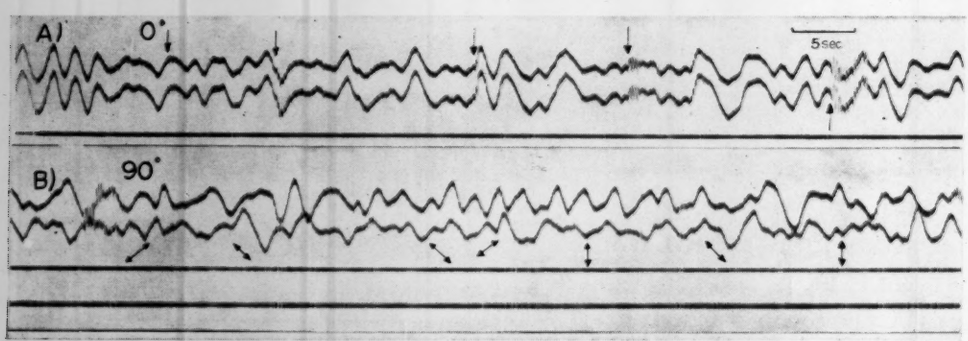

Fig. 10. An examples of the wave form of microseisms at Naarai. A) is obtained by two horizontal seismographs both installed in NS direction in order to check the similarity of their characteristics. Several arrows mean the shock waves due to the collisions of swells at the breakwater B which is approximately 200 m apart from the observational position (see Fig. 5). In B), the lower wave form was obtained by turning one of the seismographs in EW direction. Arrows show the direction of ground motion estimated by the phase relation between the two records.

to check the similarity of their characteristics, while in the lower two (B), one of the seismograph was turned to EW direction.

As will be recognized in Fig. 5, observational point O is surrounded by intricate cliffs or many small rocky islands near the coast. Beside

8) T. FURUHATA, "Atarashii Zidô Dêta Syorikikai MERIAC-1-F ni Tsuite", (in Japanese), *Kisyô to Tôkei*, **10** (1959), 23.

the two breakwaters, many concrete blocks which will be used to build a new breakwater were piled up here and there in the water. It was observed that many small standing waves took place among and behind these complicated obstacles. For this reason, the recorded microseismic waves were irregular and had rather short periods. In the record (A), we can see small and very short period waves marked by arrows. They are the waves caused by the direct collisions of high swells at the southern side of the breakwater B which projects westward into the Ocean (See Fig. 5). It must be remarked here that the elastic waves due to such direct collisions of swells with the breakwater decrease very rapidly, and do not seem to bring up any long period elastic waves in the earth.

By two records in (B), the directions of ground vibrations due to microseismic waves can be estimated from the phase relations. These are represented by arrows at the corresponding waves. As has been reported by many authors, the propagating directions of microseismic waves are not constant but frequently change at random. In this figure, this nature is also well recognized.

7. Conclusions of this paper and some discussions on the origin of microseisms

1) A new relation was discovered between the position of a cyclonic center, its travelling speed and its central pressure when it causes the largest microseismic storm at a given station. This relation was well explained by supposing an "eye of the microseismic storm" around the cyclonic center from the boundary of which the highest swells for the coast near the station were sent out. The dimensions of the radius of this swelling region were roughly estimated as several tens kilometers for the cyclones ($p_0 > 1000$ mb.) and as few hundreds kilometers for the typhoons ($p_0 < 985$ mb.) respectively.

2) Microseismic observations were made at a gauge station, and it became clearer that the energy of swells changes into microseismic waves at some steep coast. Further, the following facts could be recognized.

a) The direct collisions of swells at steep cliffs cause very short period waves, but these waves show a rapid attenuation and cannot bring up microseismic waves.

b) Sea waves much disturbed among and behind many complicated

obstacles around the station produced rather short period (three to five seconds) local microseisms. As has often been observed usually, these microseismic waves seem to come from diverged directions. The phenomenon observed at Naarai, therefore, looks like a model of usual microseisms.

c) At least in Japan where geological structure is disturbed, the microseismic amplitudes are mostly influenced by the swells near the station.

3) Period spectrum of swells were computed and no noticeable second harmonics were found. By this examination, the standing wave theory was emphasized.

Through the studies from various aspects that have been described in three papers, the writer have reached a final conclusion on the origin of microseisms. Namely, the microseismic waves are generated somewhere at a steep coast where sea waves can be reflected.

By the above conclusion, most of the complicated results which have been reached by observations at one or few stations in a limited district and have made the character of microseisms quite obscure will be clearly explained as follows:

Probably, such microseismic origins are distributed near the observational stations. Especially, stations on an Island are surrounded by many such origins with various strengths according to such conditions as the reflective coefficient of swell at these origins, the length of the steep coast, or the elastic conditions beneath the sea at these origins. (After the experimental study by R. I. B. Cooper and M. S. Longuet-Higgins[9], water waves were reflected by such gentle sloped plate as 20° with the reflective coefficient of 0.32). On the other hand, the heights of swells coming into each origin are not constant but change occasionally and independently. Therefore, when we observe microseismic waves by, for instance, the tripartite method, they look as if they come from various directions at random.

Further, when there is a strong origin somewhere, the microseismic wave from that origin will always be predominant in spite of the shift of energy source (cyclonic center) on the Ocean.

The velocity of microseismic waves cannot be measured unless we can detect the waves which come from one origin. Otherwise, we are apt to measure the apparent velocity which is uncertain.

9) *loc. cit.* (6).

8. Acknowledgements

The writer wishes to express his hearty thanks to Dr. K. Wadati, the Chief of the Japan Meteorological Agency, to Mr. S. Miyamura and to Dr. Y. Satô for their encouragement and guidance during the present studies.

Many thanks are also due to Dr. S. Unoki for his valuable advice from the oceanographical point of view.

The writer is greatly indebted to Mr. T. Kizawa for the collection of swell data.

The writer cannot forget Mr. N. Hoshino and Mr. N. Takagi for their help and kindness during the observations at Naarai.

---

14. 脈 動 源 に つ い て (第 三 報)
——波浪観測点における脈動観測——

地震研究所　三 東 哲 夫

前稿では，ある場所の脈動振巾が最大になつた時の台風や低気圧の速度，位置および中心示度などの間には，ある関係式が成立つことを述べたが，さらに本稿では，まづ低気圧や台風の中心のまわりに，ある領域を考え（第 2 b 図）脈動観測点付近の海岸に最高の波浪として到達する波がこの領域のへりから送り出されたと考えるとうまく説明のつく新しい関係式を導いた（式 (1)）．この領域の半径は，低気圧や台風の進行方向の左側では，中心示度が 1000 ミリバール以上の低気圧では数十キロメートル，中心示度が 985 ミリバール位以下の台風では 300～400 キロメートル位のもので，進行方向の右側ではこれ等よりもやや大きい．つまり，さうした領域のふちから出た波浪が，観測点付近の海岸に最高の波浪として到達し，それと同時にそこの脈動が一番大きくなる，ということで，ある場所の脈動と，それをおこすエネルギー源である低気圧や台風の速度や大きさ，およびその位置などに関係した時間的空間的な相互関係がうまく説明されてくる．

そこでつぎには，果してそれならば，ある場所での波浪が一番高くなつた時に，その同じ場所での脈動も同時に一番大きくなるだろうか，という点に関する直接の確証が望まれてくる．そこで今回，千葉県銚子市の名洗港（第 5 図）で脈動を観測し，その振巾の最大時が同じ場所で運輸省第二港湾建設局の行なつている波浪観測の波高の最大時と果して一致するかどうかを調べて見た．その結果は予想通りであつて，この両者はかなりよく一致した（第 8 図）．

さらに，今度の観測で認められたことは，

a) 防波堤に直接打ち当る衝撃力は，脈動にはならないこと（第 10 図の A）．

b) 少なくとも日本では，ある場所の脈動振巾は，ほとんどその場所の近くの波浪の高さで左右され，広い範囲にわたつて一様な地殻構造をもつた大陸で従来認められているようには脈動は伝播してゆかないこと．

c) 観測点周囲の複雑に入りこんだ崖や，妨害物等によつて，局部的な定常波が方々で見られたが，脈動による地面の動きも，これ等の局部的な定常波発生源を脈動源と考えて差支えないこと（第 10 図の B）．

等である．

また，脈動の周期がいつも波浪の周期の約半分になつているという点を説明する定常波説をより一層確認する目的で，波浪の波形の中には第二高調波がほとんどないことを，最近気象研究所の海洋研究部で完成されたスペクトル分析器による結果で確めた（第 9 図）.

以上三部にわたつて，いろいろの角度から脈動の発生する場所についての究明を試みて来たが，結局帰するところは，脈動は波浪が海岸に到達し，海岸線上のどこか，十分な反射波が生じうる場所で入射波と反射波との間に起る定常波によつて発生する，ということである．このような発生源は，当然それぞれの場所における波浪の反射率の大小，定常波発生領域の広狭，さらには，その領域の海底における弾性波の吸収係数の大小等に左右される「強さ」を一つ一つ持つているであろう．しかも，これ等の異つた強さをもつ発生源の一つ一つからやつてくる脈動波自体が，また一定の振巾ではありえない．何故ならば，それぞれの発生源に送りこまれる波浪の高さ自体が，それぞれ独立に絶えず変動をくり返す性質のものだからである．したがつて，局部的に脈動を観測する限り，脈動波は全く不規則にあちこちからやつてくるように見える．また，特に強い発生源がある方向に存在する場合には，海上をエネルギー源（低気圧や台風）が移動しても，この強い発生源からの脈動波が終始卓越して観測されることも当然ありうる．

Bulletin of the Earthquake
Research Institute
Vol. 38 (1960), pp, 255-290

15. *Geological Investigations on the Zaō Volcanoes. V Kumano Volcano.**

By Takeshi Ichimura.

(Read March 24, 1959.—Received March 22, 1960.)

Introduction

The southern half of North Zaō is occupied by the Kumano Volcano which is interposed between the Ryū-zan Volcano[1] on the north and the Byōbu Volcano[2] on the south, rising up to 1840.8 m. above the sea-level at its highest point. It is the most important center of activities in the Zaō Volcanoes and has a very complicated topography and structure due to the successive openings of craters and explosion craters where repeated eruptions of lava flows and various kinds of ejecta took place even in historic times. Some such geological features are indicated by the presence of a small crater lake called "Okama" and a central cone represented by Goshiki-dake as well as a large explosion crater surrounded by Kumano-dake, Umanose, Katta-dake and Haizuka-yama. Besides these, this volcano is remarkably destroyed and deeply dissected here and there. Accordingly, the succession of lava flows and ejecta are clearly observed at many places. It is, therefore, very easy to investigate the history of activities that happened in concert with other parts of the Zaō Volcanoes.

The geological investigation of the Kumano Volcano was first intended by A. Takada[3] many years ago, and it has also been carried on intermittently by the writer during the past ten years. In this case, his work was enlarged to the surrounding districts where such base rocks as granodiorite, plagioliparite, older or younger andesite, basalt and Neogene sediments are widely exposed.

The results of his field and laboratory works are summarized in this paper, excluding those of chemical investigations which have not

---

* Communicated by H. Tsuya.

1) T. Ichimura, *Bull. Earthq. Res. Inst.*, **35** (1957), 573–593.

2) T. Ichimura, *Bull. Earthq. Res. Inst.*, **33** (1955), 593–629.

3) A. Takada, *Graduation Theisis, Univ. Tokyo M.S.*, 1922.

yet been completed.

Location

The Kumano Volcano extends over two cities of Yamagata Prefecture (Yamagata and Kaminoyama) and three towns of Miyagi Prefecture (Kawasaki, Zaō and Shichigashiku). It is now approached very easily through several courses. For the purpose of climbing Kumano-dake and Katta-dake, which are the main peaks of this volcano, three courses are generally selected. One of them starts at the Zaō Hot Spring of Yamagata City and passes over Zange-zaka and Jizō-san on its way. It is at present utilized by many hikers. The next course has its base at the Gaga Hot Spring of Kawasaki-machi. In this case, the bus road is opened up to Sainokawara from where the summits of Katta-dake and Kumano-dake are found within a short distance. The last one is the Bōdaira course which attains directly to Umanose between Kumano-dake and Katta-dake. It is not so steep when compared with others. Besides these, there are some different courses from Aone Hot Spring and Tōgatta Hot Spring as well as from Hōzawa and Nakamaru-yama, but they are partly neglected at present.

Topographical and Geological Features of the Kumano Volcano

The Kumano Volcano is composed of Kumano-dake (1840.8 m.), Katta-dake (1759 m.), Goshiki-dake (1674 m.), Nakamaru-yama (1559 m.), Reisui-zan (1339.7 m.), Jizō-san (1764 m.), Sanpōkōjin-san (1683 m.), Yokokura-yama (1151.9 m.) and Honode-yama (751.3 m.). The area including these peaks is high on the east but low on the west, being deeply dissected here and there by the Nigori-gawa, Sumi-kawa, Happō-zawa, Sennin-zawa, Zaō-gawa, Nanba-zawa and their tributaries. Generally, it reveals a steep topography at its eastern half where a large explosion crater and central cone are surrounded by Kumano-dake, Umanose, Katta-dake, Haizuka-yama, etc., and a remarkable faultscarp constructs the northern flank of Sanpōkōjin-san and Jizō-san (Fig. 1). The western half and southeastern corner of this volcano are, however, gently sloped to a large extent, depending upon the wide distribution of ejecta and the slight undulation of underlying rock-surface (Fig. 3).

The adjoining districts are built up of older intrusives or extrusives as well as of Quaternary sediments and volcanics. They are, therefore,

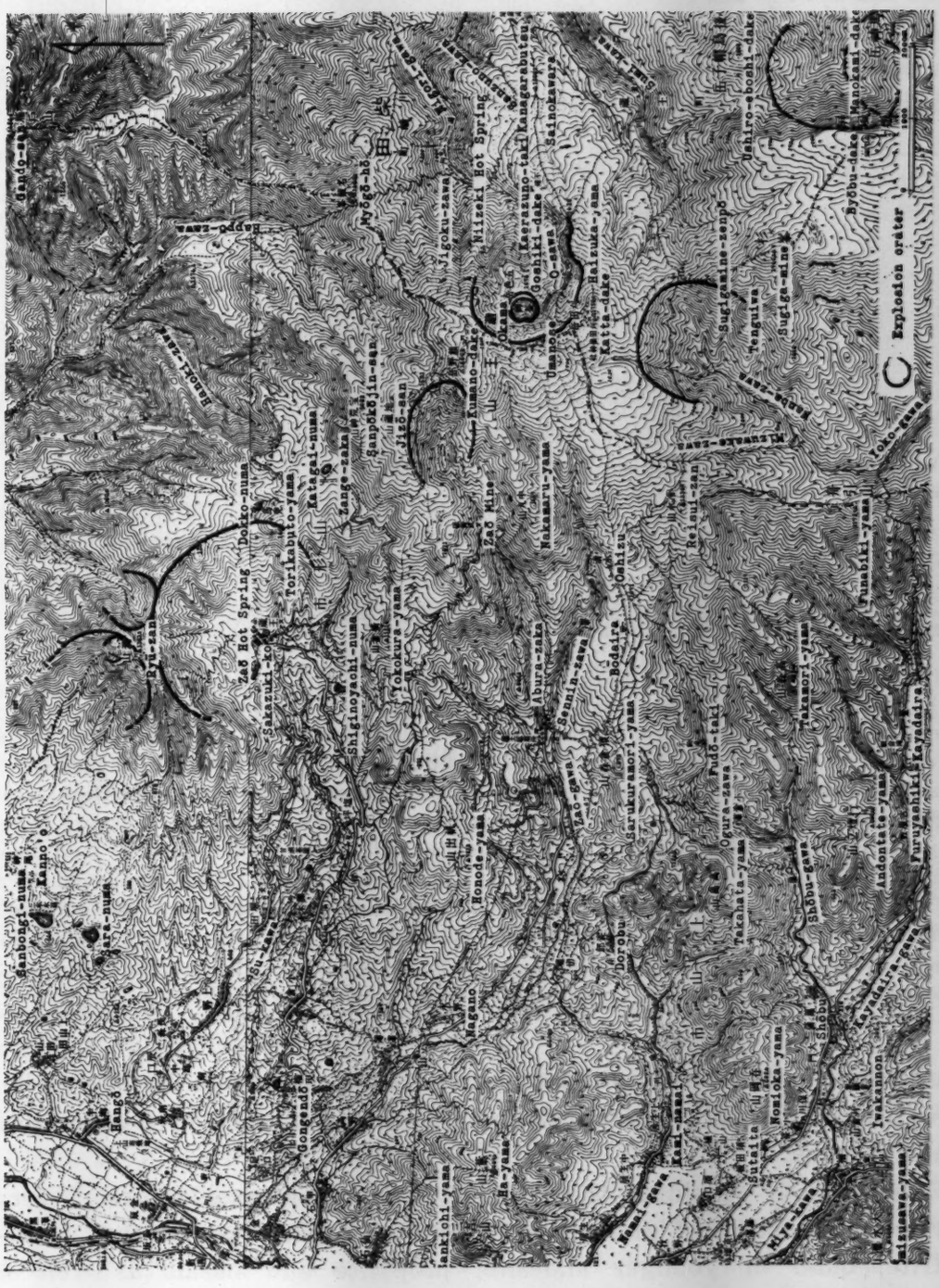

Fig. 1. Topographical map of the Kumano Volcano and its vicinity.

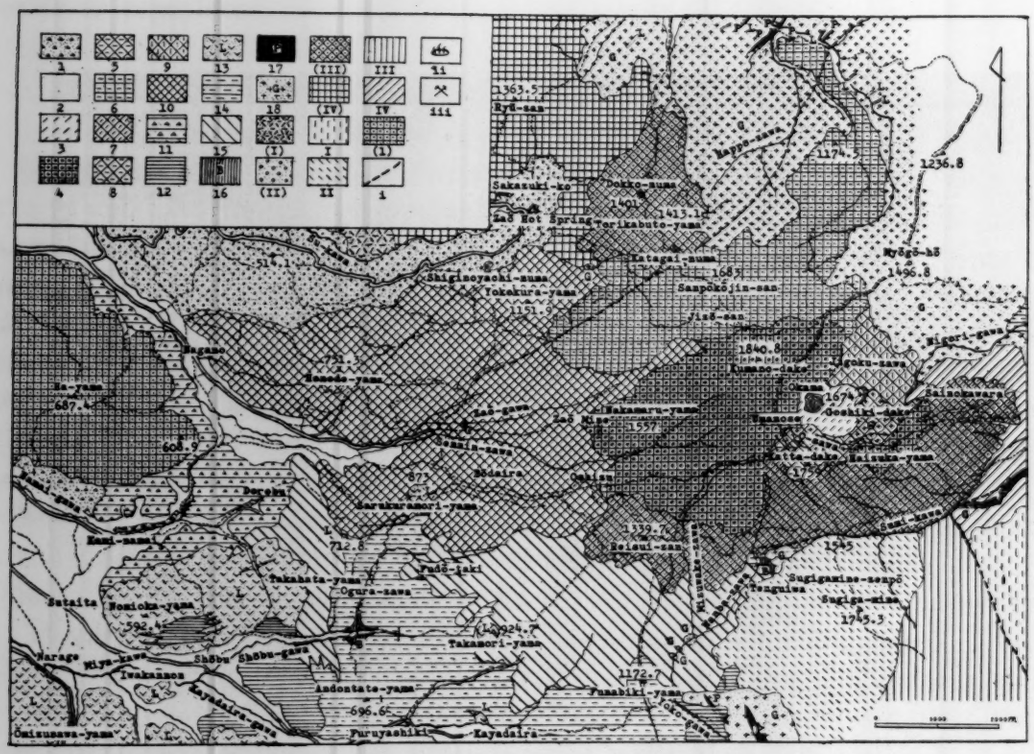

Fig. 2. Geological map of the Kumano Volcano and its vicinity.

1. Talus deposits, 2. Quaternary fluviatile deposits, 3. Goshiki-dake ejecta, 4. Kumano-dake lavas and ejecta, 5. Katta-dake lava, 6. Jizō-san lava, 7. Nanba-zawa lavas and ejecta, 8. O-sawa lavas and ejecta, 9. Jigoku-zawa lavas and ejecta, 10. Yokokura-yama lavas and ejecta, 11. Dorobu Formation, 12. Upper Green Tuff Formation, 13. Plagioliparite and associated rocks, 14. Lower Green Tuff Formation, 15. Tertiary andesite, 16. Basalt, 17. Propylite, 18. Granodiorite and granite, (I). Kanno'o mud flow (Ryū-zan Volcano), (II). Takayu mud flow (Ryū-zan Volcano), (III). Torikabuto-yama lava and mud flow (Ryū-zan Volcano), (IV). Ryū-zan lava and agglomerate (Ryū-zan Volcano), I. Ushiro-eboshi-dake lavas and ejecta (Byōbu Volcano), II. Sugiga-mine lava and agglomerate (Byōbu Volcano), III. Byōbu-dake Lava (Byōbu Volcano), IV. Sumi-kawa lava and agglomerate (Byōbu Volcano), (1). Ha-yama lavas and ejecta (Ha-yama Volcano), (i). Fault, (ii). Hot spring, (iii). Mine.

characterized by a complicated topography, as is shown by Myōgō-ho, Sarukuramori-yama, Andontate-yama, Ōmizusawa-yama, Ha-yama and Sankichi-yama.

Geologically speaking, the volcanic area under consideration is very intricate, consisting of granodiorite (granite), aplite, pegmatite, plagioliparite, older or younger andesite, propylite and basalt as well as Neogene sediments and Quaternary deposits. The lava flows and ejecta erupted from this volcano rest on the eroded surface of such base

rocks as granodiorite, aplite, pegmatite, older andesite and Neogene sediments (Fig. 2).

(1) Intrusives and extrusives prior to the first eruption of the Kumano Volcano: The oldest rock is hornblende biotite granodiorite or biotite granodiorite which is exposed at the northern or eastern periphery and southeastern corner of this area. In the former case, granodiorite extends further north and forms the base of the Gando Volcano. Its distribution is, however, restricted to a small extent in the latter case, although the rock crops out here and there in the neighbouring districts. The highest point of its exposure is known on Myōgō-hō, and it is estimated to be 1490.8 m. above the sea-level. As can be observed along the Nigori-gawa and near Kayadaira or elsewhere, the rock is overlain by Neogene sediments and older or younger andesite, being traversed by aplite, pegmatite, plagioliparite and propylite.

So far as is known at present, hornblende biotite granodiorite occurs in high frequency as compared with biotite granodiorite. They show a gradual transition into one another. It is also noteworthy that there are some textural varieties and some of them are more or less schistosed. In these cases, the common type is medium-grained or coarse-grained variety and has a darker color when it is rich in ferromagnesian minerals. Such rocks are composed of quartz, orthoclase, microcline, plagioclase, biotite, hornblende, magnetite, zircon, apatite, allanite, chlorite, epidote, titanite, leucoxene and sericite.

Aplite and pegmatite are unimportant intrusives exposed along the Nigori-gawa and Sumi-kawa where they occur as small dykes, 10 to 50 cm. in width. Of these, aplite is a fine-grained rock with a pinkish color, being composed of quartz, orthoclase, plagioclase, biotite, hornblende, zircon, magnetite, apatite, chlorite and sericite. It is biotite aplite or hornblende aplite. Pegmatite is, on the other hand, a coarse aggregate of quartz and orthoclase or microcline with a subordinate amount of plagioclase and biotite.

A noticeable feature of the base rock is the abundance of plagioliparite and older andesite at the southern margin of the volcanic area where they are mostly found as lava flows.

The plagioliparite here begins to be exposed on Sarukuramori-yama being partly concealed beneath the ejecta and lava flows of the Kumano Volcano. There is also a small exposure of plagioliparite along the irrigation ditch opened on the eastern or northern slope of the ridge just behind Dorobu and Ogurazawa. By going westwards, however, a large

lava flow is to be seen on Nomioka-yama and its adjoining peaks. It is underlain by older andesite and passes laterally or vertically into alternate beds of tuff, sandstone and hard shale. Its western half is unconformably covered by some fresh water deposits consisting mainly of brecciated tuff, shale and tuffaceous sandstone.

The plagioliparite exposed here seems to extend further south or southwest across the Miya-kawa and Kayadaira-gawa. It is supposed to have a connection with plagioliparite and trachytic andesite distributed largely in the area including Ōmizusawa-yama, Kukeji-yama and others.

The mineral ingredients of this rock is quartz, andesine, biotite, zircon, pyrite, sericite, chlorite, limonite and epidote. The specimens obtained from Nomioka-yama have a heterogeneous groundmass and contain abundantly such rock-fragments as granodiorite, propylite, green tuff and hard shale. It is biotite plagioliparite.

The Tertiary andesite is the most characteristic extrusive in the lower green tuff formation and is generally found as lava flows which interfinger occasionally with the sediments of this formation and is widely distributed in the area including Funabiki-yama, Kayadaira, Furuyashiki, Takamori-yama and Takahata-yama. The thickness of these lava flows is variable from place to place, and the appearance is quite similar to that of the older andesite exposed widely at the upper course of the Yoko-kawa and along the bus road of Niijuku-tōge. The andesite under consideration is a compact and hard rock with a porphyritic texture. It is augite andesite and has a dark grey or black color in fresh specimens, but obtain a dark greenish grey color and purplish shade when decomposed, containing labradorite, augite, magnetite, chlorite and calcite.

There is also another type of older andesite which is associated with tuffaceous sediments named the Dorobu Formation. The rock is two-pyroxene andesite with a porphyritic texture and is found at Kaminamai, Tate-yama or elsewhere, occurring as thin lava flows with such mineral ingredients as labradorite, augite, hypersthene, magnetite and glass.

Propylite is a common rock at the northern periphery of the volcanic area where granodiorite and the Lower Green Tuff Formation are exposed. The rock forms dykes, large or small, and traverses these base rocks at many places. There are two prominent exposures of this rock near the Gaga Hot Spring and also along the Sumi-kawa. The

former cuts the green tuff formation near the hot spring and is traceable about 800 m. west-northwestwards from Gaga, whereas the latter has a trend of northeast at the contact between granodiorite and green tuff which are exposed at the upper course of the Sumi-kawa. Besides them, the occurrence of small dykes is known here and there along the upper course of the Nigori-gawa. It is, however, noteworthy that such a rock is almost absent in the southern area except for the example of Kayadaira.

They are compact and porphyritic rocks, having a black color in fresh specimens and a greenish grey color when decomposed. The mineral ingredients examined by the writer are labradorite, augite, chlorite, magnetite, hematite, calcite, epidote, sericite, leucoxene, etc.

The distribution of basalt is, on the other hand, restricted to a small extent as compared with other extrusives. The writer found this rock only near the junction of the Namino-sawa and Ogura-zawa where it occurs as a lava flow and is closely associated with the Lower Green Tuff Formation. The lava flow here seems to extend further north and is supposed to be 50 m. or thereabouts at the thickest part, forming a columnar joint structure at the entrance of the Ogura-zawa. The rock has a porphyritic texture and black color. It is very hard and compact, being composed of such mineral ingredients as plagioclase, augite, magnetite, calcite and chlorite.

(2) Neogene sediments: The northern and southern margin of this volcanic area are partly occupied by Neogene sediments which are sometimes found in close association with plagioliparite, propylite, andesite and basalt. In the former case, they are represented by green tuff and rest directly upon the eroded surface of granodiorite and associated hypabyssal rocks. Some such green tuff contains imperfect remains of shells on the trail near Fudō-taki of the Sumi-kawa. Occasionally, it passes into a basal conglomerate on the surface of granodiorite and contains various kinds of pebbles represented by granodiorite, aplite, milky quartz, etc. Several good exposures can be observed along the Nigori-gawa and Sumi-kawa. The green tuff here is sometimes traversed by propylite and felsitic rock. In the latter case, however, Neogene sediments can be classified into three different types of formation.

One of these is the Lower Green Tuff Formation corresponding to the lower half of the Yoshino Formation of the neighbouring districts. It is intercalated with lava flows of andesite and basalt, but is intruded

by plagioliparite. The formation is sometimes characterized by the frequent occurrence of brecciated or conglomeratic varieties. They are rich in andesite fragments when interfinger with andesite lava flows. There are also many pebbles or fragments of granodiorite in the conglomeratic or brecciated tuff exposed at Ogurazawa. Besides these types of sediments, non-brecciated or non-conglomeratic green tuff is largely distributed together with sandstone and shale, although their lithological characters vary from place to place.

The Lower Green Tuff Formation of the area including Furuyashiki and Kayadaira is characterized by the abundance of animal fossils. Its stratigraphical investigation was recently carried out by Minakawa[4]. He obtained many fossils from the lower and upper halves of this formation. They are *Acila divaricata* (Hinds), *A. minuta* Makiyama, *Anadara* cfr. *abdita* Makiyama, *Lucinoma* sp., *Ostra gigas* Thunberg, *O. gravitesta* Yokoyama, *O. musasiana* Yokoyama, *O.* sp. in the lower half of the formation, but are *Anomia* sp., *Calyptraea tubura* Otuka sub sp., *Cardium* sp., *C.* cfr. *narusawaensis* Nomura, *Chlamys* sp., *Chione* sp., *Clinocardium shinjiense* (Yokoyama), *C.* n. sp., *Dentalium* sp., *Dosinia nomurai* Otuka, *Gloripallium crassivenium* (Yokoyama), *Glycymeris oinouyei* Nomura, *G. vestinoides* Nomura, *G.* n. sp., *Limatura kurodai* Oyama, *Lucinoma actilineata* (Conrad), *Mactra* sp., *Paphia* sp., *Patinopecten kimurai* (Yokoyama), *P.* sp., *Pitar itoi* (Makiyama), *Venericardia* sp., Brachiopoda, spine of Echinoidea and petrified wood in the upper half of the formation.

The Upper Green Tuff Formation is composed of green tuff, hard shale, conglomeratic sandstone, sandstone and conglomerate. Such a formation is to be seen along the lowest course of the Kayadaira-gawa and Shōbu-gawa. Moreover, it is noteworthy that green brecciated tuff interfingers with plagioliparite on Nomioka-yama and its adjoining ridge.

The Upper and Lower Green Tuff Formations mentioned above are unconformably overlain by the alternating beds of fresh water deposits. They are mostly tuff and shale. In this case, the tuff is usually brecciated, containing many fragments or pebbles of granodiorite, plagioliparite, andesite and hard shale. It is called "Dorobu Formation" and is characterized by the occurrence of such plant fossils as Cfr. *Acer diabolium* Blume, *Carpinus arosa* Blume, *Juglans* sp. and *Tilia protojaponica* Endo[5].

4) S. MINAKAWA, *Bull. Yamagata Univ.* (*Nat. Sc.*), **4** (1959), 565.
5) S. MINAKAWA, *op. cit.*, 566.

The Neogene sediments mentioned above are much disturbed here and there. Thus, green tuff or shale near Gaga indicates a strike of N50°–55°E and a dip of 40°–60°SE, whereas those of Kayadaira, Shōbu, Ogurazawa and Kami-namai have a strike of N–S to N85°E or N15°–40°W and a dip of 10°–30°W, 10°–50°NW or SE, 5°–40°WSW or SW and 10°–50°N respectively. These complicated structures can be seen along the Shōbu-gawa, Kayadaira-gawa, Namai-gawa and their tributaries.

(3) Extrusives of the Ha-yama Volcano: This volcano is built up of two main peaks called Ha-yama and Sankichi-yama which rise up on the wall of an explosion crater opened northwestwards. It is mostly underlain by fresh water sediments and green tuff beds as well as plagioliparite and other older extrusives. Of these, Ha-yama is 687.4 m. high above the sea-level and occupies the central part of this isolated volcano composed of lava flows and ejecta. There are at least two lava flows poured out from the pre-existing crater which was subsequently broken by the formation of an explosion crater. All of them are represented by two-pyroxene andesite and are frequently associated with agglomerates. They are named the Sengoku lava and agglomerate and Ha-yama lava and agglomerate. The thickness of lava flows is variable from place to place. The thickest part is 150 m. in the former, whereas it is 200 m. in the latter. Some of these lavas reveal a remarkable joint structure, and are broken into angular pieces, being accumulated here and there on the steep slope of the volcano. The andesites exposed here have a black color in fresh specimens, but obtain a grey color when decomposed. Moreover, they are characterized by a reddish color due to reheating. The specimens obtained by the writer are compact or porous, being always porphyritic and consisting of labradorite, bytownite, augite, hypersthene, magnetite and brown glass.

(4) Lavas and ejecta from the Kumano Volcano: The lavas and ejecta of this volcano are very complicatedly exposed, being partly overlapped by those of such adjoining volcanoes as Byōbu and Ryū-zan. They are Yokokura-yama lavas and ejecta, Jigoku-zawa (Maruyama-zawa) lavas and ejecta, O-sawa lava and agglomerate, Nanba-zawa lavas and ejecta, Jizō-san lava, Katta-dake lava, Kumano-dake lavas and ejecta and the recent ejecta from Goshiki-dake.

(i) Yokokura-yama lavas (olivine two-pyroxene andesite, olivine-bearing two-pyroxene andesite and two-pyroxene andesite) and ejecta: The large area including Yokokura-yama, Bōdaira and Honode-yama is mainly built up of the Yokokura-yama lavas and ejecta underlain by the

green tuff formation and granodiorite. These volcanic products extend westwards along the Su-kawa, Zaō-gawa and also along the Senninzawa where they disappear beneath other lavas and ejecta by going up further east. Some of them are intensely subjected to opalization or kaolinization in association with alunitization and are characterized by the presence of sulphur deposits which are now being mined to a large extent. Among various volcanic products exposed in this area, agglomerate seems to be predominantly distributed when compared with others. Such a tendency is confirmed on Honode-yama and Bōdaira as well as along the upper course of the Zaō-gawa. The total thickness of lavas and ejecta is supposed to be about 350 m. in maximum.

(ii) Jigoku-zawa (Maruyama-zawa) lavas (olivine-bearing two-pyroxene andesite or two-pyroxene andesite) and ejecta: The thick alternation of lavas and ejecta is well exposed on the steep slope just behind Goshiki-dake (Fig. 4), resting on the eroded surface of granodiorite and being overlain by younger volcanics which construct Kumano-dake, Katta-dake, Umanose, Goshiki-dake and the bottom of the O-sawa. In this case, lava flows are composed of two-pyroxene andesite or olivine-bearing two-pyroxene andesite, whereas ejecta are represented by agglomerate, sand and ash. These volcanic products are estimated to be 300 m. or thereabouts in the total thickness and are highly cliffed at many places.

(iii) O-sawa lava (two-pyroxene andesite) and agglomerate: These rocks crop out to a small extent within the Umanose explosion crater. Some of them were remarkably affected by the solfataric action and altered exceedingly to grey or white rocks mottled by a pink or dark grey color. Such features can be seen at the bottom of the O-sawa and on its neighbouring cliff (Fig. 5). These rocks are just exposed beneath the Nanba-zawa lavas and ejecta on the cliff between Haizuka-yama and Daikokuten, both containing sulphur deposits already stopped to be mined, whereas they are directly overlain by lapilli, sand and ash erupted from Goshiki-dake and also by the Kumano-dake lava exposed on the cliff of the opposite side.

The O-sawa lava and agglomerate construct the foundation of Goshiki-dake together with the Jigoku-zawa lavas and ejecta. In this case, the former is more than 150 m. in thickness and seems to cover the latter at the bottom of the O-sawa.

(iv) Nanba-zawa lavas (olivine two-pyroxene andesite) and ejecta: The distribution of the Nanba-zawa lavas and ejecta extend to Saino-

kawara on the east (Fig. 6) and Reisui-zan on the west, resting upon the eroded surface of granodiorite and older andesite as well as upon the Sumi-kawa lava and agglomerate. In the Nanba-zawa lavas and ejecta, the former is more predominant than the latter which is usually found at the bottom of such volcanic products. The relationship between them is well investigated at Sainokawara and along the Sumi-kawa. Some of these reveal a remarkable alteration due to the solfataric action, as can be seen near the source of the Nanba-zawa or elsewhere. They are 400 m. or thereabouts in the maximum thickness.

(v) Jizō-san lava (olivine two-pyroxene andesite or olivine-bearing two-pyroxene andesite: The northern part of the Kumano Volcano is mostly occupied by the Jizō-san lava which is underlain by granodiorite or the Yokokura-yama lava and seems to disappear beneath the Kumano-dake lavas and ejecta southwards. The lava flow is well exposed on Jizō-san and Sanpōkōjin-san (Fig. 7) as well as on the narrow ridge of granodiorite between the Happō-zawa and the Nabekurafudō-zawa showing a thickness of 350 m. or more at its northern periphery where it is cut down by the Hanoki-zawa fault and a steep slope is traceable along the southern side of this dislocation line.

(vi) Katta-dake lava (olivine two-pyroxene andesite): The upper half of Katta-dake is constructed by the Katta-dake lava which is covered by volcanic lapilli erupted from Goshiki-dake or the Kumano-dake lavas and ejecta and rests upon the Nanba-zawa lavas and ejecta. It is distributed to a small extent as an erosion remnant and does not go beyond 80 m. at the thickest part.

(vii) Kumano-dake lavas and ejecta (olivine two-pyroxene andesite, olivine-bearing two-pyroxene andesite and two-pyroxene andesite): The lava flows and ejecta of this stage extend mostly westwards from the pre-existing crater (Fig. 8), They rise up to 1840.8 m. above the sea-level and are highly cliffed here and there as is shown on the wall of the Umanose explosion crater and at other places. In these cases, ejecta are predominantly found as compared with lava flows, and this tendency is well to be seen on the western flank of Kumano-dake and Katta-dake where ejecta are repeatedly intercalated with thin lava flows (Fig. 9). In the same way, the top of Kumano-dake and a part of Umanose are formed by ejecta or lava flows which are thinly covered by lapilli erupted from Goshiki-dake. Besides these, the lava flow of Nakamaru-yama is traceable up to Kumano-dake, although it constructs a small peak looking like a parastic cone (Figs. 3, 11). These

volcanic products are estimated to be more than 300 m. in the total thickness.

(viii) Goshiki-dake ejecta: As has already been described in his previous paper[6], the central cone (Goshiki-dake) is built up of such ejecta as agglomerate, lapilli, sand and ash. They are well stratified with some inclination and have varying colors, being highly cliffed around Okama and along the O-sawa. The best exposure is to be seen on the southern cliff of Goshiki-dake where it is more than 150 m. at the thickest part (Figs. 5, 12).

(5) Quaternary sediments: They are younger or older fluviatile deposits and talus deposits.

(a) Younger or older fluviatile deposits: Fluviatie deposits consist of gravel, sand and clay, being distributed along the Nigori-gawa, Sumikawa, Su-kawa, Zaō-gawa, Sennin-zawa, Miya-kawa, Namai-gawa, Shōbu-gawa, Kayadaira-gawa, etc.

(b) Talus deposits: The Dorobu Formation and lava flows or ejecta of the Ha-yama Volcano are thinly covered by talus deposits composed of andesite fragments which crumbled down from this volcano.

Structure of the Kumano Volcano

The Kumano Volcano is a strato-homate born on the weak zone which connects the Ryū-zan Volcano on the north and the Byōbu Volcano on the south, forming here a characteristic composite volcano built up of a central cone and somma. It rests on such base rocks as granodiorite and Neogene sediments associated with various kinds of Neogene extrusives. The volcanic area has almost the same extension as the Byōbu Volcano, but is more complicated in form and structure.

The lava flows or ejecta of this volcano were repeatedly erupted during pre-historic times and even in historic times. They are highly cliffed frequently in the area subjected intensely to explosion and erosion. One of these are to be seen within the explosion crater where Goshiki-dake now rises up as a central cone. The crater wall here is constructed of such lava flows and ejecta as the O-sawa lava and agglomerate, Katta-dake lava and Kumano-dake lavas and ejecta as well as of Goshiki-dake ejecta. They are intricately overlapped and deeply cut down by the O-sawa. On the southern cliff of this crater, a part of the Kumano-dake lavas and ejecta bend inwards, suggesting that there were some subsidence soon after or at the time of the formation

6) T. ICHIMURA, *Bull. Earthq. Res. Inst.*, **29** (1951), 327–339.

of the explosion crater or central cone (Fig. 12).

The structure of Goshiki-dake is also confirmed at Okama and along the O-sawa. The volcanic products of the central cone are distinctly bedded, inclining 10°–30° to all directions.

The remarkable structure of this area is, furthermore, shown by the Jigoku-zawa lavas and ejecta, O-sawa lava and agglomerate and Kumano-dake lavas and ejecta. Among them, the Jigoku-zawa lavas and ejecta are underlain by granodiorite and are well stratified with an inclination of 10°–20°NE. These volcanic products are in contact with the O-sawa lava and agglomerate. Such features can be observed along the O-sawa and the uppermost course of the Nigori-gawa. The Kumano-dake lava exposed here is sporadically traceable southwards on the eroded surface of the O-sawa lava subjected intensely to the solfataric action.

It is somewhat different at Sainokawara and along the Sumi-kawa, where the Nanba-zawa lava and agglomerate directly cover the Sumi-kawa lava of the Byōbu Volcano. In the latter case, the upper half of the western cliff, about 200 m. high, is represented by the Nanba-zawa lava and agglomerate with a very gentle inclination of 5°–10°. They are, however, not found on the cliff of its opposite side.

Besides them, the present volcano is strikingly excavated along the Zaō-gawa and Sennin-zawa, where Kumano-dake lavas and ejecta can be traced downwards from the summit of Kumano-dake to Nakamaru-yama.

Moreover, the alternation of lavas and ejecta is topographically distinguishable on the western slope between Kumano-dake and Bōdaira, since the former is steeply sloped as compared with the latter (Fig. 9).

The structure of the Kumano-Volcano is furthermore complicated by the remarkable displacement caused by the Hanoki-zawa fault and Sumi-kawa—Nanba-zawa fault.

Pre-existing Crater and Explosion Craters

The pre-existing crater is destructed and obscured at present. It is, however, supposed to have almost been in the same location as the present explosion crater surrounded by Kumano-dake, Umanose, Katta-dake and others, since the lava flows and ejecta of this volcano extend from here downwards to all directions. Its central part seems to be now occupied by Goshiki-dake (Fig. 12).

Explosion craters are, on the other hand, found at several places. The largest one is represented by the explosion crater mentioned above. It opens northeastwards and constructs a semicircular hollow with a diameter of about 2 kilometers from northeast to southwest. The crater wall here is highly cliffed mostly, being built up of different lavas and ejecta intricately overlapped. It is about 200 m. high at its southern corner, where the bottom of the explosion crater was deeply dissected by the O-sawa and older lavas were strikingly subjected to the solfataric action. There is also a small but characteristic explosion crater called "Okama" on the western side of Goshiki-dake which is a central cone rising up on the bottom of the large explosion crater. It is a relic destroyed by repeated explosions since pre-histric times and has a diameter of about 300 m. Its circular hollow is now filled with water and deepens at the eastern side, where this lake is surrounded by a highly cliffed wall.

Besides these, a large explosion crater is known at the source of the Nanba-zawa between Katta-dake and Sugiga-mine. It seems to have exploded southwestwards, and its wall, about 300 m. high above the bottom, shows some intense alteration due to the solfataric action.

Similar topographical feature and solfataric alteration are seen at the source of the Zaō-gawa. The explosion crater is semicircularly opened westwards together with the small one formed just beneath the summit of Kumano-dake (Fig. 10). In the former case, it is about 100 m. wide from north to south, and its bottom is characterized by the predominant exposures of kaolinized andesite lavas.

Central Cone

As has already been stated, Goshiki-dake is a central cone formed within large explosion crater near Umanose, rising up to 200 m. or thereabouts above the bottom of the O-sawa and having a diameter of about 1000 m. at its base. It is a homate characterized by the presence of a small crater lake at the opposite side of Umanose (Fig. 12).

The volcanic products here are composed of ash, sand and agglomerate covered thinly by recent lapilli. Of these, sand and ash are more predominant than others. They rest on the O-sawa lava and agglomerate or Kumano-dake lavas and ejecta. Some of them are well exposed on the cliffs of the O-sawa and its vicinity, where the O-sawa lava was intensely altered by the solfataric action.

The central cone under consideration seems to have been built up by repeated explosions in pre-historic time, but it is uncertain how many times such volcanisms took place and where the explosion crater was first opened. The present peak is deformed by the local subsidence and is dissected by the subsequent erosion. It is, therefore, complicated in its structure and topographical features.

Fumaroles

Several fumaroles were opened on the slope near the entrance of the Jigoku-zawa (Maruyama-zawa) and also at the uppermost course of the Zaō-gawa, when some small activity of the Kumano Volcano took place in 1939.

In the beginning, the fumaroles here were hardly approached, since they were so remarkably charged with SO_2 that many animals and birds were killed at that time. Of these, the fumaroles of the Jigoku-zawa are still active even at present, emitting a small amount of superheated steam here and there from the fissure of granodorite exposed just beneath the thick accumulation of tuff and agglomerate. In this case, the mouth of each fumarole is always adorned beautifully with sulphur sublimated, and the surface of its neighbouring ground is thinly veiled with sulphur or halotrichite. Moreover, there is a hot spring flowing out from the fissure of granodiorite decomposed intensely by the solfataric action.

The fumaroles of the uppermost course of the Zaō-gawa were, on the other hand, already ruined. They are represented by those of "Keisei-iwa" which once exhaled a poisonous gas on the bottom of the valley.

Mineral Composition of Lavas and Ejecta

(1) Yokokura-yama lavas and ejecta: The Yokokura-yama lavas and the fragments of ejecta are mostly composed of olivine two-pyroxene andesite and olivine-bearing two-pyroxene andesite as well as of two-pyroxene andesite. So far as is known at present, they pass into one another, and the latter one is less predominantly exposed than others. The specimens obtained by the writer are compact or porous rocks with a black or dark grey color when they are fresh, being not infrequently rich in xenoliths as is indicated by those of Bōdaira and

Yokokurayama. They are sometimes characterized by the high frequency of platy joints and are now being quarried near the Zaō Sulphur Refinery as a building stone called "Teppei-seki". These rocks consist of plagioclase, augite, hypersthene, olivine, magnetite, quartz, tridymite, chlorite and brown glass.

Among them, plagioclase occurs as phenocryst and an important ingredient in the groundmass. The crystal is usually euhedral or subhedral in all thin sections. Its phenocryst takes mostly a rectangular form and ranges from labradorite to bytownorthite with a composition of An_{59-84}. It reveals frequently a worm-eaten structure due to the invasion of the groundmass or brown glass. In some specimens, the phenocryst is remarkably corroded along the cleavage. Moreover, the turbid zone is occasionally present and repeated, being always fringed by a narrow clear rim. In the writer's specimens, most of crystals are well zoned and enclose commonly augite and magnetite. The largest phenocryst is 3.65 mm. long and 2.49 mm. across.

The lath-shaped or tabular plagioclase of the groundmass is more acidic and generally has a length of 0.02 mm.–0.2 m. in the writer's thin sections. It is often found in a fluidal arrangement.

Augite is the commonest colored mineral and has a subhedral or anhedral form in most cases. The largest phenocryst is estimated to be 2.58 mm. long and 1.36 mm. across. It twins on (100) or (101), and its extinction angle, $Z \wedge c$, is 43°. In this case, the enclosure is a skeletal crystal of magnetite. Minute augite crystals are also contained abundantly in the groundmass. They have a prismatic or ill-defined form and are commonly 0.01 mm.–0.08 mm. in longer diameter.

Hypersthene is always found as phenocryst, and it is euhedral or subhedral, taking generally a long prismatic form, 2.8 mm. long and 0.82 mm. across in the largest one. When the crystal is intergrown with augite, the former is fringed by the latter. This mineral encloses magnetite and plagioclase.

The occurrence of olivine is also restricted only to phenocryst, and its frequency seems to be very variable even in the same lava flow. Thus, the crystal is abundantly present in the specimens obtained from near Sarukuramori-yama, Bōdaira and the pass 2000 m. west to Yokokura-yama, but is generally very scarce or entirely absent in other cases. It is subhedral or anhedral, and the largest one is 1.55 mm. in longer diameter. Some of it alters to bowlingite along the periphery or crack. Its enclosure is magnetite.

Table 1. Composition and optical characters of plagioclase, augite and hypersthene phenocrysts (measured by F. Hori).

	No. 1 (T.I. 48100304 b)	No. 2 (T.I. 48100305)	No. 3 (T.I. 50072307)	No. 4 (T.I. 52073102)
Plagioclase	$\alpha=1.559$ (n_1 min.) $\gamma=1.574$ (n_2 max.) An_{59-71}	$\alpha=1.561$ (n_1 min.) $\gamma=1.576$ (n_2 max.) An_{61-74}	$\alpha=1.562$ (n_1 min.) $\gamma=1.582$ (n_2 max.) An_{64-84}	$\alpha=1.562$ (n_1 min.) $\gamma=1.576$ (n_2 max.) An_{64-74}
Augite	$\alpha=1.694$ $\beta=1.699$ $\gamma=1.720$ $(+)2V=48°$ $Ca_{39}Mg_{37}Fe_{24}$	$\alpha=1.691$ $\beta=1.696$ $\gamma=1.718$ $(+)2V=51°$ $Ca_{41}Mg_{38}Fe_{21}$	$\alpha=1.691$ $\beta=1.697$ $\gamma=1.718$ $(+)2V=52°$ $Ca_{42}Mg_{37}Fe_{21}$	$\alpha=1.691$ $\beta=1.697$ $\gamma=1.719$ $(+)2V=51°$ $Ca_{41}Mg_{37}Fe_{22}$
Hypersthene	$\gamma=1.714$ $(-)2V=56°$ $Mg\%(2V)=60$ $Mg\%(\gamma)=59$	$\gamma=1.709$ $(-)2V=59°$ $Mg\%(2V)=63$ $Mg\%(\gamma)=69$	$\gamma=1.711$ $(-)2V=59°$ $Mg\%(2V)=63$ $Mg\%(\gamma)=61$	$\gamma=1.716$ $(-)2V=55°$ $Mg\%(2V)=58$ $Mg\%(\gamma)=58$

To confirm An, CaMgFe ratio and Mg% the charts devised by F. Chayes [Am. Jour. Sci., Bowen Volume, (1952) 95], H. H. Hess [Am. Min., 34 (1949), 634] and H. Kuno [Am. Min., 39 (1954) 40] were respectively used.

No. 1=The Yokokura-yama lava from the northern flank of Yokokura-yama.

No. 2=The Yokokura-yama lava from the trail between the Zaō Mine and Yokokura-yama.

No. 3=The Yokokura-yama lava from the cliff along the Zaō-gawa.

No. 4=The Yokokura-yama lava from the Zaō Sulphur Refinery—the Zaō Hot Spring.

Magnetite is a common ingredient in the groundmass and is known as an enclosure of phenocrystic minerals. It is mostly represented by octahedral crystals or irregular grains, 0.01 mm.–0.02 mm. in diameter. The large crystals are 0.2 mm.–0.57 mm. across, being closely associated with augite and hypersthene phenocrysts. Sometimes, it constructs an irregular aggregate together with augite grains.

Quartz is contained in two-pyroxene andesite exposed on the route between the Zaō Mine and its sulphur refinery, the trail between Shōbu and Bōdaira, etc., as well as in olivine-bearing two-pyroxene andesite collected at the southern side of Sarukuramori-yama. It is probably a xenocryst derived from granitic rocks and has a subangular or rounded form, the largest one being 3 mm. in longer diameter. The crystal is occasionally surrounded by the narrow rim composed of plagioclase, augite and magnetite. It is rich in liquid inclusions and is often traversed by cracks.

Tridymite is only an accessory mineral filling up the interstices of other ingredients. Chlorite is an alteration product of olivine and oc-

curs abundantly in the specimens obtained on the bottom of the Zaō-gawa near the Zaō Sulphur Refinery. Besides these, brown glass reveals a high frequency in some of the groundmass, and plagioclase phenocrysts are subjected to its invasion.

Moreover, one of characteristic features is the abundance of basaltic, noritic or gabbroic xenoliths, large or small, which are composed of plagioclase, augite, hypersthene, magnetite, brown glass and biotite (very rare). They have a sharp boundary against the mother rocks.

The groundmass consists chiefly of plagioclase, augite, magnetite and brown glass. It has a pilotaxitic or hyalopilitic texture.

(2) Jigoku-zawa lavas and andesite fragments in ejecta: The specimens were collected from the lava flows and ejecta exposed largely on the cliff between fumaroles and the Niizeki Hot Spring. They are commonly porous andesites rich in olivine or free of this mineral and have a black color when undecomposed, being constructed by such ingredients as plagioclase, augite, hypersthene, olivine, magnetite and brown glass.

Under the microscope, plagioclase is remarkably present as phenocryst and also an important ingredient of the groundmass. When it is phenocrystic, euhedral or subhedral form is more predominant. Besides, a rectangular or tabular habit is generally observed, being 3.4 mm. long and 1.53 mm. across in the largest crystal. Such plagioclase phenocrysts have a composition of An_{60-89} and range from labratownite to bytownorthite. Some of these are characterized by the high frequency of a worm-eaten structure and turbid zone. In the former case, the invasion of the groundmass and brown glass took place at the margin or inner part of crystals. This structure is more complicated by the inclusions of augite and magnetite.

Lath-shaped plagioclase is a main constituent of the groundmass which indicates a pilotaxitic or hyalopilitic texture. Most of its crystals are 0.02 mm.–0.3 mm. in length.

Augite reveals a wide range of its frequency. It is sometimes very abundant, but is almost or entirely absent in other cases. This variation of frequency can be seen even in the same lava flows and ejecta. The largest phenocryst is 1.58 mm. long and 0.08 mm. across. Commonly, the crystal takes a subhedral or anhedral form, twinning frequently on (100) or (101). Its extinction angle, $Z \wedge c$, is 40°–42°, and it increases inwards in zoned crystals. In general, the phenocryst encloses magnetite.

In the groundmass, augite occurs as prismatic crystals, usually 0.01 mm.–0.2 mm. in longer diameter. It is, however, nearly deficient in some fragments of agglomerate exposed on the cliff.

Another pyroxene is represented by hypersthene which is found as phenocryst. Mostly, the mineral has a long prismatic habit and subhedral form, some of it being fringed by the narrow zone of augite. The largest crystal is 1.58 mm. long and 0.47 mm. across.

Table 2. Composition and optical characters of plagioclase, augite and hypersthene phenocrysts (measured by F. Hori).

	No. 1. (T.I. 48091808)	No. 2. (T.I. 48091809)
Plagioclase	α=1 561 (n_1 min) γ=1 585 (n_2 max.) An_{61-89}*	α=1.560 (n_1 min.) γ=1.583 (n_2 max.) An_{60-87}*
Augite	α=1.694 β=1.699 γ=1.721 (+)2V=50° $Ca_{40}Mg_{36}Fe_{24}$**	α=1.690 β=1.695 γ=1.717 (+)2V=49° $Ca_{40}Mg_{39}Fe_{21}$**
Hypersthene	γ=1.714 (−)2V=56° Mg%(2V)=60*** Mg%(γ)=59****	γ=1.713 (−)2V=56° Mg%(2V)=60*** Mg%(γ)=60****

* After F. Chayes's chart.
** After H H Hess's chart.
*** After H. Kuno's chart.
**** After H. Kuno's chart.

No. 1=The andesite fragment of agglomerate collected on the cliff between the fumarole and the Niizeki Hot Spring.

No 2=The andesite fragment of agglomerate collected on the cliff between the fumarole and the Niizeki Hot Spring.

Lava flows and andesite fragments of agglomerate under consideration are occasionally characterized by the presence of olivine phenocrysts. These crystals are sometimes found in high frequency, although they are mostly less than augite phenocrysts. Most of these are subhedral or anhedral, and the largest one is 3.17 mm. long and 1.02 mm. across. When the crystal is associated with augite, the former is fringed by the latter.

Magnetite is the commonest ingredient in the groundmass where it takes an octahedral or granular form, 0.015 mm. in diameter. There

are also some phenocrystic magnetite crystals. They are not infrequently enclosed by various kinds of ferro-magnesian minerals. The largest diameter is 0.51 mm. Brown glass is contained in the groundmass and also in the phenocrystic plagioclase, but it occurs in a small amount.

Besides them, basaltic xenoliths are rarely seen in the andesite fragments of agglomerate. They are composed of plagioclase, augite, magnetite and brown glass, forming an intergranular texture in most specimens.

The groundmass has a pilotaxitic or hyalopilitic texture. It is constructed by plagioclase, augite, magnetite and brown glass.

(3) O-sawa lava and agglomerate: The bottom of the O-sawa is partly covered by the O-sawa lava and agglomerate subjected intensely to the solfataric action here and there. The andesite lava and its fragments of agglomerate exposed here have a dark grey or black color when undecomposed and are composed of plagioclase, augite, hypersthene, magnetite, quartz and brown glass, but they are opalized and alunitized in altered specimens.

Of these, the phenocrystic plagioclase ranges from labradorite to bytownite with a composition of An_{57-73}. It is generally euhedral or subhedral and has a rectangular form, being occasionally complicated by the predominance of a worm-eaten structure which is sometimes found in parallel with the crystal outline. The crystal is well zoned, and the largest one is 3.31 mm. long and 1.78 mm. across. In other cases, the phenocryst is partly or wholly turbid with a narrow fringe of clear zone. Its enclosures are augite and magnetite.

In the groundmass, minute lath-shaped or tabular crystals of plagioclase, 0.02 mm.–0.2 mm. in length, are more abundant than other ingredients, forming here a pilotaxtic or hyalopilitic texture. They are slightly acidic when compared with phenocrysts.

Subhedral or anhedral augite is one of main ferro-magnesian ingredients, and its phenocryst occurs almost in the same amount as that of hypersthene. When the phenocrystic augite is closely associated with hypersthene, the latter is always fringed by the former. The largest one is 1.7 mm. across. Some of it is corroded by the groundmass and twins on (101). The maximum extinction angle, $Z \wedge c$, is 42°. It encloses magnetite and plagioclase.

Long prismatic hypersthene is found as phenocryst which is commonly euhedral or subhedral. Its largest one is 2.62 mm. long and 0.68 mm. across. It contains magnetite and plagioclase, being partly

Table 3. Composition and optical characters of plagioclase, augite and hypersthene phenocrysts (measured by F. Hori).

	(T.I. 50072705)
Plagioclase	$\alpha=1.558$ (n_1 min.) $\gamma=1.575$ (n_2 max.) An_{57-73}*
Augite	$\alpha=1.692$ $\beta=1.698$ $\gamma=1.721$ $(+)2V=47°$ $Ca_{38}Mg_{38}Fe_{24}$**
Hypersthene	$\gamma=1.720$ $(-)2V=52°$ $Mg\%(2V)=53$*** $Mg\%(\gamma)=54$****

* After F. Chayes's chart.
** After H. H. Hess's chart.
*** After H. Kuno's chart.
**** After H. Kuno's chart.
The specimen was obtained on the bottom of the O-sawa.

chloritized in some specimens.

Magnetite is a common ingredient in the groundmass. It has an octahedral or granular form, 0.01 mm.–0.05 mm. in diameter. There are also skeletal crystals associated usually with augite and hypersthene. The maximum diameter of these crystals is 0.34 mm.

Besides them, the occurrence of quartz xenocrysts is known in the specimens obtained from the bottom of the O-sawa. They are generally corroded and have a rounded form.

The groundmass consists of plagioclase, augite, magnetite and brown glass. It has a pilotaxitic or hyalopilitic texture.

So far as has been confirmed in the specimens subjected to the solfataric action, there are various stages of alteration. In the beginning, the original mineral ingredients and textures are still preserved, although opalization and alunitization happened to some extent. The intensely altered specimens are, however, constructed by opalized and alunitized parts. They are almost free of such minerals as plagioclase, augite, hypersthene and magnetite which were formerly main ingredients.

(4) Nanba-zawa lavas and ejecta: Many specimens obtained by the writer are represented by hard and compact or porous types of

andesite with a dark grey or black color and porphyritic texture. In some specimens, however, they have a grayish white or white color caused by an opalization due to the solfataric action. Among them, the porous variety constructs the fragments of ejecta, as is indicated by the specimens collected from Sainokawara or elsewhere. In these cases, almost all of them are olivine two-pyroxene andesite and olivine-bearing two-pyroxene andesite which are composed of plagioclase, augite, hypersthene, olivine, magnetite, quartz, tridymite, goethite, limonite and brown glass.

One of important mineral is plagioclase which is found as phenocryst and an important ingredient in the groundmass. Its phenocryst ranges from labradorite to bytownite with a composition of An_{53-74} and takes an euhedral or subhedral form, 3.3 mm. long and 1.3 mm. across in the largest crystal. Exclusive of the specimens from the western area of Reisui-zan, the frequency of a worm-eaten structure is noticeable. It is also noteworthy that there are some turbid and well zoned phenocrysts. Moreover, augite and magnetite are frequently enclosed, being occasionally arranged in parallel with the crystal outline.

The plagioclase of the groundmass has a lath-shaped or rectangular form and is mostly 0.02 mm.–0.2 mm. in length. It is abundantly present in the groundmass of compact specimens, showing frequently a fluidal arrangement, and its amount decreases remarkably in such porous fragments of ejecta as those obtained from Atomizaka and its vicinity.

The augite phenocryst occurs nearly in the same frequency as hypersthene and takes commonly a subhedral or skeletal form, 2.04 mm. long and 0.85 mm. across in the largest one. The crystal twins on (100) or (101), and its extinction angle, $Z \wedge c$, is estimated to be 38°–40°. Some of it is corroded by the groundmass and encloses magnetite.

In the groundmass, augite has a stout prismatic or granular form, 0.02 mm.–0.08 mm. in length or diameter.

The occurrence of hypersthene is restricted to phenocryst which is found as a long prismatic crystal. When it is intergrown with the augite phenocryst, the former is always fringed by the latter. The largest crystal is 2.26 mm. long and 0.64 mm. across.

The phenocrystic olivine is present in almost all specimens, although its frequency is very low when compared with augite and hypersthene. This mineral is always anhedral and has frequently an irregular form, being sometimes surrounded by a granular aggregate of augite and having mostly a fresh appearance except some phenocrysts altered part-

Table 4. Composition and optical characters of plagioclase, augite and hypersthene phenocrysts (measured by F. Hori).

	No. 1 (T.I. 50072109)	No. 2 (T.I. 50072704)	No. 3 (T.I. 52100403)
Plagioclase	$\alpha=1.562$ (n_1 min.) $\gamma=1.575$ (n_2 max.) An_{64-73}*	$\alpha=1.560$ (n_1 min.) $\gamma=1.576$ (n_2 max.) An_{60-74}*	$\alpha=1.556$ (n_1 min.) $\gamma=1.572$ (n_2 max.) An_{53-68}*
Augite	$\alpha=1.696$ $\beta=1.702$ $\gamma=1.728$ $(+)2V=44°$ $Ca_{36}Mg_{36}Fe_{28}$**	$\alpha=1.692$ $\beta=1.696$ $\gamma=1.719$ $(+)2V=51°$ $Ca_{42}Mg_{38}Fe_{20}$**	$\alpha=1.690$ $\beta=1.697$ $\gamma=1.718$ $(+)2V=49°$ $Ca_{40}Mg_{38}Fe_{22}$**
Hypersthene	$\gamma=1.716$ $(-)2V=55°$ $Mg\%(2V)=58$*** $Mg\%(\gamma)=58$****	$\gamma=1.710$ $(-)2V=60°$ $Mg\%(2V)=64$*** $Mg\%(\gamma)=62$****	$\gamma=1.719$ $(-)2V=53°$ $Mg\%(2V)=55$*** $Mg\%(\gamma)=55$****

* After F. Chayes's chart.
** After H. H. Hess's chart.
*** After H. Kuno's chart.
**** After H. Kuno's chart.

No. 1=The Nanba-zawa lava from the northern wall of the Nanba-zawa explosion crater.

No. 2=The Nanba-zawa lava from the Sanzuno-kawa.

No. 3=The Nanba-zawa lava from the western flank of Reisui-zan.

ly to bowlingite. The crystal is also known to aggregate with augite, hypersthene and magnetite. It is 1.05 mm. in the maximum diameter and includes magnetite.

The octahedral or granular magnetite is a remarkable ingredient in the groundmass. Generally, it has a diameter of 0.01 mm.–0.03 mm. Besides this, there is a skeletal magnetite associated occasionally with the phenocrystic augite and hypersthene. Some of it occurs as a microphenocryst, 0.5 mm. in the maximum diameter.

Tridymite fills up the interstices of other ingredients in the groundmass. Its occurrence is restricted to a small extent, as is shown in the thin sections of olivine-bearing two-pyroxene andesite from near Resui-zan. Brown glass invades the phenocrystic plagioclase and hypersthene, but is nearly absent in the groundmass. Goethite is an alteration product derived from magnetite, and limonite is present to a negligible amount. Moreover, there are many specimens with basaltic or gabbroid xenoliths. They contain plagioclase, augite, hypersthene,

olivine, magnetite and brown glass.

The groundmass has a pilotaxitic or hyalopilitic texture, consisting of plagioclase, augite, magnetite, tridymite, quartz, apatite and brown glass.

(5) Jizō-san lava: This lava is somewhat different from older lavas and ejecta in the fact that it is quite free of the alteration due to the solfataric action. The specimens collected by the writer are represented by olivine two-pyroxene andesite or olivine-bearing two-pyroxene andesite which is compact or porous and remarkably porphyritic. They have a dark grey or black color, being composed of plagioclase, augite, hypersthene, olivine, magnetite, tridymite, quartz and brown glass. In some cases, the texture resembles that of andesite which constructs the summit of Kumano-dake and Nakamaru-yama.

Plagioclase is an important ingredient which takes generally an euhedral or subhedral form. The high frequency of rectangular phenocryst is a common feature in all specimens, most of them being occasionally complicated by the presence of a worm-eaten structure and turbid crystals as well as of such enclosures as augite and magnetite. Moreover, there are commonly well-zoned phenocrysts, and they are characterized by the frequent invasion of brown glass. The indices of refraction suggest that these crystals belong to labradorite—bytownite and have a composition of An_{54-77}. The largest crystal is 3.74 mm. long and 1.87 mm. across. The plagioclase of the groundmass occurs usually as the intricate swarm of minute lath-shaped crystals, mostly 0.015mm.–0.2 mm. in length. The crystal is slightly acidic when compared with phenocryst, and some of it shows a fluidal arrangement, particularly around phenocrystic ingredients. It is, however, poorly present in the glassy groundmass of the specimens obtained from the trail between the Zaō Sulphur Mine and Yokokura-yama.

Augite is similarly a common ingredient in all thin sections. The phenocryst of this mineral is sometimes more abundant than that of hypersthene or *vice versa*. The intergrowth between these two kinds of phenocrystic ferromagnesian minerals is to be seen in most thin sections in which augite passes into hypersthene inwards. Generally, the phenocrystic augite has a stout prismatic or long prismatic habit and reveals a subhedral or anhedral form, 2.55 mm. long and 1.78 mm. across in the largest one. It twins on (100) or (101), and its maximum extinction angle, $Z \wedge c$, is 42°. In this case, magnetite and plagioclase are enclosed. The minute crystals of stout prismatic or granular augite are generally present abundantly together with plagioclase and magnetite

Table 5. Composition and optical characters of plagioclase, augite and hypersthene phenocrysts (measured by F. Hori).

	No. 1. (T.I. 48092810 a)	No. 2. (T.I. 48100203)	No. 3. (T.I. 48100802)	No. 4. (T.I. 52100607)
Plagioclase	$\alpha=1.561$ (n_1 min.) $\gamma=1.575$ (n_2 max.) An_{61-73}*	$\alpha=1.557$ (n_1 min.) $\gamma=1.578$ (n_2 max.) An_{54-77}*	$\alpha=1.559$ (n_1 min.) $\gamma=1.575$ (n_2 max.) An_{59-73}*	$\alpha=1.562$ (n_1 min.) $\gamma=1.572$ (n_2 max.) An_{64-68}*
Augite	$\alpha=1.691$ $\beta=1.696$ $\gamma=1.719$ $(+)2V=51°$ $Ca_{42}Mg_{38}Fe_{20}$**	$\alpha=1.687$ $\beta=1.692$ $\gamma=1.713$ $(+)2V=48°$ $Ca_{40}Mg_{42}Fe_{18}$**	$\alpha=1.690$ $\beta=1.696$ $\gamma=1.718$ $(+)2V=50°$ $Ca_{41}Mg_{38}Fe_{21}$**	$\alpha=1.690$ $\beta=1.695$ $\gamma=1.717$ $(+)2V=48°$ $Ca_{40}Mg_{40}Fe_{20}$**
Hypersthene	$\gamma=1.715$ $(-)2V=56°$ $Mg\%(2V)=60$*** $Mg\%(\gamma)=59$****	$\gamma=1.713$ $(-)2V=56°$ $Mg\%(2V)=60$*** $Mg\%(\gamma)=60$****	$\gamma=1.715$ $(-)2V=55°$ $Mg\%(2V)=58$*** $Mg\%(\gamma)=59$****	$\gamma=1.715$ $(-)2V=58°$ $Mg\%(2V)=62$*** $Mg\%(\gamma)=59$****

* After F. Chayes's chart.
** After H. H. Hess's chart.
*** After H. Kuno's chart.
**** After H. Kuno's chart.
No. 1=Jizō-san lava from the summit of Jizō-san.
No. 2=Jizō-san lava from the Zange-zaka.
No. 3=Jizō-san lava from the southwestern flank of Jizō-san.
No. 4=Jizō-san lava from the western foot of Jizō-san.

in the groundmass where most of them are 0.02 mm.–0.08 mm. in length or diameter.

Hypersthene is always found as phenocryst with an euhedral or subhedral form. It is long prismatic or stout prismatic, being 2.12 mm. long and 0.68 mm. across in the largest crystal. It contains magnetite.

Exclusive of some specimens from near Wasagoya or elsewhere, the phenocrystic olivine is not important as in the case of augite and hypersthene. The mineral has an irregular form, 1.28 mm. in the maximum diameter. It includes magnetite and passes partly into bowlingite along its cracks. The periphery of the crystal is rarely opacitized.

Magnetite is the commonest ingredient in the groundmass where it takes an octahedral or granular form with a diameter of 0.01 mm. The skeletal crystal is also known, being closely associated with augite, hypersthene and olivine. In such a case, the largest crystal is 0.76 mm. in diameter.

The occurrence of quartz xenocryst is restricted to the several specimens from the trail between Zaō Sulphur Mine and Yokokura-yama, Zange-zaka and others. The mineral is magmatically corroded to the rounded crystal, and it is occasionally surrounded by minute augite grains. The diameter of the largest crystal is 1.1 mm.

Besides them, a minor amount of tridymite is present in the groundmass, filling up the interstices of other minerals. It seems to be almost or entirely absent in the groundmass where brown glass is predominant. Similarly, apatite is very rare. Its long prismatic crystal is 0.34 mm. in the maximum length and has a dark brown color due to decomposition. Xenoliths are scarcely contained and have a basaltic or gabbroic character, being composed of plagioclase, augite, hypersthene, magnetite, olivine, apatite and brown glass.

The groundmass has a pilotaxitic or hyalopilitic texture and is the fine aggregate of plagioclase, augite, tridymite, magnetite and brown glass.

(6) Katta-dake lava: The specimens obtained on the summit and southeastern flank of Katta-dake are olivine two-pyroxene andesite or olivine-bearing two-pyroxene andesite which is compact or porous rock with a dark grey, black or reddish color and a porphyritic texture. This lava is characterized by the coarse texture of the groundmass when compared with other lavas and andesite fragments of various ejecta, although it consists similarly of plagioclase, augite, hypersthene, olivine, magnetite, quartz, tridymite and brown glass under the microscope.

Most of phenocrystic plagioclase are represented by an euhedral or subhedral form which is 2.46 mm. long and 1.36 mm. across in the largest crystal. Some of them are subjected to the invasion of brown glass and the groundmass, resulting frequently in the formation of a worm-eaten structure. These phenocrysts are labradorite-labratownite and have a composition of An_{57-64}. In general, they have a zontal structure and turbid part. Augite and magnetite are sometimes found as their enclosures. Besides, more acidic plagioclase corresponding to labradorite is abundantly present in the groundmass where it occurs as a lath-shaped or tabular crystal, 0.02 mm.–0.2 mm. long in most cases.

The phenocrystic augite with a stout prismatic or long prismatic habit reveals nearly the same frequency as that of hypersthene. It is subhedral or anhedral and contains magnetite. Its maximum extinction angle, $Z \wedge c$, is 42° and twins occasionally on (100) or (101). In some thin sections, granular augite is intricately crowded to form the fine aggregate. Moreover, granular or stout prismatic augite is a predominant ingredient of the groundmass. They are mostly 0.02 mm.–0.08 mm. in length or diameter.

Another important ferro-magnesian mineral is indicated by hyper-

Table 6. Composition and optical characters of plagioclase, augite and hypersthene phenocrysts (measured by F. Hori).

	(T.I. 47101405)
Plagioclase	$\alpha=1.558$ (n_1 min.) $\gamma=1.571$ (n_2 max.) An_{57-64}*
Augite	$\alpha=1.693$ $\beta=1.698$ $\gamma=1.721$ $(+)2V=49°$ $Ca_{40}Mg_{37}Fe_{23}$**
Hypersthene	$\gamma=1.721$ $(-)2V=53°$ $Mg\%(2V)=55$*** $Mg\%(\gamma)=54$****

* After F. Chayes's chart.
** After H. H. Hess's chart.
*** After H. Kuno's chart.
**** After H. Kuno's chart.
The specimen was obtained on the summit of Katta-dake.

sthene whose occurrence is restricted to phenocryst. Its largest crystal with a subhedral form is 1.54 mm. long and 0.66 mm. across. The crystal is not infrequently fringed by augite and contains magnetite.

The irregular olivine crystal is always present as phenocryst and shows a high frequency, the largest one being 1.39 mm. in diameter. It encloses magnetite and passes partly into bowlingite.

The octahedral or granular magnetite scatters over the groundmass where it has a diameter of 0.02 mm.–0.08 mm. In the case of skeletal form, magnetite is larger and is 0.5 mm. in the maximum diameter.

The ingredients of minor amount are composed of quartz, tridymite and brown glass. Of these, quartz is a xenocryst, whereas tridymite is almost negligible as an interstitial mineral and the brown glass is nearly absent in phenocrystic plagioclase through which its invasion took place. The basaltic xenolith is constructed by plagioclase, augite, hypersthene and magnetite. It has a rounded form.

The groundmass is an aggregate of plagioclase, augite and magnetite as well as of tridymite. It is coarser than other andesites in its texture, but has a pilotaxitic character in the mineral arrangement.

(7) Kumano-dake lavas and ejecta: There are some different types of these lavas and andesite fragments of ejecta. They can be seen on Kumano-dake, Haizuka-yama, the wall of the Umanose explosion crater, Nakamaru-yama and others, being represented by olivine two-pyroxene andesite, olivine-bearing two-pyroxene andesite and two-pyroxene andesite.

Of these, the commonest lava is olivine two-pyroxene andesite or olivine-bearing two-pyroxene andesite which is a compact and finely porphyritic rock with a black color when undecomposed. Such a kind of andesite is mainly exposed at the uppermost course of the Happō-zawa and Wasagoya as well as Nakamaru-yama and the northern or northwestern flank of Kumano-dake. Besides them, the similar lava is highly cliffed on the northern or western side of the wall surrounding the Umanose explosion crater where it is intercalated and overlain by ejecta thickly accumulated. The lava of this place sometimes porous and a part of it has a reddish color due to reheating.

The exposures of two-pyroxene andesite are found on Haizuka-yama, Daikokuten, the eastern flank of Goshiki-dake and Nakamaru-yama. It is a compact or porous rock with a dark grey or reddish color.

In addition, the andesite fragments of ejecta have a wide range of size. They are remarkably porous and have a black color in fresh

specimens, as indicated by these obtained from the summit of Kumano-dake and Haizuka-yama or elsewhere.

These various types of Kumano-dake lavas and andesite fragments of ejecta are composed of plagioclase, augite, hypersthene, olivine, magnetite, tridymite, quartz, actinolitic mineral and brown glass.

The phenocrystic plagioclase is generally euhedral or subhedral with a rectangular form and ranges from bytownite to bytownorthite which have a composition of An_{74-84}. Microscopically, the crystal has the same features as those of the Jizō-san lava. Thus, it reveals a worm-eaten structure complicated occasionally by the enclosures of augite and magnetite. Some of phenocrystic plagioclase is partly or wholly turbid, being fringed by a narrow clear zone. The largest one is 3 mm. long and 1.53 mm. across. In the groundmass, plagioclase has a lath-shape or tabular form. Commonly, it is 0.02 mm.–0.2 mm. in length, and some of such crystals indicate a fluidal arrangement around phenocrystic minerals. When the specimens are porous andesite fragments of ejecta, the plagioclase of the groundmass is always found in a low frequency as compared with lava flows.

Augite is always an important mineral whether it occurs as phenocryst or minute ingredient of the groundmass. Mostly, its phenocryst takes a subhedral or anhedral form with a long or short prismatic habit. It contains magnetite and twins on (100) or (101), being 2.89 mm. long and 2.38 mm. across in the largest crystal. The extinction angle, $Z \wedge c$, is estimated to be 40°–42°. This mineral is stout primatic or granular in the groundmass. It is 0.01 mm.–0.08 mm. in length or diameter. The crystal is abundantly present in the groundmass except the porous andesite fragments contained in ejecta.

The long prismatic or stout prismatic hypersthene is always phenocrystic and has generally an euhedral or subhedral form, 2.38 mm. long and 0.59 mm. across in the largest crystal. Its frequency is sometimes higher than augite phenocryst, but is lower or nearly same in other cases, including magnetite and plagioclase in a minor amount. There are also some phenocrysts fringed thinly by augite.

Olivine is a common mineral ingredient with an euhedral, subhedral or anhedral form except in the specimens collected from Nakamaru-yama, Haizuka-yama, Daikokuten, etc. where it is entirely or almost absent in the lava and porous andesite fragments of ejecta. The mineral is, however, remarkably contained in the lava flows exposed on the northeastern flank of Kumano-dake and the wall of the

Table 7. Composition and optical characters of plagioclase, augite and hypersthene (measured by F. Hori).

	No. 1. (T.I. 47101508)	No. 2. (T.I. 48092804)	No. 3. (T.I. 50071801)	No. 4. (T.I. 50072103)	No. 5. (T.I. 52080303)
Plagioclase	$\alpha=1.566$ (n_1 min.) $\gamma=1.580$ (n_2 max.) An_{74-85}*	$\alpha=1.567$ (n_1 min.) $\gamma=1.580$ (n_2 max.) An_{77-85}*	$\alpha=1.569$ (n_1 min.) $\gamma=1.583$ (n_2 max.) An_{82-87}*	$\alpha=1.566$ (n_1 min.) $\gamma=1.579$ (n_2 max.) An_{74-79}*	$\alpha=1.567$ (n_1 min.) $\gamma=1.582$ (n_2 max.) An_{77-84}*
Augite	$\alpha=1.692$ $\beta=1.697$ $\gamma=1.720$ $(+)2V=46°$ $Ca_{38}Mg_{38}Fe_{24}$**	$\alpha=1.685$ $\beta=1.690$ $\gamma=1.712$ $(+)2V=49°$ $Ca_{41}Mg_{43}Fe_{16}$**	$\alpha=1.690$ $\beta=1.697$ $\gamma=1.719$ $(+)2V=49°$ $Ca_{40}Mg_{38}Fe_{22}$**	$\alpha=1.688$ $\beta=1.696$ $\gamma=1.719$ $(+)2V=47°$ $Ca_{38}Mg_{39}Fe_{23}$**	$\alpha=1.685$ $\beta=1.694$ $\gamma=1.715$ $(+)2V=48°$ $Ca_{39}Mg_{41}Fe_{20}$**
Hypersthene	$\gamma=1.712$ $(-)2V=58°$ $Mg\%(2V)=62$*** $Mg\%(\gamma)=61$****	$\gamma=1.713$ $(-)2V=58°$ $Mg\%(2V)=62$*** $Mg\%(\gamma)=60$****	$\gamma=1.716$ $(-)2V=56°$ $Mg\%(2V)=60$*** $Mg\%(\gamma)=58$****	$\gamma=1.715$ $(-)2V=54°$ $Mg\%(2V)=58$*** $Mg\%(\gamma)=59$****	$\gamma=1.709$ $-)2V=63°$ $Mg\%(2V)=68$*** $Mg\%(\gamma)=63$****

* After F. Chayes's chart.
** After H. H. Hess's chart.
*** After H. Kuno's chart.
**** After H. Kuno's chart.
No. 1=The Kumano-dake lava from the summit of Kumano-dake.
No. 2=The Kumano-dake lava from the northern flank of Kumano-dake.
No. 3=The Kumano-dake lava from the western wall of the Umanose explosion crater
No. 4=The Kumano-dake lava from the Katta-dake-Oshizu.
No. 5=The Kumano-dake lava from near the summit of Nakamaru-yama.

Umanose explosion crater of eleswhere. The crystal is sometimes surrounded by augite grains and passes frequently into bowlingite along its cracks. It encloses magnetite, and the largest crystal is 1.7 mm. in longer diameter.

Magnetite is found in high frequency, taking an octahedral or skeletal form in the groundmass or as a microphenocryst. The magnetite of the groundmass is mostly 0.01 mm.–0.05 mm. in diameter, but it is 0.88 mm. in the maximum diameter of skeletal crystal.

Tridymite is a negligible mineral filling up the interstices of other minerals in the groundmass. Quartz is a xenocryst with a rounded form and occurs in low frequency. The writer noticed this mineral only in the specimen from Benzaiten near Oshizu. Brown glass is, on the other hand, an important ingredient in the groundmass of some specimens, although its occurrence is quite unknown in others.

In the writer's thin sections, xenolith is restricted to the specimens from Benzaiten and Nakamaru-yama where the lowest part of the Kumano-dake lava is exposed. It is basaltic or gabbroic, being composed of plagioclase, augite, hypersthene, magnetite and brown glass. The groundmass is somewhat leucocratic around such xenoliths, and actinolitic mineral is rarely contained at this part.

The groundmass is constructed by plagioclase, augite, magnetite, tridymite, actionolitic mineral and brown glass. It has a pilotaxitic or hyalopilitic texture, but is sometimes porous without showing any such a texture.

(8) Goshiki-dake ejecta: The writer has already described the Goshiki-dake ejecta in his previous paper[7]. They are represented by ash, sand, lapilli and agglomerate. Of these, sand and ash are the most important ejecta which are well exposed on the cliff and summit of Goshiki-dake where they have some distinct stratification due to alternation of such varying colors as grey, brown, dark reddish brown, etc. Their mineral ingredients are composed of plagioclase, augite, hypersthene and magnetite embedded in tuffaceous substance and associated with minute fragments of two-pyroxene andesite.

Agglomerate is, on the other hand, found to a small extent, containing angular or subangular fragments of compact or porous two-pyroxene andesite, 1–1.5 cm. in diameter. These fragments have a black color and porphyritic texture. Most of them consist of plagioclase, augite, hypersthene, magnetite and brown glass. In such cases,

7) T. ICHIMURA, *Bull. Earthq. Res. Inst.*, **29** (1951), 327–339.

the phenocrystic plagioclase is labratownite—bytownite with a composition of An_{64-78} and always has a fresh appearance. The crystal is well zoned, and it is occasionally turbid, including augite, hypersthene, magnetite and irregular patches of brown glass. The largest one is 2.97 mm. long and 1.36 mm. across.

The subhedral or anhedral phenocrysts of augite and hypersthene are found in nearly same amount. In the largest crystal, the former is 1.65 mm. long and 1.61 mm. across, whereas the latter is 2.47 mm. long and 1.02 mm. across. Both the kinds of phenocrysts enclose magnetite, labradorite, bytownite and brown glass. The details of their optical properties are shown in his previous paper[8]. The groundmass is constructed by labradorite, augite, hypersthene, magnetite and brown glass which result in the formation of a pilotaxitic or hyalopilitic texture.

Besides the ejecta mentioned above, there are recent lapilli and ash. They are said to have been thrown out from Okama on February of 1895. These volcanic products are extensively distributed in the area surrounding this explosion crater. Microscopically and megascopically, the lapilli under consideration is quite similar to the O-sawa lava. It is a two-pyroxene andesite with a subangular or rounded form and has a light grey, grey or dark grey color. Under the microscope, light grey or grey colored fragments are characterized by a remarkable opalization due to the intense solfataric action, suggesting that they were derived from the O-sawa lava.

History of Volcanic Activities

The Kumano Volcano forms an important center of activity in the area which includes North Zaō and South Zaō, resting upon the eroded surface of biotite granodiorite and hornblende biotite granodiorite as well as of overlying Neogene sediments exposed largely together with plagioliparite, trachytic andesite, propylite, andesite and basalt. The activity of this volcano seems to have been repeated in concert with other parts of the Zaō Volcanoes, as is shown by their overlapping lavas and ejecta. It is also noteworthy that its volcanism often took place even in historic times.

The lavas and ejecta of the Kumano Volcano are supposed to have erupted from the pre-existing crater and Okama which are now broken

8) T. ICHIMURA, *op. cit.*, (1951), 334.

by the subsequent explosions to a large extent.

The first activity happened here is probably represented by the eruption of the Yokokura-yama lavas and ejecta or the Jigoku-zawa lavas and ejecta. The former is widely distributed on Honode-yama and Bōdaira as well as along the Zaō-gawa, whereas the latter is now exposed remarkably behind Goshiki-dake, forming here and there high cliffs which are built up of agglomerate and lapilli intercalated with lava flows. There is, however, no evidence to confirm the relationship between them. So far as is known at present, the Jigoku-zawa lavas and ejecta are partly covered by the O-sawa lava and agglomerate on the one hand and the Kumano-dake lavas and ejecta on the other.

The Yokokura-yama lavas and ejecta are, on the other hand, overlain only by the volcanic products younger than the O-sawa lava and agglomerate. It is, therefore, almost impossible to confirm whether the eruption of the Yokokura-yama lavas and ejecta are older or younger than that of the Jigoku-zawa lavas and ejecta.

The next activity is illustrated by the eruption of the O-sawa lava and agglomerate whose exposure is restricted to a small extent. It was followed by the large eruption of the Nanba-zawa lavas and ejecta supplied from the pre-existing crater. In these cases, the most noticeable feature is the alteration due to the solfataric action to which various kinds of lavas and ejecta mentioned above were subjected. Among them, the Yokokura-yama lavas and ejecta are most intensely affected, and this alteration is well to be seen along the Zaō-gawa. The volcanic products erupted subsequently from the pre-existing crater are, however, characterized by the absence of opalization or alunitization and sulphur deposits. Hence, the eruption of the Jizō-san lava, Kattadake lava and Kumano-dake lavas and ejecta as well as of the Goshiki-dake ejecta are easily distinguishable from those influenced by the solfataric action. Of these, the Jizō-san lava is believed to have poured out prior to the Katta-dake lava which was followed by the Kumanodake lavas and ejecta.

The destruction of the pre-existing crater took place with the great explosion succeeded to the eruption of the Kumano-dake lavas and ejecta. At that time, the crater was opened northeastwards, and the Kumano Volcano seems to have been lowered to the present altitute. In connection with this activity, there were also other explosions at the uppermost course of the Nanba-zawa and Zaō-gawa where semi-circular craters are still preserved at present. After these explosions, Goshiki-

dake was born within the pre-existing crater under consideration, and its ejecta were thickly accumulated to form a central cone which rests on the dissected surface of the O-sawa lava and agglomerate or the Kumano-dake lavas and ejecta. Subsequently, it was deformed by the opening of new explosion crater (Okama), and the former crater of Goshiki-dake was concealed under the loose beds of lapilli and sand ejected from Okama.

It is, however, unknown how many times the volcanic activity was repeated in the area of Goshiki-dake since its first eruption. The same may be said of the volcanic activities in historic times, because they are partly obscured by insufficient data. As to these activities, the historic records are complied by F. Ōmori[9], T. Kochibe[10] and others, showing that Goshiki-dake was, at least, active in 885, 1230, 1331–1333, 1623, 1624, 1669, 1821, 1867, 1873, 1894, 1918, 1927 and 1939. The details of such volcanisms have already been described in the writer's previous paper[11].

As can be understood from various facts mentioned above, the activities of the Kumano Volcano are very complicated when compared with other centers of the Zaō Volcanoes and have some noteworthy points different from them in those of historic times.

Summary

i) The Kumano Volcano occupies the southern half of the North Zaō, resting upon the eroded surface of such base rocks as biotite granodiorite, hornblende biotite granodiorite, Neogene sediments, biotite plagioliparite, trachytic andesite, propylite, andesite and basalt. It includes Kumano-dake, Umanose, Haizuka-yama, Saino-kawara, Jizō-san, Sanpōkōjin-san, Yokokura-yama, Honode-yama, Nakamaru-yama, Bōdaira, Resui-zan, etc., which are now dissected deeply by the Sumi-kawa, Nigori-gawa, Happō-zawa, Nanba-zawa, Sennin-zawa, Zaō-gawa and their tributaries. The highest point of this volcano is represented by the summit of Kumano-dake where it is estimated to be 1840.8 m. above the sea-level.

ii) The volcanic products exposed here are composed of the Yokokura-yama lavas and ejecta, Jigoku-zawa lavas and ejecta, O-sawa lava

9) F. ŌMORI, *Rep. Earthq. Inv. Comm.*, **86** (1918), 150–153.
10) F. ŌMORI, *Tōyōgakugeizasshi*, **35** (1918), 565–573.
10) T. KOCHIBE, *Geol. Mem. Geol. Surv.*, **1** (1896), 23–32.
11) T. ICHIMURA, *op. cit.*, (1951), 336–337.

and agglomerate, Nanba-zawa lavas and ejecta, Jizō-san lava, Katta-dake lava, Kumano-dake lavas and ejecta as well as of the Goshiki-dake ejecta. Among them, the oldest volcanic products are the Yokokura-yama lavas and ejecta or the Jigoku-zawa lavas and ejecta. These lavas and fragments in ejecta are mostly olivine two-pyroxene andesite and olivine-bearing two-pyroxene andesite, being associated with two-pyroxene andesite.

iii) It is noteworthy that the lavas and ejecta older than the Jizō-san lava were subjected here and there to the alteration due to the solfataric action which resulted in the formation of such sulphur deposits as the Zaō Mine and others. This characteristic feature seems to be an important key point in making clear the possibility of two different stages, older and younger, in the activities of the Kumano Volcano.

iv) The activities of the Kumano Volcano were repeated through pre-historic times and historic times. In the former case, they are likely to have taken place in concert with those of other parts of the Zaō Volcanoes. These evidences are proved by the frequent occurrence of lava flows and ejecta overlapped by the volcanic products supplied from the Byōbu Volcano and Ryū-zan Volcano.

v) The activities are believed to have started in the beginning of the Quaternary, and the first eruption happened probably in the pre-existing crater. Since that time, the eruption of lavas and ejecta took place successively from the same crater until it was broken by the great explosion by which the height of the Kumano-Volcano was lowered to some extent. After such a volcanic accident, Goshiki-dake was bown within this large explosion crater and rose up here as a central cone. Formerly, there was a crater somewhere near the present summit of Goshiki-dake. It erupted a large amount of ejecta from time to time, but was subsequently buried and disappeared with the accumulation of lapilli and sand ejected from Okama which was newly opened on the western flank.

vi) The activities of historic times are supposed to have mainly taken place in this new explosion crater. It is, however, obscured how many times such activities were repeated, because they are recorded only since 884. So far as is known at present, the largest volcanic activity is indicated by the explosion in 1895, when ash, lapilli and scoria were abundantly blown off northeastwards. The most recent one happened in 1939, and several fumaroles of the Jigoku-zawa (Maruyama-

zawa) and Keisei-iwa of the Zaō-gawa were formed in connection with it.

Acknowledgements

The writer wishes to offer his cordial thanks to Dr. N. Nasu, Dr. H. Tsuya and Mr. T. Watanabe who greatly facilitated his field and laboratory work. He is also deeply indebted to Mr. F. Hori for co-operation in his petrographical investigations of volcanic products collected from the Kumano Volcano. A part of the expense of this research was defrayed from the fund for Natural Science of the Ministry of Education.

---

15. 蔵王火山の地質学的研究 (第 5 報)

市　村　　毅

熊野火山は，北蔵王の南半を占めている．この火山は，熊野岳，刈田岳，地蔵山，三宝荒神山，灰塚山，中丸山，横倉山，帆出山，冷水山などを含み，熊野岳 (1840.8 m.) が，その最高峰である．これ等を構成する火山噴出物は，横倉山熔岩および抛出物，地獄沢熔岩および抛出物，御沢熔岩および集塊岩，難波沢熔岩および抛出物，地蔵山熔岩，刈田岳熔岩，熊野岳熔岩および抛出物，五色岳抛出物などにより代表され，花崗閃緑岩，新第三系，斜長石石英粗面岩，粗面岩質安山岩，プロピライト，安山岩および玄武岩からなる基盤岩の侵蝕面を被覆する．熔岩および抛出物中の岩片は，大部分が橄欖石複輝石安山岩または含橄欖石複輝石安山岩で，時に複輝石安山岩を雑えている．かかる熔岩および抛出物の噴出は，隣接する屏風火山および竜山火山の熔岩および抛出物の噴出と相呼応して行なわれたものであり，火山活動は，この場合，歴史時代におよんでいる点が蔵王火山群の他の火山と趣を異にする．ここでは，火山活動が，第四紀の初期に，横倉山熔岩および抛出物あるいは地獄沢熔岩および抛出物の噴出で始まり，五色岳抛出物の噴出で終つている．五色岳抛出物以外は，旧火口から供給されているが，地蔵山熔岩以前の噴出物は，硫気作用を受けている点に特徴を有する．熊野岳熔岩および抛出物の噴出後には，大爆発をやり，今日熊野岳，馬ノ背，刈田岳，灰塚山などにより囲まれている馬ノ背爆裂火口を生じた．そのために，旧噴火口は破壊され，爆裂火口内に，中央火口丘を出現させた．これが五色岳である，五色岳にも現在の御釜の南東方に噴火口があつて，この中央火口丘を生じたように考えられる．御釜の生成は，その後の爆発のためで，有史以後の火山活動は，ほとんど全てここで行なわれたものである．記録による有史以後の活動は，884 年から知られ，最近は，1939 年に起つている．

Fig. 3. A part of the Kumano Volcano viewed from the hill between Ogurazawa and Dorobu. 1=Kumano-dake, 2=Jizō-san, 3=Nakamaru-yama, 4=Umanose, 5=Sarukuramori-yama, 6=Zaō Sulphur Mine, 7=Zaō Sulphur Refinery.

Fig. 4. The exposure of the Jigoku-zawa lavas and ejecta viewed from the western end of Sainokawara. 1=lava flow, 2=ejecta, 3=Kumano-dake.

（震研彙報 第三十八号 図版 市村）

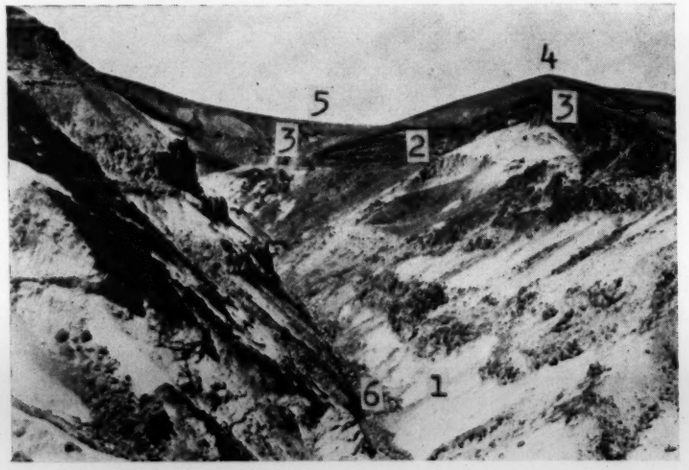

Fig. 5. The O-sawa lava and agglomerate subjected intensely to the solfataric action. 1=O-sawa lava and agglomerate, 2=Goshiki-dake ejecta, 3=Kumano-dake lava, 4=Goshiki-dake, 5=Umanose, 6=The O-sawa.

Fig. 6. Sainokawara where the Sumi-kawa lava of the Byōbu Volcano is covered by the Nanba-zawa lava and ejecta. 1=Nanba-zawa ejecta, 2=Nanba-zawa lava, 3=Katta-dake, 4=Goshiki-dake, 5=Sanzuno-kawa.

Fig. 7. Jizō-san and Sanpōkōjin-san which are built up of the Jizō-san lava. 1=Sanpōkōjin-san, 2=Jizō-san.

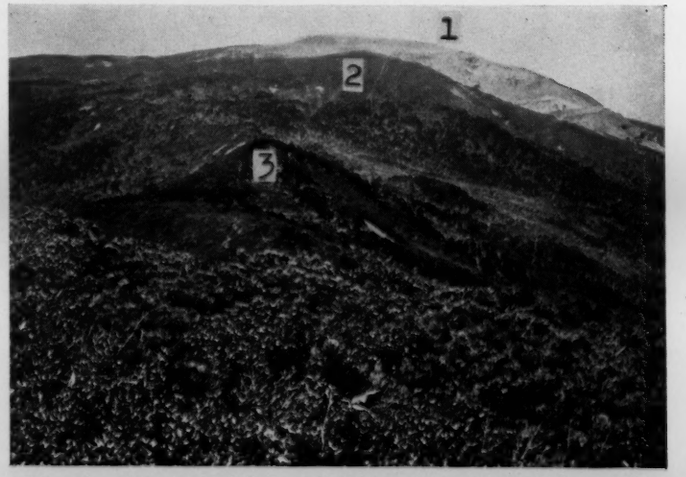

Fig. 8. Kumano-dake and Katta-dake viewed from Sugiga-mine of the Byōbu Volcano. The western side of Kumano-dake is gently sloped. 1=Kumano-dake, 2=Katta-dake, 3=Sugiga-mine-zenpō.

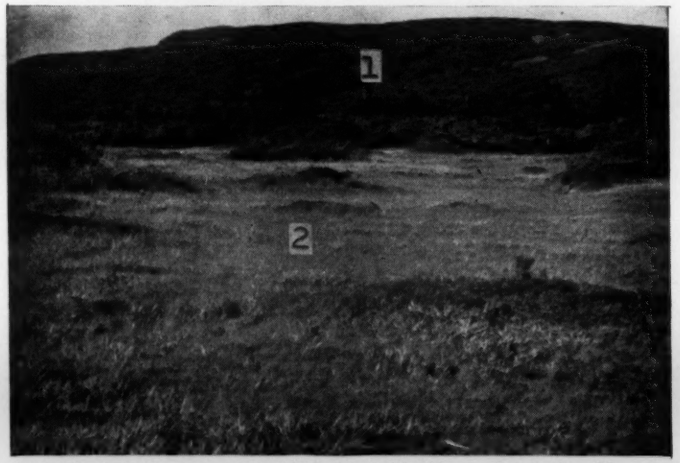

Fig. 9. A topographical feature indicated by the Kumano-dake lavas and ejecta which are exposed on the western flank of Kumano-dake. 1=Lava, 2=Ejecta.

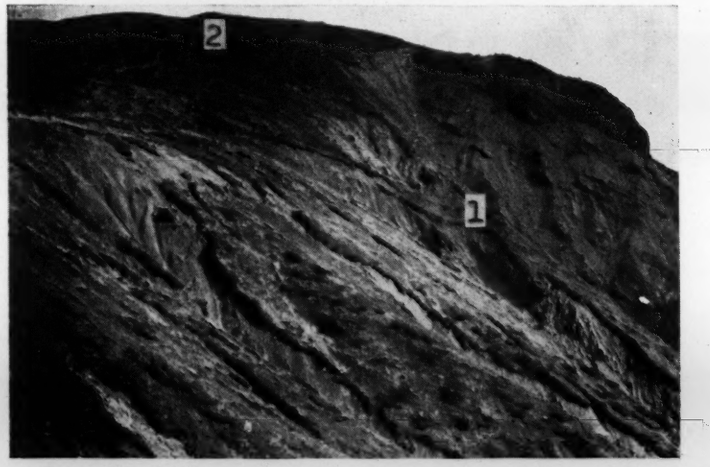

Fig. 10. The explosion crater at the source of the Zaō-gawa. 1=Crater wall, 2=Kumano-dake.

Fig. 11. The southern end of the Kumano-dake lavas and ejecta. 1=The end of lava flow at the periphery of Bōdaira, 2=Bōdaira where the Yokokura-yama ejecta are exposed, 3=Nakamaru-yama, 4=The Sennin-zawa, 5=Kumano-dake.

Fig. 12. Goshiki-dake and Okama. 1=Sand and ash, 2=Lapilli erupted in 1895, 3=Kumano-dake lavas and ejecta, 4=Goshiki-dake, 5=Okama, 6=Kumano-dake.

BULLETIN OF THE EARTHQUAKE
RESEARCH INSTITUTE
Vol. 38 (1960), pp. 291-305

16. *Composition of the Main Chemical Components in the Rocks from Hotoke-iwa Volcanic Body of Mt. Asama.*

By Eiiti MINAMI,

Earthquake Research Institute,

and Yoshito MATSUI,

Department of Chemistry, Faculty of Science,
The University of Tokyo.

(Read March 24, 1959.—Received March 23, 1960.)

1. Introduction

The Hotoke-iwa volcanic body which builds up a part of the volcano of Asama is composed of dacitic rocks including obsidian, and is in distinct contrast to the main body of Asama composed of andesitic rocks. TSUYA[1),2)] has considered the period of its activity to be between that of the old somma (Kurohu-yama) and that of the young somma (Maekake-yama). Although this volcanic body was buried almost entirely through the subsequent activities of Asama, TSUYA[2)] has suggested that the framework of present topography of the eastern part of Asama was determined by the shape of this volcanic body.

Chemical composition of the rocks of Asama volcano including Hotoke-iwa has been reported by TSUYA[1),2)] and by IWASAKI[3)]. As to the rocks of Hotoke-iwa, however, only four analyses have been made. For the consideration of the genetic relationships between the andesites of the main body of Asama and the dacites of this body, it seemed necessary to examine more samples.

In this paper, the results of analyses for main chemical components of newly collected twelve specimens and the consideration about the small compositional variation are reported. Comparison of chemical composition of these rocks with that of andesites from the main body of Asama and discussion about the relationships between these two

1) H. TSUYA, *Bull. Earthq. Res. Inst.*, **11** (1933), 575.
2) H. TSUYA, *Geography (Tirigaku)*, **2** (1934), 1265 and 1479 (in Japanese).
3) I. IWASAKI, *J. Chem. Soc. Japan, Pure Chem. Sec.*, **57** (1936), 1324 (in Japanese).

groups will be presented after the completion of analyses of andesites in the near future.

2. Specimens

Localities where specimens were collected are shown in Fig. 1. Specimens 211–215 are biotite-hornblende-bearing augite-hypersthene-dacite, and were collected at the lower cliff of Hotoke-iwa (Midagazyō-iwa) at a height of *ca.* 1900 m above the sea. Specimen 211 was taken from the exposed lowermost part of the cliff, specimen 212 at a point *ca.* 15 m above the place of 211, and so on to specimen 215 in the order of the increasing height. The last came from the middle part of the cliff. Specimens 221 and 222 are hypersthene-dacite collected near the western summit of Ko-asamayama, which has been regarded by TSUYA[1),2)] as a parastic cone of Hotoke-iwa volcanic body. Specimen 231 is hypersthene-dacite from an east-faced cliff situated *ca.* 150 m

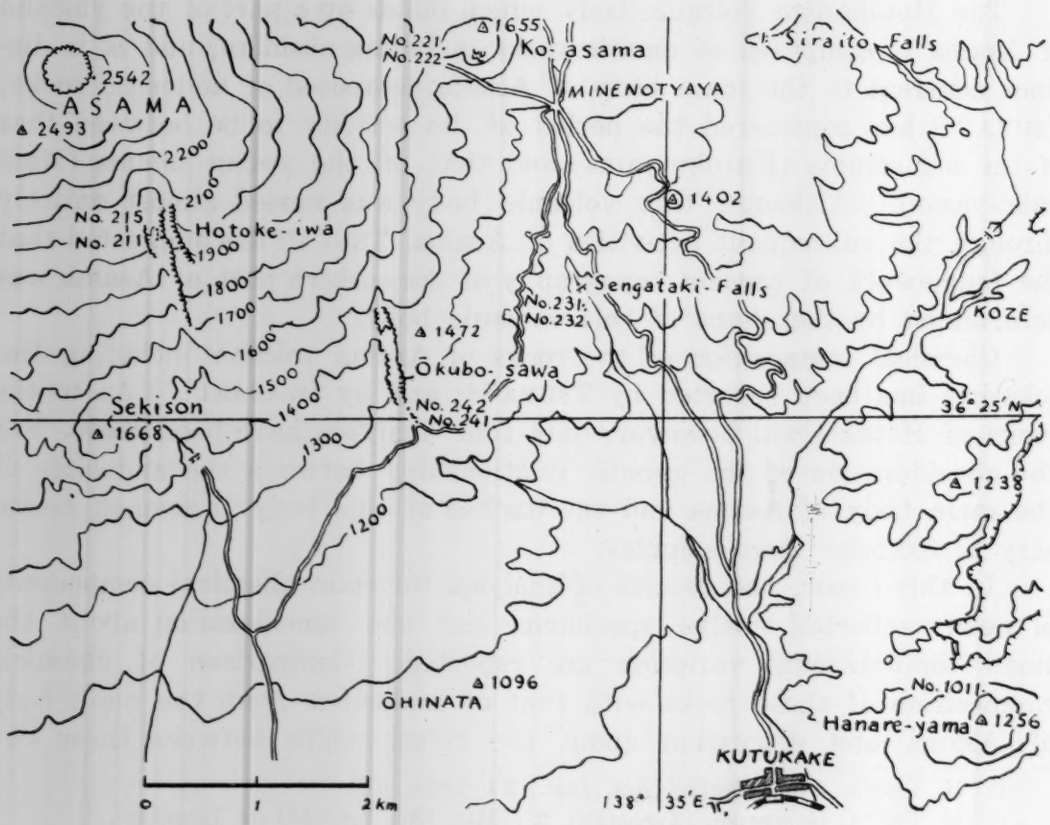

Fig. 1. Locality Map of the Specimens.

south of the Sengataki falls. In the lowermost part of this cliff, the rock, represented here by specimen 232, occurs as a kind of obsidian of hypersthene-dacite. Specimens 241 and 242A were taken from a cliff facing south-west of the dry valley of Ōkubo-sawa at a height of *ca.* 1300 m above the sea, and are obsidian of hypersthene-dacite. Specimen 242B is a globular inclusion found in specimen 242. Specimen 1011 is not of Hotoke-iwa volcanic body, but of a small volcanic body, named Hanareyama, which stands 10 km southeast of Asama, and was taken from a quarry on its northern flank. Since Hanareyama volcanic body is composed also of dacitic rocks, this specimen of augite-hypersthene-dacite was analysed for the purpose of comparison.

Features of these specimens are given in Table 1. Taking these characteristics into account, it seems to be convenient to group these rocks as follows:

Dacites of Hotoke-iwa volcanic body
- Western Dacites
- Eastern Rocks
  - Ko-asamayama Dacites } Eastern Dacites
  - Non-Ko-asama Dacites } Eastern Dacites
  - Obsidians

Table 1. Features of Specimens.

Specimen No.	Locality	Features	Phenocryst Amount*
211	Hotoke-iwa	Grey-black, with grey band.	M
212	〃	Grey-black.	M
213	〃	Grey, with grey-black band.	M
214	〃	Grey-black and dark reddish brown.	M
215	〃	Grey, with spots of black glass.	M
221	Ko-asama	Grey, without banding.	L
222	〃	Banding of grey-black and brownish grey parts.	L
231	near Sengataki	〃 〃	L
232	〃	Black obsidian.	L
241	Ōkubo-sawa	Grey-black translucent obsidian.	L
242A	〃	Black obsidian.	L
242B	〃	Included in 242A, reddish brown, with lamprophyric texture of "basic inclusion"[4].	M
1011	Hanareyama	Banding of black and grey parts.	M–A

* A: >1/3, M: 1/3~1/5, L: <1/5 of the rock.

4) H. WILLIAMS, F. J. TURNER, and C. M. GILBERT, *Petrography* (*Freeman*, 1954).

Mean modal compositions of Western Dacites and Eastern Rocks are presented in Table 2. These values are the arithmetic mean obtained by volumetry of several sections. Each specimen was represented by one section.

Table 2. Modal Compositions (in Vol. %).

	Glass	Plagioclase	Hypersthene	Augite	Iron Ore
Western Dacites	76.1	19.4	2.9	0.9	0.5
Eastern Rocks	91.3	8.0	0.5	0.1	0.3

Approximate chemical compositions of phenocryst minerals separated from the mixed powder sample of Western Dacites are given in Table 3. Composition of pyroxenes was estimated from optical characters[5], and that of plagioclase was determined by the chemical analysis of Ca, Na, and K.

Table 3. Characters of Phenocrysts of Western Dacites.

	Optical Characters*	Estimated Composition	Mode (in Wt. %)**
Plagioclase	——	$An_{55}Ab_{44}Or_1$	20.7
Hypersthene	$\alpha=1.682$, $\gamma=1.714$, $2V=(-)57°\sim60°$	$En_{62}Fs_{38}$	3.9
Augite	$\alpha=1.683$, $\gamma=1.716$, $2V=(+)51°\sim52°$	$Wo_{42}En_{41}Fs_{17}$	1.2
Iron ore	——	——	1.2

* Observed by Mr. I. KUSHIRO.
** Bulk density=2.52.

3. Analytical Methods

Chemical analysis was carried out mainly using the rapid methods described by SHAPIRO and BRANNOCK[6] and by RILEY[7]. SiO_2, TiO_2, Al_2O_3, and total Fe were determined spectrophotometrically after SHAPIRO and BRANNOCK, and MnO and P_2O_5 after RILEY. Determination of CaO[8] and MgO was made by the visual complexometric titration after the removal of Fe, Ti, and Al using urotropin[9]. Na_2O and K_2O were deter-

5) H. H. HESS, *Am. Mineralogist*, **34** (1949), 621.
6) L. SHAPIRO and W. W. BRANNOCK, *U. S. Geol. Surv. Bull.*, **1036** C (1956).
7) J. P. RILEY, *Anal. Chim. Acta*, **19** (1958), 413.
8) J. PATTON and W. REEDER, *Anal. Chem.*, **28** (1956), 1026.
9) V. PATROVSKÝ and M. HUKA, *Collection Czechoslov. Chem. Communs.*, **21** (1956), 866.

mined by the flame photometric method. Loss on ignition was substituted for H_2O content, correction being made for the oxidation of ferrous iron. FeO was determined after conventional method.

4. Results of Analyses

In Table 4 are given results of chemical analyses. Variation dia-

Table 4. Chemical Compositions of Specimens.

Specimen	211	212	213	214	215	221
SiO_2	69.3	70.0	69.4	69.3	68.8	73.1
TiO_2	0.62	0.58	0.60	0.71	0.66	0.49
Al_2O_3	15.1	15.1	15.0	15.0	15.7	14.3
Fe_2O_3	1.57	1.09	1.39	1.43	2.18	0.97
FeO	1.63	1.71	1.56	1.77	1.08	1.24
MnO	0.06	0.06	0.07	0.06	0.06	0.06
MgO	0.98	0.90	0.73	0.95	1.08	0.80
CaO	3.63	3.33	3.51	3.54	3.86	2.31
Na_2O	3.98	3.94	4.07	4.28	3.90	4.12
K_2O	1.83	1.78	1.88	2.13	1.85	2.06
H_2O	0.64	0.60	0.61	0.66	0.87	0.57
P_2O_5	0.12	0.12	0.12	0.14	0.13	0.03
Sum	99.5	99.2	98.9	100.0	100.2	100.1
Fe°*	3.38	3.01	3.12	3.38	3.44	2.37
Q	29.7	31.4	29.8	27.3	29.5	34.8
C	0.2	0.9	0.2	—	0.6	1.1
Or	10.8	10.5	11.1	12.6	10.9	12.1
Ab	33.7	33.3	33.4	36.2	33.0	34.9
An	17.3	15.7	16.6	15.4	18.3	11.3
Wo	—	—	—	0.52	—	—
En	2.44	2.25	1.82	2.37	2.69	1.99
Fs	0.78	1.39	0.86	0.99	—	0.78
Mt	2.27	1.58	2.01	2.08	1.78	1.41
Hm	—	—	—	—	0.94	—
Il	1.18	1.10	1.14	1.35	1.26	0.93
Ap	0.28	0.28	0.28	0.32	0.30	0.07
SI**[10]	9.6	9.4	7.4	8.3	10.5	8.6

* Total Fe as Fe_2O_3. ** $MgO \times 100/Fe° + MgO + Na_2O + K_2O$. (to be continued)

10) H. KUNO, *Volcanoes and Volcanic Rocks* (Iwanami, 1953, in Japanese), p. 178.

(continued)

Specimen	222	231	232	241	242A	242B	1011
SiO_2	72.9	73.0	72.7	73.7	73.0	58.9	68.2
TiO_2	0.48	0.53	0.51	0.47	0.47	0.94	0.68
Al_2O_3	14.3	14.2	14.3	14.2	14.1	16.8	15.5
Fe_2O_3	1.81	1.42	0.42	0.39	0.65	4.62	1.37
FeO	0.57	0.97	1.79	1.62	1.58	2.46	2.11
MnO	0.06	0.06	0.06	0.06	0.06	0.10	0.07
MgO	0.72	0.64	0.60	0.63	0.58	3.48	1.34
CaO	2.53	2.62	2.80	2.49	2.59	7.49	4.38
Na_2O	4.12	4.32	4.19	4.47	4.12	2.97	3.75
K_2O	2.04	2.33	2.33	2.30	2.07	1.00	1.70
H_2O	0.55	0.30	0.38	0.42	0.37	1.14	0.56
P_2O_5	0.08	0.08	0.09	0.09	0.09	0.17	0.12
Sum	100.2	100.5	100.2	100.8	99.7	100.1	99.8
Fe°	2.45	2.50	2.39	2.19	2.38	7.55	3.75
Q	35.0	32.6	31.7	31.9	34.1	18.4	28.1
C	0.9	—	—	0.0	0.6	—	—
Or	12.0	13.8	13.8	13.6	12.2	5.9	10.0
Ab	34.9	36.5	35.4	37.8	34.9	25.1	31.7
An	12.0	12.4	13.3	11.8	12.3	29.6	20.4
Wo	—	0.05	0.01	—	—	2.68	0.21
En	1.80	1.60	1.50	1.57	1.45	8.68	3 34
Fs	—	—	2.20	2.02	1.69	—	1.75
Mt	0.63	1.78	0.60	0.56	0.95	5.51	1.99
Hm	1.37	0.19	—	—	—	0.81	—
Il	0.91	1.00	0.97	0.90	0.90	1.79	1 29
Ap	0.18	0.18	0.20	0.20	0.20	0.39	0.28
SI	7.8	6.5	6.3	6.6	6.2	23.2	12.7

gram prepared from these data is shown as Fig. 2. Mean composition of each group of rocks is presented in Table 5.

5. Discussion

i) *Relation between Chemical Composition and Macroscopic Feature of Rocks.*

As may be recognized from Tables 1, 4, and 5, or Fig. 2, there seems to be no systematic difference in chemical composition between

Table 5. Mean Composition of Each Group of Rocks.

Group	I	II	III	IV	V	VI
SiO_2	69.4	73.1	73.0	73.1	73.0	73.1
TiO_2	0.63	0.49	0.50	0.48	0.49	0.50
Al_2O_3	15.2	14.3	14.3	14.2	14.3	14.2
Fe_2O_3	1.53	0.95	1.40	0.49	1.39	0.72
FeO	1.55	1.30	0.93	1.66	0.91	1.49
MnO	0.06	0.06	0.06	0.06	0.06	0.06
MgO	0.93	0.66	0.72	0.60	0.76	0.61
CaO	3.57	2.51	2.49	2.62	2.42	2.63
Na_2O	4.03	4.23	4.19	4.26	4.12	4.28
K_2O	1.89	2.19	2.14	2.23	2.05	2.26
H_2O	0.68	0.43	0.47	0.39	0.56	0.37
P_2O_5	0.13	0.08	0.06	0.09	0.06	0.09
Sum	99.6	100.3	100.3	100.2	100.1	100.3
Fe°	3.27	2.38	2.44	2.32	2.41	2.37

I: Western Dacites. III: Eastern Dacites. V: Ko-asama Dacites.
II: Eastern Rocks. IV: Eastern Obsidians. VI: Non-Ko-asama Rocks.

obsidians and non-obsidians in Eastern Rocks, and also between grey rocks and grey-black rocks in Western Dacites.

ii) *Comparison of Chemical Composition of Western Dacites and Eastern Rocks.*

It is noted from the results given in Tables 4 and 5 that there is some variation in chemical composition among specimens. Especially the difference between Western Dacites and Eastern Rocks is fairly marked.

To interpret this difference as a function of the content of phenocryst minerals, the mean composition of groundmass of Western Dacites is estimated for seven components, *i.e.*, SiO_2, Al_2O_3, total Fe as Fe_2O_3, MgO, CaO, Na_2O, and K_2O, TiO_2 being added to total Fe.

Comparing this estimated groundmass composition and the bulk composition of Western Dacites with the bulk composition of Eastern Rocks, it appears likely that the composition of the last one is given by mixing the former two (Table 6, and Fig. 3). On the other hand, the trial to explain the composition of Western Dacites as the mixture of Eastern Rocks and the basic inclusion (specimen 242B) was less successful (Fig. 4).

iii) *Interpretation of Compositional Variation among Specimens.* Even in a single group of rocks, some heterogeneity is observed. If one tries to explain this heterogeneity by the difference in the contents of phenocryst minerals, it becomes necessary to vary the relative contents of these minerals. Such a system is too complicated to be analysed graphically. Therefore, another method must be considered.

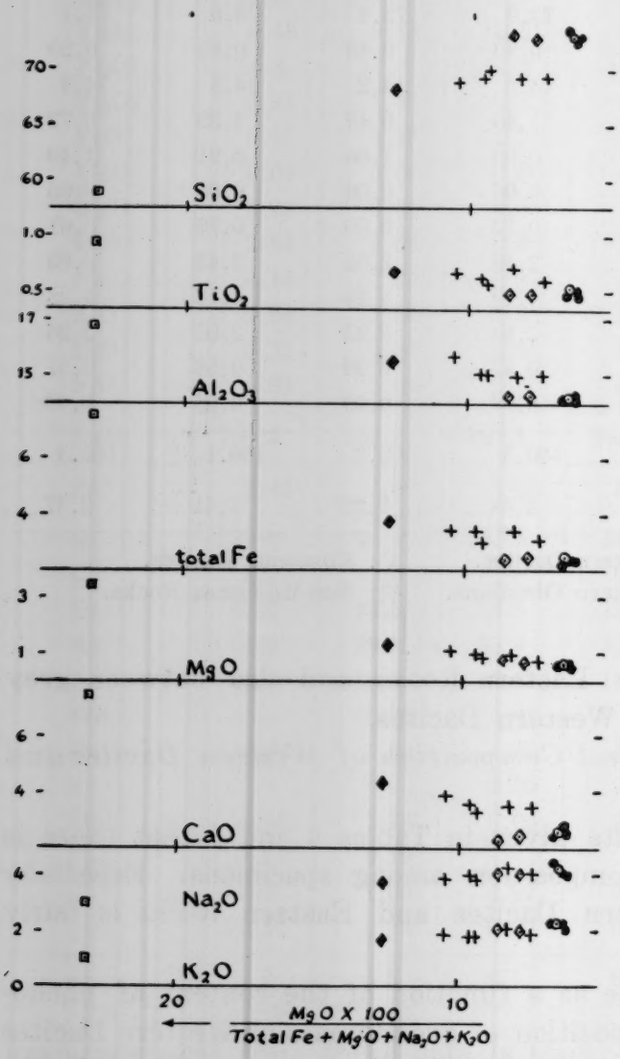

Fig. 2. Variation Diagram.

The phenocryst minerals found in Hotoke-iwa rocks are plagioclase, hypersthene, augite, magnetite, ilmenite, biotite, and hornblende. The last two are found only in minute quantities, and can left out of consideration. Combining magnetite and ilmenite as iron ore, assuming the ratio of augite to hypersthene to be constant, and considering the variation in chemical composition of plagioclase caused by its zonal structure, we have five independent end members, namely, the groundmass of Western Dacites, anorthite, albite (containing a small amount of orthoclase), pyroxene, and iron ore. Now let us examine whether chemical composition of each rock can be explained by the linear combination of those of the above-mentioned five end members (Table 7, system I). Least squares method is employed with the weight factors proportional to the reliabilities of chemical analyses for individual com-

Table 6. Compositions reduced to Seven Components.

	SiO_2	Al_2O_3	Fe_2O_3*	MgO	CaO	Na_2O	K_2O	Sum
I	51.6	22.8	8.36	3.54	9.75	3.96	0.08	100.0
II	70.2	15.4	3.94	0.94	3.61	4.08	1.91	100.0
III	73.2	14.3	2.88	0.66	2.56	4.23	2.20	100.0
IV	76.9	12.7	2.34	0.00	1.39	4.12	2.57	100.0

* including TiO_2.

I: Western Dacites, Phenocryst (estimated). II: Western Dacites, Bulk. III: Eastern Rocks, Bulk. IV: Western Dacites, Groundmass (calculated).

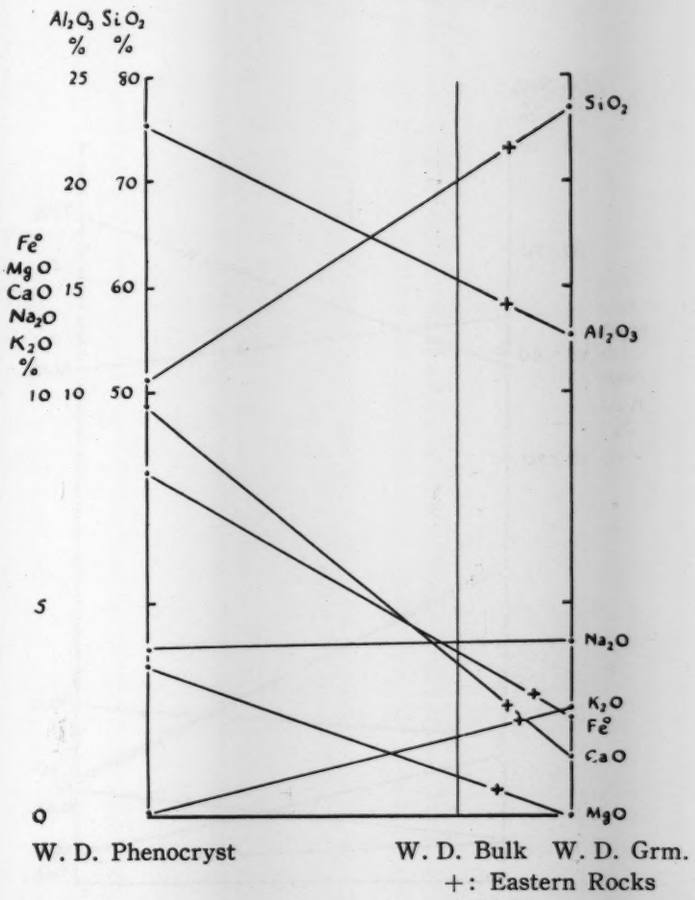

Fig. 3. Mixing Diagram of the system W. D. Phenocryst-W. D. Groundmass.

ponents. Use of this method makes it possible to take the probable analytical error into consideration, this being an important advantage over usual addition-subtraction method.

A set of the contents of the above-mentioned seven (in general, n) components for an individual specimen is regarded here as a vector matrix, **F**. Let us consider the linear combination of the contents of appropriately assumed end members $\mathbf{F}^1$, $\mathbf{F}^2$, $\cdots$, $\mathbf{F}^m$ (in our case, $m=5$):

$$\mathbf{F}^\circ = \mathbf{F}^1 x_1 + \mathbf{F}^2 x_2 + \cdots + \mathbf{F}^m x_m \,, \qquad \cdots(1)$$

here m must be smaller than $n-1$, n being number of components, since $\sum f_j \equiv 100$.

Introducing the 7×7 (in general, $n\times n$) diagonal matrix **P** of the weight factor p_{jj} which is inversely proportional to the square of the standard deviation for each component if available, or its estimated one

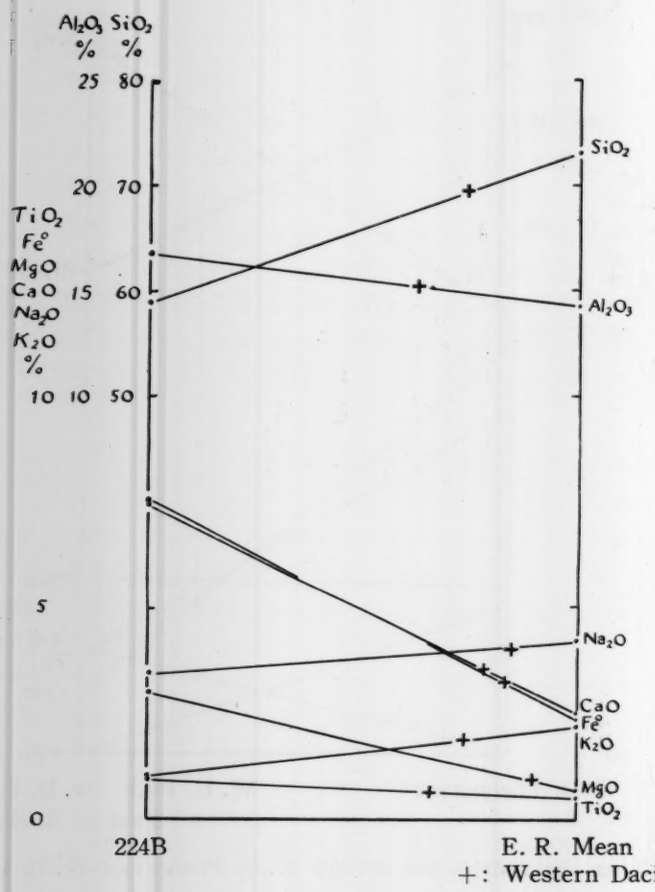

Fig. 4. Mixing Diagram of the system Basic Inclusion-Eastern Rocks.

(called here "reliability"), values of x_1, x_2, $\cdots$, x_m are calculated as they minimize the quantity,

$$\Delta^2=(\mathbf{F}-\mathbf{F}^\circ)^*\,\mathbf{P}\,(\mathbf{F}-\mathbf{F}^\circ)\,, \qquad \cdots(2)$$

where $(\mathbf{F}-\mathbf{F}^\circ)^*$ denotes the transpose of $(\mathbf{F}-\mathbf{F}^\circ)$. This criterion of weighted least squares is equivalent to

$$\mathbf{A}\,\mathbf{P}\,(\mathbf{F}-\mathbf{F}^\circ)=0\,, \qquad \cdots(3)$$

where $\mathbf{A}$ is a 5×7 (in general, $m\times n$) matrix and $a_{ij}=\partial f_j^\circ/\partial x_i=f_j^i$, *i.e.*, a_{ij} is equal to the content of j-th component in i-th end member, f_j^i. Then equation (1) is written as

$$\mathbf{F}^\circ=\mathbf{A}^*\,\mathbf{X}\,, \qquad \cdots(4)$$

where $\mathbf{X}$ is a vector matrix of $x_1, x_2, \cdots, x_m$, and we obtain the normal equations (5) by the substitution of (4) for (3) as follows:

$$\mathbf{A}\,\mathbf{P}\,\mathbf{A}^*\,\mathbf{X}=\mathbf{A}\,\mathbf{P}\,\mathbf{F}\,. \qquad \cdots(5)$$

Solution of (5) gives a $\mathbf{X}$ vector, in which x_i is the estimated fraction of i-th end member in the vector $\mathbf{F}^\circ$; and $\mathbf{F}^\circ$ can be calculated after (4).

Results of these calculations are given in Table 8. Since iron ore is chosen as one of the end members, $f^\circ_{Fe_2O_3}$ should be equal to $f^\circ_{Fe_2O_3}$, *i.e.*, the calculated and the observed contents of Fe_2O_3 agree necessarily. Therefore, this serves only as a check of calculation.

Table 7. Compositions of End Members and Estimated Reliability for Each Component

End Members	SiO_2	Al_2O_3	Fe_2O_3	MgO	CaO	Na_2O	K_2O	Sum	System I	System II
Ground-mass	76.9	12.7	2.34	0.0	1.39	4.12	2.57	100.0	*	*
Albite	68.7	19.4	0.0	0.0	0.0	11.65	0.24	100.0	*	
Anorthite	43.2	36.6	0.0	0.0	20.2	0.0	0.0	100.0	*	
Pyroxene	52.2	0.0	22.9	20.0	4.90	0.0	0.0	100.0	*	*
Iron ore	0.0	0.0	100.0	0.0	0.0	0.0	0.0	100.0	*	*
$Or_{30}Ab_{70}$	67.5	19.1	0.0	0.0	0.0	8.3	5.1	100.0		*
$Ab_{43}An_{57}$	54.3	29.1	0.0	0.0	11.5	5.1	0.0	100.0		*
Reliabilities	0.3	0.2	0.03	0.04	0.03	0.04	0.04			

Table 8. Results of the Least Squares Approximation.

	f_j							Sum	x_i†				
	SiO_2	Al_2O_3	Fe_2O_3	MgO	CaO	Na_2O	K_2O		G	F(1)	F(2)	P	O
211 F	70.0	15.3	4.05	0.99	3.67	4.03	1.85	100.0					
F°(I)	70.0	15.4	4.05	1.00	3.66	4.04	1.90	100.0	73.0	8.86	11.96	4.98	1.20
212 F	71.0	15.3	3.64	0.91	3.38	4.00	1.80	100.0					
F°(I)	70.6	15.0	3.63	0.92	3.41	4.06	1.97	99.6	75.5	8.14	10.52	4.60	0.82
213 F	70.6	15.3	3.78	0.74	3.57	4.14	1.91	100.0					
F°(I)	70.5	15.5	3.78	0.75	3.56	4.13	1.93	100.1	74.4	9.21	11.64	3.74	1.18
214 F	69.8	15.1	4.12	0.96	3.56	4.31	2.14	100.0					
F°(I)	70.5	15.5	4.12	0.94	3.53	4.22	1.90	100.6	72.6	10.58	11.37	4.71	1.34
215 F	69.3	15.8	4.13	1.09	3.89	3.93	1.86	100.0					
F°(I)	69.4	15.6	4.12	1.08	3.90	3.95	1.86	99.8	71.5	8.55	13.09	5.42	1.21
221 F	73.4	14.4	2.87	0.80	2.32	4.14	2.07	100.0					
F°(I)	73.2	13.7	2.87	0.78	2.35	4.20	2.18	99.3	84.1	6.35	4.91	3.91	−0.01
F°(II)	73.3	13.7	2.87	0.78	2.38	4.09	2.27	99.4	85.1	1.71	8.73	3.89	−0.01
222 F	73.2	14.4	2.94	0.72	2.54	4.14	2.05	100.0					
F°(I)	73.0	14.1	2.93	0.72	2.56	4.19	2.16	99.6	83.2	6.50	6.08	3.61	0.16
F°(II)	73.1	14.0	2.94	0.71	2.58	4.09	2.21	99.7	84.6	0.72	10.70	3.53	0.15
231 F	73.0	14.2	3.02	0.64	2.61	4.31	2.33	100.0					
F°(I)	73.4	14.3	3.01	0.62	2.59	4.26	2.16	100.3	83.4	7.05	6.37	3.12	0.35
F°(II)	72.9	14.5	3.02	0.65	2.60	4.30	2.31	100.2	80.2	4.90	11.53	3.23	0.41

(to be continued)

(continued)

	f_j							Sum	x_i†				
	SiO_2	Al_2O_3	Fe_2O_3	MgO	CaO	Na_2O	K_2O		G	F(1)	F(2)	P	O
232 F	72.9	14.3	2.90	0.60	2.80	4.20	2.34	100.0					
F°(I)	73.3	14.5	2.90	0.59	2.78	4.14	2.17	100.4	84.0	5.87	7.30	2.93	0.26
F°(II)	72.9	14.6	2.90	0.61	2.77	4.23	2.22	100.3	81.2	2.75	12.99	3.05	0.30
241 F	73.4	14.1	2.65	0.63	2.48	4.45	2.29	100.0					
F°(I)	73.8	14.3	2.65	0.62	2.47	4.40	2.16	100.3	83.1	8.41	5.74	3.10	0.00
F°(II)	73.3	14.5	2.65	0.63	2.48	4.37	2.38	100.0	80.2	6.34	10.55	3.10	0.05
242A F	73.5	14.2	2.87	0.58	2.61	4.15	2.09	100.0					
F°(I)	73.2	14.3	2.87	0.59	2.61	4.17	2.18	99.9	84.3	6.02	6.44	2.95	0.22
F°(II)	73.4	14.1	2.87	0.57	2.63	4.10	2.20	100.3	85.7	−0.11	11.28	2.87	0.21
Eastern Rocks, Mean F	73.2	14.3	2.88	0.66	2.56	4.23	2.20	100.0					
F°(I)	73.3	14.2	2.88	0.65	2.56	4.23	2.17	100.0	83.7	6.66	6.14	3.27	0.17
F°(II)	73.2	14.2	2.88	0.66	2.57	4.20	2.27	100.0	82.8	2.74	10.96	3.28	0.19
242B F	59.4	17.0	8.56	3.51	7.56	3.00	1.01	100.0					
F°(I)	59.2	18.2	8.56	3.53	7.52	2.93	0.99	101.0	37.3	12.00	30.41	17.67	3.64
1011 F	68.7	15.6	4.46	1.35	4.41	3.78	1.71	100.0					
F°(I)	68.5	16.0	4.46	1.37	4.39	3.78	1.78	100.2	68.3	8.29	15.46	6.83	1.30

† G: Groundmass, F(1): {Ab (System I) / $Or_{30}Ab_{70}$ (System II)}, F(2): {An (System I) / $Ab_{43}An_{57}$ (System II)}, P: Pyroxene, O: Iron ore.

Fairly good agreement is obtained between the calculated and the observed values for the rocks of Western Dacite group, as expected from the fact that the assumed end members are all taken from this group. Some discrepancies found in specimens 212 and 214 may be attributed to the anomaly in the contents of Al_2O_3 and K_2O.

Circumstances are different in the rocks of the Eastern Group: first, although the agreement in the mean composition of this group is quite remarkable, the calculated content of each end member differs considerably from its modal content (cf. Table 2); secondly, no good agreement for each specimen is obtained. These facts may imply that the relation of the two groups is not a straight one, but a parallel one, even if they have a certain genetic familiality.

In the course of crystallization, feldspar in these acidic rocks may be expected to take a little more potassium and this may cause the discrepancy as observed here. Therefore, another system of approximation was attempted (Table 7, system II). Instead of An-Ab combination, $Ab_{43}An_{57}$-$Or_{30}Ab_{70}$ combination is assumed in this system. (Phenocryst feldspar of Western Dacite lies also upon this line.) Results of calculation are given in Table 8 together with those of system I. General agreement is rather similar to that in the former system, besides against expectations, still poor in Al_2O_3 and K_2O. Thus the definite explanation as to the compositional variation is still difficult, especially in the rocks of Eastern Group.

It is interesting to note that close approximation is achieved for the rocks having no apparent relation to the Hotoke-iwa rocks, namely specimens 242B and 1011. For specimen 242B, however, some discrepancy in Al_2O_3 content is noticeable, as expected also from the normative composition.

Further investigations are needed on these points as well as on the problem of relationships among various rocks of Asama.

6. Conclusion

The rocks of Hotoke-iwa volcanic body can be divided into two groups. There is some variation in chemical composition even among the rocks of each group, and this variation can be, at least partially, explained by the variation of the content of phenocryst minerals in these rocks. The two groups of rocks may not be directly related, *i.e.*, these rocks might have traced a somewhat different course of differentiation from each other.

Acknowledgement

The authors wish to express their sincere thanks to Prof. H. TSUYA, Mr. T. WATANABE, and Dr. J. OSSAKA of this Institute, and to Assist. Prof. H. MINATO, College of General Education, for their support and advice.

The assistance of Mr. T. IIJIMA, Department of Chemistry, Faculty of Science, in carrying out the calculation using a parametron computor, PC-1, of Laboratory of Prof. H. TAKAHASI, Department of Physics, and that of Mr. I. KUSHIRO, Institute of Geology, in the microscopical observation, are also gratefully appreciated.

---

16. 浅間山仏岩火山体岩石の主化学成分組成

地震研究所 南 英一
東京大学理学部化学教室 松井義人

浅間山仏岩火山体の石英安山岩類（黒曜岩を含む）につき 12 個の試料を採集し，これを迅速法によつて分析した．その結果，この火山体の岩石に 2 つのグループが区別されたが，岩石の外見的特徴と化学組成との間には，直接的な関係は認められない．

各試料の間にみられる組成の相違を説明するために，適当に見積もられた組成をもつ 5 個の end member の一次結合で分析値を近似する試みを，最小自乗法によつて行なつた．その結果，この相違の少くともある部分は，斑晶鉱物の量の差に由来するとして説明が可能である．

Bulletin of the Earthquake
Research Institute
Vol. 38 (1960). pp. 307-315

17. *Pyroclastic Deposits distributed on the East Foot of Volcano Myôkô.*

By Isamu Murai,

Earthquake Research Institute.

(Read Feb. 23, 1960.—Received March 31, 1960.)

Introduction

Volcano Myôkô is situated in the southern part of Niigata Prefecture, in Central Japan. There is no historic record of its eruptive activity. It is a double volcano consisting of a large central dome and a somma. Fumaroles and hot springs are found on the foot of the central dome. The eastern rim of the somma is eroded deeply by a barranco. A thick bed of pyroclastic deposits occupies the barranco and spreads out extensively at the east foot of the somma, forming a vast flat plane. The writer has studied these pyroclastic deposits and obtained several new data on the nature and the origin of them, which are presented in this paper with the results of the mechanical analyses of the deposits.

The writer wishes to express his great gratitude to Professor Hiromichi Tsuya of the Earthquake Research Institute, Tokyo Univ., for his invaluable advice and encouragement. He is indebted to Mr. Ichirô Uehara of the Myôkô Sightseeing and Development Co. Ltd., and the employees of the Sekiyama Sport Hotel, for giving many facilities to his field study. He is also indebted to Mr. Yoshichi Hosoya of the Komoro Branch of the Earthquake Research Institute, for his aid in carrying out the mechanical analyses as well as for preparation of figures in this paper.

General Structure of the Volcano

Volcano Myôkô was constructed on a foundation of Tertiary formations, which are distributed on the floor of the barranco and develop on the north-east foot of the somma. The somma is composed mainly of repeated layers of lava flows of two-pyroxene-andesite. The uppermost layers of the somma consist of lava flows of olivine-bearing two-pyroxene-andesite and hornblende-pyroxene-andesite. The central lava dome, con-

sisting of quartz-olivine-bearing augite-hypersthene-andesite, develops in the caldera, the major and the minor diameter of which are 2.7 km from north to south and 2 km from east to west respectively. The eastern part of the central dome is partly destroyed, perhaps by a side-explosion. The eastern and the southern rim of the caldera are cut by barrancos, forming the deep valleys of Kita-jigoku-dani and Ôtagiri-gawa, and Minami-jigoku-dani and Shirotagiri-gawa respectively (Fig. 5). A thick bed of pyroclastic deposits dealt with in this paper develops in the eastern barranco and on the eastern skirt of the somma. The latest lava flow of hornblende-augite-hypersthene-olivine-andesite effused from the foot of the central dome and flowed into the eastern barranco.

Pyroclastic Deposits distributed on the East Foot of the Volcano

On the foot of the central dome and in the eastern barranco a thick bed of pyroclastic deposits, composed of porous lava blocks of hornblende-hypersthene-andesite and their fragments, is found under the latest lava flow of the central dome. The same bed is also distributed extensively on the east foot of the volcano, overlying the lava flows of the somma and the foundation of Tertiary formations (Fig. 1). The eastern border of its distribution lies along the course of the Seki-gawa. The flat surface of the deposits is dissected by U-shaped valleys, on the walls of which the vertical sections of the bed are exposed (Figs. 6, 7 and 8). The thickness of the bed is 50 m or more, and the area of its distribution is about 23 km^2. So the volume of the deposits is culculated at about 1.2 km^3. There is no remarkable stratification in the bed, although layering of large blocks is sometimes found in the middle and upper parts. An ash layer of about 1 m thickness is found in the upper part of the bed in the vicinity of the central dome (Fig. 9). Natural charcoal is contained in the pyroclastic deposits, showing that these pyroclastic materials were very hot when they were deposited (Fig. 10). The lava blocks in the deposits are fairly porous, and their density is within a range of 1.2 to 1.9 (1.6 on the average). The matrix of the deposits consists of lava fragments, mineral grains (mainly plagioclase, hornblende and hypersthene) and glass fragments.

The pyroclastic deposits concerned here have been formerly considered as mud-flow deposits caused by collapse of the eastearn part of the central dome[1]. They are more or less similar in features to mud-flow

1) N. YAMAZAKI, *Report, Earthq. Inv. Comm.* **8** (1896), 48-49. (in Japanese).

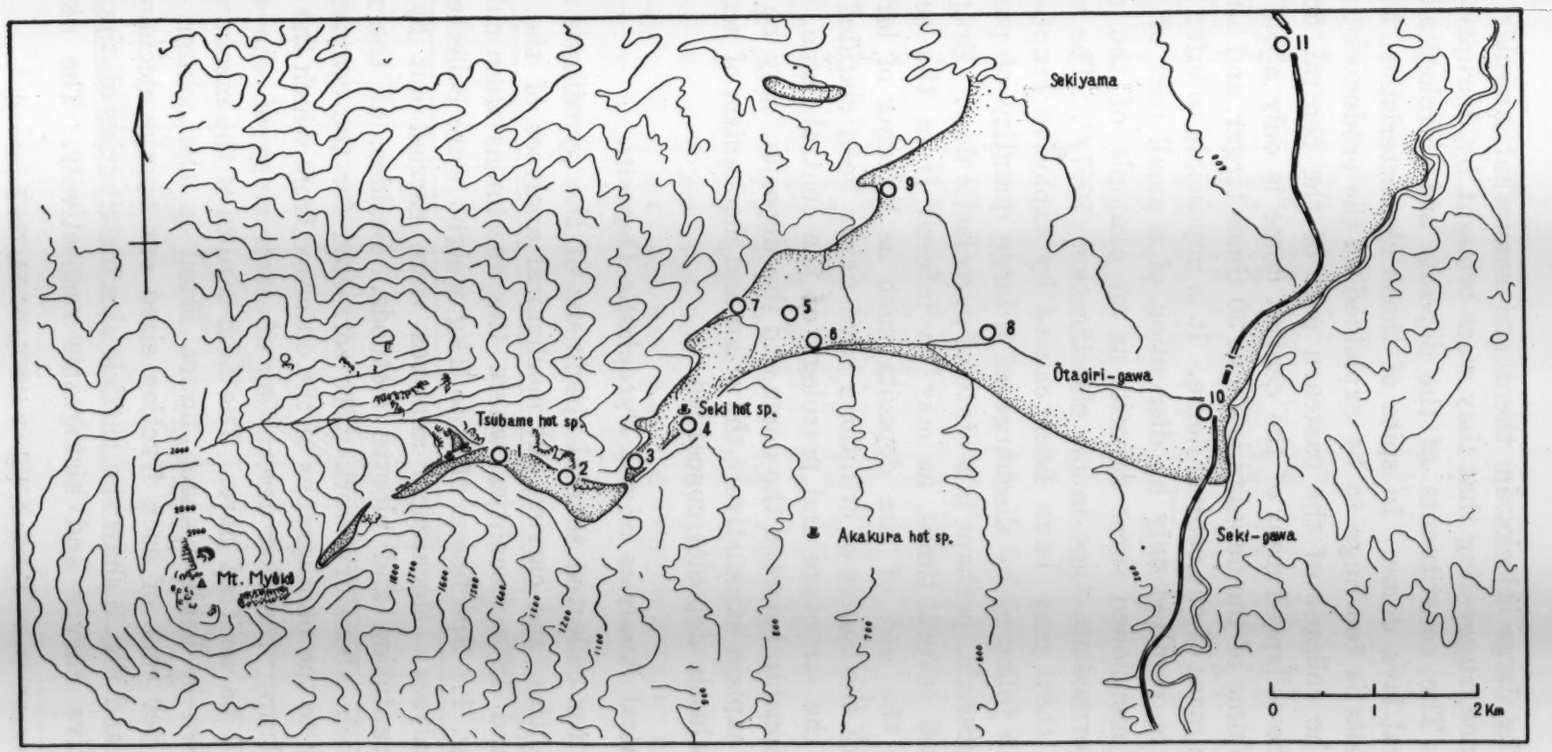

Fig. 1. Map of the eastern part of Volcano Myôkô, showing the distribution of the phyroclastic deposits and the localities of specimens collected for mechanical analyses.

deposits. The large blocks in them are somewhat angular and have faceted surface, suggesting that they were brought by disruption of solid rock mass. The constituents of the deposits are petrologically similar to the central lava dome. In spite of these characteristics, the volume of the deposits is too huge to be explained as the products of mud-flows caused by the collapse of the eastearn part of the central dome. The volume of the collapsed mass of the central dome is only about 0.03 km^3, while the volume of the deposits is about 30 times larger, and almost equal to the whole mass of the central dome. It is impossible to infer that these deposits were resulted only by disruption of a small part of the dome. S. Aramaki mentioned these deposits as an example of the pyroclastic flows of intermediate type in his classification (1957)[2]. The writer considers that they may have been caused by explosive eruptions of the central dome followed by discharge of a large quantity of porous fragmentary materials, perhaps in a state of pyroclastic flow. Eruptions may have occurred several times, as may be infered from the sedimentary features in the bed of the deposits such as layering of large blocks. The details of the course of eruptions have never been clarified. Careful studies on the structure and petrology of the central dome, as well as on the relationship between the dome and the deposits, may be necessary in order to explain exhaustively the orign and mechanism of accumulation of the pyroclastic deposits concerned.

Mechanical Analyses of the Pyroclastic Deposits.

The writer collected several specimens of the pyroclastic deposits in various localities, and carried out mechanical analyses of the specimens (Figs. 11 and 12). Localities where the specimens were collected are shown in Fig. 1. Specimens of 1 to 2 kg weight were collected for mechanical analyses. Mechanical analyses were carried out by means of sieving, decantation and pipette methods. Besides, all the results obtained by such laboratory work were corrected for the coarser fractions by referring to the photographs of the outcrops from which the specimens were picked up. Detailed description of such steps of the mechanical analyses will be omitted here. The final results of the mechanical analyses are shown in Table 1, each figure listed in the column represents the weight per cent of each fraction sized out by the mechanical analyses. Fig. 2 and Fig. 3 show the particle size distribution of the specimens by cumulative curves and histograms respectively. The diameters of

2) S. ARAMAKI, *Bull. Volcanol*, [ii], **1** (1957), 53-54, (in Japanese).

Table 1. The results of the mechanical analyses.

φ \ sp. no.	1	2	3	4	5	6	7	8	9	10	11
～−10	1.1		1.0								
−10～− 9	2.2	1.5	2.2		0.6					1.7	
− 9～− 8	2.6	2.5	3.9	2.0	1.8		2.0	0.8		2.3	
− 8～− 7	2.8	3.2	2.7	3.0	2.9	1.8	3.0	2.5	1.5	3.1	3.5
− 7～− 6	4.2	4.0	4.4	4.1	4.0	3.4	5.5	3.9	3.0	3.7	4.0
− 6～− 5	5.3	6.2	6.3	4.2	6.5	3.6	7.1	5.0	4.1	3.7	4.5
− 5～− 4	6.6	6.3	8.1	4.8	8.5	3.9	6.3	5.1	4.6	4.0	5.5
− 4～− 3	4.8	5.2	7.4	4.9	8.0	6.0	4.2	4.7	5.9	3.3	6.0
− 3～− 2	2.9	4.8	6.7	5.0	6.0	10.0	3.9	4.5	6.9	4.1	6.5
− 2～− 1	4.4	5.1	7.0	5.8	5.5	10.1	4.7	4.9	7.0	5.1	6.7
− 1～ 0	9.6	7.8	8.8	8.6	6.4	9.1	8.0	8.8	10.5	9.2	10.2
0～ 1	13.5	12.6	9.8	12.0	11.8	13.1	12.9	12.5	13.5	13.7	12.1
1～ 2	12.8	11.5	8.7	12.9	11.2	11.0	12.6	10.8	13.0	13.4	12.2
2～ 3	10.0	9.5	7.0	11.9	5.5	9.5	10.0	9.3	10.4	10.0	10.9
3～ 4	6.9	7.4	5.3	9.3	7.3	6.9	7.9	7.9	8.2	8.4	7.2
4～ 5	4.5	5.4	4.4	6.8	5.0	5.2	5.2	6.8	5.4	6.5	4.9
5～ 6	2.1	3.2	2.6	2.8	2.2	2.7	2.6	5.3	2.5	3.3	1.8
6～ 7	1.7	2.1	0.8	0.7	1.4	1,6	1.9	3.4	1.3	2.0	1.4
7～ 8	1.0	0.9	0.7	0.5	0.4	0.9	1.1	1.1	1.2	1.1	1.0
8～ 9	0.6	0.3	0.9	0.6	0.4	1.0	0.8	0.8	0.7	0.6	0.9
9～	0.4	0.5	0.3	0.1	0.6	0.2	0.3	1.9	0.3	0.8	0.7

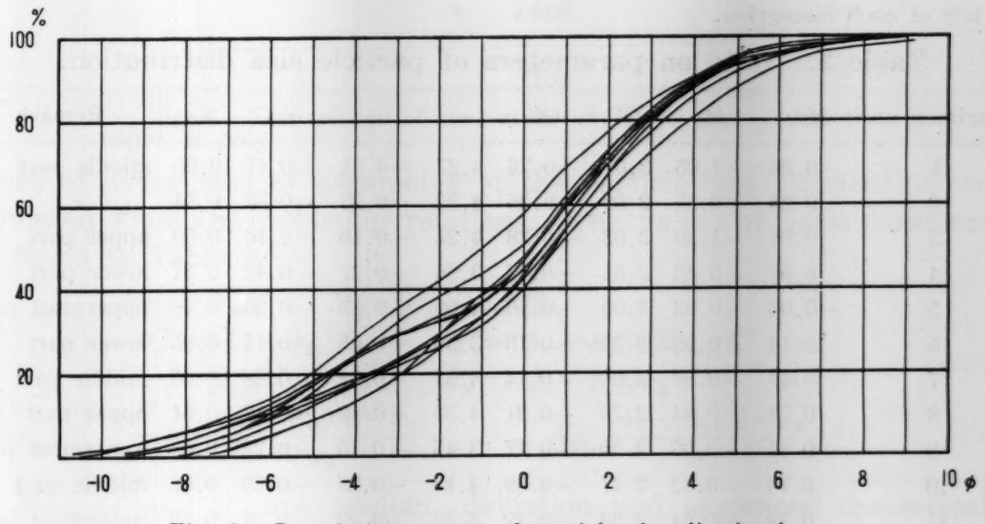

Fig. 2. Cumulative curves of particle size districation.

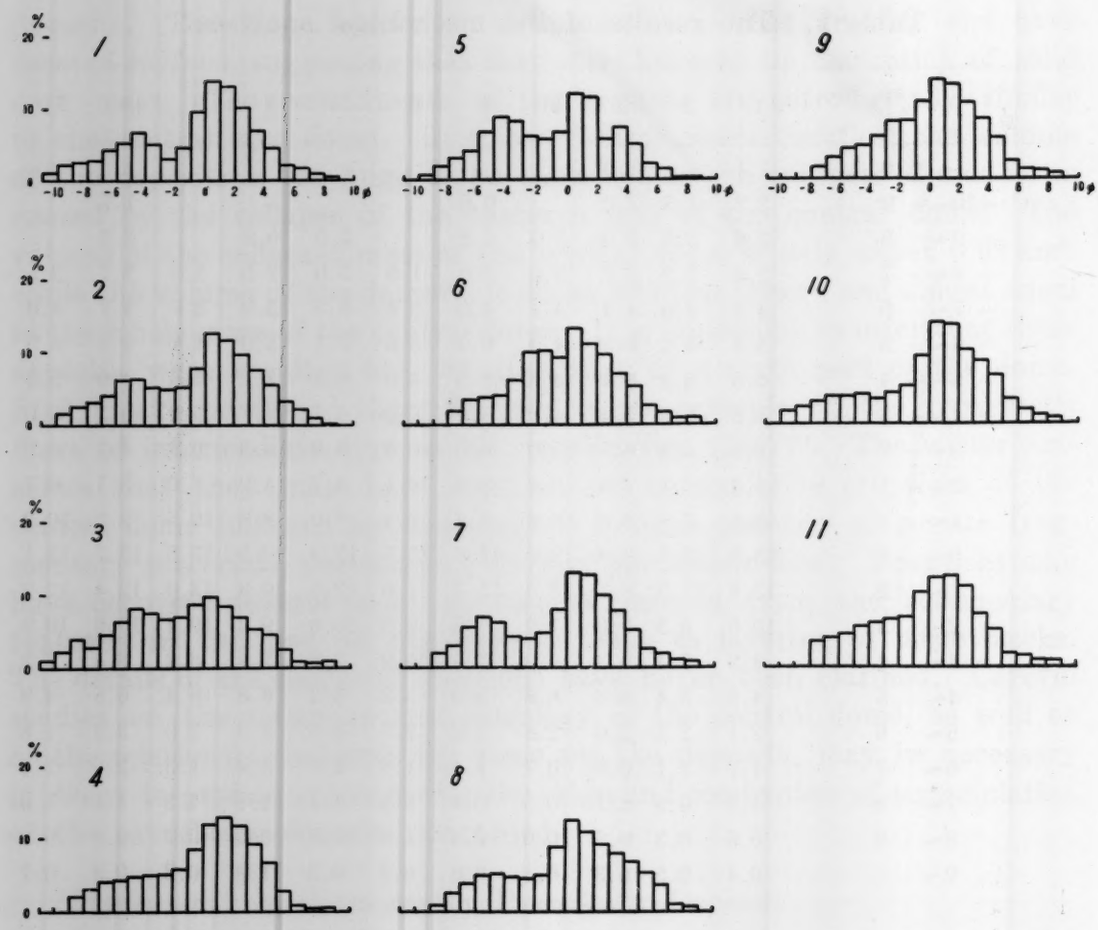

Fig. 3. Histograms of particle size distribution. The number of specimen is noted on the left of each histogram.

Table 2. Data on parameters of particle size distribution.

Specimen no.	$Md\phi$	$M\phi$	Q'	Q''	$\sigma\phi$	$\alpha\phi$	$\alpha_2\phi$	$\beta\phi$	Remark
1	0.28	−1.05	3.07	−0.76	4.27	−0.31	−0.41	0.60	middle part
2	0.28	−0.85	2.59	−0.36	4.32	−0.26	−0.32	0.54	〃
3	−0.98	−1.39	3.03	−0.28	4.24	−0.10	−0.16	0.59	upper part
4	0.63	−0.43	2.61	−0.47	3.96	−0.27	−0.42	0.51	lower part
5	−0.03	−0.92	3.05	−0.56	4.06	−0.22	−0.25	0.49	uppermost part
6	0.14	−0.05	2.30	−0.15	3.36	−0.06	−0.13	0.95	lower part
7	0.47	−0.89	3.09	−0.74	4.31	−0.32	−0.28	0.46	middle part
8	0.78	0.24	2.79	−0.21	4.35	−0.12	−0.17	0.51	upper part
9	0.47	−0.05	2.30	−0.27	3.45	−0.15	−0.22	0.63	uppermost part
10	0.74	−0.42	2.47	−0.39	4.18	−0.28	−0.39	0.62	middle part
11	0.28	−0.54	2.53	−0.42	3.76	−0.22	−0.37	0.59	uppermost part

particles in millimeters ξ are replaced here by ϕ as expressed $\phi=-\log_2\xi$ for convenience. The phi values of the percentiles ϕ_5, ϕ_{16} ϕ_{25}, ϕ_{50}, ϕ_{75}, ϕ_{84}, and ϕ_{95} were read on the cumulative curves, and the approximate

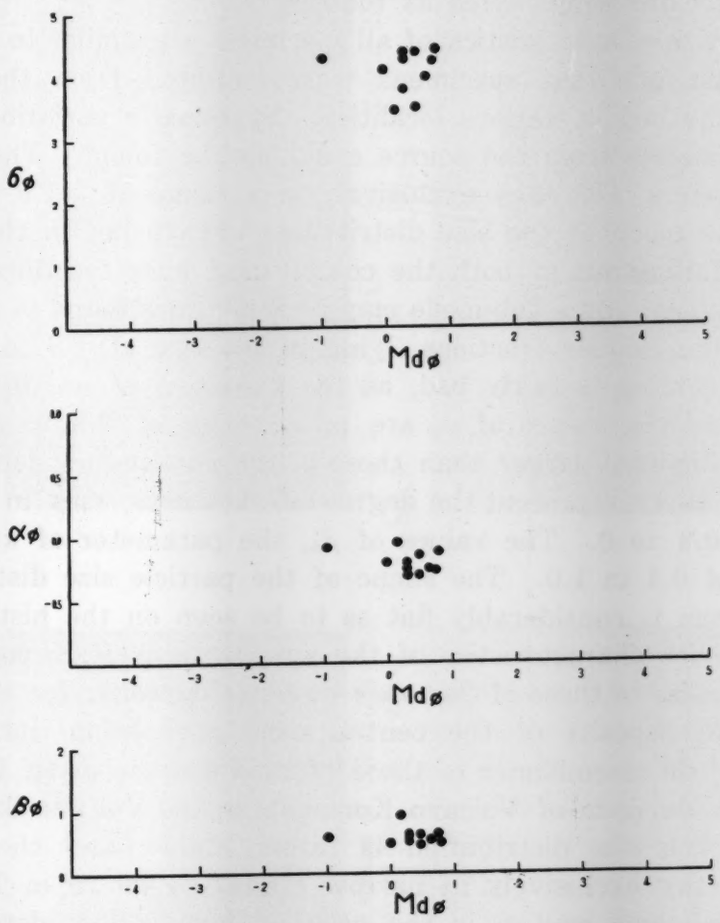

Fig. 4. The relation of the values of $\sigma\phi$, $\alpha\phi$ and $\beta\phi$ to the values of $Md\phi$.

values of every sort of parameter of the particle size distribution were calculated from the following relations. The values of these parameters are listed in Table 2.

$$Md_\phi=\phi_{50}\ , \qquad M_\phi=(\phi_{16}+\phi_{84})/2\ ,$$
$$Q'=|\phi_{75}-\phi_{25}|/2\ , \qquad Q''=(\phi_{75}+\phi_{25}-2\phi_{50})/Q'\ ,$$
$$\sigma_\phi=|\phi_{84}-\phi_{16}|/2\ , \qquad \alpha_\phi=(M_\phi-\phi_{50})/\sigma_\phi\ ,$$
$$\alpha_{2\phi}=\frac{(\phi_5+\phi_{95})/2-\phi_{50}}{\sigma_\phi}\ , \qquad \beta=\frac{(\phi_{95}-\phi_5)/2-\sigma_\phi}{\sigma_\phi}\ .$$

Md_ϕ, Q' and Q'' are median, deviation and skewness respectively, obtained by the quartile method, while M_ϕ, σ_ϕ, α_ϕ and $\alpha_{2\phi}$, and β_ϕ are

mean, deviation, skewness and kurtosis of the Inman's phi measure system[3].

The results of the mechanical analyses of 11 specimens of the pyroclastic deposits are summarized as follows:

1) The size characteristics of all specimens are similar to each other, in spite of the fact that specimens were collected from the different horizons of the bed in various localities. Systematic variation of coarseness with distance from the source could not be found. The values of median diameters Md_ϕ stay exclusively in a range of -1.0 to 0.8 in ϕ scale, and the mode of the size distribution always lies in the fractions of 0 to 2. Tailing-out of both the coarser and finer fractions are found in every specimen, and a sub-mode may be sometimes found in the tailing-out part of the coarser fractions, lying in the size of -6 to -4.

2) The sorting is fairly bad, as the values of Q' are in a range of 2.3 to 3.1, and the values of σ_ϕ are in a range of 3.3 to 4.4. These values are somewhat larger than those of the pumice-flow deposits. The values of α_ϕ, which represent the degree of skewness, stay in a negative range of -0.3 to 0. The values of β_ϕ, the parameter of kurtosis, are in a range of 0.4 to 1.0. The shape of the particle size distribution of every specimen is considerably flat as to be seen on the histogram.

3) The size characteristics of the pyroclastic deposits concerned are somewhat similar to these of the *nuée ardente* deposits, for example the *nuée ardente* deposits of the central cone of Volcano Hakone. They also show a little resemblance to these of mud-flow deposits, for example the mud-flow deposits of Volcano Komagatake and Volcano Bandai. The shape of particle size distribution is rather stable, and the values of parameters stay exclusively in narrow ranges as shown in Table 2 and Fig. 4, in the same way as in the case of pumice-flow deposits. This seems to be dissimilar to the case of mud-flow deposits in which matters may be otherwise.

Summary

It seems apparent that the pyroclastic deposits which are distributed on the east foot of Volcano Myôkô are not the products of mud-flows caused by disruption of the eastern part of the central dome, as they have been hitherto considered. They may have been the result of the explosive eruptions of the central dome followed by discharge of a large quantity of porous fragmentary materials, descending down the moun-

3) D. I. INMAN, "Measures of describing the Size Distribution of Sediments", Jour. Sed. Petrol., **22** (1952), 125-145.

Fig. 5. The central dome and the somma of Volcano Myôkô, looking from loc. no. 6 in the valley of the Ôtagiri-gawa.

Fig. 6. U-shaped valley of the Ôtagiri-gawa cutting into the pyroclastic deposits, looking from the upper side, near loc. no. 6.

Fig. 7. The surface of the pyroclastic deposits, near loc. no. 5.

Fig. 8. The vertical section of the pyroclastic deposits exposed on the valley-wall of the Ôtagiri-gawa, near loc. no. 8.

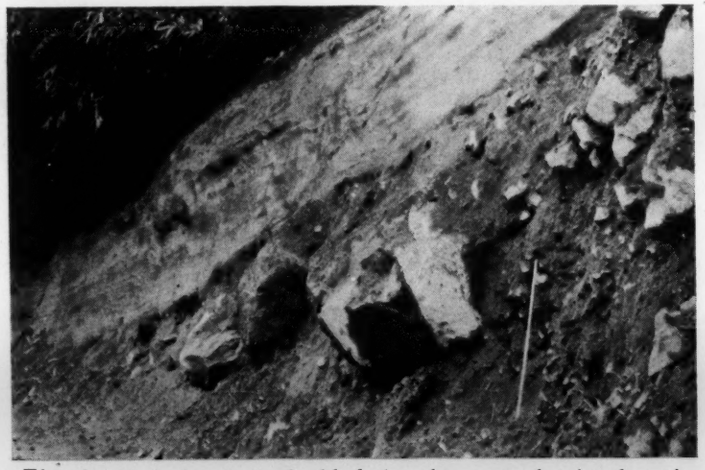

Fig. 9. Ash layer embedded in the pyroclastic deposits, near Tsubame hot spring.

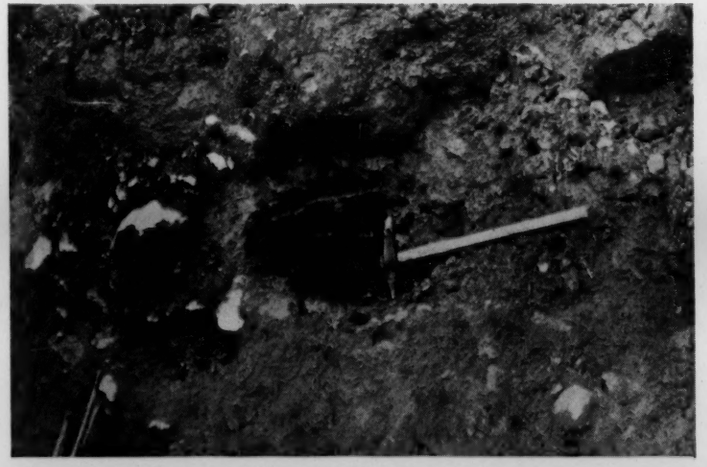

Fig. 10. Natural charcoal buried in the pyroclastic deposits, near Tsubame hot spring.

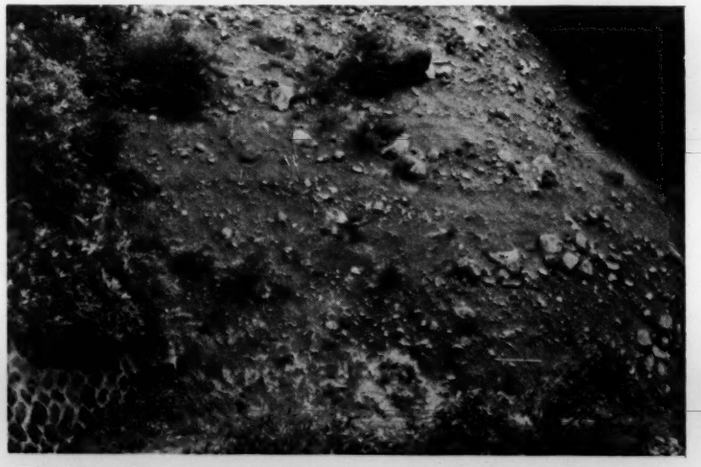

Fig. 11. The outcrop of the pyroclastic deposits from which specimen no. 1 was collected.

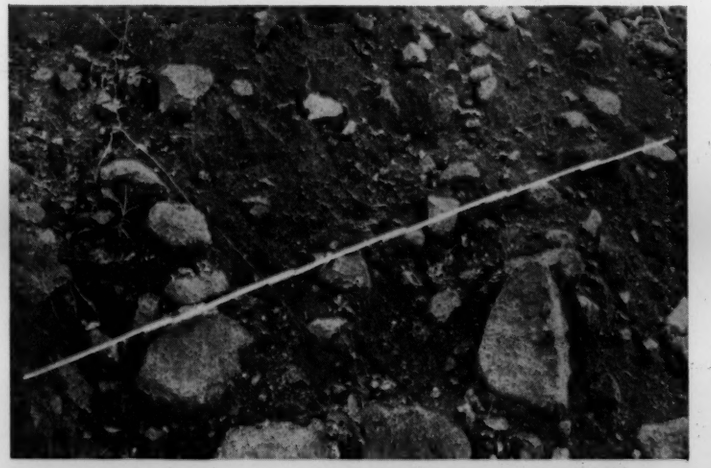

Fig. 12. The outcrop of the pyroclastic deposits from which specimen no. 10 was collected.

tain-slope in a state of pyroclastic flow. Further studies on the pyroclastic deposits as well as on the central dome are necessary in order to clarify the origin and mechanism of deposition of the pyroclastics.

---

17. 妙高火山東麓に分布する火砕堆積物

地震研究所　村　井　　勇

妙高火山は新潟県南部に位置する火山で，噴火の記録はない．二重火山で，外輪山は主として複輝石安山岩の熔岩よりなる．南北 2.7 km，東西 2 km の大きさを持つカルデラの中には，普通輝石・紫蘇輝石・角閃石・安山岩の熔岩円頂丘が大きく成長している．外輪山の東壁は火口瀬によつて深く刻まれているが，この火口瀬の内部に火山砕屑物質よりなる堆積物が厚い層をなして分布している．この堆積物は，中央円頂丘の麓では，最後に噴出した角閃石・橄欖石・安山岩の熔岩によつておおわれている．外輪山の東麓では非常に広い範囲にわたつて分布しており，その先端は中央円頂丘より約 10 km はなれた関川にまで達している．分布面積は約 23 km^2 におよび，層厚は 50 m またはそれ以上と見られるから，この火砕堆積物の総体積は約 1.2 km^3 と計算される．

この堆積物は角礫と細粒物質の混合したもので，一見したところ火山泥流の堆積物のように見受けられる．角礫はほとんどすべて多孔質のガラス質石基を持つた角閃石・紫蘇輝石・安山岩の砕片で，細粒物質は斜長石・角閃石・紫蘇輝石等の鉱物粒およびガラス破片よりなり，粘土鉱物はほとんど含まれない．その厚い層全体が均質で，なんら特別な構造を示さないが，角礫を多く含む層が部分的に見られる場合がある．中央円頂丘の付近では上部に厚さ 1 m ほどの火山灰層が挟まれている．また，天然木炭を含んでおり，堆積当時かなり高温であつたと見られる．

中央円頂丘の東側には爆裂火口状の地形が見られる．問題の火砕堆積物はこの部分の崩壊によつて発生した泥流の堆積物と従来考えられてきた．しかし崩壊部分の体積は約 0.03 km^3 にすぎず，1.0km^3 以上の体積を持つ堆積物の生因をこれで説明することは困難である．荒牧重雄はこの堆積物を中間型火砕流の例に加えている (1957 年)．中央円頂丘の構造やこの火砕堆積物との関係を詳しく調査した上でなくては確実な結論は得られないが，おそらく円頂丘の崩壊とともに火砕流が発生したものと見られ，このような噴火が繰返えされた結果火砕堆積物の厚層が東麓一帯に発達したと考えられる．

火砕堆積物の層から合計 11 個の試料を採集して機械分析を行なつたが，粒度分布はいずれもきわめてよく類似している．$Md\phi$ は −1.0 と 0.8 の範囲内にありよくそろつている．$\sigma\phi$ は 3.3〜4.4 で，一般の軽石流堆積物の場合より大きい．モードは $\phi=0$〜2 の間に常に現われる．また $\phi=-6$〜−4 の間に副モードが見られる場合が多い．$\alpha\phi$ は常に負の値をとる．$\beta\phi$ は 0.4〜1.0 で，粒度分布の形が平らであることを示している．このような粒度分布の特徴は火砕流堆積物に共通に見られるものであるが，また泥流堆積物の場合とも類似の点をもつている．ただし，泥流堆積物では粒度分布の形の変化が大きく，パラメーターの値がよくそろわないのが普通のようである．

BULLETIN OF THE EARTHQUAKE
RESEARCH INSTITUTE
Vol. 38 (1960), pp. 317-328

18. A Differential Proton Magnetometer.

By Tsuneji RIKITAKE and Iwao TANAOKA,

Earthquake Research Institute.

(Read Jan. 30, 1960.—Received Feb. 23, 1960.)

Summary

A magnetometer that records differences in total geomagnetic intensity between two points is described. By mixing the signals caused by free precession of protons from the two detecting coils, the beat signal is recorded on a pen-writing oscillograph. According to the test of the apparatus at the Oshima Geophysical Observatory, the accuracy of the differential magnetometer is found to be about $0.2\,\gamma/10\,m$ at the moment. Since it is easy to increase the distance between the two coils, the sensibility of the apparatus can be increased. The purpose of the present apparatus is to detect very accurately local anomalous changes in the earth's magnetic field which might be accompanied by activities of Volcano Mihara.

1. Introduction

A number of attempts have been hitherto made to design and construct magnetic gradiometers or differential magnetometers by which we can measure the space gradients of the geomagnetic field. A few types of such instruments have been advanced in relation to magnetic prospecting[1),2),3)]. Meanwhile, S. Chapman[4)] emphasized the importance of measuring the time rate of change of the space gradients in polar regions. On the occasion of the International Geophysical Year 1957–58, J. H. Nelson[5)] developed a differential magnetograph following S. Chapman's suggestion[6)]. Being designed for close observations of auroral electrojet over Alaska, the magnetograph records the differences between

1) A. BERROTH and A. SCHLEUSENER, *Zeits. f. Geophys.* **9** (1933), 355.
2) I. ROMAN and T. C. SERMON, *Trans. Amer. Inst. Mining Metall. Eng.*, **110** (1934), 373.
3) T. NAGATA and K. WATANABE, *Chishitsu Kosho to Butsuri Tanko*, No. 2 (1950), 106.
4) S. CHAPMAN, *Terr. Magn.*, **41** (1936), 127.
5) J. H. NELSON, *IGY Instruction Manual*, No. 3, Part 1 (1956), 37 and 39.
6) S. CHAPMAN, *IGY Instruction Manual*, No. 3, Part 1 (1956), 35.

the values of a certain component of the earth's magnetic field at a master and auxiliary stations, several kilometers apart with one another. Some careful adjustment of orientation of recording magnets as well as of electric device are necessary for a reliable observation.

The differential magnetometer that will be described in this paper differs very much from those developed so far. It is made so as to measure the difference in the total geomagnetic intensity between two points by counting the beat frequency which is produced by mixing the proton precession frequency at the respective points. Since M. Packard and R. Varian[7] proposed a method for measuring the absolute value of the earth's magnetic field by counting the free precession frequency of protons in the water, many researchers[8)-14)] have attempted to construct practicable proton magnetometers based on the principle. Even the use of the magnetometers on balloons[15)], and rockets[16)] has been successful. Seaborne proton magnetometers have been also developed by the Research Group for Proton Magnetometers[14)], M. N. Hill[17)] and others[18)].

T. Rikitake, who has been in charge of the geomagnetic observation on Oshima Island in collaboration with I. Yokoyama and others since 1950, equipped the Oshima Geophysical Observatory, which was built in 1959, with a station-use proton magnetometer constructed by the Research Group for Proton Magnetometers[14)]. Although no detailed analysis of the results observed by it has been worked out yet, it is expected that we can accurately trace changes in the earth's magnetic field relevant to activities of Volcano Mihara by the apparatus. In view of the local anomalous geomagnetic changes associated with the volcanic activities as have been reported in a series of papers in this bulletin[19)-21)] and

7) M. PACKARD and R. VARIAN, *Phys. Rev.*, **93** (1954), 941.
8) G. S. WATERS and G. PHILLIPS, *Geophys. Prosp.*, **4** (1956), 1.
9) G. S. WATERS and P. D. FRANCIS, *Journ. Sci. Instr.*, **35** (1958), 88.
10) I. TSUBOKAWA, M. TAZIMA and T. SETO, *Sokuchi Gakkai-shi*, **4** (1957), 24.
11) I. TSUBOKAWA, *Kagaku*, **28** (1958), 73.
12) S. KOZIMA, K. OOI, S. OGAWA and K. TORIZUKA, *Kagaku*, **27** (1957), 255.
13) S. KOZIMA, S. OGAWA, K. TORIZUKA and K. OOI, *Keisoku*, **7** (1957), 456.
14) RESEARCH GROUP FOR PROTON MAGNETOMETERS, *Bull. Earthq. Res. Inst.*, **36** (1958), 433.
15) L. J. CAHILL JR. and J. A. VAN ALLEN, *Journ. Geophys. Res.*, **61** (1956), 547.
16) L. J. CAHILL JR., *Journ. Geophys. Res.*, **64** (1959), 489.
17) M. N. HILL, *Deep Sea Res.*, **5** (1959), 309.
18) D. CHRISTOFFEL, *Annual Report, Geophys. Lab., Univ. of British Columbia* (1959), 3.
19) T. RIKITAKE, *Bull. Earthq. Res. Inst.*, **29** (1951), 161 and 499.
20) T. RIKITAKE, I. YOKOYAMA, A. OKADA and Y. HISHIYAMA, *Bull. Earthq. Res. Inst.*, **29** (1951), 583.

elsewhere[22], it is thought to be of further advantage for presuming the internal conditions of the volcano to add some geomagnetic observations of a different sort to those which have been hitherto conducted. As has been already suggested by I. Tsubokawa[11], the values of geomagnetic total force at two points can be simultaneously compared with one another quite easily and accurately by providing two detector coils of proton magnetometer and counting the beat frequency produced by mixing signal frequencies from them. The writers constructed a differential proton magnetometer of this sort and set it up at Oshima Geophysical Observatory in the hope of observing changes in the gradient of the geomagnetic total force that might be accompanied by grows and decays of the volcanic activity of Volcano Mihara.

2. Expected changes in the gradient of the geomagnetic total intensity

From the analyses of repeated magnetic surveys over Oshima Island, the local anomalous changes in the earth's magnetic field have been apparently interpreted as the magnetic fields due to hypothetical magnetic dipoles. The positions and strengths of the dipoles have been obtained by T. Rikitake[19] and I. Yokoyama[21] as reproduced in Table 1. The dipoles are directed to the same (+) or reverse (−) directions of the geomagnetic field according to the decaying or developing periods of volcanic activity.

Table 1. The hypothetical dipoles for various periods of the activities of Volcano Mihara

Period	Intensity of dipole (*e.m.u.*)	Depth of dipole (*km*)
July. 1950—Sept. 1950	-6.3×10^{14}	5.5
May. 1951—Aug. 1953	$+8.6\times10^{13}$	4.7
Aug. 1953—Jan. 1954	-1.2×10^{13}	1.6
Jan. 1954—June. 1954	$+1.2\times10^{13}$	1.6

Let us here estimate the gradient of the total magnetic force caused by a magnetic dipole of which the magnetic moment amounts to 10^{13} $\sim10^{14}$ *e.m.u.* Suppose a dipole at the origin of cartesian coordinates, the magnetic potential due to the dipole can be given as

21) I. YOKOYAMA, *Bull. Earthq. Res. Inst.*, **32** (1954), 17, 169; **33** (1955), 251; **34** (1956), 21.

22) T. RIKITAKE and I. YOKOYAMA, *Journ. Geophys. Res.*, **60** (1955), 165.

$$W=\frac{M_x x+M_y y+M_z z}{r^3}, \tag{1}$$

where

$$r^2=x^2+y^2+z^2, \tag{2}$$

while M_x, M_y and M_z denote respectively the moment projected to the x, y and z directions. Differentiating (1) with respect to x, y and z, the three components of the magnetic field become

$$X=M_x\frac{y^2+z^2-2x^2}{r^5}-3M_y\frac{xy}{r^5}-3M_z\frac{zx}{r^5}, \tag{3}$$

$$Y=-3M_x\frac{xy}{r^5}+M_y\frac{z^2+x^2-2y^2}{r^5}-3M_z\frac{yz}{r^5}, \tag{4}$$

$$Z=-3M_x\frac{zx}{r^5}-3M_y\frac{yz}{r^5}+M_z\frac{x^2+y^2-2z^2}{r^5}. \tag{5}$$

If we further differentiate (3), (4) and (5) with respect to x, we have

$$\frac{\partial X}{\partial x}=M_x\left(15\frac{x^3}{r^7}-9\frac{x}{r^5}\right)+M_y\left(15\frac{x^2y}{r^7}-3\frac{y}{r^5}\right)+M_z\left(15\frac{x^2z}{r^7}-3\frac{z}{r^5}\right), \tag{6}$$

$$\frac{\partial Y}{\partial x}=M_x\left(15\frac{x^2y}{r^7}-3\frac{y}{r^5}\right)+M_y\left(15\frac{xy^2}{r^7}-3\frac{x}{r^5}\right)+M_z\left(15\frac{xyz}{r^7}\right), \tag{7}$$

$$\frac{\partial Z}{\partial x}=M_x\left(15\frac{x^2z}{r^7}-3\frac{z}{r^5}\right)+M_y\left(15\frac{xyz}{r^7}\right)+M_z\left(15\frac{xz^2}{r^7}-3\frac{x}{r^5}\right). \tag{8}$$

Since the total magnetic force F is defined by

$$F^2=X^2+Y^2+Z^2, \tag{9}$$

the gradient to the x direction becomes

$$\frac{\partial F}{\partial x}=\frac{1}{F}\left(X\frac{\partial X}{\partial x}+Y\frac{\partial Y}{\partial x}+Z\frac{\partial Z}{\partial x}\right). \tag{10}$$

We can therefore calculate the gradient of F to any direction with expressions from (3) to (10) provided the direction of the coordinate axes are chosen suitably.

For an order-of-magnitude estimate, let us here consider a simple case in which $M_x=M_y=0$, $y=z=0$. In that case, we simply obtain

$$\partial F/\partial x=-\frac{3M_z}{x^4},$$

so that, if $M_z=10^{13}$ *e.m.u.*, $\partial F/\partial x$ amounts to 3.0×10^{-2}, 1.9×10^{-3}, 3.7×10^{-4} and $4.8\times10^{-5}\,\gamma/cm$ for $x=1$, 2, 3 and 5 *km* respectively. In other words, these gradients are 30, 1.9, 0.37 and $4.8\times10^{-2}\,\gamma/10\,m$.

Since the distance between the two detecting coils is about 10 *m* for the present apparatus and the accuracy of counting the beat frequency amounts to $0.01\,c/s$ or $0.2\,\gamma$, the dipole having a moment of 10^{13} *e.m.u.* cannot be detected provided it appears at a distance farther than 2 *km* or so. Even if the moment becomes 10 times larger, the detectable distance would not exceed 4 *km*.

From the above estimate of $\partial F/\partial x$, we see that it would be rather difficult to catch the dipoles supposed at some depth under the central part of the island because the observatory where the differential magnetometer has been installed is about 4 *km* distant from the crater. It will not be utterly hopeless, however, that we might catch the local anomalous changes in the magnetic field with the instrument provided the magnetized or demagnetized regions within the interior of the volcano have some volume. The gradient depends largely on the distance between the instrument and the magnetic matter.

According to the previous observations, there is some evidence that we sometimes have very localized changes which can be detected at stations only a few hundred meters distant from one another though no detailed investigation of such changes has been carried out. If we had changes of this sort, the differential magnetometer would certainly catch them. If they were once caught, we would be quite sure that some anomalous changes occurred because no correction whatever is necessary for the result unlike usual magnetometers.

It is also intended in the future to increase the distance between the two detecting coils by a factor 10 or so. In that case, the sensibility of the apparatus might be sufficient for observations of the supposed local anomalous changes.

3. Apparatus

As the principle on which a proton precession magnetometer works is well known, no detailed explanation of the proton magnetometer itself is necessary. The writers would here like to describe only some brief outline of the differential proton magnetometer.

As can be seen in the block-diagram in Fig. 1, the apparatus consists of a pair of detecting coils, electric sources for magnetization and voltage

amplifiers and also a power amplifier, a standard frequency oscillator, and a recorder.

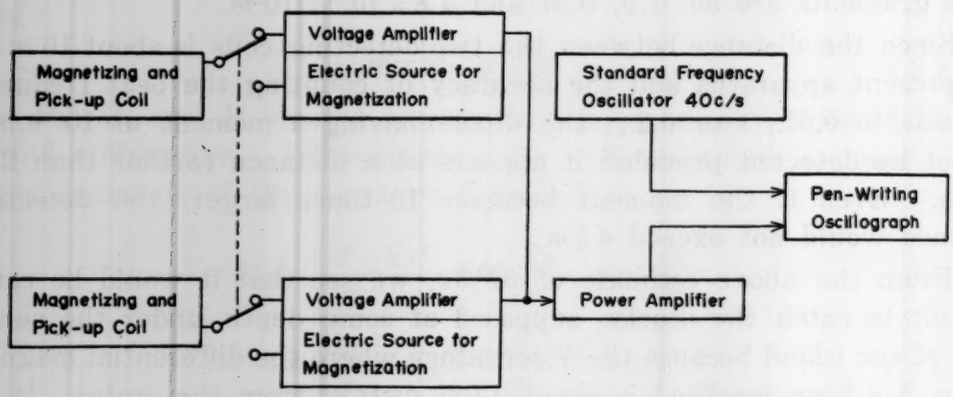

Fig. 1. Block-diagram of the differential proton magnetometer.

Detecting and magnetizing coils

Enamelled copper wire of 1 *mm* in diameter is wound about 500 *turns* on glass or vinyl bottles of about 7 *cm* in diameter and 8 *cm* in length. The bottles contain some 200 *cc* of distilled water.

In order to direct the magnetic moments of protons in the water to a direction approximately perpendicular to the geomagnetic field, electric currents of about 5 *amperes* are supplied to these coils from the electric sources. If the magnetic fields produced by the electric currents are removed suddenly, gyromagnetic motions of protons take place around the flux of the earth's magnetic field. In that case, the coils can be also used as pick-up coils for the induced voltage due to the rotating resultant magnetic moment provided the coils are switched to the amplifiers at the same time. The relation between the precession frequency $f(c/s)$ and the intensity of magnetic field $F(\gamma)$ is $F=23.4865\,f$.

Voltage amplifiers

The voltages that are induced in each coil are introduced to the coupling transformers of the respective voltage amplifiers. Through a preamplifier and a 2 *kc/s* narrow-band amplifier with two 50 *c/s* rejectors, the signal voltage is amplified attaining a gain of 130 *db* or so.

The amplifier of the station-use proton magnetometer[14] (amplifier 1) that has been reported previously is used as one of the voltage amplifiers. The electric circuit of the newly constructed amplifier (amplifier 2) is shown in Fig. 2 together with the power supply, mixing part and power amplifier. The circuit of amplifier 1 is more or less the same as that of amplifier 2.

Mixer and power amplifier

As can be seen in Fig. 2, the signal voltage that is amplified by amplifier 1 is mixed with that from amplifier 2 through terminal *J*. The beat waves thus produced are detected by means of grid detection and then introduced to the push-pull power amplifier.

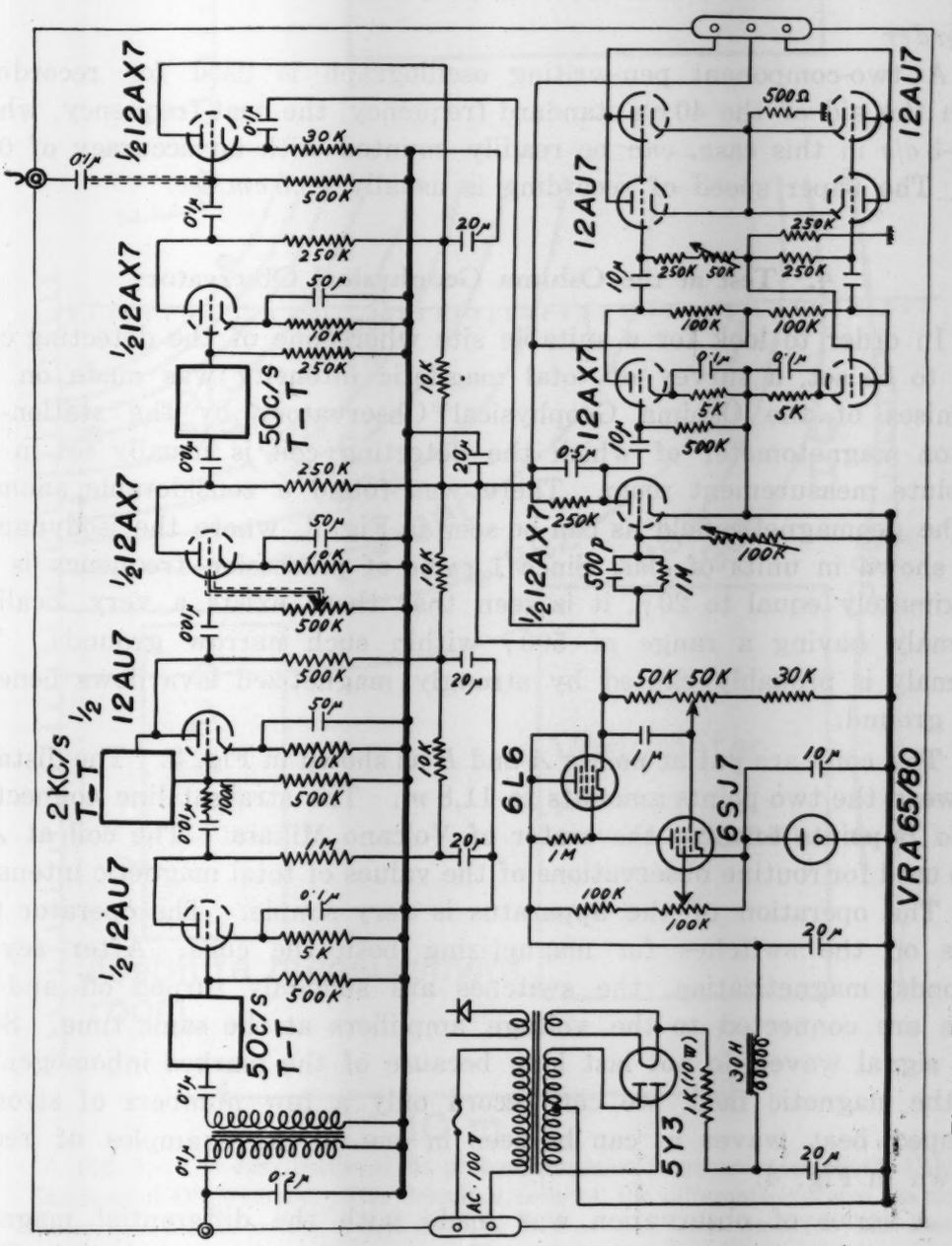

Fig. 2. Electric circuits of amplifier 2, power supply, mixing part and power amplifier.

Standard frequency oscillator

A 40 *c/s* standard frequency is provided as the time reference. The standard oscillator of the station-use proton magnetometer is used for that purpose. We may refer to the previous paper[14] for the details. Since the 40 *c/s* is used only for the time reference, a time marking watch can be utilized for the same purpose.

Recorder

A two-component pen-writing oscillograph is used for recording. With the aid of the 40 *c/s* standard frequency, the beat frequency, which is 2–3 *c/s* in this case, can be readily counted with an accuracy of 0.01 *c/s*. The paper speed of recording is usually 12.5 *cm/sec*.

4. Test at the Oshima Geophysical Observatory

In order to look for a suitable site where one of the detecting coils was to be set, a survey of total magnetic intensity was made on the premises of the Oshima Geophysical Observatory by the station-use proton magnetometer of which the detecting coil is usually set in the absolute measurement room. There was found a considerable anomaly in the geomagnetic field as can be seen in Fig. 3, where the isodynamics are shown in units of *c/s*. Since 1 *cycle* of precession frequency is approximately equal to 20 γ, it is seen that there exists a very localized anomaly having a range of 500 γ within such narrow grounds. The anomaly is probably caused by strongly magnetized lava flows beneath the ground.

The coils are put at points *A* and *B* as shown in Fig. 3. The distance between the two points amounts to 11.8 *m*. The straight line connecting *A* to *B* points towards the crater of Volcano Mihara. The coil at *A* is also used for routine observations of the values of total magnetic intensity.

The operation of the apparatus is very simple. The operator first puts on the switches for magnetizing both the coils. After several seconds' magnetization, the switches are suddenly turned off and the coils are connected to the voltage amplifiers at the same time. Since the signal waves do not last long because of the marked inhomogeneity of the magnetic field, we can record only a few numbers of strongly damped beat waves as can be seen in one of the examples of record shown in Fig. 4.

A series of observation was made with the differential magnetometer on Dec. 23 and 24, 1959. The results are summarized in Table

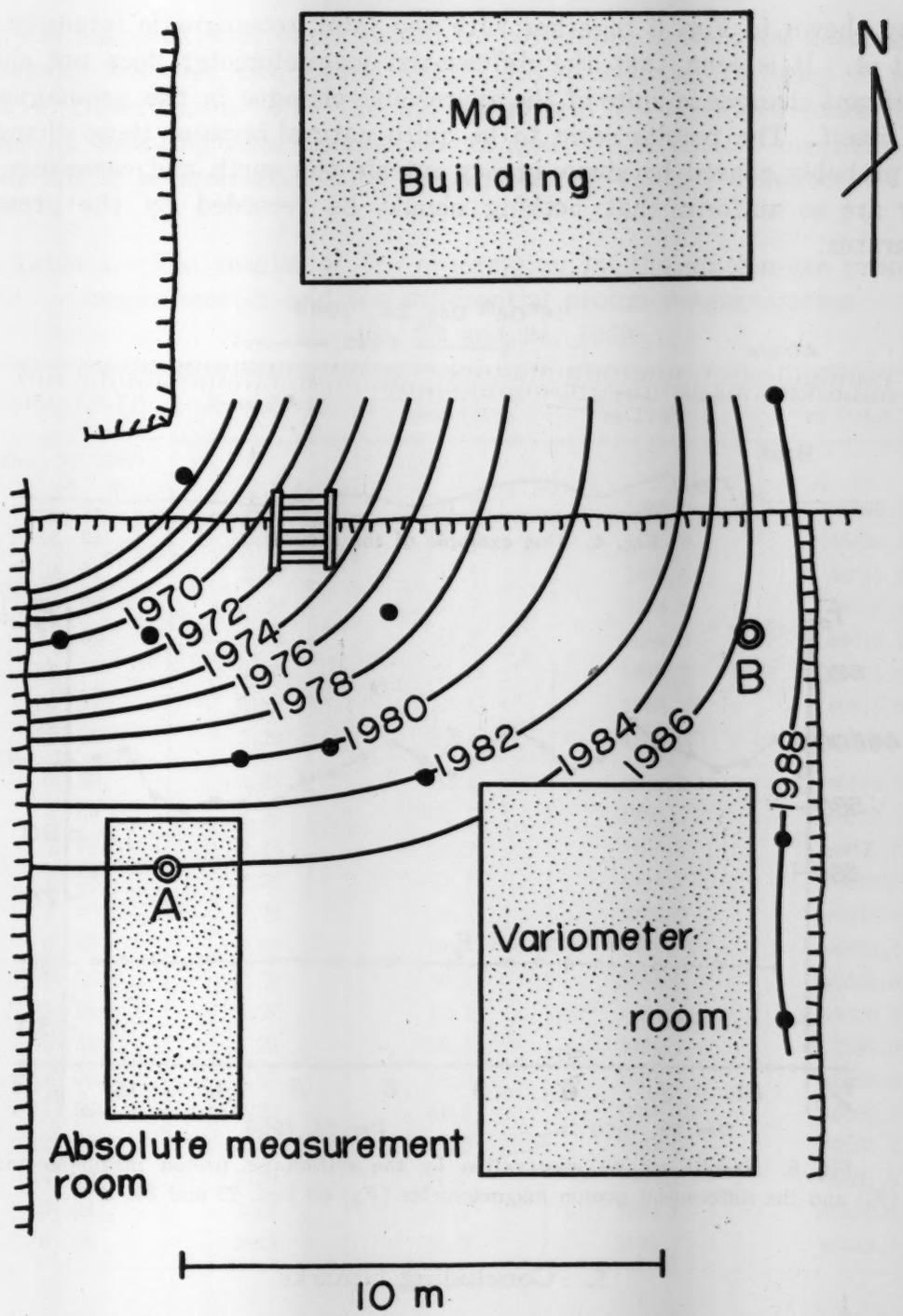

Fig. 3. The distribution of the proton precession frequencies (c/s) in the Oshima Geophysical Observatory. The detecting coils of the differential proton magnetometer are set at points A and B. The coil at A is also used for the routine observations of the total geomagnetic field by the station-use proton magnetometer.

1 and shown in Fig. 5 together with the total geomagnetic intensity at point *A*. It is seen that the differential magnetometer does not show significant changes in spite of the appreciable changes in the geomagnetic field itself. The results seem to be quite natural because those changes are probably caused by some agency outside the earth and consequently they are so uniform that nothing should be recorded by the present apparatus.

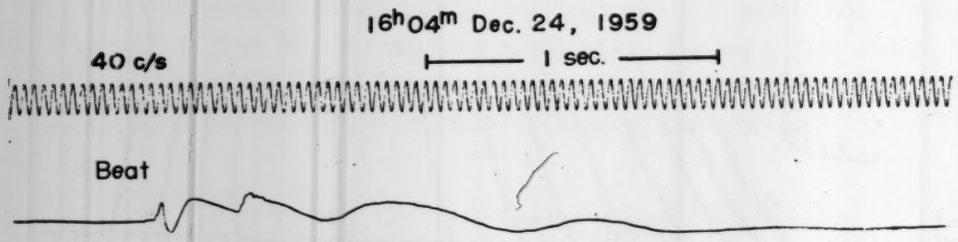

Fig. 4. One example of the records.

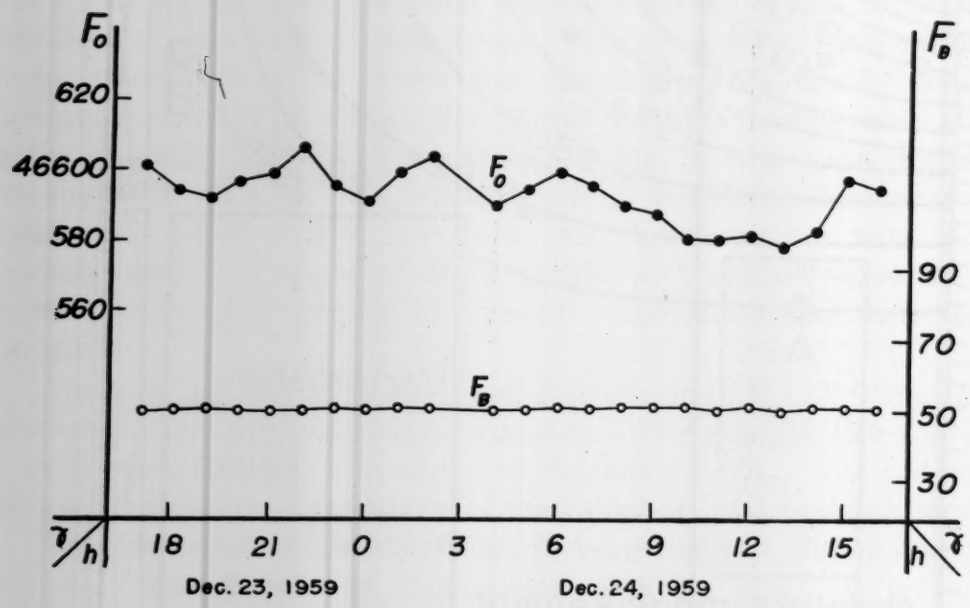

Fig. 5. Results of the observation by the station-use proton magnetometer (F_0) and the differential proton magnetometer (F_B) on Dec. 23 and 24, 1959.

5. Concluding remarks

A differential magnetometer was constructed by mixing the signal waves from two proton magnetometers. According to the test at the Oshima Geophysical Observatory, it was proved that the differential

proton magnetometer could record the difference in the total geomagnetic intensity between two points apart 11.8 *m* with an accuracy of about 0.2 γ. Observations with the apparatus will be continued there in the hope of detecting local anomalous changes in the earth's magnetic field that might be associated with the activity of Volcano Mihara.

Table 1. The results of the observation by the station-use proton magnetometer and the differential proton magnetometer on Dec. 23 and 24, 1959.

Time (J.S.T.)	Beat Freq.	Difference in total force	Signal Freq. at Point *A*	Total force at Point *A*
Dec. 23, 1959				
h *m*	*c/s*	γ	*c/s*	γ
17 01	2.20	51.7	1985.0	46620.7
18 01	2.20	51.7	1985.0	46620.7
19 01	2.22	52.1	1984.6	46611.3
19 58	2.20	51.7	1984.8	46616.0
21 02	2.18	51.2	1984.9	46618.4
21 56	2.19	51.4	1985.2	46625.4
22 57	2.22	52.1	1984.75	46614.8
23 58	2.20	51.7	1984.55	46610.1
Dec. 24, 1959				
0 58	2.22	52.1	1984.9	46618.4
2 04	2.22	52.1	1985.1	46623.1
3 59	2.18	51.2	1984.5	46609.0
4 58	2.20	51.7	1984.7	46613.7
6 00	2.22	52.1	1984.9	46618.4
6 59	2.20	51.7	1984.75	46614.8
7 58	2.22	52.1	1984.5	46609.0
8 58	2.22	52.1	1984.4	46606.6
9 58	2.22	52.1	1984.1	46599.6
11 00	2.17	51.0	1984.1	46599.6
11 58	2.22	52.1	1984.15	46600.7
12 58	2.15	50.5	1984.0	46597.2
14 00	2.20	51.7	1984.2	46601.9
15 04	2.20	51.7	1984.8	46616.0
16 04	2.18	51.2	1984.7	46613.7

18. プロトン磁力計による地磁気傾度計

地震研究所 {力武常次
棚岡巖

プロトン磁力計の2個の検出器からの信号周波数を混合して得られる唸周波数を計数して，2地点の地磁気全磁力の差を 0.2γ 程度の精度で測定する装置を考案した．

この器械は地震研究所伊豆大島観測所に設置され，三原山の火山活動に伴なうと予想される地磁気変動の精密観測に使用される予定である．

Bulletin of the Earthquake
Research Institute
Vol. 38 (1960), pp. 329-343

19. *Aseismic Properties of a Wooden House (III).*

By Genrokuro Nishimura and Masazi Suzuki,

Earthquake Research Institute.

(Read Nov. 24, 1959.—Received March 31, 1960.)

1. Introduction

This paper covers one field of our research with regard to aseismic structure. In the previous papers[1)2)], a study was made of the amplitude characteristics such as damping coefficients and natural frequencies that a wooden small house may show during the course of artificial vibration ranging from a small amplitude to a considerably large amplitude. Further the experiment was made on decentering effect (Suzikai effect) to reveal relationship among size of material, quantity, point of application, amplitude and damping coefficient. The observation was made on the effect of a natural earthquake by setting on house and land two sets of seismometers, one strain gauge and two sets of vibroscopes of variable natural frequency and damping factor. According to the results, the predominant period of the house due to earthquake vibration almost coincides with its natural period and the predominant period of model pendulum of the house due to earthquake vibration is in coincidence with that of the house when its natural frequency and damping factor are taken to be the same as that of the house. Further the observation by changing the period and damping factor of the model pendulum reveals that the predominant period is well distributed around the natural frequency of the pendulum, from which it was found that in general the vibration of a house due to earthquake can be represented by that of a pendulum having the same natural frequency and damping factor and its predominant period coinciding with its natural period.

As mentioned above, the measurement of the natural period and damping factor is essential to study the aseismic properties of a structure and it can be obtained either by analysing the results of the meas-

1) M. Suzuki and R. Shoji, "Aseismic Proparties of a Wooden House, (Part I)", *Bull. Earthq. Res. Inst.*, **34** (1956), 381.

2) M. Suzuki, "Aseismic Properties of a Wooden House, (Part II)", *Bull. Earthq. Res. Inst.*, **36** (1958), 235.

urement which will be made by giving structure artificially a natural or forced vibration or by observing the current vibration or vibration due to a natural earthquake.

Wooden houses or wooden structures have in general a greater rate of increase in the natural period with an increase in amplitude in comparison with reinforced concrete or iron frame structures. The factors that decide the natural period of a wooden structure are dependent on the weight of structural materials, material, wall, each partition, joint and connecting condition of upper and lower member of hozo (枘), but especially the importance of the vital rôle that the upper and lower hozo (枘) of a column would play under greater amplitude vibration is well accepted by the circles concerned. Therefore, in order to make a thorough study of the aseismic properties of such a structure, it is essential to make clear the amplitude characteristics by measuring the natural period and damping factor throughout the range of a smaller to larger amplitude value. In the actual measurement, a certain limitation occurs in the magnitude of amplitude on account of a fear of destroying the concerned structure, relationship between size of structure and force to be applied and sensitivity of the measuring instruments, which is especially true for the house currently being occupied or for those of an important construction.

Various measurements have already been conducted on the vibration of wooden structure or house, the most of them, however, are confined in the range of small amplitude. Among these, there is only one record relating to a large amplitude, that is, the report prepared by Saita[3] under the subject "Destruction Test on a Wooden House", which, as the authors pointed out, is just a summary report of the experiment and does not cover the range of very small amplitude.

The measurement of the vibration of a structure is, as mentioned above, subjected to so many restrictions that very often the measurement at small amplitude range is forced. Thus, it becomes pertinent here to secure any correlation in the vibration characteristics that may exist between the greater amplitude and the results for very small amplitude which have already been sought by many people or will be studied in future too. The purpose of this paper is to make a study on the vibration characteristics in the range of a very small to greater

3) T. SAITA, "Experiments in the Vibration and Destruction of a Wooden Dwelling House", *Bull. Earthq. Res. Inst.*, **17** (1939) 152.

amplitude after carefully and throughly checking the data obtained by Saida on very small amplitudes.

2. Free Vibration Having Different Restoring Force and Damping Factor in Successive Amplitude

A wooden structure subjected to deformation by an external load being applied in one direction will almost resume its original condition upon release of such force, a part of the deformation, however, will become a residual permanent deformation and remain in the structure. Again the structure is subjected to deformation in the same manner as in the first case, the deformation would differ from the previous, and such behaviour would become appreciable with an increase in the magnitude of the force applied. For such structure if it is subjected to a great deformation once, various joint and support points will be loosen with the result that its restoring force is reduced and the natural period thus increases. In other words, these restoring force and natural period would differ according to the hysterisis of the past deformation. Even though when the restoring force before the deformation is of lateral symmetry with regard to the equilibrium position, it would show the different restoring force in either side against the same amount of deformation, if it is subjected a considerably large deformation in one direction, thus its natural period assumes different values laterally. Such a phenomenon can be observed generally in such experiments as the model test of a wooden structure or free vibration test of the actual wooden structure made by the statical deformation toward one direction.

Now in the system of simple mass, designate successive amplitudes, its period and damping factor, $x_1, x_2, \cdots x_i$, $T'_1, T'_2, \cdots T'_i$ and $h_1, h_2, \cdots h_i$, equation of motion of the system is

$$\frac{d^2x_i}{dt^2}+2\varepsilon_i\frac{dx_i}{dt}+\sigma_i^2x_i=0\ . \qquad (1)$$

A function satisfied by differential equation (1) is in general

$$x_i=e^{-\varepsilon_i t}(C_{i1}\cos\sigma'_i t+C_{i2}\sin\sigma'_i t)\ , \qquad (2)$$

where

$$i=1, 2, \cdots\ , \qquad \sigma'_i=\sqrt{\sigma_i^2-\varepsilon_i^2}=\sigma_i\sqrt{1-h_i^2}\ ,$$

$$\sigma_i=2\pi/T_i\ , \qquad \sigma'_i=2\pi/T'_i\ .$$

The amplitude of the first vibratory motion x_1 is

$$x_1=e^{-\varepsilon_1 t}(C_{11}\cos\sigma_1' t+C_{12}\sin\sigma_1' t)\ . \tag{3}$$

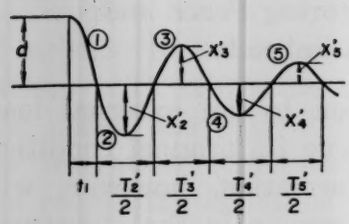

Fig. 1.

When the free vibration is considered by giving an initial deformation d, the initial condition becomes

$$t=0:\quad x_1=d,\quad \text{and}\quad dx_1/dt=0\ . \tag{4}$$

Substituting equation (4) into (3) and its derivative dx_1/dt, then

$$x_1=e^{-\varepsilon_1 t}\frac{\sigma_1 d}{\sigma_1'}\sin(\sigma_1' t+\alpha)\ , \tag{5}$$

where

$$\alpha=\tan^{-1}\left(\frac{\sigma_1'}{\varepsilon_1}\right)=\tan^{-1}(\sqrt{1-h^2}/h)\ .$$

Further,

$$\left.\begin{aligned}\frac{dx_1}{dt}&=-e^{-\varepsilon_1 t}\sigma_1 d\cos(\sigma_1' t+\alpha)\ ,\\ \alpha&=\tan^{-1}(\sqrt{1-h^2}/h)\ .\end{aligned}\right\} \tag{6}$$

Designating t_1 the time at which $x_1=0$, then t_1 and the velocity amplitude at $t=t_1$ are

$$t_1=(\pi-\alpha)/\sigma_1'\ , \tag{7}$$

$$x_{1_{t=t_1}}=-\sigma_1 d\cdot\exp\left(-\frac{\varepsilon_1'}{\sigma_1'}(\pi-\alpha)\right)=-\sigma_1 d\cdot\exp\left(-\frac{h}{\sqrt{1-h^2}}(\pi-\alpha)\right)\ . \tag{8}$$

Therefore, if h can be determined by measuring t_1, σ_1' can also be obtained, and finally T_1' can be calculated.

Next, the amplitude x_2 for the second vibratory motion is

$$x_2=e^{-\varepsilon_2 t}(C_{21}\cos\sigma_2' t+C_{22}\sin\sigma_2' t)\ , \tag{9}$$

and as this vibrations supposed to start at the initial condition,

$$t=t_1=\frac{1}{\sigma_1'}(\pi-\alpha)\ ,\quad x_2=0\ ,\quad \frac{dx_2}{dt}=\frac{dx_1}{dt}=-\sigma_1 d\exp\left(-\frac{h}{\sqrt{1-h^2}}(\pi-\alpha)\right)\ ,$$

thus,

$$\left.\begin{aligned} C_{21}\cos\gamma_2+C_{22}\sin\gamma_2&=0\ ,\\ \gamma_2&=\sigma_2'/\sigma_1'\cdot(\pi-\alpha)\ .\end{aligned}\right\} \tag{10}$$

The velocity amplitude dx_2/dt is

$$\left(\frac{dx_2}{dt}\right)_{t=\pi-\alpha/\sigma_1'}=-\sigma_1 d\exp\left(-\frac{\varepsilon_1(\pi-\alpha)}{\sigma_1'}\right).$$

Thus,

$$-C_{21}(\varepsilon_2\cos\gamma_2+\sigma_2'\sin\gamma_2)+C_{22}(\sigma_2'\cos\gamma_2-\varepsilon_2\sin\gamma_2)=-\sigma_1 d\exp\left(\frac{\pi-\alpha}{\sigma_1'}(\varepsilon_2-\varepsilon_1)\right). \tag{11}$$

From equations (10) and (11), the values C_{21} and C_{22} can be obtained namely,

$$C_{21}=\frac{\eta_2\sigma_1 d}{\sigma_2'}\sin\gamma_2\ ,$$

and

$$C_{22}-=\frac{\eta_2\sigma_1 d}{\sigma_2'}\cos\gamma_2\ ,$$

where

$$\eta_2=\frac{\pi-\alpha}{\sigma_1'}(\varepsilon_2-\varepsilon_1)\ . \tag{12}$$

Substituting equation (12) into (9),

$$x_2=-\frac{\eta_2\sigma_1 d}{\sigma_2'}e^{-\varepsilon_2 t}\sin(\sigma_2' t-\gamma_2)\ , \tag{13}$$

and the velocity amplitude dx_2/dt is

$$\frac{dx_2}{dt}=-\frac{\eta_2\sigma_1 d}{\sigma_2'}e^{-\varepsilon_2 t}\left\{-\varepsilon_2\sin(\sigma_2' t-\gamma_2)+\sigma_2'\cos(\sigma_2' t-\gamma_2)\right\}\ . \tag{14}$$

When x_2 assumes its maximum, $dx_2/dt=0$, i.e., putting $t=t_2'$, from

$$\varepsilon_2\sin(\sigma_2' t_2'-\gamma_2)=\sigma_2'\cos(\sigma_2' t_2'-\gamma_2)\ ,$$

$$\tan(\sigma_2' t_2' - \gamma_2) = \frac{\sigma_2'}{\varepsilon_2} = \frac{\sqrt{1-h^2}}{h},$$

thus,

$$t_2' = \frac{1}{\sigma_2'}\left(\tan^{-1}\frac{\sqrt{1-h^2}}{h} + \gamma_2\right).$$

The amplitude x_2' corresponding to the maximum value of x_2 is

$$x_2' = -\frac{\eta_2\sigma_1 d}{\sigma_2'} \exp\left\{-\frac{h}{\sqrt{1-h^2}}\left(\tan^{-1}\frac{\sqrt{1-h^2}}{h} + \gamma_2\right)\right\} \sin\left(\tan^{-1}\frac{\sigma_2'}{\varepsilon_2}\right).$$

Putting $\gamma_2' = \tan^{-1}(\sigma_2'/\varepsilon_2)$, $\sin\gamma_2' = \tan\gamma_2' \cos\gamma_2'$ and

$$\cos\gamma_2' = \frac{1}{\sqrt{1+\tan^2\gamma_2'}} = \frac{\varepsilon_2}{\sqrt{\sigma_2'^2+\varepsilon_2^2}} = \frac{\varepsilon_2}{\sigma_2}.$$

$$\therefore \quad \sin\left(\tan^{-1}\frac{\sigma_2'}{\varepsilon_2}\right) = \frac{\sigma_2'}{\varepsilon_2}\cdot\frac{\varepsilon_2}{\sigma_2} = \frac{\sigma_2'}{\sigma_2}.$$

Therefore,

$$x_2' = -\frac{\eta_2\sigma_1 d}{\sigma_2}\cdot\exp\left\{-\frac{h}{\sqrt{1-h^2}}\left(\tan^{-1}\frac{\sqrt{1-h^2}}{h} + \gamma_2\right)\right\}. \qquad (15)$$

The time t_3, at which x_2 again becomes zero, is

$$\sin(\sigma_2' t_3 - \gamma_2) = 0.$$

Namely,

$$t_3 = \frac{\pi+\gamma_2}{\sigma_2'}.$$

Thus,

$$\left(\frac{dx_2}{dt}\right)_{(t=t_3)} = \eta_2\sigma_1 d \exp\left(-\frac{h}{\sqrt{1-h^2}}(\pi+\gamma_2)\right). \qquad (16)$$

The amplitude x_3 for the third vibratory motion is, as before,

$$x_3 = e^{-\varepsilon_3 t}(C_{31}\cos\sigma_3' t + C_{32}\sin\sigma_3' t),$$

and as this vibration starts at the initial condition,

$$t=\frac{\pi+\gamma_2}{\sigma_2'}\,,\qquad x_3=0\,,\qquad \frac{dx_3}{dt}=\frac{dx_2}{dt}=\eta_2\sigma_1 d\exp\left(-\frac{h(\pi+\gamma_2)}{\sqrt{1-h^2}}\right),$$

thus the necessary elements can be calculated in the same way as in the second motion as above. Thus x_3 assumes the following form:

$$\left.\begin{aligned} &x_3=\frac{\eta_2\eta_3\sigma_1 d}{\sigma_3'}\,e^{-\varepsilon_3 t}\sin(\sigma_3' t-\gamma_3)\,,\\ &\text{where,}\\ &\eta_3=\exp\left\{\frac{\pi+\gamma_2}{\sigma_2'}(\varepsilon_3-\varepsilon_2)\right\},\qquad \gamma_3=\frac{\sigma_3'}{\sigma_2'}(\pi+\gamma_2)\,. \end{aligned}\right\} \tag{17}$$

The time at which x_3 assumes the maximum and its value are

$$\left.\begin{aligned} &t_3=\frac{1}{\sigma_3'}\left(\tan^{-1}\frac{\sigma_3'}{\sigma_2'}+\gamma_3\right),\\ &x_3'=\frac{\eta_2\eta_3\sigma_1 d}{\sigma_3}\exp\left\{\frac{h}{\sqrt{1-h^2}}\left(\tan^{-1}\frac{\sqrt{1-h^2}}{h}+\gamma_3\right)\right\}. \end{aligned}\right\} \tag{18}$$

And the velocity amplitude dx_3/dt at $t=\pi+\gamma_3/\sigma_3'$ is,

$$\left(\frac{dx_3}{dt}\right)_{t=\pi+\gamma_3/\sigma_3'}=-\eta_2\eta_3\sigma_1 d\cdot\exp\left\{-\frac{h}{\sqrt{1-h^2}}(\pi+\gamma_3)\right\}. \tag{19}$$

Just as being discussed above, x_4, x_5, etc. can be calculated and in general for i-suffix values,

$$\left.\begin{aligned} &x_i=\frac{\eta_2\eta_3\cdots\eta_i\sigma_1 d}{\sigma_i'}\,e^{-\varepsilon_i t}\sin(\sigma_i' t-\gamma_i)\,,\\ &\text{where}\\ &\eta_i=\exp\left\{\frac{\pi+\gamma_{i-1}}{\sigma_{i-1}'}\right\}(\varepsilon_i-\varepsilon_{i-1})\,,\qquad \gamma_i=\frac{\sigma_i'}{\sigma_{i-1}'}(\pi+\gamma_{i-1})\,,\\ &\quad\text{and}\qquad i=2,3,4,\cdots\,. \end{aligned}\right\} \tag{20}$$

And

$$\left.\begin{aligned} &x_i'=\frac{\eta_1\eta_2\cdots\eta_i\sigma_1 d}{\sigma_{i-1}}\cdot\exp\left\{\frac{h}{\sqrt{1-h^2}}\left(\tan^{-1}\frac{\sqrt{1-h^2}}{h}+\gamma_i\right)\right\},\\ &\text{where}\\ &\eta_i=\exp\left\{\frac{\pi+\gamma_i-1}{\sigma_{i-1}'}(\varepsilon_i-\varepsilon_{i-1})\right\}, \end{aligned}\right\} \tag{21}$$

$$\gamma_i=\frac{\sigma_i'}{\sigma_{i-1}'}(\pi+\gamma_{i-1}),$$
$$\text{and} \quad i=1, 2, 3, \cdots.$$

The successive amplitude ratio v_1, v_1, $\cdots$, v_i are

$$\left.\begin{aligned} v_1&=|x_1|/|x_2|=\frac{\sigma_2}{\eta_2\sigma_1}\exp\left\{\frac{h}{\sqrt{1-h^2}}\left(\tan^{-1}\frac{\sqrt{1-h^2}}{h}+\gamma_2\right)\right\},\\ v_2&=|x_2|/x_3|=\frac{\eta_2\sigma_3}{\eta_3\sigma_2}\exp\left\{\frac{h}{\sqrt{1-h^2}}(\gamma_3-\gamma_2)\right\},\\ &\cdots\cdots,\\ v_{i-1}&=|x_{i-1}|/|x_i|=\frac{\eta_{i-1}\sigma_i}{\eta_i\sigma_{i-1}}\exp\left\{\frac{h}{\sqrt{1-h^2}}\left(\gamma_i-\gamma_{i-1}\right)\right\}.\end{aligned}\right\} \quad (22)$$

When $\sigma_1=\sigma_2=\cdots=\sigma_i$, then $\gamma_i-\gamma_{i-1}=\pi$ and $\eta_i=1$, thus, $v_1=v_2=\cdots=v_{i-1}=e^{\frac{\pi h}{\sqrt{1-h^2}}}$; or when ε_1, ε_2, $\cdots$, ε_i are equal to zero, i.e., $h=0$, then $\eta_2=\eta_3=\cdots=\eta_i=1$, thus,

$$v_1=\frac{\sigma_2}{\sigma_1}=\frac{T_1}{T_2}, \qquad v_2=\frac{\sigma_3}{\sigma_2}=\frac{T_2}{T_3}, \qquad \cdots, \qquad v_{i-1}=\frac{\sigma_i}{\sigma_{i-1}}=\frac{T_{i-1}}{T_i}. \quad (23)$$

3. Free Vibration of Actual House Under Large Amplitude

Here the relationships obtained above will be applied to the experimental results of an actual house subjected to free vibrations of larger amplitude. The house[4] undergoing the experiment was a tile roof wooden small residential house of $13.2\times7.3\,m^2$ (24 tsubo) floor area. Fig. 2 is a record of the free vibration of the test house, showing A-component at 2.5 m high and the free vibration was given by releasing the load suddenly. The value P of load is that of the horizontal component of the A-component of the load at the point of application. Table 1 shows amplitudes and periods directly read from the original record of the free vibration, their averages, and the amplitude ratios obtained therefrom. And figures shown in the column of 1st, 2nd, $\cdots$ vibration are corresponding to the maximum amplitudes x_1', x_2', $\cdots$ and the values t_1, $T_2'/2$, which represent the period. Though the value of T_1' is not shown

4) *loc, cit.*, 3).

P=0.86 ton P=1.29 ton P=1.72 ton

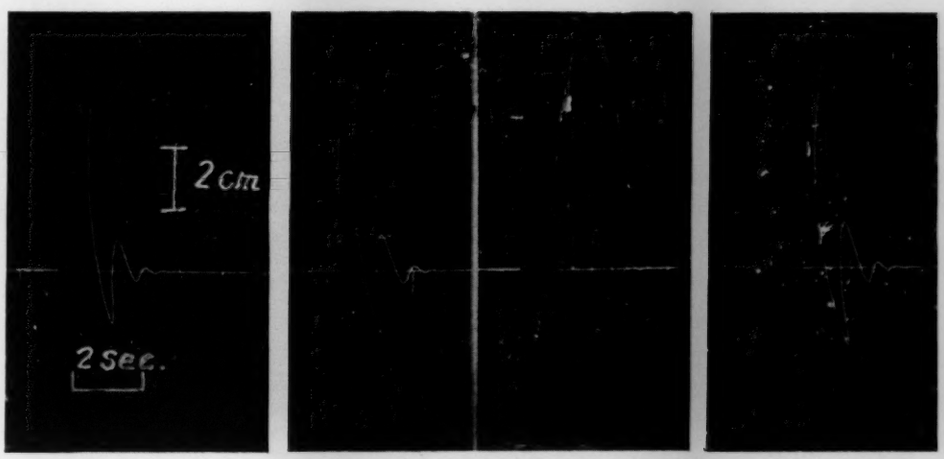

P=1.72 ton P=2.15 ton P=2.58 ton

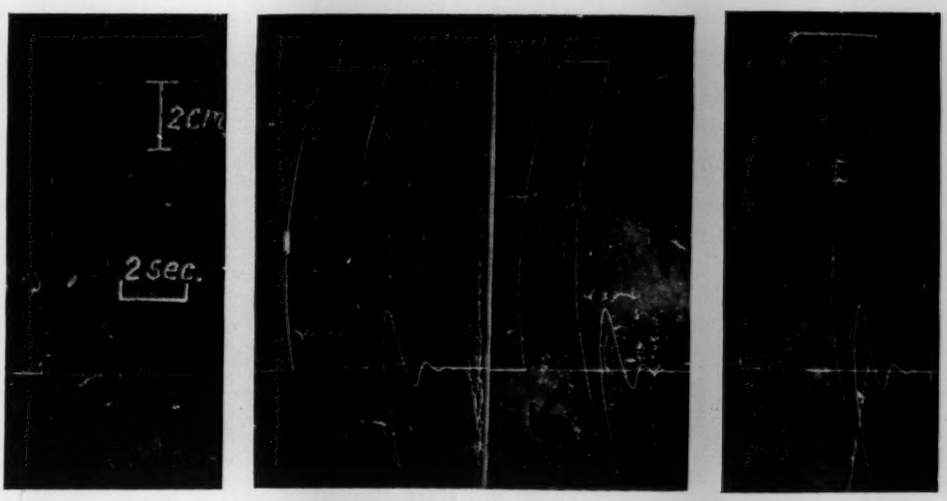

P=3.01 ton P=3.44 ton P=3.87 ton

Fig. 2. Records of free vibration of the wooden house. P: tensile loads.

Table 1. Amplitudes and periods directly read from original records of the free vibration.

Load (kg.)	No.	A			B			C			D			E			F		R
		x_1'	t_1	v_1	x_2'	T_2'	v_2	x_3'	T_3'	v_3	x_4'	T_4'	v_4	x_5'	T_5'	v_5	x_6'	T_6'	(mm)
		mm	sec.		mm	sec.		mm	mm		mm	sec.		mm	sec.		mm	sec.	
430	No. 1	5.4	0.362		1.6	0.56		0.6	0.38		0.4	0.40							⊕ 6.0
	No. 2	6.6	0.218		2.0	0.62		0.9	0.50		0.4	0.36							0
	mean	6.0	0.290	3.3	1.8	0.59	2.2	0.8	0.44	2.0	0.4	0.38							
860	No. 1	19.0	0.342		5.8	0.72		2.8	0.64		0.8	0.61		0.6	0.42		0.2	0.42	⊖ 0.2
	No. 2	21.2	0.304		6.8	0.77		2.6	0.72		1.2	0.57		0.4	0.44		0.2	0.42	⊖ 0.4
	mean	20.1	0.323	3.2	6.3	0.75	2.3	2.7	0.68	2.7	1.0	0.59	2.0	0.5	0.43	2.5	0.2	0.42	
1290	No. 1	30.0	0.304		11.3	0.76		5.8	0.96		1.8	0.60		0.7	0.59		0.3	0.42	⊖ 0.8
	No. 2	34.6	0.352		12.0	0.76		6.2	0.88		2.0	0.68		0.7	0.53		0.3	0.46	⊖ 0.1
	mean	32.3	0.328	2.8	11.7	0.76	2.0	6.0	0.92	3.2	1.9	0.67	2.7	0.7	0.56	2.5	0.3	0.44	
1720	No. 1	47.6	0.352		15.6	0.76		9.0	0.99		2.8	0.72		1.2	0.57		0.5	0.49	⊖ 1.2
	No. 2	48.8	0.333		16.8	0.80		10.0	1.09		3.0	0.72		1.2	0.53		0.4	0.49	⊖ 0.6
	mean	48.2	0.342	3.0	16.2	0.78	1.7	9.5	1.04	3.3	2.9	0.72	2.4	1.2	0.55	2.8	0.45	0.49	

(to be continued)

(continued)

2150	No. 1	60.6	0.344		19.2	0.77		11.8	1.18		3.6	0.88		1.4	0.60		0.5	0.53	⊖ 0.1
	No. 2	62.4	0.333		20.4	0.83		12.4	1.18		3.6	0.84		1.4	0.60		0.5	0.53	⊖ 1.0
	mean	61.5	0.338	3.1	19.8	0.80	1.6	12.1	1.18	3.4	3.6	0.86	2.6	1.4	0.60	2.8	0.5	0.53	
2580	No. 1	73.0	0.304		23.4	0.84		14.4	1.11		4.2	0.76		1.5	0.65		0.6	0.53	⊖ 1.2
	No. 2	74.6	0.361		24.6	0.92		14.8	1.21		4.8	0.78		1.6	0.61		0.7	0.53	① 0.6
	mean	73.8	0.333	3.1	24.0	0.88	1.6	14.6	1.16	3.7	4.5	0.77	2.8	1.6	0.63	2.5	0.65	0.53	
3010	No. 1	85.2	0.380		27.4	0.98		16.6	1.18		5.5	0.91		1.9	0.68		0.5	0.56	⊖ 0.5
	No. 2	84.6	0.374		26.8	0.87		16.8	1.18		5.5	0.87		1.8	0.72		0.6	0.53	⊕ 0.6
	mean	84.9	0.377	3.1	27.1	0.93	1.6	16.6	1.18	3.0	5.5	0.89	2.9	1.9	0.70	3.5	0.55	0.55	
3440	No. 1	95.6	0.371		31.4	0.99		18.0	1.25		5.6	0.95		1.8	0.72		0.7	0.57	⊕ 1.0
	No. 2	98.6	0.380		32.8	0.93		19.8	1.32		5.8	0.87		2.0	0.70		0.6	0.47	⊖ 0.2
	mean	97.1	0.376	3.0	32.1	0.96	1.7	18.9	1.29	3.3	5.7	0.92	3.0	1.9	0.71	2.9	0.65	0.52	
3870	No. 1	104	0.437		34.8	1.01		21.2	1.27		5.8	0.85		2.0	0.76		0.6	0.57	⊖ 0.5
	No. 2	109	0.399		34.4	0.91		20.6	1.32		5.6	0.99		2.0	0.80		0.6	0.53	⊕ 0.7
	No. 3	108	0.418		35.6	1.04		20.0	1.33		5.7	0.87		1.9	0.80		0.6	0.57	⊖ 0.6
	mean	107	0.418	3.1	34.9	0.99	1.7	20.6	1.31	3.6	7.7	0.90	2.9	2.0	0.79	3.3	0.6	0.56	

note

1. $v_1=x_1'/x_3'$, $v_2=x_2'/x_3'$..... 2. R: residual permanent deformation. ⊕.... x_1', x_3'...., ⊖.... x_9', x_4',.... side.
3. A, B, C,.... first, second, third amplitude respectively.

on the Table 1, it can be obtained from the relationship, $T_1'=2\pi t_1 \Big/ \left(\pi-\tan^{-1}\frac{\sqrt{1-h^2}}{h}\right)$, it is smaller value than $4t_1$ and it decreases with a decrease in the value of damping factor. Table 2 indicates the

Table 2. $T_1'=2\pi t_1 \Big/ \left(\pi-\tan^{-1}\frac{\sqrt{1-h^2}}{h}\right)$.

h \ t_1	sec. 0.418	sec. 0.376	sec. 0.377	sec. 0.333	sec. 0.338	sec. 0.342	sec. 0.328	sec. 0.323	sec. 0.290
	sec.	sec.	sec.	sec.	sec.	sec.	sec.	sec.	sec.
0	1.67	1.51	1.51	1.33	1.35	1.37	1.31	1.24	1.16
0.1	1.63	1.42	1.42	1.25	1.27	1.29	1.23	1.17	1.09
0.2	1.51	1.36	1.36	1.20	1.21	1.23	1.18	1.11	1.04
0.3	1.41	1.26	1.26	1.11	1.13	1.15	1.10	1.08	0.97
0.4	1.33	1.19	1.19	1.06	1.07	1.09	1.04	1.02	0.92
0.5	1.26	1.13	1.13	1.00	1.01	1.03	0.98	0.97	0.87
0.6	1.19	1.07	1.07	0.95	0.96	0.97	0.93	0.92	0.82
0.8	1.05	0.95	0.95	0.84	0.85	0.86	0.83	0.82	0.73

value of T_1' obtained from t_1, in which the greater value of T_3 is remarkably noticed in a larger range of amplitude when the period of free vibration for each load is observed. For example, at 3.87 ton of load, T_1', T_2', T_3', $\cdots$ are 1.51 sec (from $T_1'=2\pi t \Big/ \left(\pi-\tan^{-1}\frac{\sqrt{1-h^2}}{h}\right)$, at $h=0.2$) 0.99 sec, 1.31 sec, 0.90 sec, $\cdots$ respectively, which against all loads is in a same trend, as the relationship $T_1'>T_2'<T_3'$ is observed.

The damping ratios v_1, v_2, $\cdots$ are nearly of constant value except in the range of very small load, i.e., they are 2.8~3.1, 2.0~1.6 and 3.0~3.7 respectively and the damping of x_2 is extremely great in comparison with x_3, which may be attributed to the decrease in the restoring force to the direction along which a considerably large amount of the deformation was given under the free vibration. Figs. 3~6 show the relationships of x_2', x_3', x_4' against h which were obtained by giving t_1, T_2', T_3', T_4' and the mean value of $x_1'=d$ to the value of x_i' in equation (21) against four values of load varying 3.87 ton~0.86 ton. The circle mark indicates the observed value of x_2', x_3' and x_4' respectively. For 0.86 tons of load, the calculated and experimented values of x_2', x_3' and x_4' coincide at the value of damping factor $h=0.23$; for 1.72 tons load, at $h=0.21$, 0.23 and 0.25; for 3.01 tons load, at $h=0.23$, 0.24, 0.26; for 3.78 tons load, at $h=0.21$, 0.23, and 0.25 respectively. Thus the damping

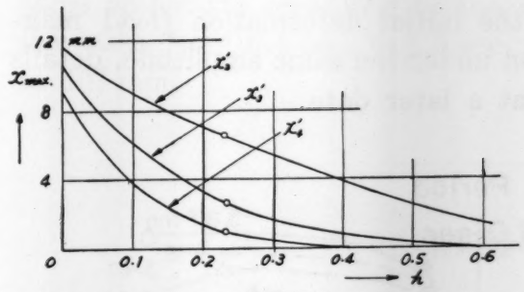

Fig. 3. The case of $x_1'=20.1$ mm, $t_1=0.320$ sec, $T_2'=0.75$ sec, $T_3'=0.68$ sec $T_4'=0.59$ sec. ○: Observed values of x_2', x_3' and x_4' respectively.

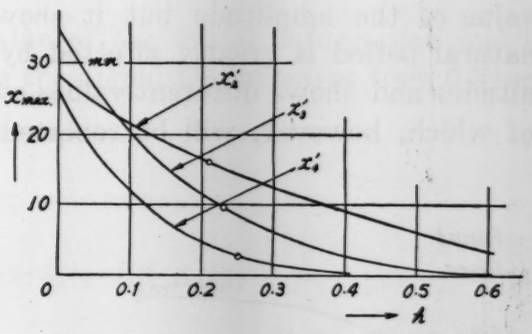

Fig. 4. The case of $x_1'=48.2$ mm, $t_1=0.340$ sec, $T_2'=0.78$ sec, $T_3'=1.04$ sec, $T_4'=0.72$ sec. ○: Observed values of x_2', x_3' and x_4'. respectively.

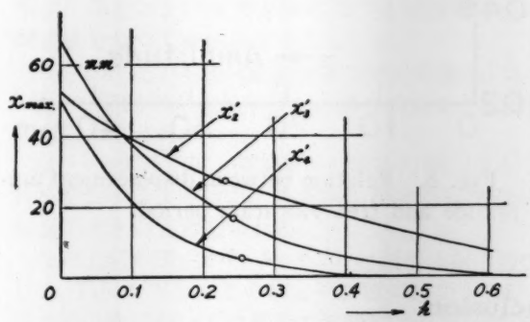

Fig. 5. The case of $x_1'=84.8$ mm, $t_1'=0.377$ sec, $T_2'=0.93$ sec $T_3'=1.18$ sec, $T_4'=0.89$ sec. ○: Observed values of x_2', x_3' and x_4' respectively.

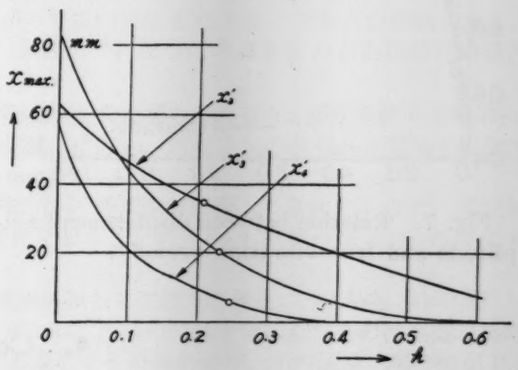

Fig. 6. The case of $x_1'=107$ mm, $t_1=0.418$ sec, $T_2'=0.99$ sec, $T_3'=1.31$ sec, $T_4'=0.90$ sec. ○: Observed values of x_2', x_3' and x_4' respectively.

factor has a tendency to increase slightly in accordance with a decrease in the amplitude (with natural period too for this case), but such trend is extremely small in comparison with a change in the amplitude ratio obtained by observation. These facts may tell that it is not a damping factor that changes by itself but it does not change by a change in the period, i.e., restoring force.

Figs. 7 & 8 show the relationship between period and amplitude under the free vibration, + side represents the periods T_1', T_3', T_5' corresponding to the amplitudes $i=1$, 3, 5, namly, x_1', x_3', x_5' and − side stands for the period T_2', T_4', T_6' corresponding to the amplitude $i=2$, 4, 6, namely x_2', x_4' and x_6', T_1' on the figure was calculated from t_1 at $h-0.2$.

The amplitude-period relationship is of similar trend on both sides of + and − and the natural period shows sharp increase up to certain

value of the amplitude but it shows downward trend thereafter. The natural period is greatly affected by the initial deformation (load magnitude) and shows different values even under the same amplitude, details of which, however, will be reported at a later date.

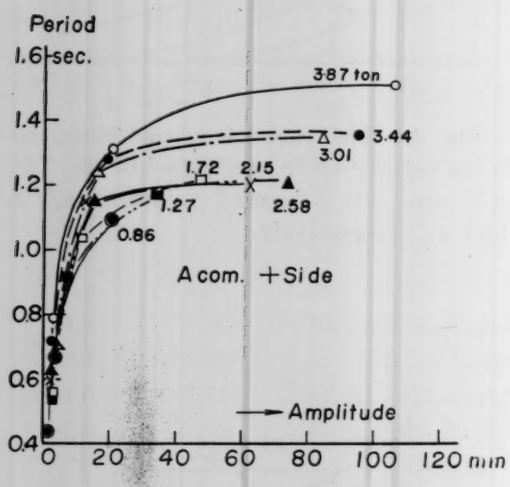

Fig. 7. Relation between displacement amplitude and free vibration period.

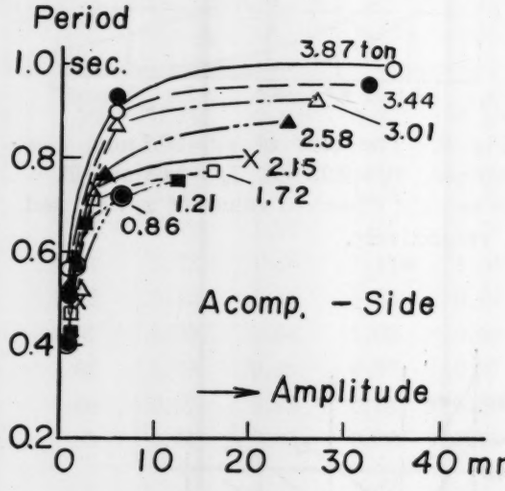

Fig. 8. Relation between displacement amplitude and free vibration period.

4. Conclusion

In this paper, a free vibration of a pendulum of simple mass system was considered, in which the restoring force varies at each amplitude and the relationships among amplitude, period & damping factor were theoretically derived and finally numerical calculations were made introducing the experimental data obtained for the free vibration of wooden house under great amplitude.

The comparison of the results and those from the actual measurements reveals that both values coincide at values of damping factor ranging $h=0.20\sim0.26$, showing a trend of slight increase with a decrease in either amplitude or period and further the fact that the amplitude ratio obtained from the measurements sharply varies at every amplitude may mean that a damping factor would change by change in the period, i.e., restoring force rather than it changes by itself. Then, T_1' was calculated from t_1 under $h=0.20$, which in turn enabled to obtain the relationship between amplitude & period of observed data, the results are that the natural period assumes different values even under the

same amplitude according to the value of the initial deformation and it increases from 0.4 sec. to 1.5 sec. as the amplitude increases from 0.2 mm to 107 mm.

---

19. 木造家屋の耐震性 (第 3 報)

地震研究所 西村源六郎 鈴木正治

構造物の振動実験には種々の条件によつて振巾に制限をうける場合が多い．現在まで多くの人々によつて測定された構造物の固有周期，減衰係数等の測定値の大部分は微小振巾による測定結果であるので大振巾時における振動特性との関連をつけておく必要がある．

この研究では，まづ単一質量系の振子の復元力が，各振巾毎に変化するような自由振動を考え，振巾，周期および減衰係数の関係を理論的に求め，大振巾で行なつた木造家屋の自由振動の実験の測定値を使つて数値計算を行なつた．

つぎに，その結果（数値計算で求めた振巾）と実測振巾とを比較して見ると，減衰係数 h が 0.20～0.26 の範囲で両者が一致し，固有周期または振巾が減少すると，減衰係数の値は多少増加する傾向にあることがわかつた．

以上の事柄より，実測値から求めた振巾比が大振巾時に各振動毎に著しく変化するのは，減衰係数が変化するよりはむしろ各振巾毎に固有周期が変化すること，すなわち家屋の復元力が変化する影響が大きいと考えられる．

なお上記の理由から $h=0.20$ 付近が大振巾時の減衰係数として適当と考え，t_1 から $h=0.20$ として T_1' を求め，この値と実測値の振巾および周期からこれ等の関係を求めた．その結果固有周期は大振巾時においては最初の変形により同一振巾でも著しくその値が異り，その値は，振巾値が 0.2 mm～107 mm に増加すると 0.40 sec～1.50 sec に増加することが認められた．

地震研究所彙報
第38号 (1960) 345-354頁

20. 地震計用トランジスター増幅器

地震研究所　松本英照

(昭和34年11月24日発表——昭和35年3月30日受理)

§1·1

簡単な装置でたかい感度と安定度をもつ地震計がてがるに使用できるならば，地震の研究はもつと多角的にすすめることができるとおもわれる．よりたかい感度をもとめ，おおくのひとびとは，それぞれことなつた目的の観測に対し，いろいろな地震計を設計してきたが，まだ充分な感度のえられていない分野もおおい．

地震計のなかで，現在もつともたかい感度と安定度のえられる方式は，動線輪型動電換振器を使用し，増幅器で増幅した出力を記録させる方式であるが，この場合換振器と増幅器の結合における増幅器入力インピーダンスの制動作用，あるいは増幅器内発生雑音および増幅器電源の安定度から，安定な感度は制限をうける．

真空管を使用した E.L.F. 増幅器はいろいろ発表されているが，信号を直接真空管で増幅する方法では入力換算の発生雑音が 1 μV 以下におさえることができず，最高の感度はこれにより限界をあたえられる．信号をチョッパーで交流化し，トランスでこの電圧を昇圧したのち増幅する方法では入力換算雑音はひくくおさえられるが，入力インピーダンスがひくく，これに結合できる高感度の小型換振器はえがたいから，総合してたかい感度の地震計はえられず，真空管を使用して構成される地震計の感度は既存の装置で限界にたつしているとおもわれる．

筆者はさきに簡単で安定堅牢な電子地震計用増幅器として H.F.S.A. (M-1), M.F.S.A. (M-2)[1] および地震計用対数増幅器[2] を発表したがこれは使用目的の関係で装置を簡略化しているから，電源の安定度が充分たかくとれず充分たかい感度をうることはできなかつた．

この感度を補足するために筆者はさきにトランジスターの前置増幅器[3] を設計し，地震計の安定度と簡易さをそこなうことなく，感度をあげることに成功したが，このことからトランジスターが地震の経常観測にも高信頼度をもつて使用しうることと，真空管増幅器よりもたかい感度の観測がトランジスター使用の増幅器では期待できることが判明した．

電子管とトランジスターの一般的な特長の比較はすでに論議しつくされているとおもわれるが，ここにトランジスターが電子管よりもすぐれている点を要約してみると，

---

1) H. MATUMOTO, *Bull. Earthq. Res. Inst.*, **37** (1959) 375.
2) H. MATUMOTO, *ditto.*, 381.
3) H. MATUMOTO, *ditto.*, 525.

1. 装置の小型軽量化が容易である.
2. 消費電力がすくなく低電圧で動作するので，電源に乾電池の長期使用が可能で電源からうけるおおかたの束縛から解放される.
3. 使用法により入力換算の回路雑音をひくくおさえることができるから，これにより制限される利得をよりたかめうることが期待できる.

以上であるが，筆者は今回これらの特長を活用するように，全部トランジスター使用の増幅器を試作したところよい結果をえたのでここに発表する.

§ 1·2

この増幅器の設計の主目的はトランジスターの利点を増幅器にいかに活用するか，そしてトランジスター使用で現存する増幅器の特性感度をいかに改良するかということにおいた.

真空管増幅器の設計上の難点である回路内発生雑音の低減と，電源の高度の安定化は，前者は前置増幅器の時にすでにトランジスターで克服できたし，後者は乾電池使用で完全に解決できるから，今回はさらに，トランジスター使用でよりひくい周波数での感度をあげることも考慮して設計したところ，おおくの目的に使用できる便利で高感度の増幅器を小型軽量しかも電源内蔵の完全な可搬型で製作することに成功した.

§ 2·1

Fig. 1 にこの増幅器の配線図をしめす.

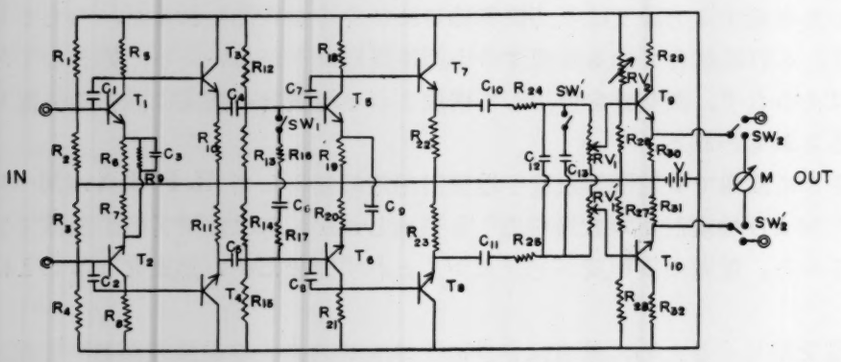

R_1. R_4. R_{12}. R_{15}.	200 KΩ.	C_4. C_5. C_{10}. C_{11}. C_{13}.	200 μF.
R_2. R_3. R_{13}. R_{14}.	100 KΩ.	C_6.	10 μF.
R_5. R_6. R_7. R_8. R_{10}. R_{11}. R_{18}. R_{19}. R_{20}. R_{21}. R_{22}. R_{23}.	50 KΩ.	C_{12}	1 μF.
R_9.	3 KΩ.	RV_1.	500 KΩ.
R_{16}. R_{17}. R_{24}. R_{25}. R_{26}. R_{27}. R_{28}.	20 KΩ.	RV_2.	30 KΩ.
R_{29}. R_{32}.	1 KΩ.	V.	6 V.
R_{30}. R_{31}.	10 KΩ.	M.	50 μA full scale DC ammeter.
C_1. C_2. C_7. C_8.	0.1 μF.	T_1. T_2.	2 T 68 (Sony).
C_3. C_9.	400 μF.	T_3. T_4. T_5. T_6. T_7. T_8. T_9. T_{10}.	2 T 65 (Sony).

Fig. 1. Circuit of the amplifier.

この増幅器は使用目的によつて特性や出力の検出器をきりかえうるように設計してある.

SW_1 は周波数特性，SW_2 は出力のきりかえスウィッチで，SW_1 により装置を地震中間周波 (Seismic medium frequency 0.3～3.0 c/s) と，地震高周波 (Seismic high frequency 3.0～30 c/s) の観測装置にきりかえ，SW_2 により，出力検出を内蔵電流計と外部記録器にきりかえることにより，装置を土地微動検出器と，普通地震計とにきりかえうる.

この増幅器の回路は雑音の低減をはかり，低周波の利得をあげるためと，出力端の直流の平衡をとるために対称型にくみたてている.

回路構成は初段はエミター接地コレクター接地の直結回路で，この結合法は温度特性がよく入力換算の雑音を他の回路に比較し，もつともひくくおさえることができる．この回路から発生する入力換算の雑音は約 0.5 μV で，このような低雑音は，真空管回路では容易にうることはできない.

この結合からは，さらに入力・出力のインピーダンスの面でも利点がえられる．入力インピーダンスは地震中間周波帯においては約 50 KΩ でトランジスター回路としては比較的たかく，現存するおおかたの換振器にたいしては増幅器から過度の制動作用をあたえない．出力インピーダンスは 10 KΩ 以下であるから，次段との結合により損失はなく，周波数特性調整回路にトランジスターが影響をあたえない利点がある．この利点を必要とするので二段目も初段と同様の結合にしたが，この結合では一段あたりの利得が約 35 db で，トランジスター使用数にたいして電圧利得はすくない.

最終出力段は電流増幅のコレクター接地回路の変形で，高感度の検流計を接続しても，ドリフトの影響をうけないよう，コレクターに直流平衡用負饋還抵抗を挿入して，回路の安定をはかつているから，可変偏倚抵抗 RV_2 の加減とあわせて，直流の平衡を安定に保持することができる.

この増幅器の総消費電流は約 1.8 mA であるから，単三乾電池を電源として連続使用しても，正常な動作を保持する電池寿命は約 1 週間である．回路構成に使用した部品はすべて市販品を使用し，電源は単三乾電池 4 本を 6 V で使用，内蔵している.

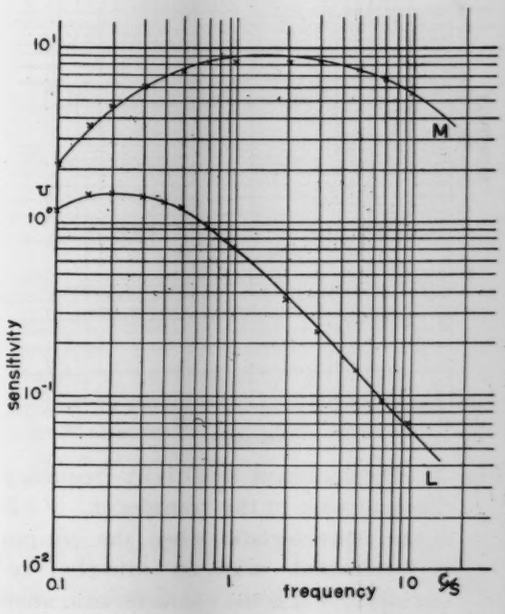

Fig. 2. Gain-frequency characteristic of the amplifier for two ways (at 20°C). M is the characteristic of the amplifier used for high frequency seismograph, and L is the characteristic of the amplifier used for medium frequency seismograph.

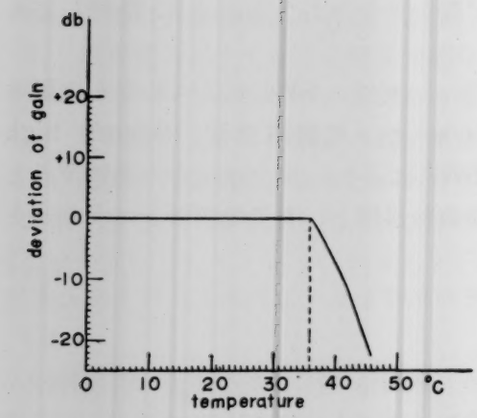

Fig. 3. Gain deviation of the amplifier versus temperature.

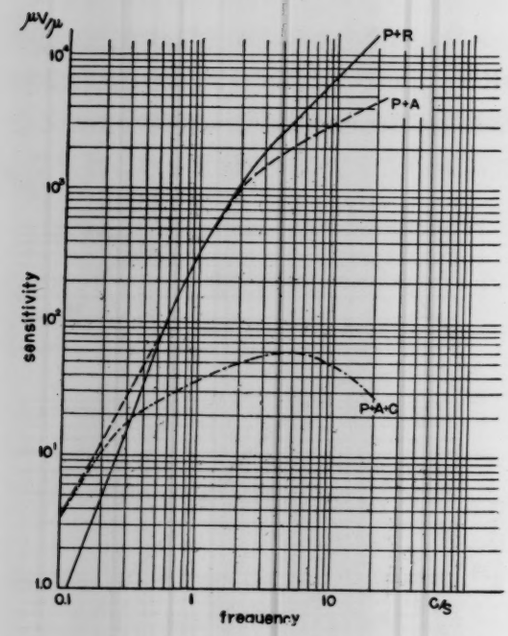

Fig. 4. Displacement sensitivity-frequency characteristic of the transducer. P+R is the characteristic when the out-put is terminated with 60 kilo-ohm resistance, P+A is the characteristic when the out-put is terminated with the amplifier directly, and it is applied to high frequency seismograph, P+C+A is the characteristic when the out-put is terminated with 10 μF capacitance and the amplifier, and it is applied to medium frequency seismograph.

Fig. 2 にこの増幅器の周波数特性をしめす．感度はトランジスターの使用数にたいして，たかいものではないが，この感度が低雑音で安定度たかくえられ，市販の高感度検流計と結合することにより，現存する地震計よりも高感度の地震計を構成できたことで，本増幅器は設計の目的を充分満足させえたものといえる．

Fig. 3 にこの増幅器の利得の温度特性をしめす．高温時に利得がさがるので使用条件に制限をうけるが，常温では満足すべき特性をしめす．

§ 2·2

この増幅器の入力インピーダンスは，小型で電圧感度のよい換振器にたいしても制動作用をつよくあたえぬように，充分たかく設計しているから真空管増幅器に結合する目的をもつて設計したおおかたの換振器を使用することが可能である．

また使用する検流計は内部抵抗が 100Ω 以下で感度 0.1 mm/1 μA 以上のものであれば記録最大振幅 100 mm まではひずみなく記録できる．市販されている電磁オッシログラフの振動子でこの増幅器の検流器として条件の適合する製品は横河電気の D 型振動子と三栄測器の 30 c/s 振動子があるから，これらの電磁オッシログラフを記録器に使用して地震計を構成すれば高感度の地震計をうることができる．

Fig. 4 に小型軽量で調整が簡単，しかも機械強度がつよく移動用換振器として便利なため今回おもに使用した地震研究所技術部製作の 1 c/s 水平動動線輪型換振器の変位感度周波数特性をしめす．図中で (P+R) は出力端に 60 KΩ の抵抗を接続し，振子の制動を，この抵抗をながれる電流の作用で，臨界

制動状態にしたときの換振器出力端における出力周波数特性をしめし，(P+A) は換振器とこの増幅器を接続したときの増幅器入力における換振器出力周波数特性，(P+A+C)は地震中間周波の波動を測定するためには不必要な高周波を換振器出力にふくませないように，10 μF のコンデンサーを出力端に並列に接続してこの増幅器に結合したときの増幅器入力における平坦化された換振器出力の周波数特性である．

Fig. 5 に上述の増幅器と 1 c/s 水平動換振器の外観写真をしめす．装置の小型化にたいするトランジスターの効用が本装置にも充分発揮されていることを証明するものである．

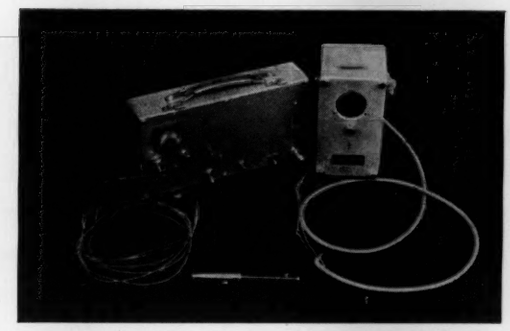

Fig. 5. Appearance of the amplifier and the transducer used.

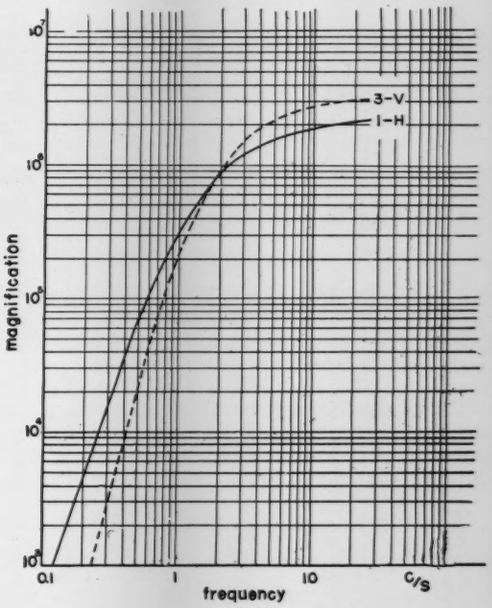

Fig. 6. Over all characteristic of the seismograph used for high frequency observation. 3-V is the characteristic obtained when a 3 c/s vertical transducer[4] (6 V/kine) is used, and 1-H is the characteristic obtained from a 1 c/s horizontal transducer (1.2 V/kine).

§ 2·3

以上にのべた換振器，増幅器，記録器から構成される地震計は地震中間周波ならびに地震高周波の観測に使用できるが，つぎにこれらの二種類のくみあわせによつて構成した二様の地震計の周波数特性をしめす．

Fig. 6 は近地地震あるいは，爆破地震動を観測するのに適当な特性をもつように構成された，地震高周波観測用途地震計の総合特性で図中 1-H は上述の 1 c/s 水平動換振器，3-V はすでに紹介した地震研究所技術部製作の 3 c/s 上下動換振器[4] を使用し，増幅器を (H) の状態において，記録器三栄測器製作の電磁オッシログラフを使用したときにえられる．

Fig. 7 にこの装置の地震中間周波用途地震計構成時における総合特性を，萩原式電磁地震計[5] の長周期型 H·E·S-L，ならびに標準型 H·E·S-B の特性と比較してしめす．図

4) H. MATUMOTO, *Bull. Earthq. Res. Inst.*, **37** (1959), 527.
5) T. HAGIWARA, *Kagaku*, **28** (1958), 342.

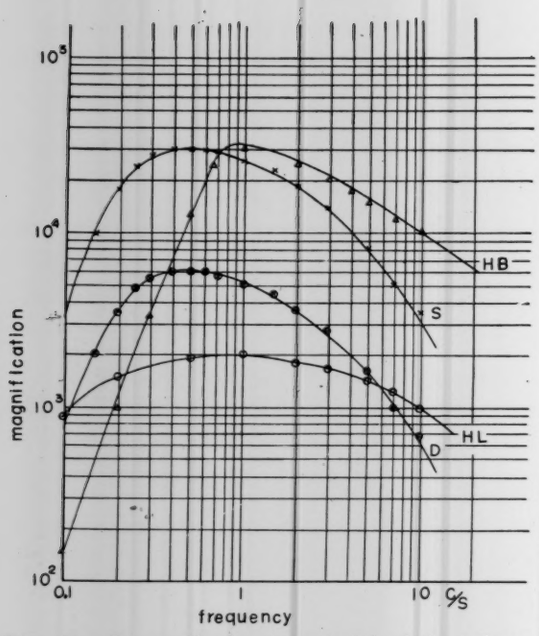

Fig. 7. Over all characteristic of the seismograph set in medium frequency way compared with two types of routine seismograph H.E.S[5].(HL……Tp = 1s, Tg = 20s,
HB……Tp = 1s, Tg = 1s,).
S is the characteristic of the seismograph with the recorder having a sensitivity of 1mm/μA at 0～30c/s. (manufactured by K.K. Saňei Sokuki).

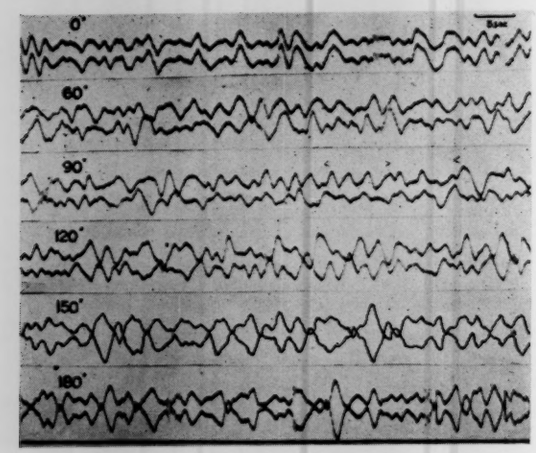

Fig. 8. Seismograms of microseisms recorded at Naarai on Oct. 21st 1959 by the two seismographs of which characteristic is indicated in Fig. 7. as D. Numerals show the directional angle between two transducers for the seismographs used.

中 (D) および (S) でしめす特性は Fig. 4 (P+A+C) でしめした換振器出力を Fig. 2 (M) でしめした状態の，この増幅器に供給して，記録器横河電気電磁オッシログラフおよび三栄測器電磁オッシログラフを使用したときにえられる，それぞれの地震計の感度特性である．

§ 3·1

この増幅器は地震中間周波の感度が携帯用とすれば，かなりたかいものであるから，三東哲夫はこの増幅器によつて構成した地震計 (D) を，颱風時の波浪とそれによつて発生する脈動とを海岸で同時に観測して，両者の関係を定量的にしらべる実験に使用し，よい結果をえた[6]．この結果からみるとこの装置の特性は脈動全般を観測するには，低周波の特性がなお不満足であるが，颱風によつて発生する脈動の主成分を観測するには，ほぼ満足すべきものであることが判明し，さらにその観測が颱風によつて誘起された停電によつて，さまたげられなかつたので，このような観測にたいするこの増幅器の価値を，充分認識させた．

Fig. 8 に千葉県下名洗港において，三東によつて颱風 59-19 号近接時に観測してえられた記録をしめす．記録から2台の装置間には振幅，位相の周波数特性の相違はみとめられず，この装置が3点観測法や波動の合成を目的とするような高度の観測に使用しうることが証明できた．

§ 3·2

この増幅器は内蔵されたメーターによつ

6) T.A. Santô, *Bull. Earthq. Res. Inst.*, **38** (1960), 241.

て，換振器と出力の周期と振幅を，よみとることができる．その感度は使用している 50 μA の直流電流計で地動 1 μ (0.1～1.0 c/s) にたいし指針が 400 μA 相当目盛の振動をするから，たいへんちいさな地動でも検出できる．爆破地震動観測の観測点の選定に，この装置を携帯使用したところ，非常によい観測点をうることができたので，この装置が観測点選定の調査に威力を発揮することを証明できた．

§ 3·3

真空管増幅器を使用した高感度地震計はいままでもよく爆破地震動の観測に使用されてきた[7]．

しかしこれらの地震計は，真空管の電源を商用交流から供給あるいは補充しなければならないため，観測点選定に相当制約をうけてきたし，その設備や附帯設備も移動用とすればおおきすぎるきらいがあつた．筆者等は 1959 年 11 月 20 日の第 5 次御母衣大爆破地震動観測に，このトランジスター増幅器を使用し，$\Delta \fallingdotseq 290$ km の地点で観測を実施し信号の記録に成功した．このときの装備は三栄測器の電磁オッシログラフと本増幅器 (H)，それからすでにのべた 3 c/s 上下動換振器と 1 c/s 水平動換振器で構成した地震計，ならびに刻時用のトランジスター短波受信機で，従来にない小設備で，設置が容易であつたから，移動用の地震計は，かくあるべきであるとおもわしめた．Fig. 9 にこの時えられた記録をしめす．

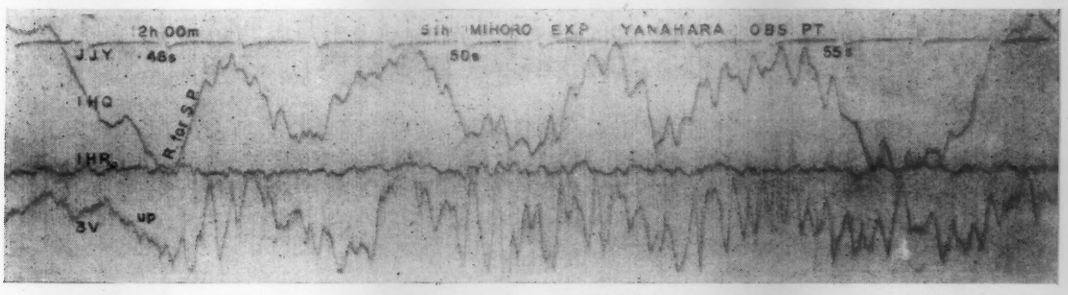

Fig. 9. Seismogram obtained at a station of 290 km distance from the shot point in the 5th Miboro explosion seismic observation by the seismograph, characteristic of which is shown in Fig. 6..

§ 4

われわれの目的は，おもにひとつの現象に着目し，記録の中からその現象を摘出してその解析をおこなうことであるが，今回設計した増幅器は多目的に使用できるようにつくられているので，ことなつた性質の現象が重畳して観測されるおそれもある．Fig. 9 の記録にもその難点が現実にあらわれ，脈動と爆破地震動が重畳して記録されているが，爆破地震動観測のためには，のぞましい状態の記録ではない．勿論このときは颱風 59—21 号

7) T. ASADA, *Zisin*, **7** (1954), 116.
N. DEN, *Zisin*, **6** (1953), 101.

が発生していて脈動の振幅もおおきかつたので，とくにそれがおおきく記録されたのではあるが，電気的に容易に除去できることであるから，今後製作するときには，SW_1 と連動で C_3, C_9 を 200 μF から 50 μF にきりかえ，入力インピーダンスをあげ，地震高周波の感度をよりたかめたうえに，中間周波の感度をさげるような回路にして，この不都合を除去することがのぞましい．

また今後は記録をテープレコーダーに記憶させて直接解析のできるような装置[8]にも，この増幅器を結合したいから，電圧利得のたかい回路構成にもきりかわるよう設計をすすめていきたい．

§ 5

以上この増幅器について利点欠点をいろいろあげてみたが，これらを総合して，トランジスターの採用は，電子地震計におおくの利点をあたえ，地震観測技術の向上に資するところがおおきいことが判明したのであるから，今後もトランジスターのすぐれた性質に着目し，すぐれた観測装置をつくりだすよう研究をつづけていきたいとおもう．

おわりにこの研究をおこなうにあたり，うけた研究室主任宮村助教授ならびに同僚三東哲夫，後藤健一の両氏の御指導と御援助を深く感謝する．

---

20. A Transistor Amplifier for Seismographs.

By Hideteru MATUMOTO,
Earthquake Research Institute.

Many seismologists realized various types of seismographs having sufficient quality to make satisfactory observations for their special research purposes.

Neverthless, at present we find no instrument to observe satisfactorily in the seismic high frequency band, which is important in a study of local small earthquakes or explosion seismology from the standpoint of sensitivity, portability, and robustness for field use.

It is really important to construct an instrument that is able to be set up easily for frequent movement in the field.

The author selected a seismograph which consists of a amplifier with a usual galvanometric recorder and an electro-dynamic transducer for those purposes, because they are robust and small relative to their quality and show excellent characteristics in sensitivity, stability and internal noise.

The sensitivity of a seismograph with vacuum tube amplifier[1),2),7)] seems to have already reached its maximum at present.

We need higher sensitivity in order to construct an adequate seismograph for the study stated above, and we must develop some techniques for decreasing internal noise of the amplifier and simplification of the instrument.

Recently the author clarified[3)] that a transistor amplifier is superior to the vacuum tube amplifier in circuit noise, and consumption of source, and size of instrument, i.e.,

8) K. AKI, *Bull. Earthq. Res. Inst.*, **35** (1957), 415.
S. MIYAMURA, M. TUJIURA, *Bull. Earthq. Res. Inst.*, **37** (1959), 359.

as a whole, in portability and quality of the instrument.

Thus the author designed and constructed a new seismograph, making use of those advantages in the amplifier.

The limit of the sensitivity due to the generated noise in the head tube and delicacy of operation could be improved in this amplifier by using transistors and dry cells instead of vacuum tubes and an eliminated DC source, and also could expand its frequency characteristic more widely to a lower frequency than before.

This amplifier has its power source in the small cabinet, and consequently it seems to be almost an ideal portable seismograph for the present.

The circuit of the amplifier is shown in Fig. 1.

The characteristics can be changed by switches according to observational purposes, namely, it is changed by SW_1 from that of seismic high frequency seismograph to that of seismic medium frequency seismograph, and SW_2 can change the instrument from a back-ground noise meter to a usual seismograph.

The circuit is set up as an all push-pull connection, in order to decrease internal noise and to increase low frequency gain or stability of the seismograph.

First and second stages of the amplifier circuit are connected as earthed emitter circuit directly coupled to earthed collector circuit.

The noise of the amplifier referred to the input level can be compressed less than $0.5\,\mu V$ by this circuitry, and such an excellent value cannot be easily obtained by the other amplifiers of existing seismographs.

This connection gives us an advantage in the input impedance, too, and most of the transducers in common use at present can be coupled to the amplifier without any over reaction.

As the out-put impedance of each stage in this circuit is less than $10\,K\Omega$, voltage loss from coupling to the next stage is not induced, and consequently design of full circuit is simplified.

Voltage gain per one stage is about 35 db. It seems rather low for the number of transistors used.

Last stage of the amplifier is earthed collector connection. A stabilizing resistor is put into the collector circuit in order to keep DC balance of the out-put more stable.

Source consumption of the amplifier is about $1.8\,mA/6\,V$, and life of dry-cells (4 UM-3 A cells) to keep ordinary characteristic of the amplifier is about a week.

Fig. 2. shows the frequency characteristics of the amplifier sensitivity in conductivity.

It does not seem so sensitive, when its sensitivity is represented with conductance, but we can detect lower level signals than any other existing amplifier without trouble from circuit noise.

Fig. 3. shows temperature effect of gain, which seems to be satisfactory within the ordinary temperature range.

Input impedance of the amplifier was designed so high that it can be connected with most of usual transducers without any over reaction, thus, we can immediately use most transducers which were designed for vacuum tube amplifiers, without introducing any change of construction.

Galvanometer for the amplifier recorder needs following conditions.

i) Internal resistance of the galvanometer must be less than $100\,\Omega$.

ii) Sensitivity of the galvanometer must be higher than $0.1\,mm/\mu A$.

We can construct a high sensitive distortionless seismograph within 100 mm amplitude range on seismogram by using such galvanometer for the amplifier recorder.

We have used Y. E. W. D type oscillograph and Sanei 30 c/s oscillograph for the recorder, because they are suitable and convenient for the amplifier.

Fig. 4. shows the characteristic of the transducer used for the several observations to examine the amplifier utility.

Fig. 5. shows the appearance of the amplifier and the transducer, and it clearly illustrates the portability of the instrument.

The characteristic of the amplifier is shown in Fig. 6., and Fig. 7. shows the overall characteristics of the seismograph in high frequency way and medium frequency way, when the seismograph was constructed with the preceding amplifier, transducer and galvanometer.

It seems the highest sensitivity in medium frequency portable existing seismographs.

T. A. Santo utilized this seismograph in a observation of microseisms at a coast in stormy weather, and succeeded to analyze the relations between microseisms and sea waves[6].

Reproduction in Fig. 8. indicates the seismograms obtained on Oct. 21 st 1959 at Harbour Naarai, Chiba Pref., by Santo.

This result cleared the effect and uniformity of the seismographs sensitivity and frequency characteristic for accurate observation of microseisms.

The amplifier has a meter in its cabinet to read frequency and amplitude of seismic signals from the transducer, and we can detect weak movement of the earth without any special recorder. The meter of 50 μA DC full scale can indicate a signal with sensitivity of about 4 divisions/10^{-6} cm in 1～10 c/s, when the seismograph is used in high frequency way.

We succeeded to search for a suitable place to do a temporary observation for distant timed blast by using this back-ground noise meter.

We had formerly used vacuum tube amplifiers[7] for such explosion seismic observations, and we were restricted ourselves by the commercial AC source both in the location of the observatory and in the upper limit of sensitivity owing to the circuit noise coming from the AC source.

We had also had to carry too heavy instruments for temporary observation. But, now we can observe equally well by small size instruments without any restriction from commercial AC source by using this amplifier.

Fig. 9. shows the seismogram obtained at a station of 290 km distance off from a shot point at Miboro on Nov. 20 th 1959 (5 th Miboro explosion) by the amplifier.

It cleared that this amplifier is superior to other vacuum tube amplifiers in sensitivity of seismograph constructed with them.

On the other hand, the frequency band of the amplifier sensitivity is so wide that microseisms and seismic waves can be recorded similarly in a seismogram. It is unnecessary and rather troublesome for explosion seismological study to record two kind of waves, but we can remove disturbance due to microseisms from such seismogram by changing capacitors C_3 C_9 from 200 μF to 50 μF in order to cut-off low frequency waves.

Thus, we conclude that the utilization of transistor to increase portability and to minimize internal noise of seismograph amplifiers was clarified by the amplifier, and the technique of seismological observation will become higher and higher by introducing transistors in future.

The author intends to develop various aspects of electronic seismometry[8] using transistors for the wider field of seismology.

地震研究所彙報
第38号 (1960) 355-359頁

21. 和歌山—御坊間水準測量結果

地震研究所 宮村摂三
岡田惇

(昭和34年12月22日発表——昭和35年2月10日受理)

1. まえがき

紀伊半島西北部紀伊水道に面する海岸地域における頻発性地震の研究の一部として，地震にともなう地殻変動調査の目的で，1954年3月および12月[1]と1959年10月にそれぞれ和歌山市より御坊市にいたる約70kmの地理調査所一等水準路線について測量をおこなつたので，その結果を報告する．

2. 測量およびその結果

再測量を実施した地域はFig. 1にしめすとおりである．1954年は都合で二期にわけ

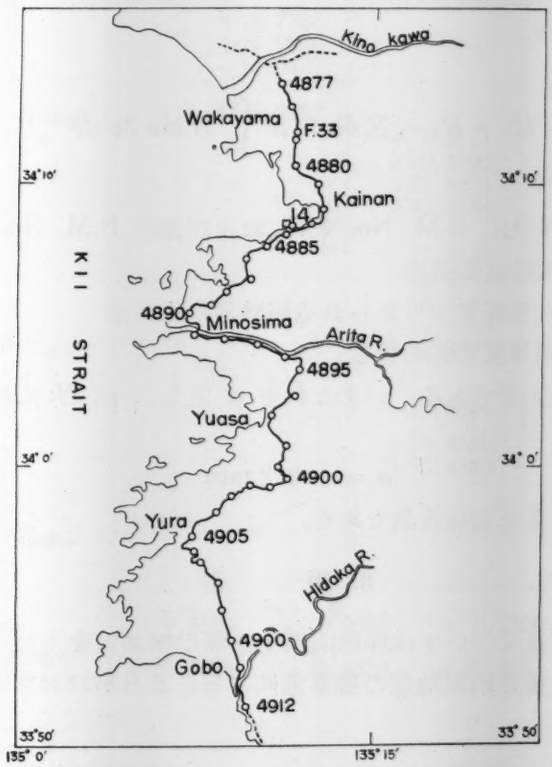

Fig. 1.

1) 地震研究所 和歌山頻発地震群の研究概要 昭和30年1月.

ておこなつた．水準測量については地理調査所一等水準測量の規格にしたがい測量の期間，使用器械等に関することは Table 1. にしめした．

Table 1. Surveying notes.

Date	Route	Instrument	Remarks
1954 March	From Wakayama, No. 4877 to Yuasa, No. 4897	Zeiss Precise Level. Invar staff. (No. 841, 842)	
1954 December	From Yuasa, No. 4897 to Gobō, No. 4912 From Kainan, No. 4881 to Simizu, No. 4884	〃	
1959 October	From Wakayama, No. 4877 to Gobō, No. 4912	Zeiss Opton Ni 2 Precise Level. Invar staff. (No. 841, 842)	Automatic level with plane-plate micrometer[2]

観測の結果は Table 2 にまとめてしめしてある．この成果は標尺の補正のみで楕円補正はなされていない．Table 3 には 1948 年観測の平均結果[3] と No. 4877 を不動としたときの各水準点の垂直変動量をしめした．なおこの路線における楕円補正量を計算してみるとつぎのようになる．

一般式は

$$H_2 - H_1 = \sum \delta h - \beta \cdot \int_{\varphi_1}^{\varphi_2} H \sin 2\varphi \, d\varphi$$

であたえられる．

ここに H_1, H_2: 和歌山 B.M. No. 4877 および御坊 B.M. No. 4912 の真高

φ_1, φ_2 : 両地点の緯度

$\sum \delta h$: 水準測量からえられる両地点の比高差

β : 標準重力式の係数

上式右辺第二項が補正項である．いまこれを α とし．φ, H に両地点の平均値をあたえるならば

$$\alpha = -0.2\,\mathrm{mm}$$

がえられて観測成果に補正される量である．

3. 謝　　辞

本調査に際し現地測量については和歌山県土木部の御助力をえた．また水準点の成果その他にかんしては地理調査所測地部の御厚意によるところがおおきい．ここに謝意を表する次第である．

2) 岡田 惇「紀伊半島南端附近の地殻変動について」地震研究所彙報，**38** (1960), 113～124.

3) Geographical Survey Institute, "Resurvey of the Southwestern Part of Japan after the Great Nankaido Earthquake of 1946", *Bull. Geogr. Surv. Inst.*, **4** (1954), 25.～26.

Table 2. Results of the Levelling Survey (1).

B.M. No.	Location	Relative Heights between Bench Marks ΔH obs.		
		1954. 3	1954. 12	1959. 10
		m		m
4877	Wakayama	− 0.5595		− 0.5704
4878		+ 0.5774		+ 0.5691
F. 33		} + 0.5048		} + 0.4928
4879				
4880		+ 4.9559		+ 4.9530
			m	
4881		− 5.3538	− 5.3453	− 5.3225
4882	Kainan	+ 1.5577	+ 1.5656	+ 1.5752
4883		+24.7934	+24.7856	+24.7501
4884	Simizu	+23.1530		+23.1544
4885		−47.3884		−47.3921
4886		+ 2.0898		+ 2.0725
4887		+16.2830		+16.2902
4888	Simotu	− 3.0652		− 3.0645
4889		−17.4331		−17.4340
4890		+ 0.0580		+ 0.0686
4891	Minosima	} + 7.8711		} + 7.8865
4892				
4893		+ 5.7328		+ 5.7205
4894		+ 0.9968		+ 1.0244
4895		−11.0427		−11.0426
4896	Yuasa	− 5.7753		− 5.7622
4897	〃		+ 9.5711	+ 9.5655
4898			+70.1690	+70.1624
4899			+67.5214	+67.5181
4900			+83.0154	+83.0099
4901			−71.8416	−71.8378
4902			−88.2851	−88.2781
4903			−48.8182	−48.8225
4904			−19.3110	−19.3044
4905	Yura		+71.2828	+71.2836
4906			} −56.6244	} −56.6205
4907				
4908			−14.8835	−14.8940
4909			+ 0.4346	+ 0.4561
4910				− 0.1124
4911	Gobō		} + 0.6134	+ 0.7075
4912				

4833 Kainan	m − 0.6954	m − 0.6998	m − 0.7330
A. 14 tide guage 4884 Simizu	+25.4888	+25.4854	+25.4831

Table 3. Results of the Levelling Survey (2).

(Level change of B. M. No. 4877 is assumed to be zero)

B. M. No.	Location	True Height	Level change		
		1948 obs. 1954 contr.	1954. 3 ~1948. 3	1954. 12 ~1948. 3	1959. 10 ~1948. 3
		m	mm		mm
4877	Wakayama	2.2617	0.0		0.0
4878		1.6828	+27.5		+16.6
F. 33		2.2344	+53.4		+34.2
4879		1.2072	—		—
4880		2.7312	+61.6		+30.4
4881		7.6957	+53.2	(+53.2)	+19.1
4882	Kainan	2.3841	+11.4	+19.9	+ 8.6
4883		3.9594	− 6.0	+10.4	+ 8.7
4884	Simizu	28.7118	+38.6	+29.8	+10.0
4885		51.8647	+38.9		+11.7
4886		4.4757	+39.9		+ 9.0
4887		6.5468	+58.7		+10.5
4888	Simotu	22.8409	+47.8		+ 6.8
4889		19.7738	+49.9		+ 9.6
4890		2.3387	+52.2		+11.0
4891	Minosima	2.4085	+40.7		+10.1
4892		5.2353	—		—
4893		11.8296	+23.4		+ 8.2
4894		17.5487	+37.3		+ 9.8
4895		18.5791	+ 3.9		+ 4.0
4896	Yuasa	7.5342	+ 6.2		+ 6.4
4897	〃	1.7909	−25.4	(−25.4)	−12.1
4898		11.3380		− 1.2	+ 6.5
4899		81.5000		+ 6.0	+ 7.1
4900		149.0187		+ 9.0	+ 6.8
4901		232.0304		+12.9	+ 5.2
4902		160.1937		+ 8.2	+ 4.3
4903		71.9217		− 4.7	− 1.6
4904		23.0959		+ 3.1	+ 1.9
4905	Yura	3.7922		− 3.9	+ 1.5
4906		75.0737		− 2.4	+ 3.8
4907		95.0950		—	—
4908		18.4551		− 7.7	+ 2.4
4909		3.5670		− 2.9	− 3.3
4910*		4.0213		− 1.7	− 1.3
		4.0006**			
4911*	Gobō	3.9097		—	—
		2.3527**			
4912*		4.6164		+ 0.1	− 0.9
		4.6125**			

** 1957. 1 removal and reestablishment.

* old values.

21. Results of Levelling Resurvey between Wakayama and Gobō, Wakayama Prefecture.

By Setumi MIYAMURA and Atusi OKADA,
Earthquake Research Institute.

A levelling resurvey was carried out for about 70 km on the route from Wakayama to Gobō in 1954 and 1959 for the purpose of geodetic investigation of present crustal movement in the local earthquake swarm area. (Fig. 1)

Necessary items of the survey are given in Table 1, and the results are listed in Table 2 and 3.

——所　　報——

◎談話会記事

第 372 回談話会 (昭和 34 年 12 月 22 日)

1. 地震の頻度と応力状態との関係 —地震発生の破壊論的考察 (続報)— 茂木清夫
2. 地震波のスペクトル構造 その2 —マグニチュードと卓越周期— 松本利松
3. 地震学のための二三の計算機プログラム 佐藤泰夫
4. 油壺，松山，間瀬において観測された地殻歪の経年変化について 萩原尊礼
5. 北海道十勝岳の泥流について 村井勇
6. 長野県諏訪地方の温泉の化学成分について 南英一，野口喜三雄，綿抜邦彦，上野精一，一国雅巳
7. 紀伊半島南端部附近の地殻変動について 岡田惇
8. 和歌山御坊間の水準再測結果 岡田惇，宮村摂三

第 373 回談話会 (昭和 35 年 1 月 26 日)

1. 褶曲境界面における弾性波の反射，屈折 その 1，SH 波の場合 (訂正と補遺) 浅野周三
2. 和歌山県北西部地震地域の地殻変動 宮村摂三
3. 地震学のための二，三の計算機プログラム (2) 表面波の分散曲線 佐藤泰夫，木沢綏，(佐藤所員紹介)，山口林造
4. 火山活動に関する地震群に出現した二つの新しい相 木沢綏，(佐藤所員紹介)，山口林造
5. フオツサマグナ西南部 (富士川流域) の地質構造とそのでき方
   I 褶曲のできる速さ
   II 衝上断層のでき方，地震断層との比較
   松田時彦 (津屋所員紹介)
6. Astatic Magnetic Variometer と地震との関係 宮本貞夫 (那須所員紹介)
7. 江の島津浪観測所におけるＩＧＹ期間中の観測 高橋竜太郎，平能金太郎，相田勇，羽鳥徳太郎，清水静子
8. 昭和 34 年 10 月 26 日の福東沖地震に伴つた微少津浪について 高橋竜太郎，相田勇

第 374 回談話会 (昭和 35 年 2 月 23 日)

1. 木造家屋の耐震性 (第4報)
   異種地盤上における二家屋の地震動観測
   西村源六郎，鈴木正治

2. 強震動の一性質 — 高橋竜太郎・羽鳥徳太郎

3. コロンビア型地震計による表面波の観測（その1）
海洋をつたわるレーリー波の分散 — 三東哲夫

4. 地震区とその系列　地体構造発達史との関係 — 宮村摂三

5. 期待震度とその危険率 — 河角広

6. 地震波の吸収係数に就いて — 河角広

7. 菊川地域の地盤調査報告 — 地盤研究会
常時微動による調査 — 金井研究室
脈動による調査 — 岸上研究室
脈動による調査 — 高橋研究室
表土層と震害 — 小坂丈予
地震探査法による調査 — 河角研究室
ボーリングによる調査 — 河角研究室

8. プロトン磁力計による地磁気傾度計 — 力武常次・棚岡巌

9. 地球熱学　第4報
マントル内熱対流その他に伴う熱流量 — 力武常次・宝来帰一

10. 妙高火山泥流堆積物 — 村井勇

11. 北海道駒ケ岳火山の軽石流堆積物 — 村井勇

12. 箱根神山附近の群発地震 — 水上武・宮崎務・行田紀也・伊東喜久子・斎藤正徳

第 375 回談話会（昭和 35 年 3 月 22 日）

1. 地球熱学　第5報
堆積岩の熱伝導率と含水量の関係 — 宝来帰一・上田誠也

2. 地球熱学　第6報
秋田県院内油田に於ける地殻熱流量 — 上田誠也・宝来帰一

3. コロンビア型地震計による表面波の観測（その2）
海洋をつたわるレーリー波の研究（続報） — 三東哲夫

4. 地震波のスペクトル構造（その3）
マグニチユードと卓越周期 — 松本利松

5. 大地震発震スペクトルの方位特性（第1報） — 笠原慶一

6. 発震機構に関する模型実験（序報） — 笠原慶一・Silva・Aynacyan・後藤健一
附　超音波実験装置の製作

7. 微動について — 赤松敬（松沢所員紹介）

8. 田無の脈動観測 — 松沢武雄・浅田敏・田望・赤松敬

9. 不均質半無限体内を伝わるラブ波の存在条件 — 佐藤泰夫・鈴木次郎

第 376 回談話会 (昭和 35 年 4 月 26 日)

1. 東京旧市内の地盤
   土質と震度の定量的関係 — 河角広, 佐藤泰夫, 高橋順子
2. 表面波の波面の拡がりと吸収係数に就いて（補遺） — 吉山良一
3. 三原山におけるガス組成の変化と火山活動（第3報） — 南英一, 野口喜三雄, 綿抜邦彦, 神谷宏, 二村芳甫
4. 地震のマグニチユードを決める公式の係数について — 松本利松

第 377 回談話会 (昭和 35 年 5 月 24 日)

1. 地磁気変化と地電流変化 — 横山泉
2. 岩石の変形及び破壊（第2報） — 茂木清夫
3. 乱れの圧力による地震波の発生について（第1報） — 桃井高夫
4. 浅間火山湧水中の白色沈澱物について（第3報） — （岸上所員紹介）南英一, 小坂丈予
5. 海洋底をつたわるレーリー波の分散（第3報） — 三東哲夫

昭和35年7月5日印刷
昭和35年7月10日発行

東京都文京区本富士町一番地
東京大学構内
編纂兼
発行者　東京大学地震研究所

東京都新宿区山吹町一八四番地
印刷者　笠井康頼

東京都新宿区山吹町一八四番地
印刷所　株式会社国際文献印刷社

売捌所
東京都中央区日本橋通二丁目六番地
丸善株式会社

Sold by Maruzen Co., Ltd., Nihonbashi-dôri, Chûô-ku, Tôkyô.
Price of this copy: 505 Yen. (Postage exclusive.)